Technische Universität München
TUM School of Engineering and Design

Physics-based and probabilistic computational approaches for nanomedicine in oncology

Barbara Wirthl

Vollständiger Abdruck der von der TUM School of Engineering and Design der Technischen Universität München zur Erlangung einer

Doktorin der Ingenieurwissenschaften (Dr.-Ing.)

genehmigten Dissertation.

Vorsitz: Prof. Dr. Julija Zavadlav

Prüfende der Dissertation:

1. Prof. Dr.-Ing. Wolfgang A. Wall
2. Prof. Dr. Bernhard A. Schrefler
3. Prof. Dr. Paolo Decuzzi

Die Dissertation wurde am 11.01.2024 bei der Technischen Universität München eingereicht und durch die TUM School of Engineering and Design am 30.09.2024 angenommen.

Dedicated to all cancer patients bravely fighting this disease and to their loved ones who support them. Your unwavering strength, resilience and faith inspire me.

There is a 'can' in

Cancer

because we CAN beat it!

Abstract

The growth and response to treatment of solid tumours are complex and multifaceted processes: in addition to biological factors, such as genetic mutations and signalling pathways, the physical properties of the tumour cells and their microenvironment are key determinants. Examples of such physical properties are the stiffness of the extracellular matrix and the flow of the interstitial fluid. Both influence the growth of the tumour and its response to treatment but also counteract the transport of drugs. We employ a computational multiphase porous-media model of tumour growth that can consider these different biological and physical factors and their interactions. To advance oncology, cancer research needs to move beyond the boundaries of a single discipline and integrate knowledge from different fields. This thesis aims to contribute to this integration by developing a physics-based computational model of nanomedicine transport in the tumour and its microenvironment. Integrating the model with probabilistic approaches to sensitivity analysis and calibration bridges the gap to experimental data.

Nanoparticle drug delivery systems have emerged as a promising approach to improve the delivery of drugs to tumours. Yet, the design of such systems is challenging. We therefore develop a computational model of nanoparticle transport in the tumour and its microenvironment, which includes major transport barriers, such as the blood vessel wall or the interstitial fluid flow. Our study of passive targeting based on the enhanced permeability and retention (EPR) effect reveals that a non-perfused core and an increased interstitial fluid pressure—typical features of solid tumours—limit nanoparticle delivery. The size of the vessel-wall pores and the permeability of the blood vessel wall have a major impact on the amount of nanoparticles that reach the tumour, and only small nanoparticles with a higher diffusivity can penetrate the tumour sufficiently to reach the core. We then extend our model to active targeting by magnetic nanoparticles guided by an external magnetic field: we study the capture of magnetic nanoparticles under the combined effect of fluid flow and magnetic forces. Our multiphase porous-media approach enables us to model interstitial fluid flow around the tumour fully coupled to the flow in the tumour. The combination of a Smoluchowski diffusion-advection equation for the nanoparticle transport with the derived analytical expression for the magnetic force exerted by a cylindrical magnet allows us to efficiently investigate different magnet configurations.

Such a model is subject to uncertainties for a number of reasons, in particular the lack of knowledge about the exact values of the model parameters. Determining the uncertain model parameters is often very elaborate and costly. Identifying the most influential parameters is therefore essential in order to focus efforts on them. To this end, we perform a sensitivity analysis based on the Sobol method. We demonstrate that the use of a Gaussian process as a metamodel enables a global variance-based sensitivity analysis even of complex, computationally expensive models, including a transparent declaration of the uncertainties involved in the estimation process. Relatively small numbers of evaluations of the full model suffice to separate the most influential parameters from the non-influential ones, and even higher-order interaction effects can be quantified. With the most influential parameters identified, we bridge the gap to experimental data: we perform a Bayesian calibration to experimental data of neuroblastoma tumour spheroids in collagen hydrogels

in microfluidic devices. While the inferred posterior distribution allows us to match the experimental data, including the high variability, the knowledge gained for the uncertain parameters is limited by the insufficient and noisy experimental data.

The physics-based *in silico* model developed in this thesis enables an efficient and systematic exploration of the design space of nanoparticle drug delivery systems, combined with a better understanding of the underlying physical mechanisms, the uncertainties involved, and the integration of experimental data. As an effective tool for enhanced hypothesis testing and strategy generation, it expedites translation to *in vivo* scenarios and ultimately to clinical practice, thereby improving therapeutic outcomes and limiting adverse side effects for cancer patients.

Zusammenfassung

Tumorwachstum und das Ansprechen auf eine Therapie sind komplexe Prozesse. Neben biologischen Faktoren, wie Genmutationen und Signaltransduktion, sind auch die physikalischen Eigenschaften der Tumorzellen und ihrer Mikroumgebung von entscheidender Bedeutung. Beispiele hierfür sind die Steifigkeit der extrazellulären Matrix und der Fluss des interstitiellen Fluids. Diese beeinflussen das Wachstum des Tumors und sein Ansprechen auf die Behandlung, während sie gleichzeitig dem Transport von Medikamenten entgegenwirken. Wir verwenden ein physikbasiertes Mehrphasenmodell, das auf der Theorie der porösen Medien beruht, um das Tumorwachstum zu modellieren und die Wechselwirkungen zwischen den verschiedenen biologischen und physikalischen Faktoren zu berücksichtigen. Um die Hürden auf dem Weg zu neuen und verbesserten Therapien zu überwinden, muss die Krebsforschung interdisziplinär werden und das Wissen aus verschiedenen Bereichen zusammenführen. Die vorliegende Arbeit leistet dazu einen Beitrag, indem sie ein physikbasiertes Simulationsmodell für den Transport von Nanopartikeln als Wirkstoffträger im Tumor und seiner Mikroumgebung entwickelt. Um die Lücke zu experimentellen Daten zu schließen, wird dieses Modell weiter mit probabilistischen Ansätzen der Sensitivitätsanalyse und Bayes'scher Kalibrierung verknüpft.

Wirkstofftransportsysteme auf der Basis von Nanopartikeln haben sich als vielversprechender Ansatz für den Transport von Medikamenten zu Tumoren erwiesen. Die Optimierung solcher System stellt jedoch eine Herausforderung dar. Wir entwickeln daher ein Simulationsmodell für den Transport von Nanopartikeln im Tumor und seiner Mikroumgebung, das wichtige Transportbarrieren wie die Blutgefäßwand oder den Fluss des interstitiellen Fluids berücksichtigt. Unsere Studie zum passiven Targeting zeigt, dass ein nicht durchbluteter Tumorkern und ein erhöhter Druck im Tumor – beides typische Eigenschaften von soliden Tumoren – den Transport von Nanopartikeln einschränken. Die Größe der Poren und die Permeabilität der Blutgefäßwand haben einen starken Einfluss darauf, wie viele Nanopartikel den Tumor erreichen. Zudem können nur kleine Nanopartikel mit einer hohen Diffusivität den Tumor ausreichend durchdringen, um auch die Zellen im Tumorkern zu erreichen. Anschließend erweitern wir unser Modell auf das aktive Targeting durch magnetische Nanopartikel, die durch ein externes Magnetfeld gesteuert werden. Wir untersuchen das Einfangen von magnetischen Nanopartikeln unter dem Einfluss von Fluidströmung und magnetischen Kräften. Unser Ansatz, der auf der Theorie der mehrphasigen porösen Medien basiert, erlaubt es uns, die Strömung des interstitiellen Fluids um den Tumor herum vollständig gekoppelt mit der Strömung im Tumor zu modellieren. Die Kombination einer Smoluchowski-Diffusions-Advektions-Gleichung für den Nanopartikeltransport mit dem hergeleiteten analytischen Ausdruck für die magnetische Kraft eines zylindrischen Magneten ermöglicht eine effiziente Untersuchung verschiedener Magnetkonfigurationen.

Ein solches Modell ist aus verschiedenen Gründen mit Unsicherheiten behaftet. Insbesondere sind die genauen Werte der Modellparameter oft nicht bekannt und ihre Bestimmung ist aufwendig und kostspielig. Es ist daher unerlässlich, zunächst die wichtigsten Parameter zu identifizieren und sich dann auf diese zu konzentrieren. Dazu führen wir eine Sensitivitätsanalyse basierend auf der Sobol-Methode durch und zeigen, dass die Verwendung eines Gauß-Prozesses als Metamodell eine

globale varianzbasierte Sensitivitätsanalyse auch für komplexe, rechenintensive Modelle ermöglicht, einschließlich einer transparenten Angabe der beinhalteten Unsicherheiten. Wenige Auswertungen des Simulationsmodells reichen aus, um die einflussreichsten Parameter von den nicht einflussreichen zu unterscheiden und auch Interaktionseffekte höherer Ordnung quantifizieren zu können. Sobald die einflussreichsten Parameter identifiziert sind, schlagen wir die Brücke zurück zu den experimentellen Daten: Wir führen eine Bayes'sche Kalibrierung mit experimentellen Daten von Neuroblastom-Tumorsphäroiden in Kollagen-Hydrogel in einem mikrofluidischen Chip durch. Während die *A-posteriori*-Wahrscheinlichkeitsverteilung eine Übereinstimmung mit den experimentellen Daten erreicht, einschließlich der hohen Variabilität, ist der Erkenntnisgewinn für die unsicheren Modellparameter begrenzt durch die unzureichenden und verrauschten experimentellen Daten.

Das in dieser Arbeit entwickelte physikbasierte Simulationsmodell ermöglicht eine effiziente und systematische Untersuchung des Designraums von Nanopartikel-Wirkstofftransportsystemen, verbunden mit einem besseren Verständnis der zugrunde liegenden physikalischen Mechanismen, der damit verbundenen Unsicherheiten und der Integration experimenteller Daten. Als wirksames Instrument für eine verbesserte Hypothesenprüfung und Strategieentwicklung beschleunigt es die Übertragung auf *in vivo*-Szenarien und schließlich auf die klinische Praxis. Dadurch können therapeutische Ergebnisse verbessert und schwerwiegende Nebenwirkungen für Krebspatienten begrenzt werden.

Contents

1 Introduction

> As we launch ourselves into this story, there's one thing we all might agree on: cancer is complicated. However, and you might find this surprising, what emerges from short answers to a handful of rather obvious questions is that cancer is a great paradox.
>
> *Understanding Cancer*, Robin Hesketh [1]

1.1 Motivation

Why are some tumours benign while others are malignant? Why do some tumours metastasise while others do not? Why do some tumours respond to treatment initially but then become resistant? And, why is this different for each patient? These are some of the questions that cancer researchers have been trying to answer for decades and that are part of the paradox of cancer.

A tumour (Latin, *swelling*) is an abnormal, autonomously growing mass of tissue resulting from uncontrolled cell proliferation: the cells have escaped the normal regulatory circuits of cell growth, divide at an uncontrollably high rate, and evade apoptosis (programmed cell death) [2, 3]. As long as tumours remain localised, they are considered benign. However, if tumour cells acquire the ability to invade neighbouring tissue and metastasise to distant sites, they are considered malignant—what we commonly refer to as cancer [4, 5]. While most benign tumours can be removed surgically and do not pose a threat to the patient, malignant tumours cause the vast majority of cancer-related deaths. Today, many cancers are treatable and have a 5-year survival rate of 90% or more [6]. Yet, despite an intense scientific effort with several decades of research and nearly two million papers on cancer [5], the global societal and personal burden of cancer continues to grow [7]. Despite many important insights and therapies, the improvement of cancer mortality rates still lags behind that of other diseases [8]. So much progress has been made, yet so much remains to be done, and so many paradoxes remain to be solved.

While tumour growth has traditionally been considered a disease of the cell alone, e.g., caused by genetic changes, recent advances in cancer research have highlighted the critical role of the tumour microenvironment [9]. In addition, the link between signalling pathways and the physical properties of the tumour and its microenvironment plays a pivotal role in comprehending the growth of tumours and enhancing cancer therapies. From a biological point of view, in a tumour with millions of cells,

every cell could theoretically have a different genetic mutation [10]. From a physical point of view, cancer is not solely a genetic disease but also depends on the physical properties of the tumour and its microenvironment [11]: for example, an elevated interstitial fluid pressure induces treatment resistance, or an increased stiffness of the extracellular matrix (ECM) promotes invasiveness and metastasis [9]. Hence, the tumour and its microenvironment form a biologically and physically complex system. Specifically, this comprises transport barriers that limit the delivery of drugs to the tumour, consequently impeding the efficacy of cancer therapies.

Among the different therapeutic approaches to cancer, chemotherapy is widely used and has significantly reduced mortality rates associated with various types of cancer [12]. Yet, chemotherapy causes tremendous side effects, physically and psychologically [13], during treatment and even long-term after the treatment has ended [14, 15]. The problem is that not only diseased tissue is exposed to the drugs, but healthy tissue is also attacked: drugs are systemically distributed throughout the body and are not specific to the tumour. The maximum dose tolerated by the patient is therefore limited by the toxicity to healthy tissue and still not sufficient to kill all tumour cells [16, 17]. This was the basis for Paul Ehrlich's idea of a *magic bullet*, which selectively kills cancer cells while leaving surrounding healthy tissue undamaged [18, 19]. The concept of a magic bullet has been present for over a century. However, it is only in recent years that the development of nanomedicine appears to have brought it within reach. Nanoparticles have emerged as a promising tool for more specific tumour targeting because of their unique physical properties and their potential for sophisticated functionalisation, e.g., loading them with chemotherapeutic drugs [20], coating them with cancer-cell recognising ligands [21], or guiding magnetic nanoparticles to the tumour using an external magnetic field [22, 23]. Yet, despite this potential, the transport of nanoparticles to the cancer cells is challenging due to the transport barriers that the nanoparticles have to overcome to reach the cancer cells: Dai *et al.* [21] showed that less than 14 out of 1 million (0.0014% injected dose) intravenously injected nanoparticles coated with cancer-cell recognising ligands actually reached the tumour cells.

To understand and overcome these transport barriers, experimental research is indispensable, e.g., based on *in vitro* and *in vivo* experiments. However, control over the experimental conditions and measurement techniques limits its scope. Besides, experiments are often expensive and time-consuming, and even with unlimited resources, testing all possible scenarios, conditions, and configurations is impossible. In recent decades, considerable attention has therefore been devoted to the development of computational models that simulate tumour growth and treatment strategies. Computational models are a powerful tool to explore a large number of possible model scenarios in a systematic and efficient way—thereby complementing experimental research. Such an integrated approach combining computational models and experimental research improves hypothesis testing, strategy generation, and clinical relevance [24]. The goal of computational models is to provide predictions to better understand the underlying biological phenomena and ultimately support decision-making in a medical context.

The predictions of computational models are inherently subject to uncertainties. On the one hand, the computational model includes sources of uncertainty, e.g., due to the simplifications and assumptions made, the numerical methods used, or the input parameters, which are often not known precisely. On the other hand, the experimental data used to calibrate the model is additionally subject

to uncertainties, e.g., due to measurement errors. To consider these uncertainties, probabilistic approaches are used.

The essential characteristic of a probabilistic approach is the explicit use of probability distributions to describe the involved uncertainty [25]. The number of uncertain input parameters, which have to be calibrated, is often large. In this context, a sensitivity analysis first allows the separation of the most influential parameters from the non-influential parameters. Subsequently, Bayesian calibration allows inferring knowledge about the uncertain input parameters from experimental data—while accounting for the underlying uncertainties.

The complexity of tumour growth and drug delivery requires an interdisciplinary approach to understand the underlying mechanisms and develop new therapies. This thesis follows such an approach by developing a physics-based computational model of nanomedicine for cancer treatment and combining it with probabilistic methods to quantify the uncertainties and integrate experimental data. The following sections introduce these two main aspects of this thesis.

1.1.1 Physics-based computational modelling of cancer nanomedicine

Mathematical and computational modelling is playing an increasingly prominent role in cancer research—so much so that a large consortium of researchers recently published a roadmap for the future [26]. Computational models of tumour growth span a wide range of scales, from the molecular level to the tissue level, and a wide range of approaches, from discrete to continuum models, as reviewed by Deisboeck *et al.* [27].

Models at the molecular level investigate signalling pathways based on ordinary differential equations, e.g., [28, 29]. At the next scale, the microscopic scale, models focus on the interactions between individual cells and are therefore called cell-based, agent-based or discrete models. Metzcar *et al.* [30] provide a comprehensive review of cell-based models of tumour growth. While cell-based models account for the diversity of cellular dynamical features and thus explore tumour heterogeneity, their computational cost limits their application to millions of cells in a larger tumour growing over a longer time scale. In contrast, models at the macroscale do not consider individual cells but instead describe the tumour as a continuum based on partial differential equations, such as conservation laws. Continuum-based models can capture volumetric tumour growth on a larger scale (in time and space)—which is also accessible to conventional clinical imaging modalities. Most importantly, continuum-based models are based on fundamental physical principles and can thus describe stresses, strains, fluid flow, and diffusion in the tumour microenvironment—physical quantities which cell-based models cannot describe but which have been recognised as crucial to understanding tumour growth in recent years [9]. Finally, hybrid models combine the strengths of both cell-based and continuum-based approaches, e.g., Phillips *et al.* [31] combine an agent-based model of vascular changes with a continuum model of nutrient dynamics.

We will use a multiphase computational model based on porous media to simulate the growing tumour and its microenvironment [32, 33]. Based on the theory of porous media, the model consists of a solid phase, the ECM, with the pore space filled with fluid phases, the interstitial fluid, the tumour cells and the healthy host cells. Such a physics-based approach at the continuum scale is a powerful

tool to build a versatile model able to investigate a wide range of biological processes. In particular, building the model on first principles provides a physically plausible description of the tumour and its microenvironment, including mass transport through biological and physical barriers—also known as transport oncophysics barriers [34–37]. Exploiting these transport characteristics to overcome barriers is the key to improving the design of therapeutic strategies.

Amongst the multifarious therapeutic approaches to cancer, nanomedicine is a promising approach to improve the delivery of drugs to the tumour. Nanoparticles are organic or inorganic particles with a size of 1 nm to 100 nm, which puts them on the same length scale as important building blocks of the human body: the DNA has a diameter of 2.5 nm, and a red blood cell has a diameter of 7 µm [38]. Nanoparticles are very versatile because of the vastness of their design space and because their size, shape, stiffness, and surface functionalisation can be tailored to the application [39]. Compared to conventional chemotherapeutics, nanomedicine provides several approaches to more specific tumour targeting. On the one hand, passive targeting exploits the enhanced permeability and retention (EPR) effect: due to the leakiness of the tumour vasculature and the inhibited lymphatic drainage, nanoparticles passively accumulate in the tumour [40–42]. On the other hand, active targeting exploits the overexpression of certain receptors on the surface of cancer cells by functionalising the nanoparticles with ligands that bind to these receptors. Alternatively, magnetic nanoparticles can be guided to the tumour using an external magnetic field—a technique known as magnetic drug targeting, which we will further explore in this thesis.

Due to their small size, magnetic nanoparticles form a single magnetic domain: they become highly magnetic in the presence of an external magnetic field but revert to a non-magnetic state when the field is removed—a property known as superparamagnetism [43]. To capture the magnetic nanoparticles in the tumour, the magnetic force must be strong enough to overcome counteracting forces, e.g., fluid forces caused by the blood flow or interstitial fluid flow, and further transport barriers, e.g., the wall of the blood vessels. However, this is hard to achieve because of the inherently weak magnetic forces—especially deeper in the body. These challenges make the design and successful application of magnetic nanoparticle-based cancer therapy impossible purely via trial-and-error approaches in experimental research. Here, computational models can help by predicting the transport of the nanoparticles and hence guide the design of novel prototypes.

1.1.2 Probabilistic approaches: sensitivity analysis and Bayesian calibration

Physics-based computational models can describe the behaviour of a system and predict the outcome, even under unobserved circumstances. Nevertheless, Saltelli [44] states that physics-based models are customarily over-parametrised: they include more laws and parameters than available data would support. This becomes particularly critical when model parameters are to be determined, e.g., by inverse analysis. Here, sensitivity analysis becomes a crucial part of model development [45].

For most input parameters of a model, the value is not known precisely but is subject to uncertainty. This uncertainty in the model input parameters propagates through the model, resulting in uncertainty in the model output. Uncertainty quantification (UQ) quantifies this uncertainty in the model output. Sensitivity analysis apportions the uncertainty in the model output to the uncertainty

in the model input parameters [46, 47]. This enables threefold conclusions: first, we can identify the most influential parameters on which further experimental research should focus; second, we can identify parameters with little or no effect, which can be set to a fixed value within their range; third, we can identify and quantify interactions between parameters. This knowledge avoids wasting resources on determining non-influential parameters and, thus, expedites the efficient design of future studies both computationally and experimentally.

We will use the Sobol method [48, 49], a variance-based global sensitivity analysis method. A global sensitivity analysis is usually computationally expensive, and therefore modellers often rely on local methods alone: local methods provide a local measure at a base point, only exploring one point in the input space and resulting in a deficient sensitivity analysis [50]. Global methods, such as the Sobol method, explore the entire input space and provide a global measure of sensitivity but are computationally expensive because they require a large number of model evaluations. We mitigate this drawback by introducing a Gaussian process as a metamodel for the full model [51]. This introduces an additional source of uncertainty in the estimation of the Sobol indices, which we will quantify and include in the analysis based on Le Gratiet *et al.* [52].

After identifying which parameters are the most influential, the next step is to infer knowledge about these parameters from experimental data. Direct measurements are often impossible, and the parameters must be estimated based on inverse analysis. There are two main approaches to inverse analysis: deterministic and probabilistic. Deterministic optimisation techniques, e.g., the Levenberg–Marquardt algorithm [53, 54], yield a point estimate for the best fit to the experimental data but cannot quantify how certain this estimate is. Probabilistic (Bayesian) approaches infer the entire probability distribution of the model parameters, naturally including the uncertainty in the experimental data and the uncertainty in the inferred parameters. We will use the sequential Monte Carlo method [55–57] to perform Bayesian calibration: this state-of-the-art Bayesian approach comes at a high computational cost, which we will mitigate again using a Gaussian process as a metamodel.

1.2 Contributions of this thesis

This thesis aims to contribute to unravelling the complexity of cancer and its treatment through an interdisciplinary approach spanning computational modelling, probabilistic approaches, physics, and experimental research in biology and medicine. Fig. 1.1 presents the main contributions, how they are connected, and how they connect different disciplines. The main contributions of this thesis are:

(1) A continuum-based model of the passive transport of drug-loaded nanoparticles to and in a vascular tumour [58]. We extend the multiphase porous-media model of tumour growth to include the passive transport of drug-loaded nanoparticles via the interendothelial pathway, the transendothelial pathway, and lymphatic drainage. Our model reproduces transport characteristics known from experimental and clinical data: the non-perfused core and the increased interstitial pressure in the tumour core (resulting in an outward flow of interstitial fluid) limit nanoparticle delivery. In particular, we show that the number of nanoparticles reaching the tumour depends on the size of the vessel-wall pores and the permeability of the blood vessel endothelium. The nanoparticles

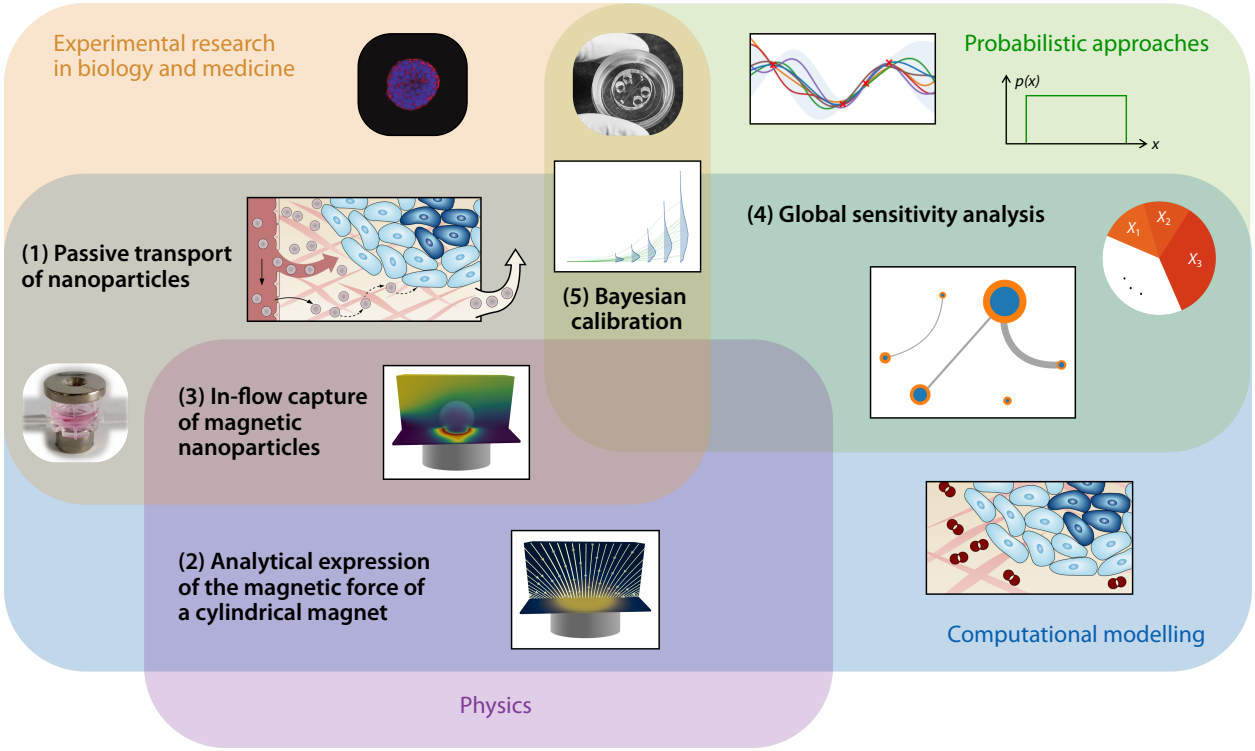

Figure 1.1 The main contributions of this thesis and how they connect different disciplines: (1) A continuum-based model of the passive transport of drug-loaded nanoparticles to and in a vascular tumour [58], (2) An analytical expression for the magnetic force of a cylindrical permanent magnet of finite length on magnetic nanoparticles [59], (3) A continuum-based model of the capture of magnetic nanoparticles under the combined effect of fluid flow and an external magnetic field [60], (4) Global sensitivity analysis based on Gaussian-process metamodelling [61], and (5) Bayesian calibration based on *in vitro* observations of neuroblastoma spheroids in a hydrogel microenvironment [62].

only reach the tumour core if the transport in the interstitial fluid is diffusion-dominated, i.e., in the case of small nanoparticles with a higher diffusivity.

(2) An analytical expression for the magnetic force of a cylindrical permanent magnet of finite length on magnetic nanoparticles [59]. We derive an analytical expression for the magnetic force based on elliptic integrals, which enables us to directly evaluate the magnetic force with minimal computational effort compared to numerically solving Maxwell's equations. We can then study different magnet configurations in three dimensions—instead of the two-dimensional models commonly used in the literature. A Python implementation of the analytical expression is made available under an open-source license [63]

(3) A continuum-based model of the capture of magnetic nanoparticles under the combined effect of fluid flow and an external magnetic field [60]. We present a continuum approach to model the in-flow capture of magnetic nanoparticles based on the Smoluchowski advection-diffusion equation. The fluid flow around the tumour spheroid is fully coupled to the flow inside the tumour spheroid—which is naturally included in our multiphase porous-media approach. Investigating the capture of magnetic nanoparticles in a controlled flow environment with a tumour spheroid, as commonly used in experimental *in vitro* setups, forms the basis for the study of more complex *in vivo* or *ex vivo* scenarios.

(4) Global sensitivity analysis based on Gaussian-process metamodelling [61]. We demonstrate how a global variance-based sensitivity analysis can be performed using Gaussian-process metamodelling to estimate the Sobol indices. Since employing a Gaussian process as a metamodel introduces additional uncertainty, we include a transparent declaration of the uncertainties involved in the estimation process. This approach enables a global sensitivity analysis for computationally expensive models with a moderate number of input space dimensions at a manageable computational cost—including higher-order Sobol indices to quantify interaction effects. We show that we can identify the most influential parameters and separate them from the non-influential parameters with a small number of training samples.

(5) Bayesian calibration based on *in vitro* observations of neuroblastoma spheroids in a hydrogel microenvironment [62]. We combine our tumour growth model with *in vitro* experiments with tumour spheroids in a collagen hydrogel in microfluidic devices such that both include the interactions between the tumour and its microenvironment—a unique combination of state-of-the-art techniques on the computational and experimental side. We apply Bayesian calibration based on the sequential Monte Carlo approach to infer knowledge about the uncertain input parameters. While the inferred posterior distribution allows us to match the experimental data, the knowledge gained about the uncertain input parameters is still limited—even with state-of-the-art techniques in all parts of the workflow.

The contributions and achievements of this thesis resulted in the following publications:

- B. Wirthl*, J. Kremheller*, B. A. Schrefler and W. A. Wall. 'Extension of a Multiphase Tumour Growth Model to Study Nanoparticle Delivery to Solid Tumours'. *PLOS ONE* 15.2 (2020), e0228443 [58]. *Co-first authorship

- B. Wirthl, V. Wirthl and W. A. Wall. 'Efficient Computational Model of the In-Flow Capturing of Magnetic Nanoparticles by a Cylindrical Magnet for Cancer Nanomedicine'. *Physical Review E* 109.6 (2024), 065309 [59].
- B. Wirthl, C. Janko, S. Lyer, B. A. Schrefler, C. Alexiou and W. A. Wall. 'An in silico model of the capturing of magnetic nanoparticles in tumour spheroids in the presence of flow'. *Biomedical Microdevices* 26.1 (2024) [60].
- B. Wirthl, S. Brandstaeter, J. Nitzler, B. A. Schrefler and W. A. Wall. 'Global Sensitivity Analysis Based on Gaussian-process Metamodelling for Complex Biomechanical Problems'. *International Journal for Numerical Methods in Biomedical Engineering* 39.3 (2023), e3675 [61].
- S. Hervas-Raluy*, B. Wirthl*, P. E. Guerrero, G. Robalo Rei, J. Nitzler, E. Coronado, J. F. de Mora Sainz, B. A. Schrefler, M. J. Gomez-Benito, J. M. García-Aznar and W. A. Wall. 'Tumour Growth: An Approach to Calibrate Parameters of a Multiphase Porous Media Model Based on in Vitro Observations of Neuroblastoma Spheroid Growth in a Hydrogel Microenvironment'. *Computers in Biology and Medicine* 159 (2023), 106895 [62]. *Co-first authorship

1.3 Outline

The remainder of this thesis is organised as follows. Chapter 2 introduces the multiphase porous-media model of tumour growth, which the subsequent chapters build upon. Chapter 3 extends the model to include drug-loaded nanoparticle transport: first focusing on passive transport based on the EPR effect and then on active transport using magnetic nanoparticles and an external magnetic field. Chapter 4 presents a global sensitivity analysis based on estimating the Sobol indices of the model parameters using Gaussian-process metamodelling. Chapter 5 shows how state-of-the-art experimental data can be integrated into the model using Bayesian inverse analysis. Finally, the conclusion and outlook in Chapter 6 summarise the main findings of this thesis and give an outlook on future research directions.

2 A multiphase porous-media model of tumour growth

2.1 Methods

The following subsections provide a concise summary of the multiphase porous-media model of tumour growth, which forms the basis of the work presented in this thesis. The model has previously been presented in various forms [32, 33, 64–74], including features such as a deformable ECM [33], invasion of host tissue [67] and different approaches to model the vasculature and angiogenesis [72–74]. Kremheller [75] presented an extensive description of the model equations and their derivation.

2.1.1 General concepts

A porous-media approach to model tumour growth. In the tumour microenvironment, the ECM forms a porous network around cells: it guarantees the structural integrity of the tissue and modulates processes such as cell migration [76]. The cells and the interstitial fluid fill the pore space of the ECM, flow and move through it, and interact with it. As such, the ECM, the cells, and the interstitial fluid form a multiphase porous medium. The ratio of the ECM pore volume to the total volume is the porosity ε

$$\varepsilon \, \mathrm{d}\Omega_t = \mathrm{d}\Omega_t^f \tag{2.1}$$

with Ω_t being the current total volume and Ω_t^f the current fluid volume, composed of cells and interstitial fluid, at a specific time t. The porosity is a function of time and changes as the tumour grows and *pushes* the ECM aside. Considering the tumour cells and host cells as (viscous) fluid phases directly allows us to model the relative movement of the different phases, which is essential for the invasion of host tissue, to name one example. The vasculature is modelled as an additional independent porous network where blood flows. We also include several species which are transported by the different phases, namely oxygen (as the nutrient driving the growth of the tumour), necrotic tumour cells (formed when deprived of oxygen) and nanoparticles (used to deliver drugs to the tumour). All components are schematically depicted in Fig. 2.1A.

When describing a porous medium, we distinguish between two scales: the microscale and the macroscale, depicted in Fig. 2.1B. At the microscale, all of these components are clearly distinguishable, and the interfaces are fully resolved. Also, the physical laws—according to classical continuum mechanics—are formulated at the microscale. However, the exact interface geometry is often not of interest and experimental methods to determine it are not available or not efficient. So, we

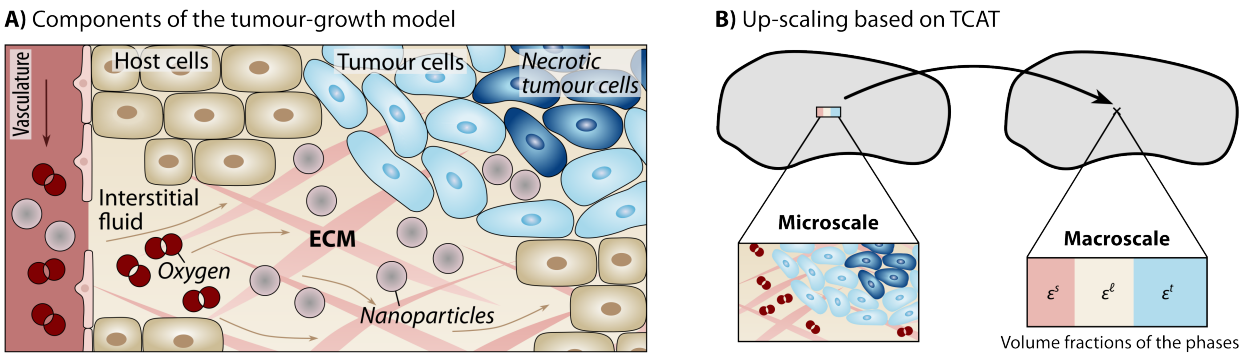

Figure 2.1 A) Components of the multiphase tumour growth model. The model comprises a solid phase (the extracellular matrix, ECM), three fluid phases (host cells, tumour cells, and interstitial fluid) flowing through the pore space, and the vasculature (which is modelled as an additional independent porous network). The arrows indicate the flow of the fluid phases through the ECM. In addition, the phases transport species, namely necrotic tumour cells, oxygen, and nanoparticles. B) Microscale to macroscale up-scaling. At the microscale, all components are resolved. Up-scaling results in a continuous description at the macroscale, where the phases are described by volume fractions ε^α. Employing the thermodynamically constrained averaging theory (TCAT) ensures a firm connection between the two scales.

describe the system at the macroscale. This leads to a continuous description of the porous medium with the phases modelled as overlapping continua. Hence, at the macroscale, the phases cannot be distinguished any more and occupy a shared domain.

When up-scaling from the microscale to the macroscale, we employ the thermodynamically constrained averaging theory (TCAT), developed by Gray and Miller [77, 78], to maintain a firm connection between the two scales. This brings the added benefit that all macroscale quantities maintain a distinct connection to their microscale counterparts—lending the model a high degree of physical interpretability [32].

At the macroscale, the different phases are described by volume fractions ε^α with $\alpha = t, h, \ell$, where the superscript α generically denotes the fluid phases, the superscript t the tumour cells, h the host cells, and ℓ (*liquid*) the interstitial fluid. We further assume that the porous medium is fully saturated, i.e., the fluid phases completely fill the pore volume, and hence

$$\varepsilon = \varepsilon^t + \varepsilon^h + \varepsilon^\ell. \tag{2.2}$$

Together with the volume fraction of the ECM (indicated by the superscript s) and the volume fraction of the vasculature (indicated by the superscript v) the volume fractions sum up to unity:

$$\varepsilon^s + \varepsilon^t + \varepsilon^h + \varepsilon^\ell + \varepsilon^v = 1. \tag{2.3}$$

The saturation of the fluid phases in the pore space is given by

$$S^\alpha = \frac{\varepsilon^\alpha}{\varepsilon} \quad \text{for} \quad \alpha = t, h, \ell, \tag{2.4}$$

and the saturations hence also have to sum up to unity:

$$S^t + S^h + S^\ell = 1. \tag{2.5}$$

Since the ECM is deformable, the porosity, volume fractions, and saturations change as the tumour grows.

Employing a multiphase porous-media approach to model tumour growth has several unique advantages, which, based on [79], comprise:

1. The macroscopic behaviour of the porous medium is rigorously connected to the microscale physics and microstructure.
2. The different phases of the porous medium may consist of several species, e.g., tumour cells subdivide into living and necrotic tumour cells.
3. If the system is not in equilibrium, e.g., the tumour grows, mass transport between the different phases and species can capture this.
4. Interactions and momentum exchange occur between the individual fluid phases and between these and the solid phase. Therefore, fluid-solid mechanical interactions contribute to the strains and stresses in the solid phase.

Thermodynamically constrained averaging theory (TCAT) for up-scaling. To achieve the up-scaling from the microscale to the macroscale, we employ the thermodynamically constrained averaging theory (TCAT) [80, 81]: by explicitly employing all approximations, TCAT ensures that resultant macroscale models are consistent with microscale variable definitions and conventions [77].

Fig. 2.2 schematically summarises the elements of the TCAT and their connection, based on [77, 80, 81]. The yellow boxes denote the starting point: the standard microscale conservation equations of mass, momentum, and energy for all entities—including fluid and solid phases, interfaces, common curves, and common points. In addition, microscale thermodynamic equations are postulated for each entity, setting the TCAT apart from other averaging theories. Thermal and mechanical equilibrium conditions are obtained based on variational techniques. Subsequently, averaging theorems are employed to change the scale from microscale to macroscale. This averaging process results in five types of larger-scale equations presented in maroon boxes.

Particular attention needs to be paid to the evolution equations. At the microscale, interfaces that separate phases are fully resolved and specified as boundary conditions. At the macroscale, however, phases are co-located: each phase occupies a fraction of the total volume, defined using porosity, volume fraction, and saturation. These properties are functions of time and do not exist on the microscale. We hence need additional equations, the so-called evolution equations, to describe the evolution of the volume fractions.

Yet, this still yields a system with more unknowns than equations, and we need additional closure relations to produce a closed, solvable model. An essential concept of the TCAT is using an entropy inequality to derive these closure relations. Miller *et al.* [82] recently presented the general simplified entropy inequality (SEI) for multiphase porous-media models and showed how to use the flux-force

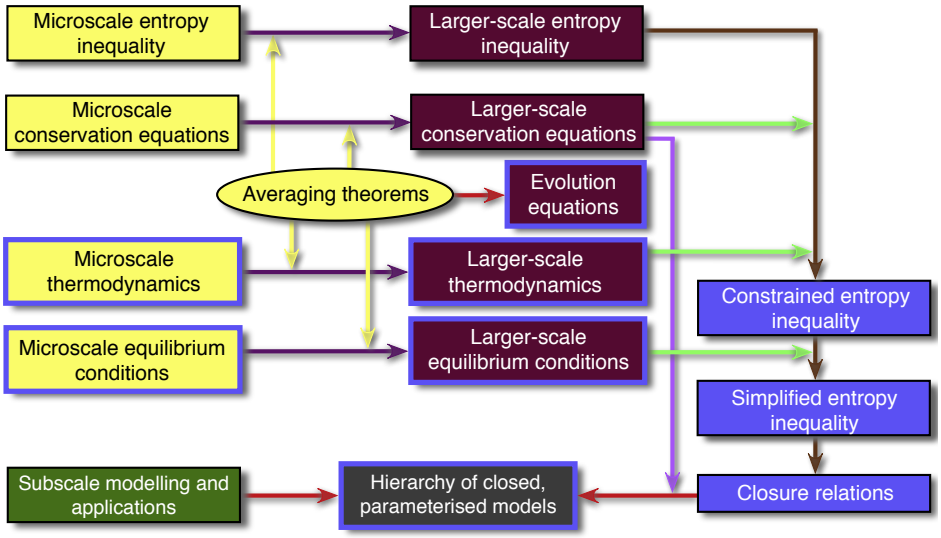

Figure 2.2 Elements of the thermodynamically constrained averaging theory. The figure is reproduced in a slightly modified version from [81] with permission from Elsevier.

pairs in the SEI to formulate a permissible set of closure relations. Although the tumour growth model employed in this thesis exploits several aspects of TCAT formulations, a complete and rigorous hierarchy of models formulated and closed using TCAT procedures remains to be established [82].

To demonstrate how the volume fractions and mass transfer terms enter the macroscale equations directly through rigorous up-scaling based on TCAT, we exemplarily present the averaging techniques for up-scaling the mass balance of a fluid phase α, based on [77, 83]. The microscale conservation of mass $\mathcal{M}_\alpha$ for the generic phase α with mass density ρ_α and velocity $\boldsymbol{u}_\alpha$ is given as

$$\mathcal{M}_\alpha = \frac{\partial \rho_\alpha}{\partial t} + \nabla \cdot (\rho_\alpha \boldsymbol{u}_\alpha) = 0, \tag{2.6}$$

where the time derivative in the first term is the time derivative at a fixed spatial position $\boldsymbol{x}$. Note that the subscripts denote the microscale quantities. We now employ the averaging operator

$$\langle \mathcal{P}_i \rangle_{\Omega_j, \Omega_k, w} = \frac{\int_{\Omega_j} w \mathcal{P}_i \, \mathrm{d}\tau}{\int_{\Omega_k} w \, \mathrm{d}\tau} \tag{2.7}$$

with the first subscript denoting the domain over which the property $\mathcal{P}$ is averaged. The second subscript denotes the averaging domain in the denominator of the right-hand side of the equation. The third subscript denotes an optional weight, which we set to $w = 1$ when no third subscript is given. The averaging operator can be split across sums of terms, and hence averaging Eq. (2.6) results in

$$\mathcal{M}^{\overline{\overline{\alpha}}} = \langle \mathcal{M}_\alpha \rangle_{\Omega_\alpha, \Omega} = \left\langle \frac{\partial \rho_\alpha}{\partial t} \right\rangle_{\Omega_\alpha, \Omega} + \langle \nabla \cdot (\rho_\alpha \boldsymbol{u}_\alpha) \rangle_{\Omega_\alpha, \Omega}, \tag{2.8}$$

the macroscopic mass balance of the fluid phase α. To evaluate the time derivative of the microscale density, we average it according to the transport averaging theorem [77, p. 213]

$$\left\langle \frac{\partial \rho_\alpha}{\partial t} \right\rangle_{\Omega_\alpha,\Omega} = \frac{\partial}{\partial t}\langle \rho_\alpha \rangle_{\Omega_\alpha,\Omega} - \sum_{\kappa \in \mathcal{J}_{c\alpha}} \langle \boldsymbol{n}_\alpha \cdot \boldsymbol{u}_\kappa \rho_\alpha \rangle_{\Omega_\kappa,\Omega} = \frac{\partial \left(\varepsilon^\alpha \rho^\alpha\right)}{\partial t} - \sum_{\kappa \in \mathcal{J}_{c\alpha}} \langle \rho_\alpha \boldsymbol{u}_\kappa \cdot \boldsymbol{n}_\alpha \rangle_{\Omega_\kappa,\Omega} \tag{2.9}$$

with outward normal vector $\boldsymbol{n}$. Following the standard TCAT notation, $\mathcal{J}_{c\alpha}$ denotes the connected set of phases and common curves to interface α, i.e., all interfaces separating phase α from adjacent phases. In Eq. (2.9), we used the following definition based on [77, p. 208]

$$\langle \rho_\alpha \rangle_{\Omega_\alpha,\Omega} = \langle \rho_\alpha \rangle_{\Omega_\alpha,\Omega_\alpha} \langle 1 \rangle_{\Omega_\alpha,\Omega} = \rho^\alpha \varepsilon^\alpha \tag{2.10}$$

with the macroscale mass density $\rho^\alpha = \langle \rho_\alpha \rangle_{\Omega_\alpha,\Omega_\alpha}$ and the volume fraction $\varepsilon^\alpha = \langle 1 \rangle_{\Omega_\alpha,\Omega}$—which is how the volume fraction enters the macroscopic mass balance. Note that the superscripts denote the macroscale quantities.

To evaluate the divergence in the second term in Eq. (2.8), we apply the divergence averaging theorem [77, p. 213]

$$\langle \nabla \cdot (\rho_\alpha \boldsymbol{u}_\alpha) \rangle_{\Omega_\alpha,\Omega} = \nabla \cdot \langle \rho_\alpha \boldsymbol{u}_\alpha \rangle_{\Omega_\alpha,\Omega} + \sum_{\kappa \in \mathcal{J}_{c\alpha}} \langle \rho_\alpha \boldsymbol{u}_\alpha \cdot \boldsymbol{n}_\alpha \rangle_{\Omega_\kappa,\Omega} \tag{2.11}$$

and evaluate the averaging operator of the first term as

$$\nabla \cdot \langle \rho_\alpha \boldsymbol{u}_\alpha \rangle_{\Omega_\alpha,\Omega} = \nabla \cdot \left(\langle \boldsymbol{u}_\alpha \rangle_{\Omega_\alpha,\Omega_\alpha,\rho_\alpha} \langle \rho_\alpha \rangle_{\Omega_\alpha,\Omega_\alpha} \langle 1 \rangle_{\Omega_\alpha,\Omega} \right) = \nabla \cdot \left(\overline{\boldsymbol{u}^\alpha} \rho^\alpha \varepsilon^\alpha \right). \tag{2.12}$$

Here, we introduce the macroscale velocity $\overline{\boldsymbol{u}^\alpha}$, which is a mass-averaged quantity with the weighting function $w = \rho_\alpha$ denoted by the overbar. We further combine the sums from Eqs. (2.9) and (2.11)

$$\sum_{\kappa \in \mathcal{J}_{c\alpha}} \langle \rho_\alpha \boldsymbol{u}_\alpha \cdot \boldsymbol{n}_\alpha \rangle_{\Omega_\kappa,\Omega} - \sum_{\kappa \in \mathcal{J}_{c\alpha}} \langle \rho_\alpha \boldsymbol{u}_\kappa \cdot \boldsymbol{n}_\alpha \rangle_{\Omega_\kappa,\Omega} = \sum_{\kappa \in \mathcal{J}_{c\alpha}} \langle \rho_\alpha \left(\boldsymbol{u}_\alpha - \boldsymbol{u}_\kappa \right) \cdot \boldsymbol{n}_\alpha \rangle_{\Omega_\kappa,\Omega} \tag{2.13}$$

and define the mass transfer between the κ interface and the phase α based on [77, p. 222]

$$\sum_{\kappa \in \mathcal{J}_{c\alpha}} \overset{\kappa \to \alpha}{M} = \sum_{\kappa \in \mathcal{J}_{c\alpha}} \langle \rho_\alpha \left(\boldsymbol{u}_\kappa - \boldsymbol{u}_\alpha \right) \cdot \boldsymbol{n}_\alpha \rangle_{\Omega_\kappa,\Omega}. \tag{2.14}$$

We finally recombine all macroscale quantities and rewrite the macroscopic mass balance as

$$\mathcal{M}^{\overline{\alpha}} = \frac{\partial \left(\rho^\alpha \varepsilon^\alpha\right)}{\partial t} + \nabla \cdot \left(\rho^\alpha \varepsilon^\alpha \overline{\boldsymbol{u}^\alpha} \right) - \sum_{\kappa \in \mathcal{J}_{c\alpha}} \overset{\kappa \to \alpha}{M} = 0. \tag{2.15}$$

All other equations necessary for the tumour growth model are derived similarly. The exemplary derivation of the macroscopic mass balance shows how the volume fractions and the mass transfer term—two characteristic quantities of the multiphase porous-media approach—enter the macroscale equations. For the sake of readability, we drop the overlines denoting the mass-averaged macroscale quantities in the following.

2.1.2 Solid phase: the extracellular matrix

The solid phase, often called the skeleton, of our porous medium is the extracellular matrix (ECM): its components (e.g., collagens, proteoglycans, elastin, and cell-binding glycoproteins) link together to form an intricate, structurally stable network [84]. The cells and the interstitial fluid fill the pore space of the ECM, move through it, and interact with it. The pressure of these fluid phases in the pore space influences the stress state of the solid. Based on Terzaghi's effective stress principle [85], the total Cauchy stress $\boldsymbol{\sigma}_{\text{tot}}$ is defined as the effective Cauchy stress $\boldsymbol{\sigma}_{\text{eff}}$ in the solid phase minus the solid pressure p^s

$$\boldsymbol{\sigma}_{\text{tot}} = \boldsymbol{\sigma}_{\text{eff}} - p^s \boldsymbol{I} \tag{2.16}$$

with the solid pressure p^s defined as the weighted sum of fluid pressures p^α, saturations S^α, and the blood pressure p^v in the vasculature

$$p^s = \frac{\varepsilon}{\varepsilon + \varepsilon^v} \sum_{\alpha \in \{t,h,\ell\}} S^\alpha p^\alpha + \frac{\varepsilon^v}{\varepsilon + \varepsilon^v} p^v, \tag{2.17}$$

as introduced by [72].

The governing equation of the solid phase is the balance of momentum, which pulled back into material configuration reads

$$\nabla_{\text{o}} \cdot (\boldsymbol{F} \cdot \boldsymbol{S}_{\text{tot}}) = \nabla_{\text{o}} \cdot \left(\boldsymbol{F} \cdot \boldsymbol{S}_{\text{eff}} - \boldsymbol{F} \cdot p^s J \boldsymbol{F}^{-1} \boldsymbol{F}^{-T}\right) = \boldsymbol{0}, \tag{2.18}$$

with the material divergence operator ∇_{o}, the second Piola–Kirchhoff stress tensor $\boldsymbol{S}$, the deformation gradient $\boldsymbol{F}$ and its determinant J. In Eq. (2.18), we assume that no body forces act on the solid phase, and we neglect inertia, i.e., acceleration is assumed to be zero.

While the total stress governs the balance of momentum, it is the effective stress that produces the strain of the solid and which we can hence relate to the deformation of the solid [86, Sec. 2.5.2]: the effective second Piola–Kirchhoff stress tensor $\boldsymbol{S}_{\text{eff}}$ is related to the right Cauchy–Green strain tensor $\boldsymbol{C}$ via a strain-energy function Ψ as

$$\boldsymbol{S}_{\text{eff}} = 2 \frac{\partial \Psi(\boldsymbol{C})}{\partial \boldsymbol{C}}. \tag{2.19}$$

For most examples throughout this thesis, we use a simple compressible Neo-Hookean model [87, p. 247] with a strain-energy function of the form

$$\Psi_{\text{NH}}^{\infty} = \frac{G}{2} \left(\text{tr}(\boldsymbol{C}) - 3\right) + \frac{G}{2\beta} \left(J^{-2\beta} - 1\right) \quad \text{with} \quad \beta = \frac{\nu}{1 - 2\nu} \tag{2.20}$$

with the shear modulus G and the Poisson's ratio ν.

In Chapter 5, we apply the multiphase porous-media model to *in vitro* experiments with collagen hydrogel. Experimental characterisation of the mechanical properties of these hydrogels revealed a visco-elastic behaviour [88–90], and we use a visco-hyperelastic material model to describe the mechanical behaviour of the hydrogel. The Neo-Hookean material model describes the hyperelastic

part, while the viscous part is added as a generalised Maxwell model, based on [91]. The strain-energy function of the visco-hyperelastic material is given as

$$\Psi = \Psi_{\mathrm{NH}}^{\infty} + \gamma(\boldsymbol{C}, \Gamma_\alpha), \tag{2.21}$$

where $\Psi_{\mathrm{NH}}^{\infty}$ describes the hyperelastic part (characterising the equilibrium state of the solid) and γ describes the visco-elastic contribution (characterising the non-equilibrium state, i.e., creep or relaxation). The dissipative potential γ is a function of the right Cauchy–Green strain tensor $\boldsymbol{C}$ and a set of strain-like internal (history) variables denoted by Γ_α.

Similar to the right Cauchy–Green strain tensor $\boldsymbol{C}$ and its kinematic conjugate being the second Piola–Kirchhoff stress tensor $\boldsymbol{S}$, the strain-like internal variables Γ_α result in a non-equilibrium stress tensor $\boldsymbol{Q}$ given by

$$\boldsymbol{Q} = -2\frac{\partial \gamma(\boldsymbol{C}, \Gamma_\alpha)}{\partial \Gamma_\alpha}. \tag{2.22}$$

The Maxwell model follows as

$$\dot{\boldsymbol{Q}} + \frac{1}{\tau}\boldsymbol{Q} = \dot{\boldsymbol{S}}_{\mathrm{eff}} \tag{2.23}$$

with the relaxation time τ and the superimposed dot denoting the material time derivative. Based on the shear modulus G and the dynamic viscosity of the ECM μ^s, we calculate the relaxation time τ as

$$\tau = \frac{\mu^s}{G}.$$

2.1.3 Fluid phases: the interstitial fluid and the cells

We consider multiple fluid phases that fill the pore space of the ECM: the interstitial fluid and the cells. Usually, we include two cell phases: the tumour cells and the healthy host cells. This results in a total of three fluid phases. For *in vitro* experiments with tumour spheroids, no host cells are present, and we only consider two fluid phases. It is important to note that our approach, based on porous media, directly considers the flow of the fluid phases, which is particularly important for the interstitial fluid as the interstitial fluid flow is an important factor of the tumour microenvironment [92, 93].

While we model the interstitial fluid as a fluid with a low viscosity μ^ℓ, similar to that of water, the cell phases have a considerably higher viscosity μ^t and μ^h. Hence, the tumour is modelled as a (highly) viscous fluid growing and moving in the ECM. The fluid phases are further characterised by their density ρ^α, which we assume to be constant and thus only consider the incompressible case.

The governing equations of the fluid phases (except the last fluid phase) are the mass balance equations based on the pressures p^α of the phases

$$\varepsilon \frac{\partial S^\alpha}{\partial t}\bigg|_{\boldsymbol{X}} - S^\alpha \frac{\partial \varepsilon^\nu}{\partial t}\bigg|_{\boldsymbol{X}} + S^\alpha \left(1 - \varepsilon^\nu\right) \nabla \cdot \boldsymbol{v}^s - \nabla \cdot \left(\frac{\boldsymbol{k}^\alpha}{\mu^\alpha} \nabla p^\alpha\right) = \frac{1}{\rho^\alpha} \sum_{\kappa \in \mathcal{J}_{c\alpha}} \overset{\kappa \to \alpha}{M}. \tag{2.24}$$

For the last fluid phase, we do not use Eq. (2.24) as the governing equation but instead sum up the mass balance equations of all fluid phases, resulting in

$$-\frac{\partial \varepsilon^{\nu}}{\partial t}\bigg|_{X} + \left(1-\varepsilon^{\nu}\right)\nabla\cdot\boldsymbol{v}^{s} - \sum_{\gamma\in\{t,h,\ell\}}\left(\nabla\cdot\left(\frac{\boldsymbol{k}^{\alpha}}{\mu^{\alpha}}\nabla p^{\alpha}\right)\right) = \sum_{\gamma\in\{t,h,\ell\}}\left(\frac{1}{\rho^{\gamma}}\sum_{\kappa\in\mathcal{J}_{c\gamma}}^{\kappa\to\gamma} M\right), \tag{2.25}$$

which includes several simplifications, e.g., based on the sum of saturations given by Eq. (2.5). Further details are presented in [33]. Note that the time derivatives in Eqs. (2.24) and (2.25) are local time derivatives at a fixed material point $\boldsymbol{X}$, which introduces an additional convective term based on Eq. (2.27), similar to the fundamental Arbitrary Lagrangian-Eulerian (ALE) equation [94].

Remark (The Arbitrary Lagrangian-Eulerian (ALE) approach)**.** *In continuum mechanics, the two commonly used descriptions are the material configuration with all material points $\boldsymbol{X}$ and the spatial configuration with all spatial points $\boldsymbol{x}$, also called Lagrangian and Eulerian descriptions. The total material time derivative with respect to the solid phase of a material quantity $(\bullet)(\boldsymbol{X},t)$ is given as*

$$\frac{d(\bullet)(\boldsymbol{X},t)}{dt} = \frac{\partial(\bullet)(\boldsymbol{X},t)}{\partial t}\bigg|_{X}, \tag{2.26}$$

and the local time derivative at a fixed spatial position $\boldsymbol{x}$ of a spatial quantity $(\bullet)(\boldsymbol{x}(\boldsymbol{X},t))$ is given as

$$\frac{\partial(\bullet)(\boldsymbol{x}(\boldsymbol{X},t))}{\partial t}\bigg|_{\boldsymbol{x}} = \frac{\partial(\bullet)(\boldsymbol{x}(\boldsymbol{X},t))}{\partial t}\bigg|_{X} - \boldsymbol{v}^{s}\cdot\nabla(\bullet), \quad \textit{with} \quad \boldsymbol{v}^{s} = \frac{\partial \boldsymbol{x}}{\partial t}\bigg|_{X} \tag{2.27}$$

being the velocity of the solid phase. The ALE description combines features from the Lagrangian and Eulerian approaches: the nodes neither follow the particle movement nor are they fixed in space; instead, they move in some arbitrarily specified way. In poromechanics, the observer is not arbitrary but follows the motion of the solid phase.

In Eq. (2.24), we describe the convective flow with Darcy's law as

$$\varepsilon^{\alpha}\left(\boldsymbol{u}^{\alpha}-\boldsymbol{v}^{s}\right) = -\frac{\boldsymbol{k}^{\alpha}}{\mu^{\alpha}}\nabla p^{\alpha}, \tag{2.28}$$

where $\boldsymbol{k}^{\alpha}$ is the effective permeability tensor of the fluid phase.

Remark (The Darcy equation as momentum balance of the fluid phase)**.** *A more general form of the momentum balance of the fluid phase α is given by the Darcy–Brinkman equation*

$$\varepsilon^{\alpha}\left(\boldsymbol{u}^{\alpha}-\boldsymbol{v}^{s}\right) = \frac{\boldsymbol{k}^{\alpha}}{\mu^{\alpha}}\Bigg[-\nabla p^{\alpha} - \underbrace{\rho^{\alpha}\frac{\partial \boldsymbol{u}^{\alpha}}{\partial t}}_{\text{Inertia}} + \underbrace{\frac{\mu^{\alpha}}{\varepsilon^{\alpha}}\nabla\cdot\left(\varepsilon^{\alpha}\nabla\boldsymbol{u}^{\alpha}\right)}_{\text{Viscous term}} + \underbrace{\rho^{\alpha}\boldsymbol{b}}_{\text{Body forces}}\Bigg], \tag{2.29}$$

with $\boldsymbol{b}$ denoting the body forces, e.g., gravity. The viscous term is called Brinkman term and accounts for the viscous forces in the fluid phase, similar to the viscous term in the Navier–Stokes equations. It is interesting to note that Eq. (2.29) can be derived as a homogenisation of the Stokes problem on the

microscale, assuming a no-slip condition at the interface between the fluid and the solid phase [95, 96]. In our case, we assume a steady state, i.e., we neglect inertia, and we also neglect the viscous contribution and body forces. This results in Eq. (2.28) and allows us to condense the momentum balance into the mass balance of the fluid, resulting in a single governing equation, that is Eq. (2.24). A pure Darcy flow has no shear stresses, and no curvature of the flow is possible, i.e., a no-slip condition at the macroscale for a pure Darcy flow without the viscous term is an ill-posed problem [97, Sec. 3.6.3].

As the three fluid phases share the pore space of the ECM, they interact with each other and with the ECM. These interactions influence the permeability and interfacial tension.

The effective permeability tensor $\boldsymbol{k}^\alpha$ describes how easily a specific phase can flow through the solid scaffold, and we define it as $\boldsymbol{k}^\alpha = k^\alpha_{\mathrm{rel}}\, k\, \boldsymbol{I}$ based on the scalar intrinsic permeability k of the ECM. The intrinsic permeability characterises how easily one single fluid phase filling the entire pore space can flow through the scaffold. In our case, we have multiple fluid phases sharing the pore space: each phase interferes with and impedes the flow of the other phases. Therefore, the relative permeability k^α_{rel} is a function of the corresponding saturation given by

$$k^\alpha_{\mathrm{rel}} = \left(S^\alpha\right)^{A_\alpha} \tag{2.30}$$

with a model coefficient A_α, as proposed by [67]. We use the simple empirical relation given by Eq. (2.30) for the relative permeability since no detailed measurements are available for our particular multiphase system. This simple form still agrees with the classical models commonly used in porous-media mechanics [98]. However, a more specific model for our multiphase system should be determined, e.g., from specific experiments, through micro-models, or Lattice-Boltzmann modelling [67].

Although the fluid phases are adjacent and share one pore space, they are immiscible. Pressure differences $p^{h\ell}$ and p^{th} between the fluid phases must be sustained to preserve this immiscibility. These pressure differences result from the interfacial tensions σ_{th} and $\sigma_{h\ell}$ and the curvature of the interface between the fluid phases [65], and we use the following heuristic model at the macroscale:

$$p^{h\ell}\left(S^\ell\right) = p^h - p^\ell = a\, \tan\left[\frac{\pi}{2}\left(1 - S^\ell\right)^b\right] \tag{2.31}$$

$$p^{th}\left(S^t\right) = p^t - p^h = a\frac{\sigma_{th}}{\sigma_{h\ell}} \tan\left[\frac{\pi}{2}\left(S^t\right)^b\right] \tag{2.32}$$

with two model constants a and b. These pressure-saturation relationships also provide the link back to the fluid saturations to close the system of equations. A higher interfacial tension causes higher infiltration of one fluid phase into the other and hence a less compact tumour [67]. Eqs. (2.31) and (2.32) are phenomenological approximations at the macroscale to account for the curvature of the interface, similar to those commonly used for geophysical multiphase systems [99], and therefore Miller *et al.* [82] present a detailed approach to link pressures to saturations based upon the simplified entropy inequality in the TCAT formulation.

The remaining saturation of the host cells S^h then follows as

$$S^h\left(p^{th}, p^{h\ell}\right) = 1 - S^\ell\left(p^{h\ell}\right) - S^t\left(p^{th}\right). \tag{2.33}$$

2.1.4 Species: oxygen and necrotic tumour cells

The phases can transport further subcomponents. In the basic form of the tumour growth model, we include oxygen as a nutrient and necrotic tumour cells. The lack of nutrients causes living tumour cells to become necrotic, and these necrotic tumour cells are a subcomponent of the tumour cell phase. The mass fraction of necrotic tumour cells is denoted by ω^{Nt}. Similarly, nutrients are modelled as a species in the interstitial fluid. The nutrient mass fraction $\omega^{n\ell}$ drives the growth of the tumour.

The governing equation used for a species i with mass fraction $\omega^{i\alpha}$ in the fluid phase α is the reaction-diffusion-advection equation

$$\rho^\alpha \varepsilon S^\alpha \left.\frac{\partial \omega^{i\alpha}}{\partial t}\right|_{\boldsymbol{X}} - \nabla\cdot\left(\rho^\alpha \varepsilon S^l D^{i\alpha}_{\text{eff}} \nabla \omega^{i\alpha}\right) - \rho^\alpha \frac{\boldsymbol{k}^\alpha}{\mu^\alpha}\nabla p^\alpha \cdot \nabla \omega^{i\alpha} = \sum_{\kappa\in\mathcal{J}_{c\alpha}} \overset{i\kappa\to i\alpha}{M} + \varepsilon S^\alpha r^{i\alpha} - \omega^{i\alpha} \sum_{\kappa\in\mathcal{J}_{c\alpha}} \overset{\kappa\to\alpha}{M} \tag{2.34}$$

with a diffusive contribution based on Fick's law and an advective contribution based on Darcy's law. The right-hand side of Eq. (2.34) includes the mass transfer terms between species and between phases and the intra-phase reaction term $r^{i\alpha}$.

We describe the diffusion of oxygen in the interstitial fluid by

$$D^{n\ell}_{\text{eff}} = D^{n\ell}_{\text{o}}\left(\varepsilon S^\ell\right)^\delta \tag{2.35}$$

with the diffusion coefficient in the interstitial fluid $D^{n\ell}_{\text{o}}$ and a constant δ: the effective diffusion coefficient $D^{n\ell}_{\text{eff}}$ of oxygen has a nonlinear dependence on the volume fraction of interstitial fluid, as it is also related to the connectivity grade of the extracellular spaces and tortuosity of the porous network, and the parameter δ was calibrated experimentally by [65]. We assume the necrotic cells do not diffuse, thus setting their diffusion coefficient to zero.

In Section 2.2.3, we include further species, e.g., tumour angiogenic factors (TAFs) and matrix metalloproteinases (MMPs), to investigate the complex interactions of biochemical and biophysical cues of the microenvironment on tumour growth.

2.1.5 Vasculature and angiogenesis

We include the vasculature as an additional porous network, resulting in a double-porosity formulation with two separate porous networks: the first porous network is the pore space between the ECM fibres with the host cells, tumour cells, and the interstitial fluid; the second porous network is the vasculature, with blood flow and species transport alongside the pores of the ECM. Here, we only employ this homogenised representation of the vasculature. Kremheller *et al.* [73–75] additionally presented a discrete and a hybrid approach.

In the homogenised approach, the blood flow in the vasculature is governed by the mass balance written as

$$\left.\frac{\partial \varepsilon^v}{\partial t}\right|_X + \varepsilon^v \nabla \cdot \boldsymbol{v}^s - \nabla \cdot \left(\frac{\boldsymbol{k}^v}{\mu^v} \nabla p^v \right) = -\frac{1}{\rho^v} \overset{v \to \ell}{M}_{\text{leak}}, \tag{2.36}$$

with the permeability tensor $\boldsymbol{k}^v$ in the Darcy equation for the convective velocity to evaluate the blood pressure p^v. Like the other phases, the vasculature can also transport species, e.g., oxygen as a nutrient, governed by Eq. (2.34).

The vasculature of tumours exhibits abnormalities compared to the vasculature of healthy tissue: it is highly disorganised, with high tortuosity and a heterogeneous distribution of blood vessels [100]. In particular, the tumour vasculature is leaky, i.e., it is hyperpermeable to macromolecules [101] and has endothelial gaps [102]. This leakiness is highly relevant for the delivery of drugs to the tumour: on the one hand, it allows drugs to escape from the vasculature; but, on the other hand, it also results in higher interstitial fluid pressure in the tumour, causing an outward flow that impedes drug delivery [103]. We include this leakiness by a leakage term M_{leak} in Eq. (2.36).

Moreover, the vasculature is not a static network but can grow and remodel—a process actively driven by the tumour. Including a suitable model of angiogenesis, the formation of new blood vessels from pre-existing vasculature, is crucial for modelling tumour growth for two main reasons. First, angiogenesis is a critical step in the progression of tumours: in the absence of neovascularisation, tumours cannot grow beyond a size of 2 mm to 3 mm due to a lack of nutrients and oxygen, while vascularisation on the other side results in a rapid growth [104]. Second, tumour cells can escape the primary tumour and metastasise to other parts of the body via the newly formed vasculature [105].

Angiogenesis is a multistep process: due to a lack of oxygen and nutrients, tumour cells become hypoxic and secrete tumour angiogenic factors (TAF); these TAFs stimulate the migration of endothelial cells from the existing vasculature towards the tumour, forming a new vascular network that supplies the tumour with oxygen and nutrients. In the simplest case, we assume that the motion of endothelial cells and, thus, the angiogenesis is driven by two factors: random motility and chemotaxis in response to TAF gradients. We only consider one type of TAF, which is secreted by the tumour cells, diffuses in the interstitial fluid, and drives the angiogenesis. This could, for example, be vascular endothelial growth factor (VEGF), one of the most potent TAFs [92]. In addition, we only consider the soluble isoform of VEGF, i.e., it is dissolved in and transported by the interstitial fluid, and we model it as a species in the interstitial fluid with mass fraction $\omega^{\text{TAF}\ell}$ governed by Eq. (2.34).

We write the evolution equation of angiogenesis as introduced by [72]

$$\left.\frac{\partial \varepsilon^v}{\partial t}\right|_X + \varepsilon^v \nabla \cdot \boldsymbol{v}^s + \nabla \cdot \left(\boldsymbol{j}^v - \varepsilon^v \boldsymbol{v}^s \right) = C_{\text{coll}}, \tag{2.37}$$

with C_{coll} denoting a model for blood vessel collapse [58, 75]. The flux term is modelled as

$$\boldsymbol{j}^v - \varepsilon^v \boldsymbol{v}^s = \underbrace{-\nabla \cdot \left(D^v \nabla \varepsilon^v \right)}_{\text{Random motility}} + \underbrace{\nabla \cdot \left(\varepsilon^v \varepsilon S^\ell \chi \left(\omega^{\text{TAF}\ell} \right) \nabla \omega^{\text{TAF}\ell} \right)}_{\text{Chemotaxis}}. \tag{2.38}$$

Table 2.1 Mass transfer terms for the different phases of the tumour growth model. The extracellular matrix is the solid phase. Host cells, tumour cells, and the interstitial fluid are modelled as fluid phases occupying the pores of the ECM.

Entity	Symbol		Term
Extracellular Matrix	$\sum_{\kappa\in\mathcal{J}_{cs}} \overset{\kappa\to s}{M}$	$=$	0
Interstitial fluid	$\sum_{\kappa\in\mathcal{J}_{cl}} \overset{\kappa\to \ell}{M}$	$=$	$-\overset{\ell\to t}{M}_{\text{growth}} + \overset{v\to \ell}{M}_{\text{leak}} - \overset{\ell\to \text{ly}}{M}_{\text{drain}}$
Tumour cells	$\sum_{\kappa\in\mathcal{J}_{ct}} \overset{\kappa\to t}{M}$	$=$	$\overset{\ell\to t}{M}_{\text{growth}}$
Host cells	$\sum_{\kappa\in\mathcal{J}_{ch}} \overset{\kappa\to h}{M}$	$=$	0

This formulation includes random motion of endothelial cells due to molecular diffusion with mass diffusivity D^v. It further describes chemotaxis with a non-constant chemotactic coefficient $\chi(\omega^{\text{TAF}\ell})$, as employed in [72].

Altogether, this results in a two-way coupling between the tumour and angiogenesis: the tumour cells secrete TAF, which drives the angiogenesis, and the newly formed vasculature supplies the tumour with nutrients, which in turn drives the growth of the tumour.

Including only one soluble isoform of TAF is the most straightforward approach to model angiogenesis. However, the biochemical pathways regulating angiogenesis include many more key players: tip endothelial cells, TAF bound to the ECM and matrix metalloproteinases (MMPs), which degrade ECM proteins and release soluble TAF, to name a few [92, 106]. In addition, biophysical cues attract increasing interest, in particular, the interstitial fluid flow [92, 93]. We leverage the flexibility of our model to include these biochemical and biophysical cues as additional factors in Section 2.2.3.

2.1.6 Mass transfer terms governing tumour growth

To bring everything together, we are left with the question of what actually drives the growth of the tumour in the multiphase porous-media model: as long as the tumour cells are supplied with enough oxygen, the tumour phase grows.

The mass transfer terms for the different phases are summarised in Table 2.1. Based on Sciumè *et al.* [67], tumour growth is captured by the mass transfer term from the interstitial fluid to the tumour phase

$$\overset{\ell\to t}{M}_{\text{growth}} = \gamma^t_{\text{growth}} \left\langle \frac{\omega^{n\ell} - \omega^{n\ell}_{\text{crit}}}{\omega^{n\ell}_{\text{env}} - \omega^{n\ell}_{\text{crit}}} \right\rangle_+ \left(1 - \omega^{Nt}\right) \varepsilon S^t, \tag{2.39}$$

where $\overset{\ell\to t}{M}_{\text{growth}}$ represents the inter-phase exchange of mass between the phases ℓ and t (representing the mass of interstitial fluid which becomes tumour due to cell growth) and γ^t_{growth} denotes the growth coefficient [65]. The parameter $\omega^{n\ell}_{\text{crit}}$ is the critical nutrient threshold below which cells starve and become necrotic, and $\omega^{n\ell}_{\text{env}}$ is the reference mass fraction of oxygen available in the environment (i.e., in interstitial fluid without a tumour). The Macaulay brackets $\langle\cdot\rangle_+$ indicate the positive value of the argument if the argument is positive but zero if it is not.

As discussed in Section 2.1.5, the tumour vasculature is leaky due to abnormal vessel characteristics. This is highly relevant since the leakage of fluid from the vasculature into the interstitial fluid can transport drugs into the tumour but at the same time causes an increase in the interstitial fluid pressure, which impedes the delivery of drugs to the tumour—one of the many paradoxes of tumour drug delivery. We include the leakage of fluid from the vasculature into the interstitial fluid as

$$\overset{v\to\ell}{M}_{\text{leak}} = \rho^v \varepsilon^v L_p^v \frac{S}{V} \left\langle p^{\text{eff}} - p^\ell \right\rangle_+ , \tag{2.40}$$

where a net outflow from the vessel into the interstitial fluid occurs when the effective pressure p^{eff}, given by

$$p^{\text{eff}} = p^v - \sigma \left(\pi^v - \pi^\ell \right), \tag{2.41}$$

is higher than the interstitial pressure p^ℓ. In Eq. (2.40), we employ a Starling equation with a hydraulic conductivity of the membrane L_p^v and surface-to-volume ratio S/V to describe the transendothelial fluid exchange in capillaries. The plasma protein oncotic pressure is denoted as π^v, the interstitial oncotic pressure as π^ℓ and the Staverman's reflection coefficient as σ. Together, $\sigma(\pi^v - \pi^\ell)$ is the oncotic pressure difference between the blood vessels and the interstitial fluid. Based on [107], we define the hydraulic conductivity L_p^v of the blood vessel wall as

$$L_p^v = \frac{\gamma_{\text{pore}}\, r_{\text{o}}^2}{8 \mu^v t}, \tag{2.42}$$

with the fraction of pores γ_{pore}, the pore radius r_{o} and the vessel wall thickness t.

The fluid that leaks from the vasculature into the interstitial fluid is collected by the lymphatic system and transported back into the blood circulation. Tumours however impair the lymphatic system by collapsing lymphatic vessels and blocking lymphatic drainage [108–110]. Based on [72, 111], we include lymphatic drainage, again based on a Starling equation, as

$$\overset{\ell\to\text{ly}}{M}_{\text{drain}} = \rho^\ell \left(L_p \frac{S}{V} \right)^{\text{ly}} \left\langle p^\ell - p^{\text{ly}} \right\rangle_+ \left\langle 1 - \frac{p^t}{p^{\text{ly}}_{\text{coll}}} \right\rangle_+ , \tag{2.43}$$

with $\left(L_p \frac{S}{V} \right)^{\text{ly}}$ being the lymphatic filtration coefficient. When the tumour pressure p^t exceeds the critical lymphatic pressure $p^{\text{ly}}_{\text{coll}}$, the lymphatic vessels collapse, and the lymphatic drainage is blocked. In combination with the leakiness of the blood vessels, the inhibited lymphatic drainage results in fluid retention in the tumour, causing an increase in the interstitial fluid pressure. We consider the fluid drainage but do not explicitly resolve the lymphatic system.

Mass transfer also occurs between the species, which we summarise in Table 2.2. In the following, we only consider oxygen as a nutrient and necrotic tumour cells as species. Tumour cells become necrotic when not supplied with enough oxygen. Based on [67], we include the increase in the necrotic fraction of tumour cells as

$$\varepsilon^t r^{Nt} = \gamma^t_{\text{necrosis}} \left\langle \frac{\omega^{n\ell}_{\text{crit}} - \omega^{n\ell}}{\omega^{n\ell}_{\text{env}} - \omega^{n\ell}_{\text{crit}}} \right\rangle_+ \left(1 - \omega^{Nt} \right) \varepsilon S^t, \tag{2.44}$$

Table 2.2 Mass transfer terms for species. Necrotic tumour cells are the necrotic portion of the tumour cells, and oxygen is dissolved in the interstitial fluid.

Species	Phase	Terms on the right-hand side of Eq. (2.34)
Necrotic tumour cells	Tumour cells	$\varepsilon^t r^{Nt} - \omega^{Nt} \overset{\ell\to t}{M}_{\text{growth}}$
Oxygen	Interstitial fluid	$-\overset{n\ell\to t}{M}_{\text{cons}} - \overset{n\ell\to h}{M}_{\text{cons}} + \overset{nv\to n\ell}{M}_{\text{tc}} + \omega^{n\ell}\overset{\ell\to t}{M}_{\text{growth}}$

where $\gamma^t_{\text{necrosis}}$ is the necrosis coefficient.

The tumour is supplied with oxygen by its vasculature. The oxygen transported by the blood flow is exchanged with the interstitial fluid via the capillary walls. We include this transcapillary exchange of oxygen as

$$\overset{nv\to n\ell}{M}_{\text{tc}} = \rho^n \gamma_{\text{tv}} \frac{S}{V} \left\langle P^v_{\text{oxy}} - P^\ell_{\text{oxy}} \right\rangle_+ \varepsilon^v, \tag{2.45}$$

with the oxygen partial pressures P^v_{oxy} and P^ℓ_{oxy}, as presented in [73].

Living tumour cells consume oxygen dissolved in the interstitial fluid, as described by

$$\overset{n\ell\to t}{M}_{\text{cons}} = \left(\gamma^{nt}_{\text{growth}} \left\langle \frac{\omega^{n\ell} - \omega^{n\ell}_{\text{crit}}}{\omega^{n\ell}_{\text{env}} - \omega^{n\ell}_{\text{crit}}} \right\rangle_+ + \gamma^{nt}_{\text{o}} \sin\left(\frac{\pi}{2} \frac{\omega^{n\ell}}{\omega^{n\ell}_{\text{env}}} \right) \right) \left(1 - \omega^{Nt}\right) \varepsilon S^t, \tag{2.46}$$

again based on [67]. The first addend describes the consumption of oxygen during tumour growth proportional to the coefficient $\gamma^{nt}_{\text{growth}}$, and the second addend accounts for the normal metabolism of tumour cells proportional to the coefficient γ^{nt}_{o}[1]. Oxygen consumption due to the normal metabolism of the host cells is considered in a similar way as

$$\overset{n\ell\to h}{M}_{\text{cons}} = \gamma^{nh}_{\text{o}} \sin\left(\frac{\pi}{2} \frac{\omega^{n\ell}}{\omega^{n\ell}_{\text{env}}} \right) \varepsilon S^h, \tag{2.47}$$

where γ^{nh}_{o} describes the oxygen demand of the host cells [73].

2.1.7 Computational solution approach

To solve the governing equations in space and time, we use the standard Galerkin procedure to obtain the weak form of the equations and then discretise the equations in space and time; for the discretisation in space, we employ the finite element method and a one-step-θ scheme for the discretisation in time. The resulting system of equations is strongly coupled, and we apply a monolithic solution algorithm with a single Newton–Raphson loop per time step. The linear system of equations has a block structure. We therefore solve it using a generalised minimal residual method (GMRES) iterative solver with a preconditioner based on a block Gauss–Seidel (BGS) method

[1] Since the oxygen mass fraction $\omega^{n\ell}$ is always smaller or equal to $\omega^{n\ell}_{\text{env}}$, the argument of the sine function varies between 0 and $\pi/2$, and the oxygen consumption due to normal metabolism of the cells reaches its maximum for $\omega^{n\ell} = \omega^{n\ell}_{\text{env}}$. The sine function is chosen for numerical reasons because of its horizontal tangent.

combined with an algebraic multigrid (AMG) method (for further details see, e.g., [112–114]). As a computational framework, we use our in-house parallel multi-physics research code BACI [115].

The standard Galerkin procedure can lead to numerical instabilities when the convective terms dominate the advection-diffusion equation. To overcome this issue, we use the streamline-upwind Petrov–Galerkin (SUPG) method [116] to stabilise the convective terms, and we choose the stabilisation parameter τ as proposed by [117].

2.2 Tumour growth examples and discussion

In the following, we present and discuss three numerical examples of tumour growth. The first example in Section 2.2.1 is a three-dimensional simulation of tumour growth without host tissue and vasculature, similar to *in vitro* experiments with multicellular tumour spheroids. The second example in Section 2.2.2 is a two-dimensional simulation of vascular tumour growth in host tissue—similar to an *in vivo* setup—which serves as a starting point for the third example in Section 2.2.3, where we demonstrate the flexibility of our approach to model complex interactions between different species and fields to investigate the influence of biochemical and biophysical cues on angiogenesis and tumour growth.

2.2.1 *In vitro* growth of a tumour spheroid

This section presents a three-dimensional example of tumour growth without host tissue or vasculature. Such a setup aims to reproduce experimental assays of multicellular tumour spheroids grown *in vitro* in a collagen hydrogel, which we later use for the Bayesian calibration in Chapter 5, as published in [62]. The model is reduced to two fluid phases flowing in the pore space: tumour cells and culture medium (instead of interstitial fluid). Fig. 2.3 summarises the initial and boundary conditions of the numerical analysis.

We assume the spheroids to be spherical, with an initial mean radius of 10 µm. Due to the assumed spherical symmetry, only a segment of a spherical 3D geometry is computationally resolved. The total spherical computational domain has a radius of 100 µm, and we only consider a segment of 0.16 rad × 0.16 rad.

Concerning the solid phase of the porous medium, we employ the visco-hyperelastic constitutive law given by Eqs. (2.21) and (2.23) because the experimental characterisation of the mechanical properties of commonly used hydrogels revealed a visco-elastic behaviour [88–90]. The domain is fixed at the inner surface with a Dirichlet boundary condition and can deform in the radial direction.

Tumour cells initially occupy the inner part Ω^t with a radius of 10 µm, simulating the initial cell seed. At the initial time, the tumour saturation is $S^t = 0.875$ in Ω^t and zero in the rest of the domain. Our assumption is that there are no necrotic cells in the early stages. We also assume a constant nutrient supply, as the culture medium in the experiment is changed every two days to ensure a constant nutrient concentration. Therefore, the mass fraction of nutrients in the culture medium is set as constant and equal to $\omega_D^{n\ell} = 4.2 \times 10^{-6}$ [72], which is applied as a Dirichlet boundary condition at the outer surface Γ of the domain. All employed parameters are listed in Appendix A.1.

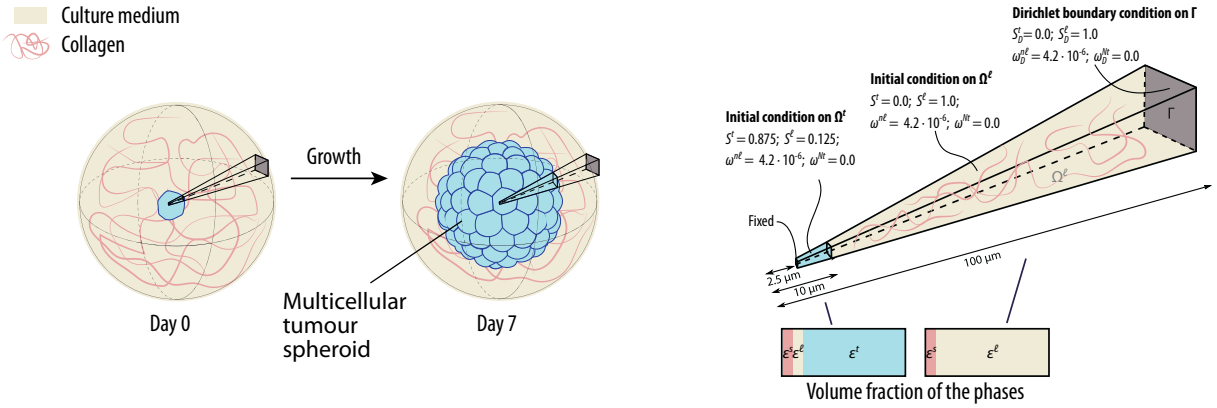

Figure 2.3 Computational setup. The tumour is assumed to be spherical, so only a segment of the spherical 3D geometry is modelled using the symmetry of the problem. The initial tumour domain Ω^t (in blue) contains tumour cells and culture medium in the pore space. In the domain Ω^ℓ (in beige), the pore space is initially filled with culture medium only. Dirichlet boundary conditions for the fluid phases and species are applied on the outer surface, marked in grey. This figure is based on [62], where it is licensed under CC BY-NC-ND 4.0.

The domain is discretised in space with 250 3D trilinear hexahedral elements aligned in the radial direction. The time discretisation is based on the one-step-theta scheme with $\theta = 0.52$ and a time step of $\Delta t = 450\,\mathrm{s}$. In total, 1344 time steps are evaluated; thus, the simulation describes the growth of a spheroid over seven days.

The results, depicted in Fig. 2.4, demonstrate characteristic features of tumour growth. The volume of the tumour spheroid increases exponentially over time, as shown in Fig. 2.4A and as observed in experiments [118]. In more detail, we will discuss experimentally observed growth in Chapter 5. In the tumour spheroid, the saturation of the tumour cells is above 90% after seven days, as shown in Fig. 2.4B, with the remaining pore space occupied by culture medium. The growing tumour displaces the surrounding ECM, as shown in Fig. 2.4C: the highest displacement is observed at the outer surface of the tumour spheroid, where the ECM is pushed outwards. Sciumè *et al.* [33] showed that the ECM stiffness influences the growth of the tumour, hence an important factor to consider. Even though, currently, only the measurement of the tumour volume is experimentally accessible, the displacement of the tumour microenvironment could be a promising input for calibration of the model based on coupled multi-physics observations—as we will sketch in Section 5.5.

The mass fraction of oxygen—the only nutrient we consider—in the interstitial fluid $\omega^{n\ell}$ is shown in Fig. 2.4D. Without vasculature, the oxygen supply is limited to diffusion. As the tumour cells consume oxygen, the oxygen level in the core of the tumour drops below the critical value of $\omega^{n\ell}_{\mathrm{crit}}$, and the tumour cells become necrotic. Accordingly, Fig. 2.4E shows that a necrotic core develops in the centre of the tumour.

2.2.2 *In vivo* growth of a vascularised tumour

Moving away from the controlled environment of the *in vitro* experiments in the previous example, we will now focus on a *in vivo* scenario. We study the growth of a tumour in host tissue, which is

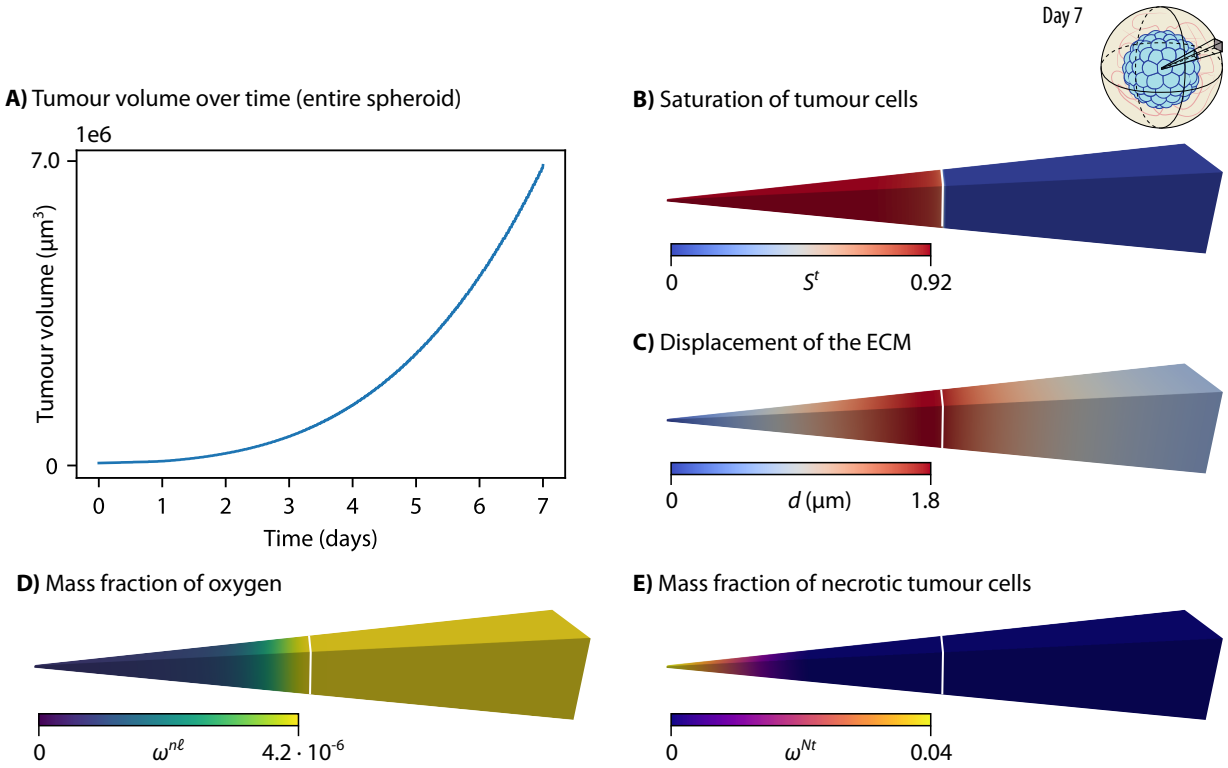

Figure 2.4 Results of *in vitro* tumour spheroid growth over 7 days. The white line indicates the edge of the tumour. A) Volume of the tumour spheroid over time. Note that this is the volume of the entire spheroid, not only the simulated segment. B) Saturation of tumour cells S^t. C) Displacement d of the extracellular matrix (ECM). D) Mass fraction of oxygen $\omega^{n\ell}$. E) Mass fraction of necrotic tumour cells ω^{Nt}.

vascularised with a network of blood vessels—adding a layer of complexity to the problem. As a result, the tumour microenvironment is now composed of the ECM, interstitial fluid, tumour cells, host cells, and blood vessels. As such, this scenario later serves as a starting point for investigating nanoparticle-mediated drug delivery in Section 3.1. This example was published in B. Wirthl, J. Kremheller, B. A. Schrefler and W. A. Wall. 'Extension of a Multiphase Tumour Growth Model to Study Nanoparticle Delivery to Solid Tumours'. *PLOS ONE* 15.2 (2020), e0228443 [58].

We analyse a domain of 1 mm × 1 mm where, due to the symmetry of the problem, only one quarter is actually simulated (0.5 mm × 0.5 mm). A circular tumour Ω^t with an initial radius of $r_o = 25\,\mu m$ is growing in host tissue Ω^h (see Fig. 2.5). This could either be a primary tumour or a metastasis seeded by a parental tumour. The tissue is vascularised with an initial blood vessel volume fraction of $\varepsilon_o^v = 0.02$: this value is estimated based on the data of Secomb *et al.* [119, 120] and in accordance with Jain [121], who stated that the vascular space occupies between 1% and 20% in tumours. In this example, we only consider the collapse of blood vessels but not the formation of new blood vessels. We further set the mass fraction of oxygen in the vasculature to $\omega_D^{nv} = 2.88 \times 10^{-4}$, which corresponds to an oxygen partial pressure in the vasculature of $P_{oxy}^v \approx 100$ mmHg. Because we do not study transport phenomena in the vasculature here, we assume that ω_D^{nv} is constant and apply it as a Dirichlet boundary condition on the entire domain $\Omega^t \cup \Omega^h$. Oxygen is provided via transcapillary exchange from blood vessels and thereby reaches the interstitial fluid. Initially, tumour cells have a saturation of $S^t = 0.5$ in the tumour domain Ω_o^t and $S^t = 0$ in the host domain Ω_o^h. Moreover, we do not have any necrotic tumour cells at the initial state: those depend on reaction terms of the tumour growth model and form at later time steps. The domain for each field is discretised with 120 × 120 bilinear elements, assuming a plain strain case. The structure, fluid, and species transport meshes are conforming. The time discretisation is based on the backward Euler method with a time step of $\Delta t = 1800$ s. In total, 320 time steps are simulated, describing tumour growth in a time frame of 160 hours (≈ 6.5 days). Appendix A.2 lists all parameters: most parameters are based on available literature and have been previously employed [70, 72]. As the constitutive law for the ECM, we employ the Neo-Hookean material law with an initial volume fraction of the ECM of $\varepsilon_o^s = 0.2$.

The volume fraction of living tumour cells $\varepsilon^{LTC} = \varepsilon\,(1 - \omega^{Nt})$ after 160 hours is shown in Fig. 2.6A, where the white contour line indicates the edge of the tumour. The slightly non-spherical shape of the tumour results from the boundary conditions being applied to a quadratic domain. After a growth phase of 160 hours, the tumour has reached a radius of 440 µm. Here and in the following, the edge of the tumour is defined as $S^t = 0.1$. Based on this, the radius is estimated as the mean value of the Euclidean distance of the edge to the centre of the tumour (upper left corner of the domain). Fig. 2.6A further shows that the majority of living tumour cells can be found in the tumour periphery, whereas the tumour core consists of necrotic cells. The volume fraction of vasculature depicted in Fig. 2.6B presents the effect of our model for blood-vessel collapse: considerably fewer blood vessels can be found in the tumour area, including an inner core of approximately 100 µm containing no vessels at all. Vessel compression is a hallmark shared by all solid tumours [122]. The growing tumour pushes against its surrounding microenvironment, collapsing both blood and lymphatic vessels. Provenzano *et al.* [123] concluded from their experimental study that elevated interstitial fluid pressure induces blood vessel collapse. By contrast, Chauhan *et al.* [124] stated that

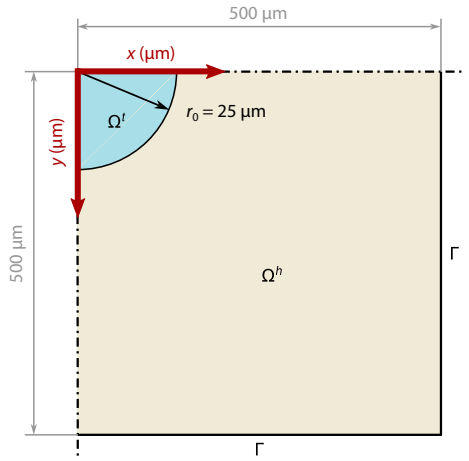

Type of condition	Domain	Fluid	Species
Boundary conditions	$\Omega^t \cup \Omega^h$		$\omega_D^{nv} = 2.88 \times 10^{-4}$
	Γ	$S_D^h = 0.2$ $S_D^t = 0.0$ $S_D^\ell = 0.8$	$\omega_D^{Nt} = 0$
Initial conditions	$\Omega_0^t \cup \Omega_0^h$	$\varepsilon^v = 0.02$	$\omega^{n\ell} = 1.0 \times 10^{-6}$ $\omega^{Nt} = 0$ $\omega^{nv} = 2.88 \times 10^{-4}$
	Ω_0^t	$S^h = 0$ $S^t = 0.5$ $S^\ell = 0.5$	
	Ω_0^h	$S^h = 0.2$ $S^t = 0.0$ $S^\ell = 0.8$	

Figure 2.5 Computational setup. Geometry of the two-dimensional growth of a vascular tumour with the boundary and initial conditions. Note that the initial tumour radius is not sketched to scale.

interstitial fluid pressure cannot compress and collapse blood vessels; instead, the compression of blood vessels is caused by solid stresses. Based on the findings of Padera *et al.* [110], which indicated that proliferating tumour cells cause the collapse of blood vessels, we use p^t as the critical value in the collapse model. Compared to the model for blood vessel collapse employed in Vavourakis *et al.* [125], we use a heuristic approach where we set the parameters in such a way that blood vessel collapse is restricted to the tumour region. Notwithstanding, we are aware of the fact that more complex models are necessary to further investigate the exact reasons for blood vessel collapse.

The distribution of oxygen in the interstitial fluid $\omega^{n\ell}$, depicted in Fig. 2.6C, follows a similar pattern. While the oxygen level in the host cells' region around the tumour is $\omega^{n\ell} = 3.25 \times 10^{-6}$, the oxygen level drops significantly when moving towards the central region of the tumour. The innermost part of the tumour is poorly supplied with oxygen. Therefore, tumour cells in this region become necrotic, and a necrotic core evolves. In the centre of the tumour approximately 50% of the tumour cells are necrotic, as can be seen in Fig. 2.6D. A temporal analysis of the size of the tumour and its necrotic core, as presented in Fig. 2.6E, shows that the necrotic core starts to develop when the tumour reaches a radius of more than 100 µm, which is the case after 65 hours of growth. Similar to other tumour models [126, 127], our results show that the central region of the tumour mainly contains necrotic cells, while the outer shell consists of proliferating cells. This tumour structure (necrotic core + viable outer shell) is attributed to the non-uniform nutrient distribution [126]. The tumour cells close to the outer surface receive sufficient oxygen to proliferate. On the contrary, the oxygen level inside the tumour core falls below the critical limit, thereby causing cell death. According to Carmeliet and Jain [128], cells located more than 100 µm away from the closest capillary become hypoxic because 100 µm is the diffusion limit for oxygen. The development of a necrotic core therefore starts when the tumour reaches a radius of more than 100 µm, as the temporal analysis of tumour growth shows in Fig. 2.6E.

Fig. 2.6F shows the increased interstitial pressure in the tumour: the maximum pressure reached in the interstitial fluid is $p^\ell_{\text{max}} = 840$ Pa $= 6.3$ mmHg. As seen in Fig. 2.6F, the interstitial fluid pressure

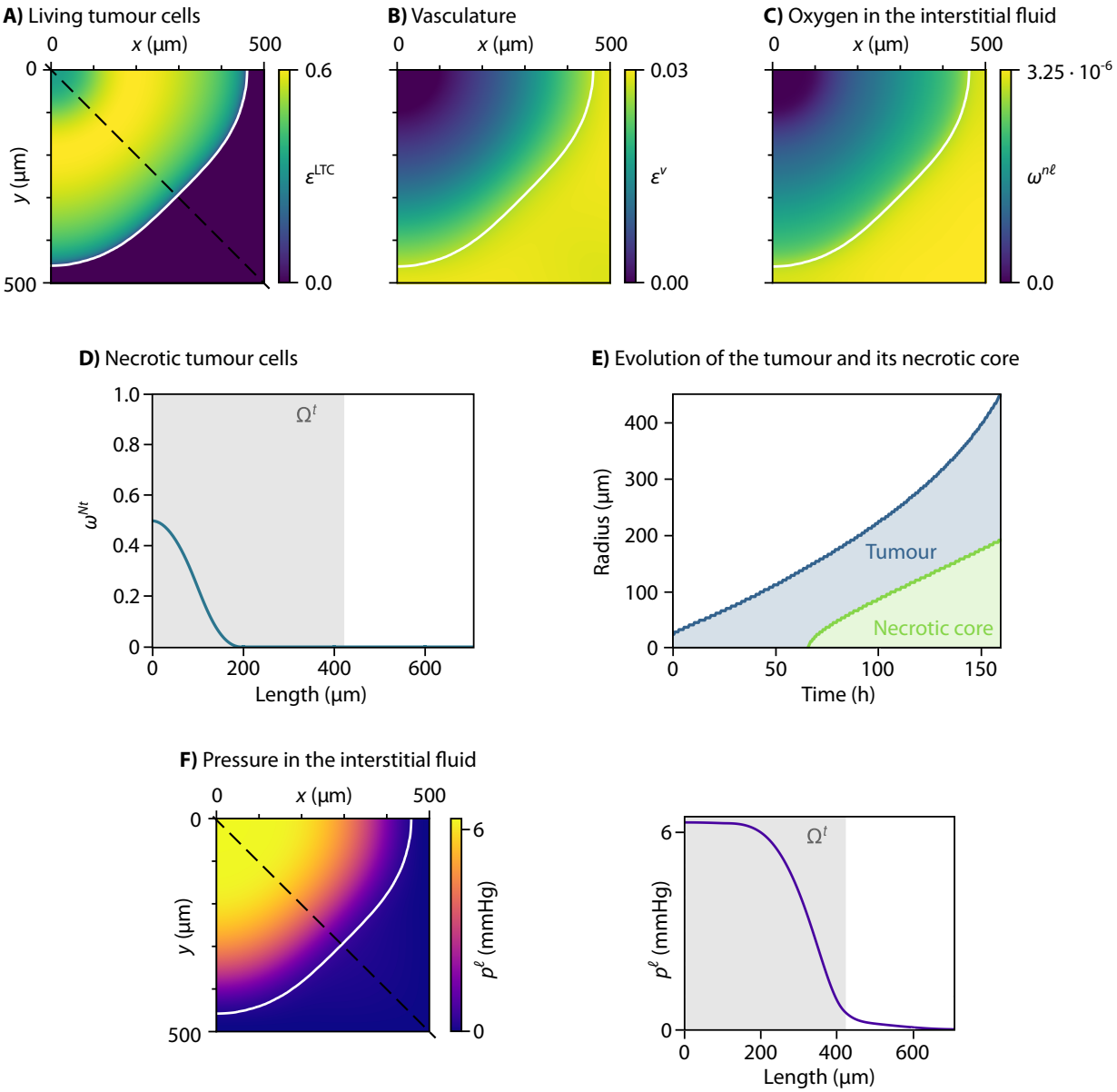

Figure 2.6 Results of vascular tumour growth after 120 hours. The white contour line indicates the edge of the tumour defined as $S^t = 0.1$. A) Volume fraction of living tumour cells $\varepsilon^{\mathrm{LTC}} = \varepsilon\left(1 - \omega^{Nt}\right)$. B) Volume fraction of vasculature ε^v. C) Mass fraction of oxygen in the interstitial fluid $\omega^{n\ell}$. D) Mass fraction of necrotic tumour cells ω^{Nt} visualised over the cut marked by the dashed line in subfigure A. E) Temporal evolution of the radius of the tumour and of its necrotic core. F) Pressure p^ℓ in the interstitial fluid. This figure is taken from [58], where it is licensed under CC BY 4.0.

is high and constant in the central region of the tumour but decreases steeply in the periphery. The maximum interstitial fluid pressure predicted by our model lies within the range of 5 mmHg to 10 mmHg proposed by Dewhirst and Secomb [129]. Nevertheless, the raised interstitial fluid pressure can reach values as high as 60 mmHg [103]. A plateau of interstitial fluid pressure in the central region of the tumour is typical [103, 130] and has also been observed in *in vivo* experiments [131]. As described by Heldin *et al.* [103], the elevated interstitial fluid pressure stems from deficiencies in blood and lymph vessel function. Due to blood vessel leakiness, fluid from the vasculature is transported into the interstitial fluid, while at the same time, lymphatic drainage inside the tumour is impaired. This combination results in fluid accumulation in the tumour region, causing increased interstitial fluid pressure.

To conclude, the results of this example demonstrate that our model is able to reproduce the characteristic features of tumour growth in host tissue: the development of a necrotic non-perfused core, the formation of a tumour periphery with proliferating cells, and the increased interstitial fluid pressure in the tumour region.

2.2.3 Complex *in vivo* interactions in the tumour microenvironment

Kremheller *et al.* [72, 73] investigated angiogenesis based on one soluble isoform of TAF: when the tumour grows, the oxygen level in the core drops below a critical value, and the tumour cells secrete TAF, which induces angiogenesis. However, the biochemical pathways of angiogenesis are complex and involve many different factors [92, 106], which additionally are regulated by biophysical factors such as interstitial fluid flow. In this section, we present a simulation of tumour growth with a complex model for angiogenesis, which includes the influence of interstitial fluid flow on the biochemical pathways of angiogenesis. This work was part of a student term paper and Master's thesis by B. Lince Valadares Onofre [132, 133], supervised by the author of this thesis.

Recent advances in experimental techniques with microfluidics have enabled the investigation of the influence of interstitial fluid flow on angiogenesis but the results are puzzling: some studies observe angiogenesis in the direction of the flow [134, 135], others in the opposite direction [136–138], and some report no influence of interstitial fluid flow on angiogenesis [139]. To unravel these contradictory results, Moure *et al.* [93] presented a computational model of angiogenesis that includes the influence of interstitial fluid flow on the biochemical pathways of angiogenesis: they showed that angiogenesis occurs in the direction of the flow when controlled by initially matrix-bound TAF and in the opposite direction when controlled by soluble TAF. Nevertheless, Moure *et al.* [93] considered the interstitial fluid velocity to be given, and Vilanova *et al.* [92] stated that a model accounting for coupled intravascular and extravascular flow on a time-evolving vascular network is an open challenge.

We here demonstrate that our approach to model the tumour and its microenvironment as a multiphase porous medium directly enables the investigation of all these aspects: the interaction between different forms of TAF (matrix-bound and soluble), the influence of interstitial fluid flow, and the coupling of intravascular and extravascular flow on a time-evolving vascular network.

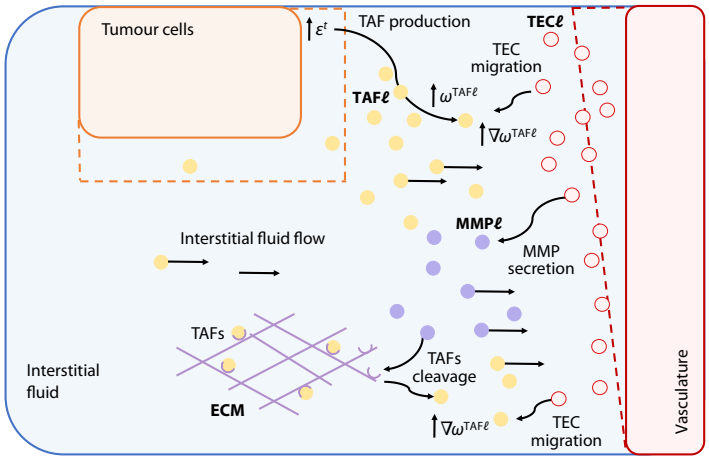

Figure 2.7 Complex interactions in the tumour microenvironment. Tip endothelial cells (TEC) are moving with the leading edge of the growing vasculature. TECs secrete matrix metalloproteinases (MMP), which cleave matrix-bound tumour angiogenic factors (TAF), thereby releasing it into the interstitial fluid as soluble TAF. Soluble TAF chemotactically governs angiogenesis. This figure is adapted from [133].

To investigate interactions between different cues of the biochemical pathways of angiogenesis, we extend our setup by including the following additional species: tip endothelial cells (TECs), matrix metalloproteinases (MMPs), matrix-bound TAF, and soluble TAF, as depicted in Fig. 2.7.

First, the TECs are moving with the leading edge of the growing vasculature. While Moure *et al.* [93] include the TECs as a discrete compartment, we model them in a continuum approach as an additional species with mass fraction $\omega^{\mathrm{TEC}\ell}$, governed by a diffusion-reaction equation similar to Aubert *et al.* [140]

$$\begin{aligned}\varepsilon S^\ell \frac{\partial \omega^{\mathrm{TEC}\ell}}{\partial t}\bigg|_X - \nabla\cdot\left(D_{\mathrm{eff}}^{\mathrm{TEC}\ell}\varepsilon S^\ell \nabla\omega^{\mathrm{TEC}\ell}\right) - \nabla\cdot\left(D^{\mathrm{TEC}v}\varepsilon S^\ell \omega^{\mathrm{TEC}\ell}\nabla\varepsilon^v\right) + \nabla\cdot\left(\chi_{\mathrm{o}}^{\mathrm{TEC}}\varepsilon S^\ell \omega^{\mathrm{TEC}\ell}\nabla\omega^{\mathrm{TAF}\ell}\right)\\ = \frac{1}{\rho^\ell}\left(\sum_{\kappa\in\mathcal{J}_{c\ell}} {}^{\mathrm{TEC}\kappa\to\mathrm{TEC}\ell}M + \varepsilon S^\ell r^{\mathrm{TEC}\ell} - \omega^{\mathrm{TEC}\ell}\sum_{\kappa\in\mathcal{J}_{c\ell}} {}^{\kappa\to\ell}M\right).\end{aligned} \tag{2.48}$$

The second term on the left-hand side describes the diffusion of TECs in the interstitial fluid with a diffusion coefficient $D_{\mathrm{eff}}^{\mathrm{TEC}\ell}$. The third term describes the movement away from the vasculature with a diffusion coefficient $D^{\mathrm{TEC}v}$. The fourth term describes the chemotactic movement towards a higher concentration of TAF with a chemotactic sensitivity $\chi_{\mathrm{o}}^{\mathrm{TEC}}$. Since TECs stay at the leading edge of the vasculature, we assume that they are not influenced by interstitial fluid flow. Additionally, we include an intra-phase reaction term, based on Aubert *et al.* [140], given by

$$\varepsilon S^\ell r^{\mathrm{TEC}\ell} = \gamma_{\mathrm{branching}}^{\mathrm{TEC}}\omega^{\mathrm{TEC}\ell} - \gamma_{\mathrm{tip\text{-}anastomosis}}^{\mathrm{TEC}}\left(\omega^{\mathrm{TEC}\ell}\right)^2 - \gamma_{\mathrm{NV\text{-}anastomosis}}^{\mathrm{TEC}}\omega^{\mathrm{TEC}\ell}\varepsilon^v, \tag{2.49}$$

which describes the tip branching, tip-tip anastomosis (fusing with another vessel), and tip-capillary anastomosis.

Second, we assume that the TECs secrete MMPs, which we also include in a continuum approach as an additional species in the interstitial fluid. The mass fraction of MMPs $\omega^{\mathrm{MMP}\ell}$ in the interstitial

fluid is governed by the convection-diffusion-reaction equation Eq. (2.34) with an intra-phase reaction term, based on [93], given by

$$\varepsilon S^{\ell} r^{\mathrm{MMP}\ell} = \beta_m \left(\omega^{\mathrm{MMP}}_{\mathrm{max}} - \omega^{\mathrm{MMP}\ell}\right) \omega^{\mathrm{TEC}\ell} - \gamma^{\mathrm{MMP}}_{\mathrm{decay}} \omega^{\mathrm{MMP}\ell} - \gamma^{\mathrm{MMP}}_{\mathrm{uptake}} \omega^{\mathrm{TEC}\ell} \varepsilon^{\nu}, \tag{2.50}$$

including secretion of MMPs with a rate β_m until a maximum concentration $\omega^{\mathrm{MMP}}_{\mathrm{max}}$ of MMPs is reached, decay of MMPs with a rate $\gamma^{\mathrm{MMP}}_{\mathrm{decay}}$, and uptake of MMPs by the vasculature with a rate $\gamma^{\mathrm{TEC}}_{\mathrm{uptake}}$.

Third, we include matrix-bound TAF $\omega^{\mathrm{TAF}s}$ as a species in the ECM, as introduced in [141]. MMPs proteolytically cleave matrix-bound TAF, thereby releasing it into the interstitial fluid as soluble TAF $\omega^{\mathrm{TAF}\ell}$. We define the corresponding mass transfer term, based on [93], as

$$\overset{\mathrm{TAF}s \to \mathrm{TAF}\ell}{M} = -\beta_c \omega^{\mathrm{TAF}s} \omega^{\mathrm{MMP}\ell}, \tag{2.51}$$

with the cleaving rate β_c. The soluble TAF $\omega^{\mathrm{TAF}\ell}$ chemotactically governs angiogenesis based on Eqs. (2.37) and (2.38).

Finally, the interstitial fluid flow in our model directly results from the coupling of the intravascular and extravascular flow based on leakage and lymphatic drainage: as demonstrated in Section 2.2.2, this combination results in fluid accumulation in the tumour region, causing increased interstitial fluid pressure and hence an outward flow. However, to investigate the influence of the interstitial fluid flow on the biochemical pathways of angiogenesis and to compare our results to the literature, we additionally apply an interstitial fluid flow through the domain, similar to [93].

We study an example of a tumour growing between two blood vessels, as depicted in Fig. 2.8A, over a time of 27 days. The initial radius of the tumour is $r_0 = 25\,\mu\mathrm{m}$, and the initial mass fraction of matrix-bound TAF is $\omega^{\mathrm{TAF}s}_0 = 7.68 \times 10^{-9}$ in the entire domain. In addition, as mentioned above, we apply an interstitial fluid flow of $u^{\ell} = 0.3\,\mu\mathrm{m\,s^{-1}}$ in the direction of the x-axis (see Fig. 2.8B). The details of the computational setup and the parameters are given in [133].

We compare two scenarios: in the first scenario, we assume that the TECs secrete MMPs, which cleave matrix-bound TAF, thereby releasing it into the interstitial fluid as soluble TAF, which chemotactically governs angiogenesis; in the second scenario, the tumour cells additionally secrete soluble TAF.

The results show that the interstitial fluid flow influences the distribution of the chemical cues in the tumour microenvironment, as depicted in Fig. 2.8C: while the TECs stay at the leading edge of the vasculature, the MMPs and soluble TAF are transported in the direction of the flow to the right side of the domain. Matrix-bound TAF is not directly influenced by the interstitial fluid flow, but since the MMPs are transported to the right side of the domain, the matrix-bound TAF is cleaved there. This demonstrates the complexity of the interactions between different species and fields in the tumour microenvironment. The comparison of the two scenarios shows that when we also consider the secretion of soluble TAF by the tumour cells, the angiogenesis is more pronounced, and the angiogenic pattern is more complex.

This example demonstrates the flexibility of our approach to model complex interactions between different species and fields to be able to investigate the influence of biochemical and biophysical cues on angiogenesis.

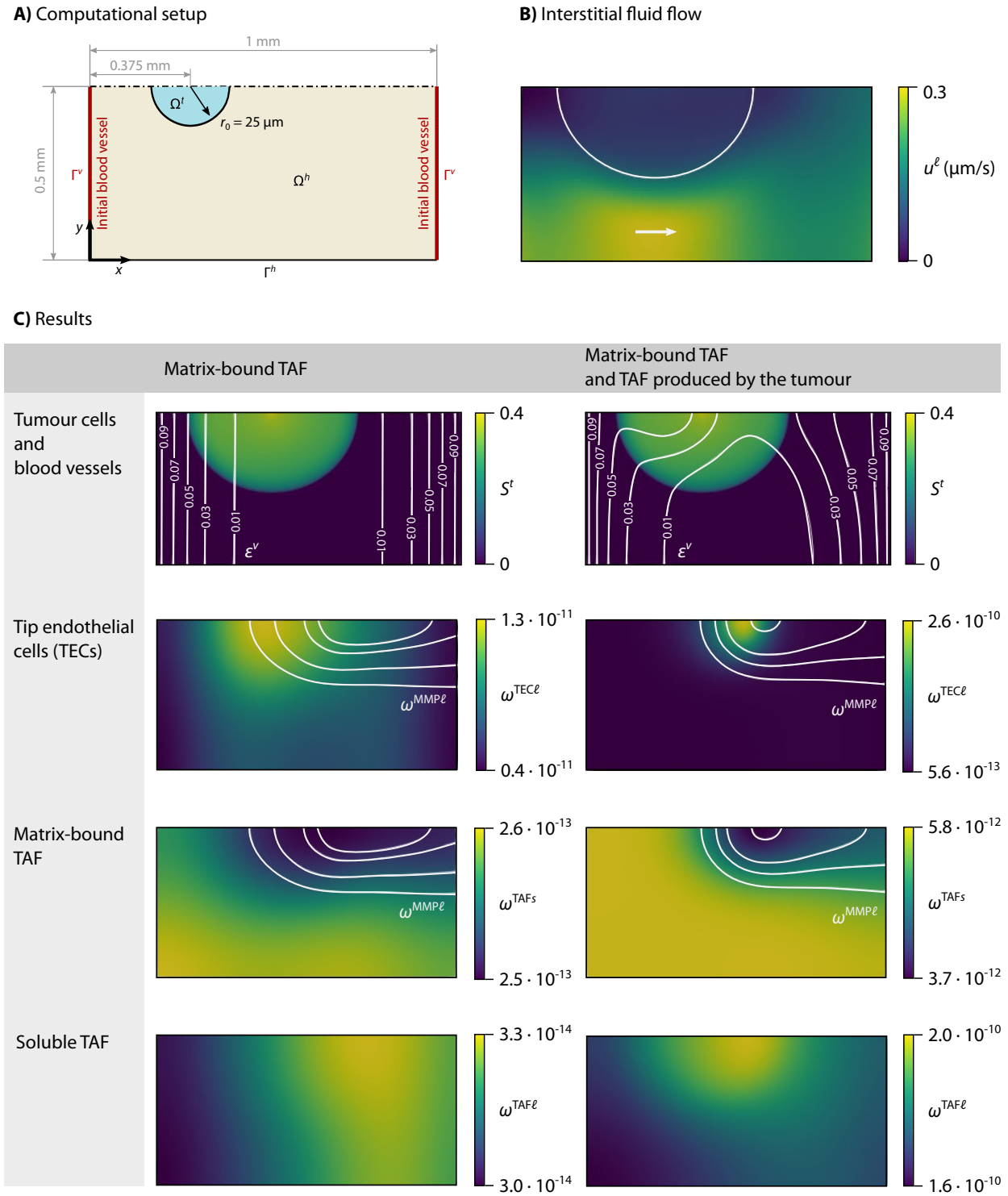

Figure 2.8 Complex interactions in the tumour microenvironment. A) Computational setup. B) Interstitial fluid flow. C) Results for the saturation of tumour cells S^t, the volume fraction of blood vessels ε^v (white contour lines), and for the mass fractions of tip endothelial cells $\omega^{TEC\ell}$, matrix metalloproteinases $\omega^{MMP\ell}$, matrix-bound tumour angiogenic factors (TAF) ω^{TAFs}, and soluble TAF $\omega^{TAF\ell}$. The subfigures are adapted from [133].

3 Nanoparticle-mediated drug delivery

While chemotherapy is one of the most common treatments for cancer, it comes with a significant drawback: the administered drugs do not reach the cancer cells at sufficiently high doses while at the same time attacking healthy tissue. This causes significant side effects and suffering in cancer patients. Nanoparticles have emerged as a promising approach to overcome this deficiency by achieving more specific tumour targeting.

Nanoparticles are nanosized (1 nm to 100 nm) organic or inorganic materials which can be designed with different physicochemical properties, e.g., size, shape, stiffness and surface functionalisation, and programmed with various biological and medical functions [39, 142, 143]. For example, a chemotherapeutic agent can be encapsulated in the nanoparticles or attached to their surface. Drug-loaded nanoparticles can then be used for cancer therapy in two ways: *passive targeting* and *active targeting*. In passive targeting, nanoparticles are injected into the bloodstream, and their size and properties allow them to accumulate in the tumour tissue through the enhanced permeability and retention (EPR) effect [40–42]. In active targeting, nanoparticles are conjugated with ligands of cancer-specific tumour biomarkers, which enables them to bind to the tumour cells [39, 143, 144], or magnetic nanoparticles are guided to the tumour by an external magnetic field [145–147]—thereby achieving a more specific tumour targeting.

While nanoparticles have shown great potential for cancer therapy, their transport to the tumour cells is indeed challenging [148–150]: Dai *et al.* [21] prominently showed that less than 14 out of 1 million (0.0014% injected dose) intravenously injected nanoparticles actually reached the tumour cells. A key role in this disappointing result is likely to be played by transport barriers, which include transport through the circulatory system, extravasation from the blood vessels into the tumour tissue, and transport in the interstitial fluid to the tumour [24, 151]. Our limited understanding of the underlying mechanisms makes it even more difficult to overcome the transport barriers [152]. Hence, to improve the efficacy of nanoparticle-based drugs, we need a more detailed understanding of the mechanisms of nanoparticle transport to and in the tumour, combined with effective design strategies.

To achieve this goal, the tumour and its microenvironment must be considered in their entirety. Historically, new anti-cancer drugs and treatment strategies were developed and tested in classical 2D cell cultures. However, 2D cell cultures cannot reproduce the properties of *in vivo* tumours, especially the complex 3D tumour architecture and microenvironment, and the results of such experiments often do not translate to *in vivo* conditions [153]. Therefore, 3D cell cultures, such as multicellular

tumour spheroids, have emerged in recent decades [154], and microtechnologies facilitated the controlled, reproducible development of uniform tumour spheroids [155]. The same holds for computational models: including a suitable model of the tumour microenvironment—particularly of the relevant transport barriers—is essential to overcome current limitations of nanoparticle-based drug delivery. A new area called *transport oncophysics* has emerged in this context. The driving idea behind it is to describe and address cancer with a focus on the physical phenomena of mass transport [34]. Tumours are classified according to their transport phenotype based on specific transport properties instead of merely genetic characteristics [36].

In this chapter, we start with a computational model of passive targeting in Section 3.1 and then extend it to active targeting with magnetic nanoparticles in Section 3.2.

3.1 Passive targeting

To better understand the characteristics, particularly the barriers to nanoparticle transport and the factors that enhance or limit their clinical application, we extend our tumour-growth model to include nanoparticle transport. The model aims to predict the accumulation of nanoparticles in the tumour and allows a deeper insight into nanoparticle transport mechanisms. As we do not restrict the model to a specific therapeutic approach at this stage, the term *nanoparticle* is used in a generic way. The transport barriers encountered by nanoparticles on their way from (systemic) injection to the tumour are shared by all nanoparticle drugs [151]. Nanoparticles used in cancer treatment could, for instance, be drug-loaded nanoparticles [156] or magnetic nanoparticles mediating hyperthermia [157, 158]. Also, our framework could also easily be extended to include multistage delivery systems [159–161].

This section on passive targeting is largely based on B. Wirthl*, J. Kremheller*, B. A. Schrefler and W. A. Wall. 'Extension of a Multiphase Tumour Growth Model to Study Nanoparticle Delivery to Solid Tumours'. *PLOS ONE* 15.2 (2020), e0228443 [58]. *Co-first authorship

3.1.1 Methods

We include the nanoparticles as additional species in our tumour growth model. The mass balance equation of nanoparticles with a mass fraction $\omega^{\mathrm{NP}\alpha}$ in a generic phase α, e.g., the interstitial fluid, is then given by

$$\begin{aligned}\rho^\alpha \varepsilon S^\alpha \frac{\partial \omega^{\mathrm{NP}\alpha}}{\partial t} - \nabla \cdot \left(\rho^\alpha \varepsilon S^\alpha D^{\mathrm{NP}\alpha} \nabla \omega^{\mathrm{NP}\alpha}\right) - \rho^\alpha \frac{\boldsymbol{k}^\alpha}{\mu^\alpha} \nabla p^\alpha \cdot \nabla \omega^{\mathrm{NP}\alpha} \\ = \sum_{\kappa \in \mathcal{J}_{c\alpha}} \overset{\mathrm{NP}\kappa\to\mathrm{NP}\alpha}{M} + \varepsilon^\alpha r^{\mathrm{NP}\alpha} - \omega^{\mathrm{NP}\alpha} \sum_{\kappa \in \mathcal{J}_{c\alpha}} \overset{\kappa\to\alpha}{M},\end{aligned} \tag{3.1}$$

similar to the other species (see Eq. (2.34)). The nanoparticles can be dissolved in the blood in the vasculature and the interstitial fluid, hence $\alpha, \kappa \in \{v, \ell\}$. Further, $D^{\mathrm{NP}\alpha}$ denotes the diffusion coefficient of nanoparticles in the fluid.

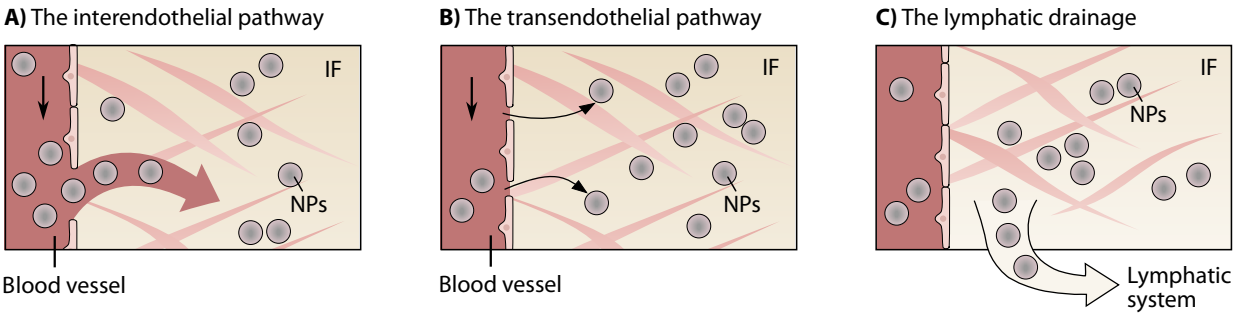

Figure 3.1 Mechanisms of nanoparticle transport to and from the interstitial fluid (IF). Transcapillary exchange of nanoparticles from the vasculature to the IF consisting of A) the interendothelial and B) the transendothelial pathway; C) Lymphatic drainage for transport from the IF to the lymphatic system. This figure is taken from [58], where it is licensed under CC BY 4.0.

We assume that nanoparticles are intravenously injected and subsequently advected by blood flow. However, we do not explicitly model transport in the vasculature and assume a constant mass fraction of nanoparticles in the vasculature $\omega^{\mathrm{NP}v}$. The capillary walls are semipermeable [162], and due to their small size, nanoparticles can extravasate into the interstitial fluid and diffuse towards the tumour. We do not have any source term on the right-hand side of Eq. (3.1), i.e., $\varepsilon^{\alpha} r^{\mathrm{NP}\alpha} = 0$.

The remaining mass transfer terms on the right-hand side of Eq. (3.1) are discussed in the following. In sum, the mass transfer of nanoparticles to and from the interstitial fluid (denoted by the superscript ℓ) comprises three different mechanisms, namely the interendothelial pathway, the transendothelial pathway, and lymphatic drainage, as depicted in Fig. 3.1. Those are given by

$$\sum_{\kappa \in \mathcal{J}_{v\ell}} {}^{\mathrm{NP}\kappa\to\mathrm{NP}\ell}M = \underbrace{{}^{\mathrm{NP}v\to\mathrm{NP}\ell}M_{\mathrm{inter}}}_{\substack{\text{Interendothelial}\\ \text{Fig. 3.1A}}} + \underbrace{{}^{\mathrm{NP}v\to\mathrm{NP}\ell}M_{\mathrm{trans}}}_{\substack{\text{Transendothelial}\\ \text{Fig. 3.1B}}} - \underbrace{{}^{\mathrm{NP}\ell\to\mathrm{NPly}}M_{\mathrm{drain}}}_{\substack{\text{Drainage}\\ \text{Fig. 3.1C}}}. \tag{3.2}$$

The extravasation of nanoparticles from the capillaries into the interstitial fluid occurs through two different pathways: the interendothelial and the transendothelial pathway [163, 164]. We describe the mass transfer from the vasculature to the interstitial fluid based on the Staverman–Kedem–Katchalsky equation [165–167], a commonly used model for membrane transport. Based on Jain [168], the mass transfer is given by

$$\begin{aligned} {}^{\mathrm{NP}v\to\mathrm{NP}\ell}M &= {}^{\mathrm{NP}v\to\mathrm{NP}\ell}M_{\mathrm{inter}} + {}^{\mathrm{NP}v\to\mathrm{NP}\ell}M_{\mathrm{trans}} \\ &= \underbrace{\rho^v \varepsilon^v L_p^v \frac{S}{V}\left[p^v - p^\ell - \sigma\left(\pi^v - \pi^\ell\right)\right]\Delta\omega_{\mathrm{lm}}^{\mathrm{NP}}}_{\substack{\text{Interendothelial}\\ \text{pathway}}} + \underbrace{\rho^v \varepsilon^v P^v \frac{S}{V}\left\langle \omega^{\mathrm{NP}v} - \omega^{\mathrm{NP}\ell}\right\rangle_+}_{\substack{\text{Transendothelial}\\ \text{pathway}}}. \end{aligned} \tag{3.3}$$

The first term describes transport through the interendothelial pathway, also called intercellular extravasation [163]: this is a convective process, meaning that the nanoparticles are dragged by the transvascular fluid flow [168]. The endothelial cells around normal capillary vessels are tightly lined

so that larger molecules are not able to pass through the space between cells. Due to abnormal vessel characteristics of the tumour vasculature, endothelial cells in this area are poorly aligned, leading to gaps which reach a size of 100 nm to 500 nm [163, 169]. The vessel walls are leaky and hyperpermeable, which results in fluid extravasation and passively transports nanoparticles from the vasculature through pores or fenestrations into the interstitial fluid [164]. This mass transfer via the interendothelial pathways is described by a Starling equation based on the hydraulic conductivity L_p^v of the blood-vessel wall, given by Eq. (2.42), and the log-mean concentration $\Delta\omega_{\mathrm{lm}}^{\mathrm{NP}}$ within the pore, given by

$$\Delta\omega_{\mathrm{lm}}^{\mathrm{NP}} = \frac{\omega^{\mathrm{NP}v} - \omega^{\mathrm{NP}\ell}}{\log(\omega^{\mathrm{NP}v}/\omega^{\mathrm{NP}\ell})} \simeq \frac{\omega^{\mathrm{NP}v} + \omega^{\mathrm{NP}\ell}}{2}. \tag{3.4}$$

The second transport mechanism across the vessel walls is the transendothelial pathway: nanoparticles can diffuse through the capillary vessel wall, e.g., through interconnected cytoplasmic vesicles and vacuoles [163]. This diffusive flux through the transendothelial pathway depends on the vascular permeability P^v and the mass fraction difference of nanoparticles across the vessel wall. By using Macaulay brackets $\langle\cdot\rangle_+$, we only allow diffusive flux from the vessels to the interstitial fluid and not vice versa.

In addition to blood vessels, lymphatic vessels contribute to mass transfer with the interstitial fluid. In normal tissues, the lymphatic vessels absorb extravasated fluid and molecules [170]. However, tumours lack a functioning lymphatic system, resulting in inefficient drainage of fluid [128]. The uptake of nanoparticles dispersed in the interstitial fluid by the lymphatic system can be written as

$$\overset{\mathrm{NP}\ell\to\mathrm{NPly}}{M}_{\mathrm{drain}} = \rho^\ell \omega^{\mathrm{NP}\ell} \left(L_p \frac{S}{V}\right)^{\mathrm{ly}} \left\langle p^\ell - p^{\mathrm{ly}}\right\rangle_+ \left\langle 1 - \frac{p^t}{p_{\mathrm{coll}}^{\mathrm{ly}}}\right\rangle_+ \tag{3.5}$$

with the lymphatic filtration coefficient $\left(L_p \frac{S}{V}\right)^{\mathrm{ly}}$. This is similar to the mass transfer term for fluid drainage from the interstitial fluid (see Eq. (2.43) and [72, 73]). We assume $p^{\mathrm{ly}} \approx 0$ in the following. Above the collapsing pressure $p_{\mathrm{coll}}^{\mathrm{ly}}$, lymphatic drainage is impaired, and the lymphatic system does not take up fluid or nanoparticles.

We further prescribe that tumour growth does not influence the mass balance of nanoparticles dispersed in the interstitial fluid and that nanoparticles have no intra-phase reaction term. That is, we set

$$\overset{\mathrm{NP}\ell\to\mathrm{NP}t}{M} + \varepsilon^\ell r^{\mathrm{NP}\ell} - \omega^{\mathrm{NP}\ell}\left(-\overset{\ell\to t}{M}_{\mathrm{growth}}\right) = 0 \tag{3.6}$$

in Eq. (3.1).

3.1.2 Numerical examples and discussion

The pathway nanoparticles take from an intravenous infusion site to the tumour comprises three main phases [129], schematically shown in Fig. 3.2: transport in the vasculature with subsequent crossing of the vessel walls; transport in the interstitial fluid; and finally, removal by the lymphatic system. The transport of nanoparticles along the described pathway is affected by several biophysical

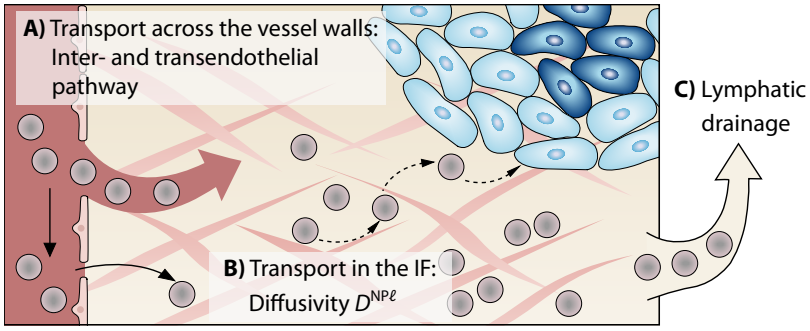

Figure 3.2 Transport barriers to nanoparticle transport. A) Transport across the vessel wall via the interendothelial and/or the transendothelial pathway. B) Transport in the interstitial fluid characterised by the diffusivity $D^{\mathrm{NP}\ell}$. C) Removal by the lymphatic system via lymphatic drainage. This figure is adapted from [58], where it is licensed under CC BY 4.0.

barriers [171], and we therefore investigate the distribution of nanoparticles in the interstitial fluid based on a systematic variation of the parameters which characterise these three transport phases.

We use the result of a grown tumour and its microenvironment—studied in Section 2.2.2—as a starting point for a systematic nanoparticle transport study. The setup of the example is inspired by the experiments conducted by Ziemys *et al.* [172] and thus is of practical biological and clinical relevance. We study the influence of different parameters, which also are of biological interest: they serve to characterise the transport phenotype of the tumour. Here, we investigate how those parameters affect the distribution of nanoparticles in the tumour microenvironment.

To simulate the transport and accumulation of nanoparticles within the tumour, we use the final result after 160 hours of tumour growth (see Fig. 2.6) as initial condition for the nanoparticle simulations. At this point, the tumour displays common characteristics of solid tumours, as described in Section 2.2.2, which complicate efficient nanoparticle delivery.

We then simulate a treatment with an intravenous infusion of the particles: we assume that an intravenous infusion of nanoparticles directly influences their mass fraction in the blood in the entire systemic circulation [129] and that it reaches a steady state where the drug concentration in the blood is constant [173]. Therefore, we prescribe a constant value of $\omega_D^{\mathrm{NP}v} = 2.0 \times 10^{-3}$ as a Dirichlet boundary condition on the entire domain $\Omega^t \cup \Omega^h$ to account for the administered nanoparticles in the vasculature. This value is of the same order of magnitude as the nanoparticle reference concentration of Nabil *et al.* [158] and is small enough not to influence the global physical properties of the solvent, in this case blood [65]. Terentyuk *et al.* [174] used a 20 min injection period for experiments where a nanoshell suspension is tested for tumour treatment in rats. Similarly, Nabil *et al.* [158] started with an initial injection period of 20 min for numerical experiments with nanoparticles. Based on these examples, we analyse a time interval of 20 min with a time step of $\Delta t = 60\,\mathrm{s}$ for all following simulations. The tumour growth equations are still evaluated, but due to the different time scales of tumour growth and nanoparticle transport, the tumour is effectively stationary in the configuration depicted in Fig. 2.6.

Transport across the blood vessel wall. In the first part of the transport study, we investigate the influence of the two transvascular pathways on the distribution of nanoparticles in the interstitial fluid: the interendothelial pathway versus the transendothelial pathway.

We start with varying the influence of the interendothelial pathway and change the amount of convective transport across the vessel walls while keeping a constant vascular permeability of $P^v = 3.5 \times 10^{-4}$ mm/s [175]. Based on Eq. (2.42), we consider different pore sizes, namely

$$r_0 \in \{50\,\text{nm},\ 100\,\text{nm},\ 150\,\text{nm},\ 200\,\text{nm}\}\,, \tag{3.7}$$

which is within the range proposed by Stylianopoulos and Jain [107]. In this first part, we do not consider lymphatic drainage but only analyse transport across the blood vessel wall.

The results in Fig. 3.3A1 show that the nanoparticles mainly accumulate in the region with a high volume fraction of vasculature, which in our case coincides with the region of host cells around the tumour—the still well-perfused part (see Fig. 2.6B and C). The mass fraction of nanoparticles in the interstitial fluid rises from 1.0×10^{-3} to 1.7×10^{-3} for a pore radius of $r_0 = 50$ nm and $r_0 = 200$ nm, respectively. In contrast, considerably fewer particles reach the tumour core in all four cases, on average 0.3×10^{-3} in the tumour centre.

We further investigate the contribution of the transcellular pathway where particles are transported across endothelial cells either through a series of linked vesicles or through a single vesicle [163]. We now vary the vascular permeability P^v while keeping a constant pore radius of $r_0 = 150$ nm: we choose dextran as a model carrier to analyse the effect of different vascular permeabilities on the distribution of nanoparticles in the interstitial fluid. In Fig. 3.4, we summarise permeability coefficients of dextrans with different molecular weights, as determined by Dreher *et al.* [176], Chou *et al.* [177], and Ho *et al.* [175]: the measured permeability coefficients differ by more than one order of magnitude. As a baseline, we use the purely convective transport via the interendothelial pathway and set $P^v = 0$. We then choose the values for 10 kDa, as an example, to study the influence on the distribution of nanoparticles in the interstitial fluid.

The results are depicted in Fig. 3.3A2: compared to the results for the interendothelial pathway, the qualitative distribution of nanoparticles in the interstitial fluid does not change under the influence of transcellular transport; only the absolute mass fraction of nanoparticles in the interstitial fluid changes. In our example with a fixed pore radius of $r_0 = 150$ nm, a permeability coefficient of $P^v = 3.2 \times 10^{-5}$ mm/s—as determined by Dreher *et al.* [176]—has little influence on the nanoparticles distribution, which rises by only 5% when compared to the baseline simulation with $P^v = 0$. In contrast, the values $P^v = 3.5 \times 10^{-4}$ mm/s by Ho *et al.* [175] and $P^v = 1.28 \times 10^{-3}$ mm/s by Chou *et al.* [177] result in an increase of the mass fraction of nanoparticles in the interstitial fluid by 41% and 84%, respectively.

Together, the variation of the pore radius r_0 and the vessel wall permeability P^v shows that particles mainly accumulate in the region outside the tumour in both cases. This distribution of nanoparticles is due to the fact that the convective mass transfer M_{inter} and the diffusive mass transfer M_{trans} of nanoparticles across the vessel walls, as prescribed by Eq. (3.3), is most significant in the

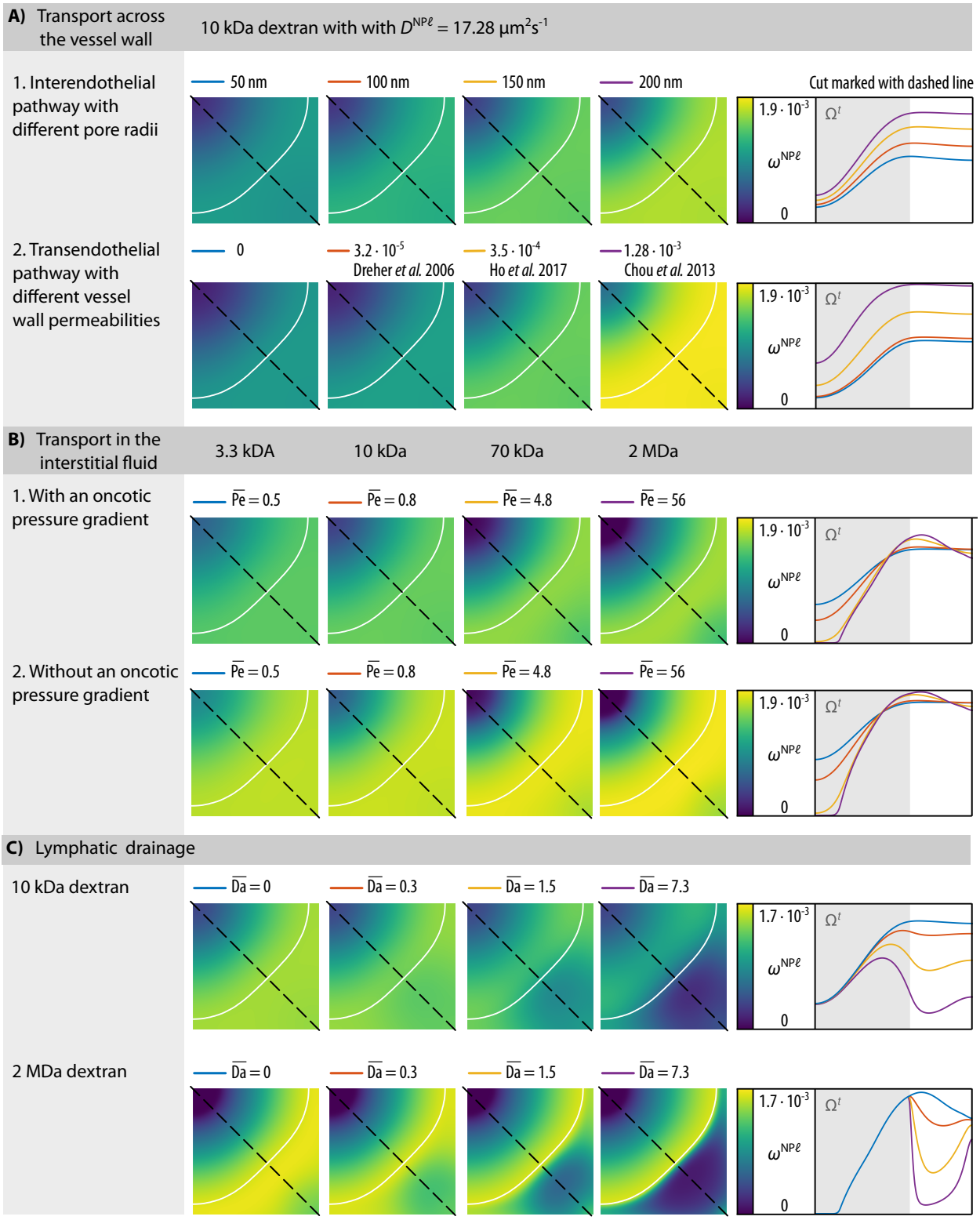

Figure 3.3 Nanoparticle distribution in the interstitial fluid after a 20 min injection period. A) Influence of transport across vessel walls via the inter- and the transendothelial pathway. B) Influence of transport characteristics in the interstitial fluid with different Péclet numbers. C) Influence of lymphatic drainage with different Damköhler numbers. This figure is adapted from [58], where it is licensed under CC BY 4.0.

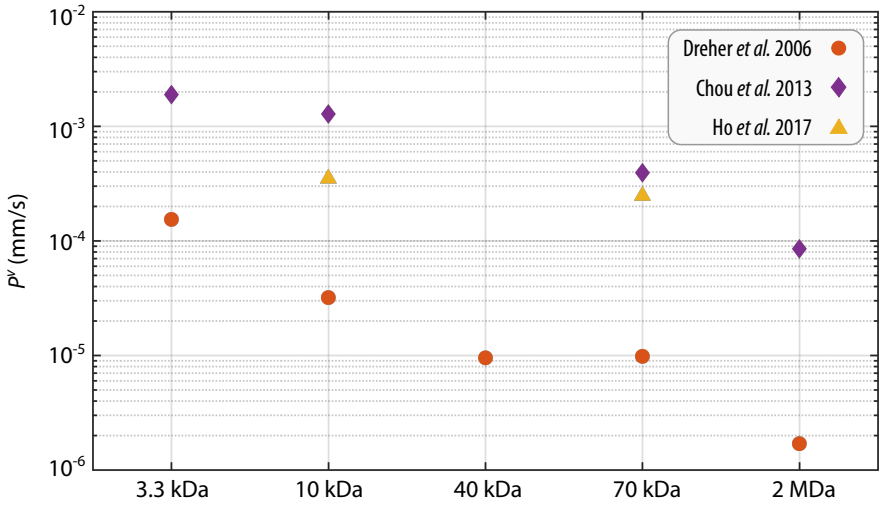

Figure 3.4 Values for the vascular permeability coefficient. Vascular permeability coefficient P^v of dextrans with a molecular weight of 3.3 kDa, 10 kDa, 40 kDa, 70 kDa and 2 MDa summarised from data by Dreher *et al.* [176], Chou *et al.* [177] and Ho *et al.* [175]. This figure is taken from [58], where it is licensed under CC BY 4.0.

Table 3.1 Parameters for nanoparticle transport across vessel walls.

Symbol	Parameter	Value	Units	Ref.
γ_{pore}	Fraction of pores	10×10^{-4}	—	[125]
μ^v	Viscosity of blood	4×10^{-3}	Pa s	[107]
t	Thickness of vessel wall	1	µm	[178]
S/V	Surface-to-volume ratio	20	mm^{-1}	[130]
r_0	Pore radius	50, 100, **150***, 200	nm	[107]
P^v	Blood-vessel wall permeability of 10 kDa dextran	0, 3.2×10^{-5}, **3.5×10^{-4}***, 1.28×10^{-3}	mm/s	[175–177]

* The bold value marks the default values used for the nanoparticle transport study.

region outside the tumour which is well perfused. However, to reach the core of the tumour, diffusion inside the interstitial fluid is necessary, which is the inhibiting factor here.

As depicted in Fig. 3.4, the permeability coefficients measured by Dreher *et al.* [176], Chou *et al.* [177] and Ho *et al.* [175] differ by more than one order of magnitude. Dreher *et al.* [176] used a mouse model to measure the apparent permeability *in vivo*: their setup includes an unknown influence of convection, as stated by the authors. Chou *et al.* [177] used the Kedem–Katchalsky equation to fit the permeability and diffusivity of dextrans to the data of Dreher *et al.* [176]. In contrast, Ho *et al.* [175] reasoned that a systematic quantitative study of permeabilities utilising animal models is difficult and instead proposed an *in vitro* model based on microfluidics. This model allows a quantitative study of the extravasation and control over the pathway the nanoparticles take. Therefore, we employ the permeability coefficient determined by Ho *et al.* [175] as the default value for the following simulations (see Table 3.1).

Our findings are consistent with the fact that the extravasation of nanoparticles through both pathways (trans- and interendothelial route) influence the number of nanoparticles reaching the tumour. The remaining question however is which mechanism is dominant. Wilhelm *et al.* [163]

summarise that the distinction between transvascular transport through intercellular gaps or transendothelial cell pores is complex and that intercellular gaps have not yet been definitively established. Nevertheless, nanotechnology has focused on transport through intercellular gaps as described by the *enhanced permeability and retention* (EPR) effect, and so far has not overcome major problems with poor delivery efficiency [163, 179, 180]. We therefore use a combination of trans- and interendothelial routes, where both pathways contribute a considerable amount of nanoparticle transport to the interstitial fluid by setting the pore radius to $r_0 = 150\,\text{nm}$ and the vascular permeability coefficient to $P^v = 3.5 \times 10^{-4}\,\text{mm/s}$ [175] for all following simulations. Jain and Stylianopoulos [169] nonetheless stated that tumour vasculature is not always as leaky as postulated in the description of the EPR effect, and Wilhelm *et al.* [163] concluded that future research should concentrate on the transendothelial transport mechanism. Here, we have shown that the transendothelial pathway indeed plays a major role and can increase the efficiency of drug delivery.

Transport in the interstitial fluid. We further investigate the transport of nanoparticles in the interstitial fluid, which is driven by diffusion and convection. To study the transport in the interstitial fluid, we use the Péclet number as the ratio of convective transport rate to diffusive transport rate in the interstitial fluid

$$\text{Pe} = \frac{u^\ell L}{\varepsilon S^\ell D^{\text{NP}l}} = \frac{(S^\ell)^{A_{\ell-1}}\, kL}{\varepsilon \mu^\ell D^{\text{NP}\ell}} \nabla p^\ell, \tag{3.8}$$

where we use the Darcy equation for the convective velocity u^ℓ. The characteristic length is set to $L = (A_{\text{tumour}}/P_{\text{tumour}}) = 220\,\mu\text{m}$, with A_{tumour} being the surface of the tumour and P_{tumour} its perimeter. The pressure gradient ∇p^ℓ is calculated using central differences. For the further analysis, we use the mean value $\overline{\text{Pe}}$ of the Péclet number on the entire domain $\Omega^t \cup \Omega^h$. We now include both inter- and transendothelial pathways for transport across the vessel walls. Here, we use a constant permeability coefficient of $P^v = 3.5 \times 10^{-4}\,\text{mm/s}$ [175] and a pore radius of $r_0 = 150\,\text{nm}$, as discussed in the previous section. In order to investigate nanoparticle distributions in different transport regimes, we compare dextrans with different molecular weights, similar to the experiments performed by Ziemys *et al.* [172]. The interstitial diffusivities for 3.3 kDa, 10 kDa, 70 kDa and 2 MDa dextran determined by Chou *et al.* [177] result in Péclet numbers in the range of 0.5 to 56 (see Table 3.2). This allows us to compare diffusion-dominated with convection-dominated transport in the interstitial fluid. The convective transport rate is influenced by the pressure gradient ∇p^ℓ, while the diffusive transport rate depends on the particle size and on the ECM, which—due to its dense structure—impedes diffusive transport [169, 171]. We use the Péclet number to collectively analyse the influence of all these factors.

Fig. 3.3B1 presents the distribution of dextrans with various molecular weights in the interstitial fluid. In the diffusion-dominated case, where $\overline{\text{Pe}} = 0.5$ and $D^{\text{NP}\ell} = 30.83\,\mu\text{m}^2/\text{s}$ for 3.3 kDa, the nanoparticles spread more uniformly across the domain. In contrast, in the convection-dominated case, where $\overline{\text{Pe}} = 56$ and $D^{\text{NP}\ell} = 0.26\,\mu\text{m}^2/\text{s}$, the particles accumulate at the tumour edge. In particular, no particles reach the core of the tumour, which coincides with the region without blood vessels (see Fig. 2.6B). We thus observe that the nanoparticles can only reach the whole tumour domain if diffusion dominates the transport in the interstitial fluid. If however convection dominates the flow

Table 3.2 Characteristics of dextrans of different molecular weights with values based on Chou *et al.* [177].

Dextran molecular weight (kDa)	**Diffusivity** $D^{\mathrm{NP}\ell}$ ($\mu m^2/s$)	**Péclet number**	**Size** (nm)*
3.3	30.83	0.5	1.6
10	17.28	0.8	2.8
70	3.01	4.8	7.3
2000 (= 2 MDa)	0.26	56	25

* Molecular size is expressed as the hydrodynamic radius determined by the Stokes–Einstein equation. The values are taken from Dreher *et al.* [176].

characteristics, particles do not reach the core of the tumour or any regions located further away from functioning blood vessels.

For all simulations so far, we included an oncotic pressure difference of $\sigma\left(\pi^{v}-\pi^{\ell}\right)=1333\,\mathrm{Pa}$ [111, 181]. This implies two things: first, the oncotic pressure in the tumour interstitium π^{ℓ} differs significantly from the oncotic pressure in blood plasma π^{v} and hence, an oncotic pressure gradient is present; second, the reflection coefficient σ, which influences the effectiveness of the pressure gradient, must be greater than zero. In contrast to the findings of Baxter and Jain [181], Stohrer *et al.* [182] stated that, based on their measurements, the oncotic pressure gradient across the blood-vessel wall is low. Moreover, Tong *et al.* [183] assumed a reflection coefficient close to zero because of large pores in the vessel walls and the consequent leakiness. Hence, the question arises as to whether and how the presence of an oncotic pressure difference across the tumour microvascular wall influences the distribution of nanoparticles. We therefore analyse the distributions of dextran in the extreme case of $\sigma\left(\pi^{v}-\pi^{\ell}\right)=0\,\mathrm{Pa}$. The results in Fig. 3.3B2 show that the qualitative distribution of particles in the interstitial fluid is similar to the results with an oncotic pressure gradient (compare Fig. 3.3B1). However, a quantitative comparison reveals that approximately 20% more particles reach the interstitial fluid when no significant oncotic pressure gradient is present.

After crossing the vascular barrier, nanoparticles must navigate the tumour microenvironment to reach cancerous cells. The interstitial fluid pressure in the tumour can be 10 to 40 times higher than in host tissue, creating an outward pressure gradient [103]. This increases the outward interstitial flow, thereby limiting convective transport into the tumour region [163]. Nanoparticle transport to the centre of the tumour is thus impeded, and nanoparticles hardly reach the tumour core or any regions located further away from functioning vasculature, as shown in Fig. 3.3B. As Zhang *et al.* [184] summed up, the elevated interstitial fluid pressure is one of the main factors hindering effective nanoparticle tumour penetration, and Goel *et al.* [185] stated that vascular normalisation reduces tumour hypoxia and the interstitial fluid pressure. Based on those findings, Chauhan *et al.* [186] suggested that vascular normalisation improves the convective delivery of nanoparticles.

Ziemys *et al.* [172] concluded that the dominant transport mechanism is diffusion. Our results show that only if diffusive transport in the interstitial fluid is significant do nanoparticles penetrate the centre of the tumour [187]. However, Nichols and Bae [179] and Danhier and Preat [188] stated that the higher and heterogeneous density of human ECM leads to regions that are inaccessible to nanoparticles. Consequently, the interstitial fluid pressure gradient impedes convective transport, while the denser structure of the tumour ECM limits diffusive transport [169].

In summary, the movement of nanoparticles in the interstitial fluid is significantly limited, and the particles remain close to where they cross the vascular barrier. Consequently, nanoparticles only reach well-vascularised regions and the highest concentrations are located near the vascular surface [176]. Since tumour cores are poorly perfused [38], nanoparticles and anti-cancer agents transported by nanoparticles do not reach those regions. Our model has proven to be well-suited to capture this behaviour.

Lymphatic drainage. We now include lymphatic drainage of interstitial fluid and the nanoparticles contained therein: the lymphatic system generally drains excessive fluid, thereby removing waste products and foreign substances [189]. To analyse its influence on the distribution of nanoparticles in the tumour, we assume that the lymphatic system recognises the nanoparticles as foreign bodies and thus removes them at an increased rate. Similar to the Péclet number, we define the Damköhler number as the ratio of reactive timescale to convective timescale, as proposed by Shipley and Chapman [190]

$$\mathrm{Da} = \frac{\lambda L}{u^{\ell}}, \tag{3.9}$$

where λ represents the rate of species loss in the interstitial fluid due to lymphatic drainage given by

$$\lambda = \frac{M_{\mathrm{drain}}^{\mathrm{NP}\ell\to\mathrm{NPly}}}{\rho^{\ell}} = \left(L_p \frac{S}{V}\right)^{\mathrm{ly}} \left\langle p^{\ell} - p^{\mathrm{ly}} \right\rangle_{+} \left\langle 1 - \frac{p^{t}}{p_{\mathrm{coll}}^{\mathrm{ly}}} \right\rangle_{+} \tag{3.10}$$

and the convective velocity u^{ℓ}, as also employed in Eq. (3.8). We analyse the resulting distribution of nanoparticles in the interstitial fluid for different Damköhler numbers. To that end, we vary the hydraulic conductivity of lymphatic vessels. Baxter and Jain [187] used a lymphatic filtration coefficient $\left(L_p \cdot \frac{S}{V}\right)^{\mathrm{ly}} = 1.04 \times 10^{-6}\ (\mathrm{Pa\,s})^{-1}$ for the lymphatic vessels. To investigate different transport regimes, we employ different values for the lymphatic filtration coefficient, resulting in a mean value of the Damköhler number of $\overline{\mathrm{Da}} = 0.3$, 1.5 and 7.3 on the entire domain. We again use a constant permeability coefficient of $P^{v} = 3.5 \times 10^{-4}$ mm/s [175] and a pore radius of $r_{\mathrm{o}} = 150$ nm.

Above the collapsing pressure $p_{\mathrm{coll}}^{\mathrm{ly}}$, interstitial hypertension in the tumour causes lymphatic vessels to collapse, and thus no fluid is drained [72]. This is the case in the whole tumour zone; hence, lymphatic drainage is impaired. The drainage of the lymphatic system therefore only influences regions outside the tumour. The amount of drained fluid increases with increasing hydraulic conductivity, as shown in Fig. 3.3C. In particular, in the case of 2 MDa dextran, where transport in the interstitial fluid is convection-dominated, the particles clearly accumulate at the outer edge of the tumour.

This interplay of transvascular transport and lymphatic drainage results in an accumulation of nanoparticles in the tumour—a phenomenon called *enhanced permeability and retention* (EPR) effect. Endothelial cells in the vasculature are poorly aligned, leading to large fenestrations. This effect causes extensive leakage of blood plasma components, including macromolecules and nanoparticles, into the interstitium. At the same time, lymphatic clearance is inhibited by the increased interstitial pressure of the tumour. This combination of vascular leakage and impaired lymphatic drainage leads

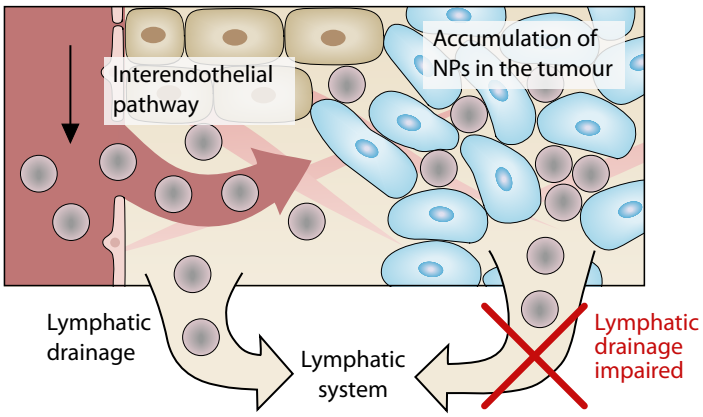

Figure 3.5 The enhanced permeability and retention (EPR) effect. Nanoparticles (NPs) leak from the vasculature to the interstitial fluid. In the tumour region, the lymphatic drainage is impaired, and hence the particles are not removed by the lymphatic system. This results in a passive accumulation of nanoparticles in the tumour called the EPR effect [40]. This figure is taken from [58], where it is licensed under CC BY 4.0.

to the passive retention of nanoparticles in the tumour. The EPR effect, as depicted in Fig. 3.5, was first described by Matsumura and Maeda [40] in 1986. It became a gold standard for the design of anti-cancer agents based on macromolecules and nanoparticles to selectively target tumour sites [42].

Since the first mention of the EPR effect more than 30 years ago, the number of publications citing it has increased exponentially [179]. Nichols and Bae [179] however stated that despite good documentation and the experimental validation of the EPR effect in small animal models, in particular with nanoparticles, the clinical translation of nanomedicine is still limited. A literature summary [163] revealed that only 0.7% of the administered nanoparticles reach solid tumours in mouse models, and only 14 out of 1 million nanoparticles reach the cancer cells [21]. In addition, human tumours differ from murine tumours in several major characteristics: the fact that rodent tumours grow much faster than human tumours leads to several differences [188]. In some human tumours, blood vessels are less leaky than expected, limiting extravasation and delivery of nanoparticles [169]. Heterogeneous blood flow in tumours and resulting hypoxic areas hinder the delivery of nanoparticles and drugs to these tumour zones [191].

Our results confirm that our model can capture the EPR effect. Nevertheless, proper calibration of the model is crucial to determine the transport regimes that occur *in vivo*. In particular, better experimental characterisation of lymphatic drainage is essential to validate the mechanisms contributing to the EPR effect. Our results show that the EPR effect might reduce the accumulation of nanoparticles or drugs in host tissue and prevent side effects of conventional chemotherapy. At the same time, it does not improve delivery to the tumour, particularly not to the tumour centre.

Many studies assume homogeneous tumours and a uniform distribution of the nanoparticles [192, 193]. In contrast, we model and observe highly uneven distributions which, in a similar form, have been observed *in vivo* as summarised by Wilhelm et al. [163] and limit the clinical translation of nanomedicine. Our model in particular captures the high interstitial pressure in tumours, which hinders nanoparticles from reaching all regions of the tumour.

3.1.3 Conclusion

We have extended our vascular multiphase tumour growth model to include a suitable model for passive nanoparticle transport by the tumour microenvironment and have investigated the resulting nanoparticle distributions. We especially considered the transport barriers proposed by transport oncophysics [36]: medical and clinical studies in this context have revealed that several anatomical and physiological factors hinder sufficient penetration of nanoparticles to reach the whole tumour zone. Our tumour model reproduces those transport characteristics, particularly the EPR effect. We have shown that the accumulation of nanoparticles in the tumour depends on several parameters and that nanoparticles do not reach the entire tumour in all cases.

Our model predicts that considering the transendothelial pathway could increase the amount of nanoparticles reaching the tumour. Until now, nanotechnology has focused solely on transport through the interendothelial pathway and has not overcome major delivery problems. Conversely, a comprehensive characterisation of the transendothelial pathway lacks precise parameters from a biological point of view, e.g., for vascular permeability. We further deduce from our results that nanoparticles can reach the tumour core if (or even *only if*) transport in the interstitial fluid is diffusion-dominated. However, diffusion is limited to about 100 µm [129], and the structure of the ECM impairs diffusion. If, on the contrary, the transport is convection-dominated, the high interstitial pressure counteracts transport into the tumour. As a result, nanoparticles remain in proximity to where they cross the vascular border. Since tumour cores are poorly perfused, nanoparticles cannot reach the central regions of the tumour.

One possible treatment strategy to overcome these difficulties is vascular normalisation to restore the functionality of the tumour vasculature and thereby improve drug delivery [194]. Studying drug delivery in combination with a tumour growth model could have several benefits in future work: for instance, the effect of periodic treatments with intermittent tumour growth can be assessed, or novel therapies—such as vascular normalisation followed by treatment with a conventional drug—can be integrated more easily. This can give valuable insight into transport characteristics and accumulation of nanoparticles in tumours, which can be transferred to medical studies.

3.2 Magnetic targeting

As passive targeting is limited by the EPR effect, active targeting is a promising approach to improve the efficacy of nanoparticle-based drugs. For example, an external magnetic field is applied to direct magnetic nanoparticles to the target tissue, i.e., the tumour [195]. Such magnetic carriers allow targeting the tumour with enhanced uptake at the target site while reducing the systemic toxicity of the drug [196].

Magnetic nanoparticles possess unique physical properties: due to their small size (1 nm to 100 nm), they form a single magnetic domain. Therefore, they become highly magnetic in the presence of an external magnetic field but revert to a non-magnetic state when the field is removed, called superparamagnetism [197]. The nanoparticles are injected intravenously, and then a magnet placed on the body surface concentrates the nanoparticles at the target site. The translational magnetic

force pulling the particles towards the magnet depends on their magnetic properties and the applied magnetic field and field gradients [198]. However, the magnetic field and the field gradient decrease rapidly with increasing distance [199]. Additionally, counteracting hydrodynamic forces further complicate capturing particles from flow, e.g., blood flow or flow in the interstitium. The pressure gradient between the tumour and the surrounding host tissue causes an outward flow of interstitial fluid from the tumour—an additional transport barrier for nanoparticles [103].

To study the magnetic capturing of nanoparticles in tumour spheroids in the presence of flow, we use a simplified *in vitro* test setup: a tumour spheroid is placed in a flow chamber with a magnet underneath to capture the nanoparticles, as presented by [200]. We retain the essential characteristics and transport barriers of the tumour microenvironment while reducing the complexity of the *in vivo* scenario to a controlled and monitorable setup.

On the way towards a comprehensive computational model for effective nanoparticle-mediated drug design, we start with a model for our experimental test setup, where we can control the environmental conditions and measure the relevant quantities. The potential of our physics-based computational model will provide a stepping stone to *in vivo* scenarios where control and measurement are limited, and ultimately, such an *in silico* tool can accelerate translation into the clinical setting.

Here, we develop a computational model of the transport of magnetic nanoparticles in the experimental test setup described above: we integrate a model for the transport of magnetic nanoparticles in an external magnetic field with a tumour model, which includes the fluid flow. We use a continuum approach to model the nanoparticle transport based on a diffusion-advection equation and integrate it with our multiphase porous-media model for the tumour spheroid and the fluid flow.

Several computational models have previously been developed to study individual aspects of the transport of nanoparticles under the combined effect of flow and magnetic forces in the tumour microenvironment. Chauhan *et al.* [186], Welter and Rieger [201], Cattaneo and Zunino [202], and Vilanova *et al.* [92] developed tumour models which study the interstitial fluid flow in the tumour microenvironment but without including nanoparticle transport. Concerning computational models of tumour spheroids, Deisboeck *et al.* [27], Karolak *et al.* [203] and Metzcar *et al.* [30] comprehensively reviewed the state of the art. Frieboes *et al.* [204], Curtis *et al.* [156], and Wirthl *et al.* [58] presented models of nanoparticle-based cancer therapy limited to the passive transport of nanoparticles without a magnetic field. Furlani and Ng [205], Furlani and Furlani [206], and Hewlin and Tindall [207] studied the capture of magnetic nanoparticles in flow but focused on blood vessels. Detailed computational models which study magnetic nano-drug delivery systems under consideration of transport barriers of the tumour microenvironment include Shamsi *et al.* [208] and Rezaeian *et al.* [209].

The novelty of our approach lies in the coupling of fluid flow around and through the tumour spheroid integrated into a theoretically sound and consistent physics-based multiphase porous-media model together with the transport of magnetic nanoparticles in an external magnetic field, which is evaluated in a numerically efficient way based on analytical expressions for the magnetic field and force. We focus on an *in vitro* test setup in a perfused microfluidic device. Such setups are a powerful tool because of the control over the environmental conditions, and they even replace *in*

vivo experiments in preclinical drug testing [210, 211]. Developing a computational model for such a setup is hence highly relevant to improving the efficacy of nanoparticle-based drugs.

The content of this section is largely based on the author's following publications: B. Wirthl, V. Wirthl and W. A. Wall. 'Efficient Computational Model of the In-Flow Capturing of Magnetic Nanoparticles by a Cylindrical Magnet for Cancer Nanomedicine'. *Physical Review E* 109.6 (2024), 065309 [59], which is copyrighted by the American Physical Society and reused here with permission from the American Physical Society and B. Wirthl, C. Janko, S. Lyer, B. A. Schrefler, C. Alexiou and W. A. Wall. 'An in silico model of the capturing of magnetic nanoparticles in tumour spheroids in the presence of flow'. *Biomedical Microdevices* 26.1 (2024) [60], which is licensed under CC BY 4.0.

3.2.1 Motivational experimental test setup

In our test setup, we study the magnetic accumulation of superparamagnetic iron oxide nanoparticles (SPIONs) in a flow chamber. Among the various types of magnetic nanoparticles, SPIONs are the most extensively investigated because of their biocompatibility [212]. The experimental setup is sketched in Fig. 3.6A and described in detail in [200]. Therefore, we only give a brief summary below. Tumour spheroids of melanoma cells and fibroblasts were grown for three days. The SPIONs were loaded with a chemotherapeutic drug, in this case, mitoxantrone. To investigate the accumulation of the SPIONs under dynamic conditions, the tumour spheroids were placed in MIVO®single flow chambers without transwell insert (React4Life, Genova, Italy). The flow chamber was perfused using a peristaltic pump, and the SPIONs were injected into the flow. The SPIONs are then accumulated at the tumour spheroid by permanent magnets.

3.2.2 Methods

To investigate the transport of magnetic nanoparticles in the test setup described above, we develop a computational model that specifically tackles the following novel challenges (compared to passive transport as discussed in the previous subsection):

1. Model the free fluid flowing around the tumour spheroid in the flow chamber coupled to the flow in the tumour spheroid.
2. Model the magnetic nanoparticles transported with the fluid and within the tumour spheroid subjected to the force of an external cylindrical magnet.

The computational setup is depicted in Fig. 3.6B.

The magnetic nanoparticles are dispersed in the fluid and transported by its flow. Additionally, a cylindrical magnet is positioned below the flow chamber and exerts a magnetic force on the nanoparticles. Many publications [213–217] use particle-based approaches for the nanoparticles, where the forces are computed for each individual particle. However, tumour spheroids are on the scale of a few hundred micrometres, while nanoparticles are several orders of magnitude smaller. Investigating the transport of nanoparticles with a particle-based approach at the scale of the tumour spheroid thus involves up to a billion particles—an enormous computational burden [215]. But as we are not interested in the movement of the individual nanoparticles, there exist much more efficient approaches. We therefore use a continuum approach for the nanoparticles, where we employ a

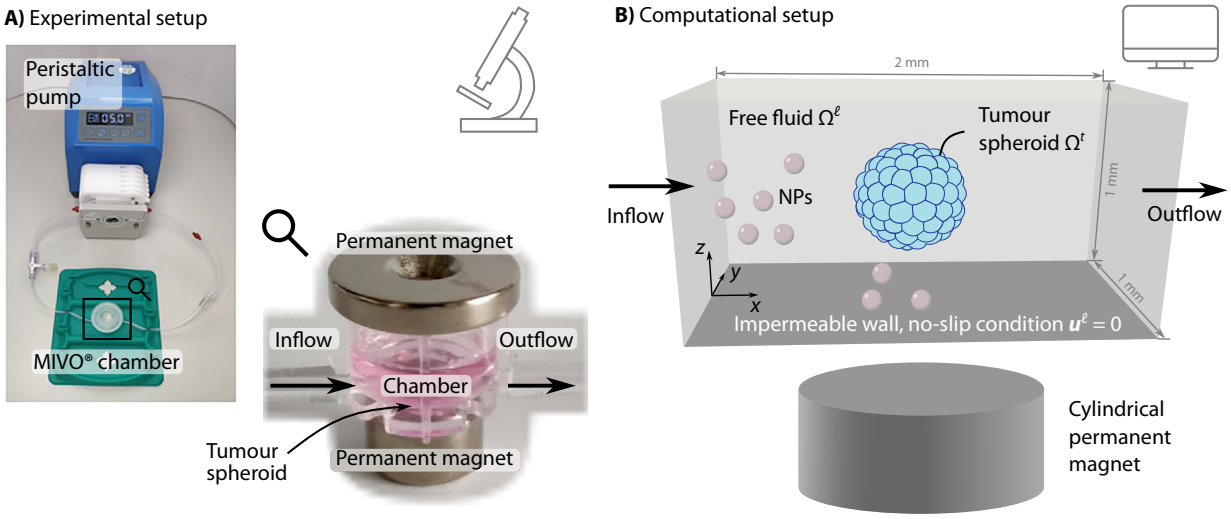

Figure 3.6 Experimental and computational setup A) Experimental setup for magnetic accumulations of superparamagnetic iron oxide nanoparticles (SPIONs) in a flow system. The tumour spheroid is placed in a MIVO®chamber connected to a peristaltic pump. Permanent magnets guide the SPIONs to the tumour spheroid. The pictures are adapted from [200], licensed under CC BY 4.0. B) Computational setup combining the flow of the free fluid in Ω^ℓ with a multiphase porous medium for the tumour spheroid in Ω^t. A cylindrical permanent magnet is positioned below the flow chamber. The nanoparticles (NPs) are transported with the fluid and guided by the magnetic field. This figure is taken from [60], where it is licensed under CC BY 4.0.

diffusion-advection equation directly at the macroscale. The bottom wall is also impenetrable for the magnetic nanoparticles.

3.2.2.1 Multiphase porous-media model for the tumour spheroid and the free fluid

The tumour spheroid consists of the tumour cells, the extracellular matrix (ECM) and the interstitial fluid (*in vivo*) or the culture medium (in the test setup), as sketched in Fig. 3.7. We decompose this system into two distinct but fully coupled regions, which we model as a multiphase porous medium: the region of the free fluid Ω^ℓ and the region of the tumour spheroid Ω^t. To model the flow in both regions, Ω^ℓ and Ω^t, we use a one-domain approach, i.e., we solve the same equation in the entire domain $\Omega = \Omega^\ell \cup \Omega^t$: the mass balance equation with a Darcy momentum equation condensed into a single equation. The bottom wall of the domain is impermeable and has a no-slip boundary condition.

Here, we write the mass balance of the fluid phases as

$$\rho^\alpha \varepsilon \frac{\partial S^\alpha}{\partial t} + \nabla \cdot \left(\rho^\alpha \varepsilon S^\alpha \boldsymbol{u}^\alpha\right) = 0, \tag{3.11}$$

where we define the tensor $\boldsymbol{K}^\alpha$ as the permeability tensor divided by the dynamic viscosity μ^α of the fluid phase

$$\boldsymbol{K}^\alpha = \frac{k_{\text{rel}}^\alpha k \boldsymbol{I}}{\mu^\alpha} \quad \text{with} \quad k_{\text{rel}}^\alpha = \left(S^\alpha\right)^{A_\alpha} \tag{3.12}$$

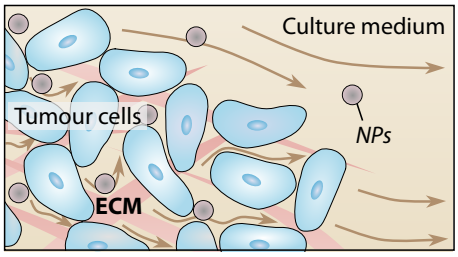

Figure 3.7 Porous medium with the pore space of the extracellular matrix (ECM) occupied by the tumour cells and the culture medium. The brown arrows indicate the flow of the culture medium, which is transporting the nanoparticles (NP).

and the velocity of the fluid phase as

$$\boldsymbol{u}^{\alpha} = -\frac{1}{\varepsilon S^{\alpha}} \boldsymbol{K}^{\alpha} \nabla p^{\alpha}. \tag{3.13}$$

As described above, we use a one-domain approach and solve one equation (in this case Eq. (3.11)) on the entire domain. Outside the tumour spheroid, the culture medium is the only phase, and no ECM is present; thus, $\varepsilon = 1.0 = \text{const}$ and $S^{\ell} = 1.0$. In Ω^{ℓ}, we set the tensor $\boldsymbol{K}^{\ell}$ and the pressure gradient so that the average velocity of the culture medium is $\boldsymbol{u}^{\ell} = 0.25\,\mathrm{mm\,s^{-1}}$ based on Eq. (3.13). We assume the flow to be laminar and the Reynolds number to be small, as is typically the case in microfluidic devices [218, 219][2]. In addition, we only consider a steady state, i.e., the velocities do not change in time, and neglect body forces, e.g., the gravitational force. At the bottom wall, we apply a no-slip boundary condition, i.e., $\boldsymbol{u}^{\ell} = 0$.

The mass balance equation of the free fluid then reduces to

$$\nabla \cdot \boldsymbol{u}^{\ell} = 0 \quad \text{with} \quad \boldsymbol{u}^{\ell} = \boldsymbol{K}^{\ell} \nabla p^{\ell}. \tag{3.14}$$

For the free fluid, $\boldsymbol{K}^{\ell}$ can be interpreted as an apparent permeability tensor field, similar to the approach presented by Valdés-Parada and Lasseux [220]. Hence, the mass balance equation is the well-known continuity equation, e.g., as included in the Navier–Stokes equations, but we condensed a Darcy momentum equation into it to obtain a single equation (see Section 2.1.3 for details).

In sum, employing the multiphase porous-media model captures essential aspects: the fluid flow around and through the tumour spheroid and the interaction of the flow with the tumour cells. The implications of the fluid flow are crucial both to understand tumour growth better and to improve the design of drug delivery systems [221, 222].

In the following, we refer to the flow of the culture medium as the *fluid flow* because we do not further investigate the flow of the tumour cells as the second fluid phase.

We again employ the tumour-growth model to generate a physically plausible initial condition for the tumour spheroid: it results in a saturation of the tumour cell phase of $S^{t} = 0.8$ and a saturation of the culture medium phase of $S^{\ell} = 0.2$. We then use these results as an initial condition for studying the transport of magnetic nanoparticles in the flow chamber.

[2] Given a domain width of $w = 1\,\mathrm{mm}$ and assuming an average flow velocity of $u^{\ell} = 0.25\,\mathrm{mm\,s^{-1}}$ results in a Reynolds number of $\mathrm{Re} = \rho^{\ell} u^{\ell} w / \mu^{\ell} = 0.25 < 1$.

3.2.2.2 Transport of the magnetic nanoparticles

We model the transport of the magnetic nanoparticles with a diffusion-advection equation as a continuum approach. We assume that the magnetic nanoparticles are dispersed in the fluid in a stable colloidal suspension, so the particle mass fraction $\omega^{\mathrm{NP}\ell}$ is small ($\omega^{\mathrm{NP}\ell} \ll 1$). We therefore assume that nanoparticles do not interact with each other, i.e., we neglect the inter-particle forces for now, and we assume that the nanoparticles do not influence the fluid flow.

The mass fraction $\omega^{\mathrm{NP}\ell}$ of the magnetic nanoparticles in the medium is governed by the mass balance equation

$$\rho^\ell \varepsilon S^\ell \frac{\partial \omega^{\mathrm{NP}\ell}}{\partial t} + \nabla \cdot \left(\rho^\ell \boldsymbol{q}^{\mathrm{NP}}\right) = 0, \tag{3.15}$$

where $\boldsymbol{q}^{\mathrm{NP}}$ is the flux of the magnetic nanoparticles. We assume that no (chemical) reaction within the phase occurs and no mass transfer to other phases. The flux is the sum of three transport mechanisms: diffusion, advection with the fluid flow, and magnetophoresis (= the motion of magnetic particles in response to an external magnetic field [223]), i.e.,

$$\boldsymbol{q}^{\mathrm{NP}} = \boldsymbol{q}^{\mathrm{NP}}_{\mathrm{diff}} + \boldsymbol{q}^{\mathrm{NP}}_{\mathrm{adv}} + \boldsymbol{q}^{\mathrm{NP}}_{\mathrm{mag}} \tag{3.16}$$

with the diffusive and the advective flux as defined in Section 2.1.4.

When the nanoparticles are also subjected to a magnetic force, we include an additional magnetophoretic flux $\boldsymbol{q}_{\mathrm{mag}}$ depending on the magnetic force $\boldsymbol{F}_{\mathrm{mag}}$. Typically, the resulting magnetophoretic velocity $\boldsymbol{u}_{\mathrm{mag}}$ is assumed to be directly proportional to the applied force, e.g., see [205, 224], resulting in a magnetophoretic flux of

$$\boldsymbol{q}^{\mathrm{NP}}_{\mathrm{mag}} = \omega^{\mathrm{NP}\ell} \varepsilon S^\ell \boldsymbol{u}_{\mathrm{mag}} = \omega^{\mathrm{NP}\ell} \zeta^{-1} \boldsymbol{F}_{\mathrm{mag}}, \tag{3.17}$$

where $\zeta = 6\pi\mu^\ell R^{\mathrm{NP}}$ is the mobility of a particle of radius R^{NP} in a fluid with dynamic viscosity[3] μ^ℓ, based on Stokes' law.

Eq. (3.17) assumes that the velocity is always directly proportional to the applied force. Now consider an example of a channel with an impenetrable wall and a force perpendicular to the wall, as sketched in Fig. 3.6: the force results in a velocity perpendicular to the wall, which in turn results in the nanoparticles leaving the domain through the impenetrable wall—which is obviously not physical.

We therefore introduce the mobility tensor $\boldsymbol{\mathcal{M}}$, which relates the magnetophoretic velocity to the magnetic forces, i.e.,

$$\boldsymbol{u}_{\mathrm{mag}} = \boldsymbol{\mathcal{M}} \boldsymbol{F}_{\mathrm{mag}}, \tag{3.18}$$

or more explicitly,

$$\begin{bmatrix} u_x \\ u_y \\ u_z \end{bmatrix} = \begin{bmatrix} \mathcal{M}_{xx} & \mathcal{M}_{xy} & \mathcal{M}_{xz} \\ \mathcal{M}_{yx} & \mathcal{M}_{yy} & \mathcal{M}_{yz} \\ \mathcal{M}_{zx} & \mathcal{M}_{yz} & \mathcal{M}_{zz} \end{bmatrix} \begin{bmatrix} F_x \\ F_y \\ F_z \end{bmatrix}, \tag{3.19}$$

[3] The parameter μ^ℓ denotes the dynamic viscosity of the fluid by the superscript ℓ (*liquid*) to distinguish it from the magnetic vacuum permeability μ_0 introduced in Section 3.2.2.3.

similar to [225, 226]. The mobility is a tensor field $\mathcal{M}(\boldsymbol{x})$ that depends on the position $\boldsymbol{x}$. Now, a force in a specific direction does not necessarily result in a velocity in that direction, but only if the particle can move in this direction, i.e., if the mobility is non-zero. At an impenetrable wall, the nanoparticles cannot move in the direction perpendicular to the wall, i.e., into the wall, and thus the mobility is zero in this direction, resulting also in zero velocity. All off-diagonal entries of the mobility tensor $\mathcal{M}$ are also zero: a force in one direction only causes a velocity in the same direction and no *shear* contribution.

We further introduce a relative mobility m^ℓ_{rel} similar to the relative permeability k^ℓ_{rel} in Eq. (3.12). All diagonal entries of the mobility tensor inside the domain are given by

$$\mathcal{M}_{xx} = \mathcal{M}_{yy} = \mathcal{M}_{zz} = \frac{m^\ell_{\text{rel}}}{6\pi\mu^\ell R^{\text{NP}}} \quad \text{with} \quad m^\ell_{\text{rel}} = \left(S^\ell\right)^{A_\ell}. \tag{3.20}$$

At the impenetrable wall, the diagonal entries tangential to the wall are also given by Eq. (3.20). But, the entry perpendicular to the wall is zero $\mathcal{M}_{zz} = 0$. The key point here is that we employ the mobility as a tensor field—instead of a scalar.

Remark (The mobility tensor in other applications)**.** *Pimponi* et al. *[225] used the mobility tensor to model microspheres moving on a superhydrophobic wall, and Chen* et al. *[226] applied the mobility tensor to the grain-boundary mobility during the evolution of polycrystalline microstructures, explicitly arguing that mobility must be a tensor (not a scalar).*

The advantages of our approach based on the mobility tensor field are twofold: firstly, we include a simple approach to model nanoparticle accumulation at the wall—as opposed to [206, 227] where the boundary condition at the wall is unclear; secondly, the relative mobility allows us to consider the interaction of the nanoparticles with other phases—which is especially relevant for the interaction with the ECM [152].

The final form of the Smoluchowski advection-diffusion equation [228] is then given by

$$\rho^\ell \varepsilon S^\ell \frac{\partial \omega^{\text{NP}\ell}}{\partial t} - \nabla \cdot \left(\rho^\ell \varepsilon S^\ell D^{\text{NP}\ell} \nabla \omega^{\text{NP}\ell}\right) - \rho^\ell \boldsymbol{K}^\ell \nabla p^\ell \cdot \nabla \omega^{\text{NP}\ell} + \nabla \cdot \left(\rho^\ell \omega^{\text{NP}\ell} \mathcal{M}^{\text{NP}} \boldsymbol{F}_{\text{mag}}\right) = 0. \tag{3.21}$$

3.2.2.3 Magnetic force on the nanoparticles

Due to the permanent magnet, the magnetic nanoparticles are subjected to a static non-homogenous external magnetic field $\boldsymbol{H}$ leading to a force $\boldsymbol{F}_{\text{mag}}$. This force however does not only depend on the magnetic field but also the magnetic response of the particles.

Due to the small size of the particles, we assume that they can be modelled as an equivalent point dipole located at the centre of the particle (*effective dipole moment approach* [205, 229, 230]). Also, due to the small size, the nanoparticles are superparamagnetic: they are magnetised with a large magnetic susceptibility χ^{NP} when an external magnetic field is applied but do not retain their magnetisation after the external magnetic field is removed. Hence, when a superparamagnetic nanoparticle is placed in an external magnetic field, it magnetises, resulting in a magnetic moment

$\boldsymbol{m}^{\mathrm{NP}}$. The force on the magnetic dipole induced in the nanoparticle is given by

$$\boldsymbol{F}_{\mathrm{mag}} = \mu_{\mathrm{o}} \left(\boldsymbol{m}^{\mathrm{NP}} \cdot \nabla\right) \boldsymbol{H}, \tag{3.22}$$

with the magnetic vacuum permeability μ_{o}[4]. Using the magnetisation $\boldsymbol{M}^{\mathrm{NP}}$ as the magnetic moment per volume, i.e., $\boldsymbol{M}^{\mathrm{NP}} = \boldsymbol{m}^{\mathrm{NP}}/V^{\mathrm{NP}}$ with V^{NP} being the volume of the nanoparticle, the force can be written as

$$\boldsymbol{F}_{\mathrm{mag}} = \mu_{\mathrm{o}} V^{\mathrm{NP}} \left(\boldsymbol{M}^{\mathrm{NP}} \cdot \nabla\right) \boldsymbol{H}. \tag{3.23}$$

Thus, the force depends on the magnetisation of the nanoparticle and the derivatives of the applied magnetic field.

The magnetised nanoparticles also produce a magnetic field, affecting the nearby nanoparticles. For now, we assume that the magnetic force that the nanoparticles exert on each other is negligible compared to the magnetic force exerted by the external magnetic field—which is a valid assumption for low concentrations of nanoparticles and hence large distances between the nanoparticles [205, 232–235]. We will investigate and discuss the validity of this assumption in Section 3.2.3.4.

Magnetisation model. To relate the magnetisation of the nanoparticle to the applied magnetic field, we use a linear magnetisation model with saturation, given by

$$\boldsymbol{M}^{\mathrm{NP}} = f(|\boldsymbol{H}|)\boldsymbol{H} \quad \text{with} \quad f(|\boldsymbol{H}|) = \begin{cases} \frac{3\chi^{\mathrm{NP}}}{3+\chi^{\mathrm{NP}}} & \text{if } |\boldsymbol{H}| < H_{\mathrm{sat}} \\ \frac{M_{\mathrm{sp}}}{|\boldsymbol{H}|} & \text{if } |\boldsymbol{H}| \geq H_{\mathrm{sat}} \end{cases} \tag{3.24}$$

with M_{sp} being the saturation magnetisation and H_{sat} the field strength for which the particle reaches saturation, as presented by [205, 224, 230]. An example of such a magnetisation curve is shown in Fig. 3.8. If the particle is below saturation, its magnetisation is proportional to the applied magnetic field

$$\boldsymbol{M}^{\mathrm{NP}} = \frac{3\chi^{\mathrm{NP}}}{3 + \chi^{\mathrm{NP}}} \boldsymbol{H}, \tag{3.25}$$

and the particle reaches saturation for

$$H_{\mathrm{sat}} = \frac{\chi^{\mathrm{NP}} + 3}{3\chi^{\mathrm{NP}}} M_{\mathrm{sp}}, \tag{3.26}$$

which can be derived based on the effective dipole moment approach [205, 229]. Above saturation, the magnetisation is equal to the saturation magnetisation M_{sp}, i.e.,

$$\boldsymbol{M}^{\mathrm{NP}} = M_{\mathrm{sp}} \frac{\boldsymbol{H}}{|\boldsymbol{H}|}. \tag{3.27}$$

The magnetisation is always aligned with the applied magnetic field.

[4] We assume that the fluid (water) and air are non-magnetic, and thus assume that their permeability is equal to the vacuum magnetic permeability defined as $\mu_{\mathrm{o}} = 1.256\,637\,062\,12(19) \times 10^{-6}\,\mathrm{N\,A^{-2}}$ [231]. The exact values for water and air differ from the value for vacuum at the fifth and seventh decimal place, respectively.

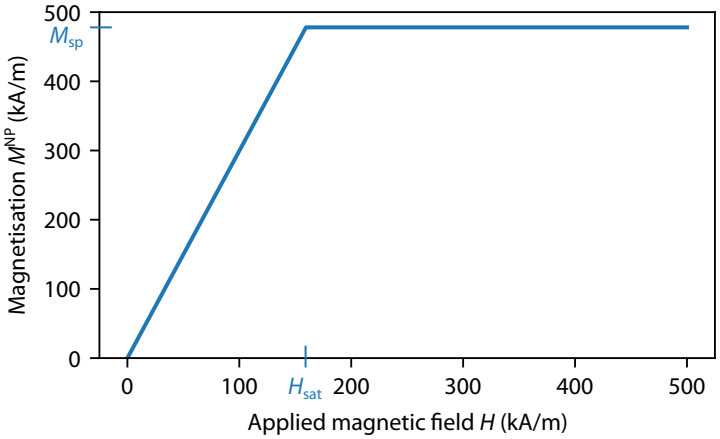

Figure 3.8 Magnetisation curve for a superparamagnetic nanoparticle with linear magnetisation and saturation above an applied magnetic field of H_{sat}, assuming a saturation magnetisation of $M_{sp} = 478\,\mathrm{kA\,m^{-1}}$ [205] and a magnetic susceptibility of $\chi^{NP} \gg 1$ [205, 212, 236]. This figure is reprinted with permission from [59], where it is copyrighted by the American Physical Society.

Finally, as discussed above, the particles are superparamagnetic: their magnetic susceptibility is much higher than the magnetic susceptibility of paramagnetic materials, i.e., $\chi^{NP} \gg 1$ [205, 212, 236]. Eq. (3.24) can then be simplified to

$$f(|\boldsymbol{H}|) = \begin{cases} 3 & \text{if } |\boldsymbol{H}| < \frac{1}{3} M_{sp} \\ \frac{M_{sp}}{|\boldsymbol{H}|} & \text{if } |\boldsymbol{H}| \geq \frac{1}{3} M_{sp} \end{cases} . \tag{3.28}$$

In sum, the magnetic force on the nanoparticles is given by

$$\boldsymbol{F}_{mag} = \mu_o V^{NP} f(|\boldsymbol{H}|) (\boldsymbol{H} \cdot \nabla) \boldsymbol{H}, \tag{3.29}$$

which shows that the magnetic force depends both on the strength of the magnetic field and its derivatives.

Analytical expression for the magnetic field. Usually, the magnetic field $\boldsymbol{H}$ is obtained by solving Maxwell's equations numerically. Analytic expressions are only well-known for some classic textbook cases: the magnetic field of point multipoles or infinitely long wires carrying a current [237]. However, for a finite-length cylindrical magnet, which we have here, Derby and Olbert [238] and Caciagli *et al.* [239] presented analytic expressions based on the elliptic integrals. These analytic expressions are beneficial because the magnetic quantities can be evaluated at all coordinates with minimal computational effort compared to numerically solving Maxwell's equations, e.g., using the finite element method.

In the following, we summarise the analytic expression for the magnetic field, as presented by [238, 239], and then extend this by deriving the analytic expressions for the magnetic force. The cylindrical magnet is magnetised in the longitudinal direction. The field components of the magnetic

field $\boldsymbol{H}$ in cylindrical coordinates (ρ, ϕ, z) are given by

$$H_\rho(\rho, z) = \frac{M_s R_{\text{mag}}}{\pi} \left[\alpha_+ P_1(k_+) - \alpha_- P_1(k_-)\right], \tag{3.30}$$

$$H_z(\rho, z) = \frac{M_s R_{\text{mag}}}{\pi(\rho + R_{\text{mag}})} \left[\beta_+ P_2(k_+) - \beta_- P_2(k_-)\right], \tag{3.31}$$

and $H_\phi = 0$ due to the radial symmetry of the system [238, 239][5]. Here, M_s denotes the magnetisation of the cylindrical magnet and R_{mag} its radius. The origin of the cylindrical coordinate system is located at the centre of the magnet. The two auxiliary functions P_1 and P_2 are defined as

$$P_1(k) = \mathcal{K}(1 - k^2) - \frac{2}{1 - k^2}\left[\mathcal{K}(1 - k^2) - \mathcal{E}(1 - k^2)\right] \tag{3.32}$$

$$P_2(k) = -\frac{\gamma}{1 - \gamma^2}\left[\Pi(1 - \gamma^2, 1 - k^2) - \mathcal{K}(1 - k^2)\right] - \frac{1}{1 - \gamma^2}\left[\gamma^2 \Pi(1 - \gamma^2, 1 - k^2) - \mathcal{K}(1 - k^2)\right], \tag{3.33}$$

with the following auxiliary variables

$$\rho_\pm = R_{\text{mag}} \pm \rho, \quad \zeta_\pm = \frac{L_{\text{mag}}}{2} \pm z, \quad \alpha_\pm = \frac{1}{\sqrt{\zeta_\pm^2 + \rho_+^2}}, \quad \beta_\pm = \zeta_\pm \alpha_\pm, \quad \gamma = -\frac{\rho_-}{\rho_+}, \quad k_\pm = \sqrt{\frac{\zeta_\pm^2 + \rho_-^2}{\zeta_\pm^2 + \rho_+^2}},$$

and L_{mag} being the length of the cylindrical magnet. Eqs. (3.32) and (3.33) are based on the complete elliptic integrals of the first, second and third kind, which in Legendre's notation are written as

$$\mathcal{K}(m) = \int_0^{\pi/2} \frac{\mathrm{d}\theta}{\sqrt{1 - m \sin^2\theta}} \tag{3.34}$$

$$\mathcal{E}(m) = \int_0^{\pi/2} \sqrt{1 - m \sin^2\theta}\, \mathrm{d}\theta \tag{3.35}$$

$$\Pi(n, m) = \int_0^{\pi/2} \frac{\mathrm{d}\theta}{(1 - n \sin^2\theta)\sqrt{1 - m \sin^2\theta}}. \tag{3.36}$$

All three kinds of elliptic integrals can be efficiently evaluated using Carlson's functions R_F, F_D and R_J [240, 241] as

$$\mathcal{K}(m) = R_F(0, 1 - m, 1) \tag{3.37}$$

$$\mathcal{E}(m) = R_F(0, 1 - m, 1) - \frac{m}{3} R_D(0, 1 - m, 1) \tag{3.38}$$

$$\Pi(n, m) = R_F(0, 1 - m, 1) + \frac{n}{3} R_J(0, 1 - m, 1 - n). \tag{3.39}$$

[5] Eqs. (3.30) and (3.31) are mathematically well-behaved except on the edge of the magnet at $\rho = \pm R_{\text{mag}}$ and $z = \pm \frac{L_{\text{mag}}}{2}$ [238].

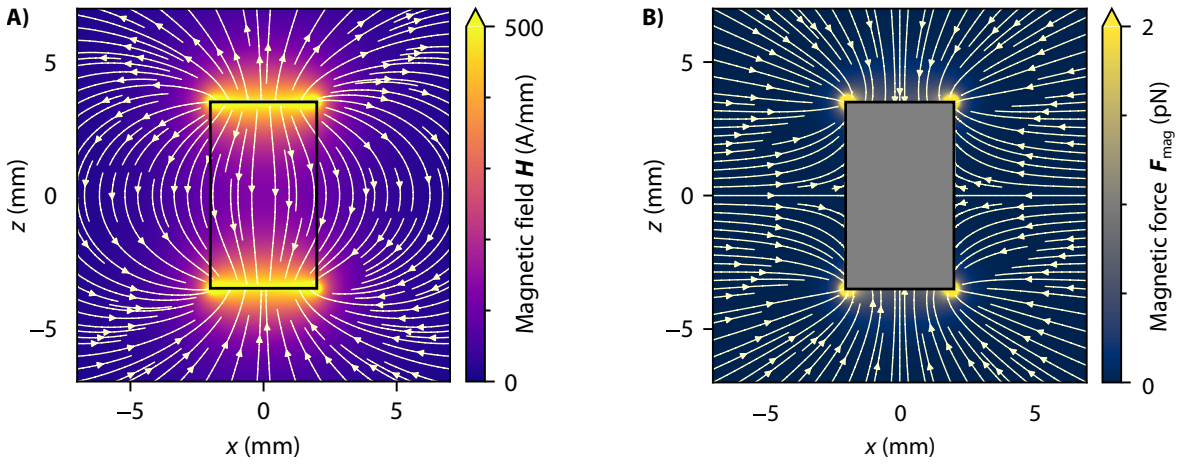

Figure 3.9 Magnetic field $\boldsymbol{H}$ (A) and magnetic force $\boldsymbol{F}_{\text{mag}}$ (B) on the nanoparticles of a cylindrical magnet with radius $R_{\text{mag}} = 2\,\text{mm}$ and length $L_{\text{mag}} = 7\,\text{mm}$. This figure is reprinted with permission from [59], where it is copyrighted by the American Physical Society.

Numerical Recipes [242] provides algorithms and source code for evaluating Carlson's functions, which are also implemented in Mathematica [243] and SciPy [244].

Remark (Parameter and sign conventions in the elliptic integrals)**.** *Note that Numerical Recipes [242, p. 315] uses a different sign convention for the variable n in the third elliptic integral, such that*

$$\Pi(n,m) = \int_0^{\pi/2} \frac{d\theta}{(1+n\sin^2\theta)\sqrt{1-m\sin^2\theta}} = R_F(0,1-m,1) - \frac{n}{3}R_J(0,1-m,1+n). \tag{3.40}$$

Additionally, Caciagli et al. *[239] use the convention with parameter k, where* $m = \tilde{k}^2 = \sqrt{1-k^2}$ *in their Eq. (6). Mathematica [243] and SciPy [244] however use the parameter m, as presented here in Eqs.* (3.34) *to* (3.36).

Fig. 3.9A shows an example of the magnetic field $\boldsymbol{H}$ of a cylindrical magnet with radius $R_{\text{mag}} = 2\,\text{mm}$, length $L_{\text{mag}} = 7\,\text{mm}$ and magnetisation $M_s = 1 \times 10^6\,\text{A m}^{-1}$. Inside the magnet, the magnetic field is given by

$$\boldsymbol{H} = \frac{\boldsymbol{B}}{\mu_0} - \boldsymbol{M}_s, \tag{3.41}$$

with the magnetic flux density $\boldsymbol{B}$. For a longitudinally magnetised magnet, the magnetisation vector is $\boldsymbol{M}_s = M_s\boldsymbol{e}_z$, with $\boldsymbol{e}_z$ being the unit vector in z-direction. The magnetisation vector is constant inside and zero outside the magnet. The result for the magnetic field $\boldsymbol{H}$ in Fig. 3.9A is qualitatively well known: the magnetic field lines originate at one pole and end at the other, forming fanned-out circular segments around the magnet.

Analytical expression for the magnetic force. As discussed above, the magnetic force $\boldsymbol{F}_{\text{mag}}$ depends on the magnetic field and its derivatives. Since the first derivatives of the elliptic integrals are

known analytically, we can derive an analytical expression for the magnetic force $\boldsymbol{F}_{\text{mag}}$. Evaluating Eq. (3.29) for the analytical expression for the magnetic field results in the force components given by

$$F_\rho(\rho,z) = \frac{\mu_0 V^{\text{NP}} f(|\boldsymbol{H}|) M_s^2}{4\pi^2 \rho_+ \rho^3 a_1 a_2 a_3 a_4}\left[\left(\frac{a_4 c_1 \zeta_+ \mathcal{E}(\psi_+)}{\alpha_-} + \frac{a_3 c_2 \zeta_- \mathcal{E}(\psi_-)}{\alpha_+} - \frac{a_3 a_4 \zeta_+ \mathcal{K}(\psi_+)}{\alpha_-} - \frac{a_3 a_4 \zeta_- \mathcal{K}(\psi_-)}{\alpha_+}\right)\rho^2 Q_2 + \left(\frac{a_4(b_1^2 + b_3\rho^2)\mathcal{E}(\psi_+)}{\alpha_-} - \frac{a_3(b_2^2 + b_4\rho^2)\mathcal{E}(\psi_-)}{\alpha_+} + \frac{a_3 a_4 b_2 \mathcal{K}(\psi_-)}{\alpha_+} - \frac{a_3 a_4 b_1 \mathcal{K}(\psi_+)}{\alpha_-}\right)\rho_+ Q_1\right] \tag{3.42}$$

and

$$F_z(\rho,z) = \frac{\mu_0 V^{\text{NP}} f(|\boldsymbol{H}|) M_s^2}{4\pi^2 a_1 a_2 a_3 a_4}\left[\left(\frac{a_3 a_4 \zeta_+ \mathcal{K}(\psi_+)}{\alpha_-} + \frac{a_3 a_4 \zeta_- \mathcal{K}(\psi_-)}{\alpha_+} - \frac{a_4 c_1 \zeta_+ \mathcal{E}(\psi_+)}{\alpha_-} - \frac{a_3 c_2 \zeta_- \mathcal{E}(\psi_-)}{\alpha_+}\right)\frac{Q_1}{\rho^2} + \left(\frac{a_3 c_4 \mathcal{E}(\psi_-)}{\alpha_+} - \frac{a_4 c_3 \mathcal{E}(\psi_+)}{\alpha_-} + \frac{a_3 a_4 \mathcal{K}(\psi_+)}{\alpha_-} - \frac{a_3 a_4 \mathcal{K}(\psi_-)}{\alpha_+}\right)\frac{Q_2}{\rho_+}\right], \tag{3.43}$$

with two auxiliary functions Q_1 and Q_2 based on the elliptic integrals

$$Q_1(\alpha_+,\alpha_-,\psi_+,\psi_-,a_1,a_2,c_1,c_2) = \frac{a_2\mathcal{E}(\psi_-)}{\alpha_+} - \frac{a_1\mathcal{E}(\psi_+)}{\alpha_-} + \frac{c_1\mathcal{K}(\psi_+)}{\alpha_-} - \frac{c_2\mathcal{K}(\psi_-)}{\alpha_+},$$

$$Q_2(\alpha_+,\alpha_-,\psi_+,\psi_-,\rho_+,\rho_-,\zeta_+,\zeta_-,\beta) = \frac{\rho_+\zeta_+\mathcal{K}(\psi_+)}{\alpha_-} + \frac{\rho_+\zeta_-\mathcal{K}(\psi_-)}{\alpha_+} + \frac{\rho_-\zeta_+\Pi(\beta,\psi_+)}{\alpha_-} + \frac{\rho_-\zeta_-\Pi(\beta,\psi_-)}{\alpha_+}.$$

and the following auxiliary variables[6]

$$\rho_\pm = R_{\text{mag}} \pm \rho, \qquad \zeta_\pm = \frac{L_{\text{mag}}}{2} \pm z, \qquad \beta = \frac{4\rho R_{\text{mag}}}{\rho_+^2}$$

$$a_1 = \rho_+^2 + \zeta_+^2, \quad a_2 = \rho_+^2 + \zeta_-^2, \quad a_3 = \rho_-^2 + \zeta_+^2, \quad a_4 = \rho_-^2 + \zeta_-^2,$$

$$\alpha_+ = \frac{1}{\sqrt{a_1}}, \quad \alpha_- = \frac{1}{\sqrt{a_2}}, \quad \psi_+ = \frac{4\rho R_{\text{mag}}}{a_1}, \quad \psi_- = \frac{4\rho R_{\text{mag}}}{a_2},$$

$$b_1 = \zeta_+^2 + R_{\text{mag}}^2, \quad b_2 = \zeta_-^2 + R_{\text{mag}}^2, \quad b_3 = \zeta_+^2 - R_{\text{mag}}^2, \quad b_4 = \zeta_-^2 - R_{\text{mag}}^2,$$

$$c_1 = b_1 + \rho^2, \quad c_2 = b_2 + \rho^2, \quad c_3 = b_3 + \rho^2, \quad c_4 = b_4 + \rho^2.$$

The coordinate transformations from cylindrical coordinates to cartesian coordinates are given by

$$F_x(x,y,z) = F_\rho(\rho,z)\cos(\varphi) \tag{3.44}$$

$$F_y(x,y,z) = F_\rho(\rho,z)\sin(\varphi) \tag{3.45}$$

$$F_z(x,y,z) = F_z(\rho,z) \tag{3.46}$$

[6] Note that Eqs. (3.42) and (3.43) are undefined at $\rho = 0$ and $\rho = \pm R_{\text{mag}}$. Outside the magnet, these singularities are removable and $\boldsymbol{F}_{\text{mag}}$ is extendable.

with $\rho = \sqrt{x^2 + y^2}$ and $\varphi = \arctan\left(\frac{x}{y}\right)$[7].

Fig. 3.9B shows the magnetic force $\boldsymbol{F}_{\text{mag}}$ for a cylindrical magnet with radius $R_{\text{mag}} = 2\,\text{mm}$ and length $L_{\text{mag}} = 7\,\text{mm}$. Calculating the magnetic force is only meaningful outside the magnet. The magnetic force is on the order of pN, similar to the order of magnitude estimated in [215] for a similar configuration.

We also provide a Python implementation of the analytical expressions for the magnetic field and force, see [63].

3.2.3 Numerical examples and discussion

In the following, we present and discuss numerical examples to demonstrate the capabilities of the proposed model. In Section 3.2.3.1, we start with a two-dimensional example where we investigate the influence of the mobility tensor field on the nanoparticle capture at the impenetrable wall. Next, in Section 3.2.3.2, we investigate the nanoparticle distribution in three dimensions for different positions and orientations of a finite-length cylindrical magnet, leveraging the analytical expression for the magnetic force, which we derived. In Section 3.2.3.3, we extend the previous example to include a tumour spheroid. Finally, in Section 3.2.3.4, using the analytical expressions for the magnetic field and force, we examine the validity of the assumption that the inter-particle forces are negligible compared to the magnetic force exerted by the external magnetic field.

3.2.3.1 Influence of the mobility tensor field

We first present a two-dimensional example where we investigate the influence of the mobility tensor field $\mathcal{M}(\boldsymbol{x})$ on the distribution of the magnetic particles. This example was published in B. Wirthl, V. Wirthl and W. A. Wall. 'Efficient Computational Model of the In-Flow Capturing of Magnetic Nanoparticles by a Cylindrical Magnet for Cancer Nanomedicine'. *Physical Review E* 109.6 (2024), 065309 [59], where it is copyrighted by the American Physical Society. It is reused here with permission from the American Physical Society.

The computational setup is depicted in Fig. 3.10A. We study a two-dimensional slice in the XZ-plane with a size of $9\,\text{mm} \times 3.5\,\text{mm}$, which is discretised with 180×70 linear rectangular elements. The time step size is $\Delta t = 1\,\text{s}$ and the total simulation time is 150 s. For simplicity, we consider a constant advective flow velocity $u_{\text{adv}} = 0.1\,\text{mm}\,\text{s}^{-1}$ along the x-axis and a constant magnetic force $F_{\text{mag}} = 0.2\,\text{pN}$ along the z-axis, which is a reasonable order of magnitude for the considered cylindrical magnets (see Fig. 3.9B). For a water-like fluid with a viscosity of $\mu^{\ell} = 1 \times 10^{-3}\,\text{Pa}\,\text{s}$ and nanoparticles with a radius of $R^{\text{NP}} = 100\,\text{nm}$, this corresponds to a magnetophoretic velocity of $u_{\text{mag}} \approx 0.1\,\text{mm}\,\text{s}^{-1}$. We assume a diffusion coefficient of $D^{\text{NP}\ell} = 3 \times 10^{-3}\,\text{mm}^2\,\text{s}^{-1}$. On the inflow boundary at $x = 0$, we prescribe the mass fraction of nanoparticles as a Dirichlet boundary condition given by

$$\omega_D^{\text{NP}\ell}(z) = \frac{2.0 \times 10^{-6}}{0.8\sqrt{2\pi}} \exp\left(-\frac{(z - 2.5)^2}{2 \cdot 0.8^2}\right), \tag{3.47}$$

[7] Most programming languages provide a function $\arctan2(\text{y},\text{x})$ which is defined for all $x, y \in \mathbb{R}$ and returns the correct angle φ with respect to the quadrant of the point (x, y).

which is a bell-shaped function with a maximum value of $\omega^{\mathrm{NP}\ell} = 1.0 \times 10^{-6}$.

The wall at the bottom of the domain is impenetrable, and we prescribe a Dirichlet boundary condition for the mass fraction of nanoparticles given by $\omega_D^{\mathrm{NP}\ell} = 0$. Additionally, the z-component of the mobility tensor field is zero at the bottom wall, i.e., $\mathcal{M}_{zz} = 0$. We compare the results for the nanoparticle distribution given different functions for $\mathcal{M}_{zz}(z)$. The functions are given in Fig. 3.10B. On the one hand, we consider the Heaviside function $\mathcal{M}_{zz}(z) = \mathcal{H}(z-\delta)$, with δ being the boundary layer thickness: this means that the mobility of the nanoparticles is zero in the boundary layer. We choose δ so that the boundary layer is two or three elements wide (given an element size of 0.05). On the other hand, we consider different smooth functions for $\mathcal{M}_{zz}(z)$, which have the value one inside the domain and have different slopes towards the boundary.

Fig. 3.10C presents the results given the different functions for $\mathcal{M}_{zz}(z)$. In all cases, the nanoparticles accumulate at the impenetrable wall at the bottom of the domain, which was the primary motivation for introducing the mobility tensor field. All functions lead to a similar distribution of the nanoparticles, with the thickness of the layer of captured nanoparticles depending on the function $\mathcal{M}_{zz}(z)$. However, it shall be noted that the smooth functions are numerically better behaved than the Heaviside function, which can cause convergence issues.

Defining a tensor field $\boldsymbol{\mathcal{M}}(\boldsymbol{x})$ is a simple way to model the accumulation of nanoparticles at an impenetrable wall. It is worth noting that most similar studies in the literature, e.g., [205, 206, 227], do not clarify the boundary conditions for the nanoparticles at the wall and also seem to not use appropriate boundary conditions for the nanoparticles at the wall. This allows for studying the trajectories of the nanoparticles in the bulk of the fluid, but it is impossible to investigate the capture of the nanoparticles at a wall. Only Khashan *et al.* [232] presented and discussed an approach for an impermeability condition at the wall: they set the combined advective-diffusive flux to zero, i.e.,

$$\omega^{\mathrm{NP}\ell}\left(\boldsymbol{u}_{\mathrm{adv}} + \boldsymbol{u}_{\mathrm{mag}}\right) \cdot \boldsymbol{n} - D^{\mathrm{NP}} \nabla \omega^{\mathrm{NP}\ell} \cdot \boldsymbol{n} = 0. \tag{3.48}$$

We drop the advective velocity because any physically plausible velocity field cannot have a component perpendicular to an impermeable wall, either by directly imposing a physically plausible velocity field (as we do here) or by prescribing a no-slip boundary condition and solving the fluid equations. Khashan *et al.* [232] subsequently set the normal component of the magnetophoretic velocity at the wall also to zero. Eq. (3.48) then reduces to the classical Neumann boundary condition $D^{\mathrm{NP}} \nabla \omega^{\mathrm{NP}\ell} \cdot \boldsymbol{n} = 0$, which we also impose. In sum, their boundary condition is equivalent to our approach based on setting the normal component of the mobility tensor to zero, i.e., $\mathcal{M}_{zz} = 0$. Nevertheless, Khashan *et al.* [232] also stated that their employed boundary condition poses a numerical challenge due to the steep concentration gradient at the wall. They solve this problem by prior grid refinement adaptive to the magnetic field gradient. We circumvent this problem by setting the mobility to zero on several elements or by using a smooth function.

3.2.3.2 Nanoparticle capture with a cylindrical magnet of finite length

We now investigate a three-dimensional example with a cylindrical magnet positioned below the fluid domain. The analytical solution for the magnetic force enables us to efficiently compare different

A) Computational setup

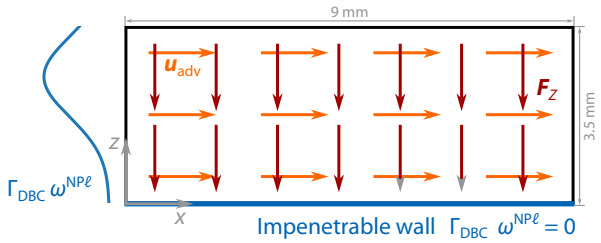

B) Functions for the z-component $\mathcal{M}_{zz}(z)$ of the mobility tensor field

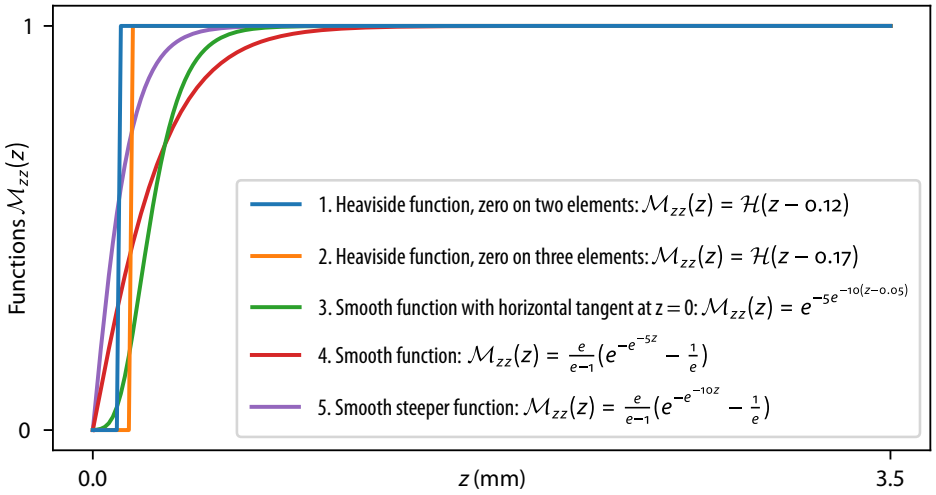

C) Results for the nanoparticle distributions

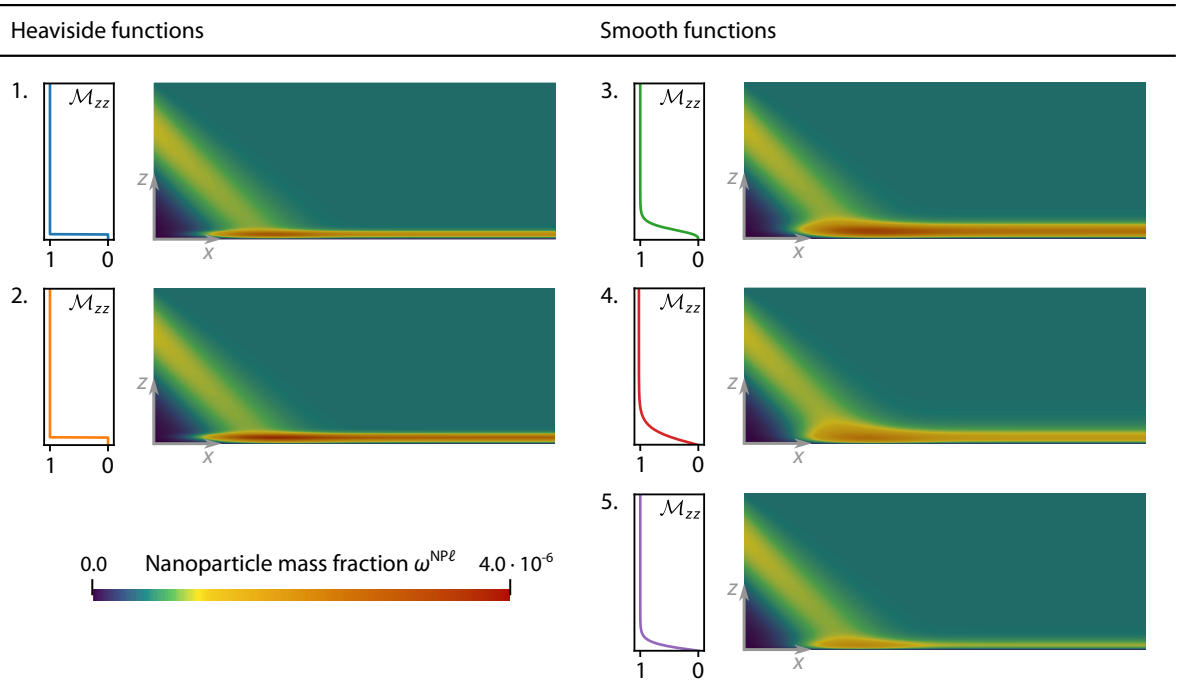

Figure 3.10 Investigation of the influence of the mobility tensor field on the nanoparticle distribution. A) Computational setup. B) Functions for the z-component $\mathcal{M}_{zz}(z)$ of the mobility tensor field. C) Results for the nanoparticle distributions. The colourbar applies to all plots. This figure is reprinted with permission from [59], where it is copyrighted by the American Physical Society.

Table 3.3 Parameters for the magnetic nanoparticles, the magnet, and the fluid

Symbol	Parameter	Value	Units	Ref.
Magnetic nanoparticles				
R^{NP}	Radius of the nanoparticles	100	nm	[205]
D^{NP}	Diffusion coefficient	3×10^{-3}	$\mathrm{mm^2\,s^{-1}}$	Assumed
M_{sp}	Saturation magnetisation	478	$\mathrm{kA\,m^{-1}}$	[205]
Magnet				
R_{mag}	Radius of the magnet	2.5	mm	Assumed
L_{mag}	Length of the magnet	5.0	mm	Assumed
M_s	Magnetisation of the magnet	1×10^6	$\mathrm{A\,m^{-1}}$	[205]
Fluid (water)				
μ^{ℓ}	Dynamic viscosity	1×10^{-3}	Pa s	Known

orientations of a cylindrical magnet. This example was published in B. Wirthl, V. Wirthl and W. A. Wall. 'Efficient Computational Model of the In-Flow Capturing of Magnetic Nanoparticles by a Cylindrical Magnet for Cancer Nanomedicine'. *Physical Review E* 109.6 (2024), 065309 [59], where it is copyrighted by the American Physical Society. It is reused here with permission from the American Physical Society.

The computational setup is the one sketched in Fig. 3.6. The domain has a size of 9 mm × 4 mm × 3.5 mm, which is discretised with 180 × 160 × 70 linear hexahedral elements. The time step size is again $\Delta t = 1\,\mathrm{s}$ and the total simulated time 150 s. For simplicity, we also again assume a constant advective flow velocity of $u_{\mathrm{adv}} = 0.1\,\mathrm{mm\,s^{-1}}$. The parameters for the magnetic nanoparticles, the magnet, and the fluid are given in Table 3.3. The nanoparticle mass fraction on the inflow boundary is again defined by Eq. (3.47) and zero at the bottom wall. We use a smooth function for the mobility tensor field, i.e., Function 4 shown in Fig. 3.10B and discussed in the previous subsection. The cylindrical magnet has a radius of $R_{\mathrm{mag}} = 2.5\,\mathrm{mm}$ and a length of $L_{\mathrm{mag}} = 5.0\,\mathrm{mm}$ and is centered below the domain with a distance of 0.2 mm to the bottom wall. In the first step, we compare three different orientations of the magnet: A) The magnet is oriented vertically (along the z-axis); B) The magnet is oriented horizontally (along the x-axis); C) The magnet is rotated 45° around the y-axis.

Fig. 3.11 shows the mass fraction of the nanoparticles for the three different orientations of the magnet. For the vertical orientation, the nanoparticles are attracted to the magnet and accumulate at the bottom wall in a circular shape directly above the magnet, similar to experimental results, e.g., [245]. For the horizontal orientation, the nanoparticles accumulate above the two ends of the magnet, forming two ellipses. For the 45° orientation, the nanoparticles form one ellipse above where the edge of the magnet is closest to the bottom wall. Examples in the literature are restricted to a single orientation of a cylindrical magnet of infinite length, e.g., [205, 207]. In particular, we show that the nanoparticles accumulate above the ends of the magnet—which can obviously not be investigated with a magnet of infinite length.

Further, we here leverage what Derby and Olbert [238] and Caciagli *et al.* [239] stated: their derived analytical expressions for the magnetic field of magnetised cylinders are especially convenient for applications where magnetic forces on magnetic dipoles are required—nanoparticles being one such example. Note that our results for the magnetic force are restricted to a cylindrical magnet

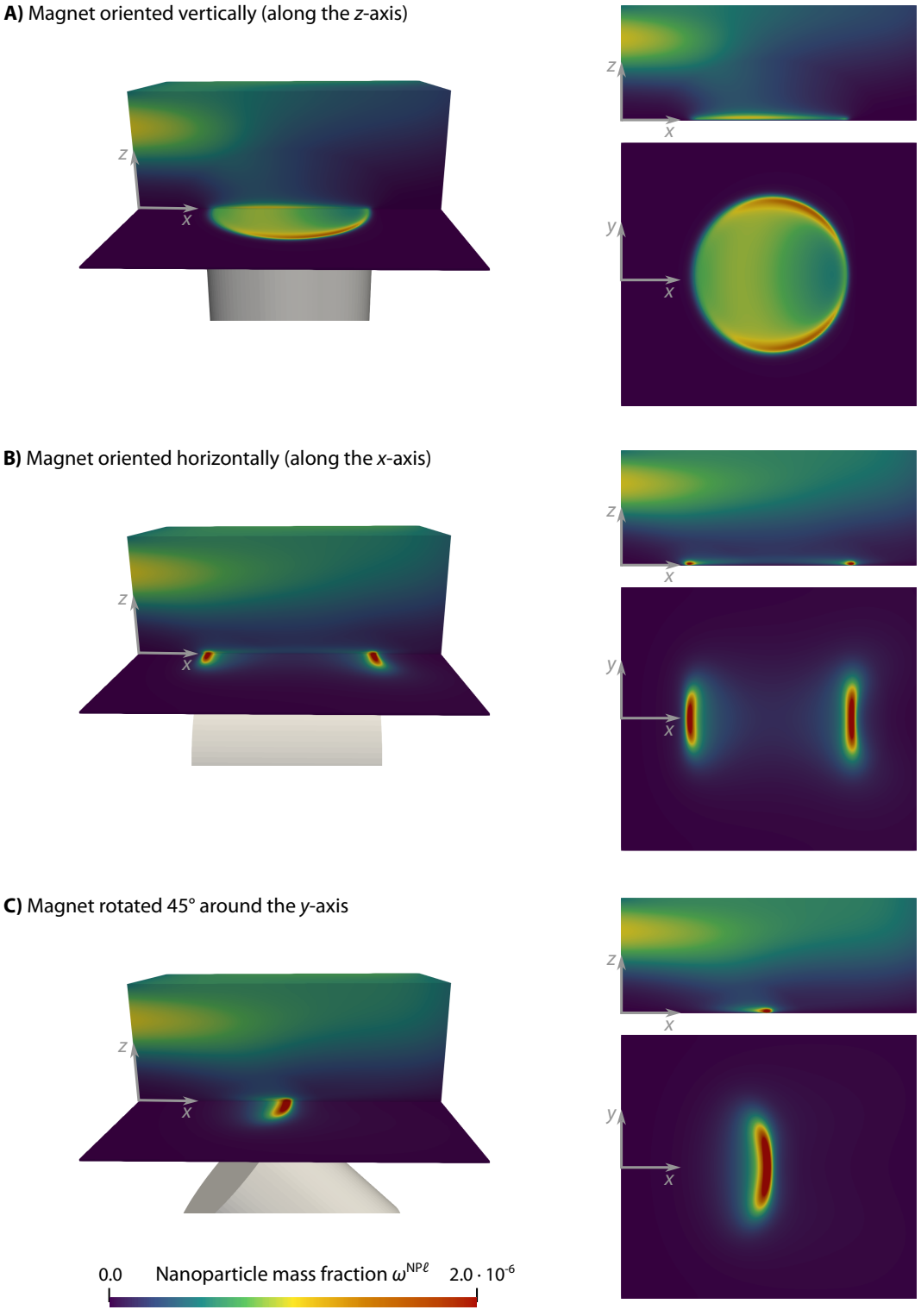

Figure 3.11 Results for the nanoparticle capture with a cylindrical magnet of finite length positioned below the domain. The colourbar applies to all plots. This figure is reprinted with permission from [59], where it is copyrighted by the American Physical Society.

with longitudinal magnetisation. Similar analytical solutions for cylindrical magnets with arbitrary magnetisation can also be derived based on the respective analytical expressions for the magnetic field, which Caciagli *et al.* [239] presented. However, if the magnet is of an arbitrary shape, the magnetic field and force must be evaluated based on numerically solving Maxwell's equations.

Several studies in the literature, e.g., [205–207, 246–248] reduced the setup to a two-dimensional problem in the XZ-plane and assumed the cylindrical magnet to be infinitely long. In this case, the magnetic force can also be expressed analytically, as derived in [205], and is given by

$$F_x = -\mu_0 V^{\mathrm{NP}} f(|\boldsymbol{H}|) M_s^2 R_{\mathrm{mag}}^4 \frac{x}{2\left(x^2+z^2\right)^3} \tag{3.49}$$

$$F_z = -\mu_0 V^{\mathrm{NP}} f(|\boldsymbol{H}|) M_s^2 R_{\mathrm{mag}}^4 \frac{z}{2\left(x^2+z^2\right)^3}, \tag{3.50}$$

where the coordinate system is at the centre of the magnet, and the longitudinal axis of the magnet is perpendicular to the XZ-plane. We now compare results based on this assumption of an infinitely long magnet to the results for a finite-length magnet. In both cases, we assume that the magnet has a radius of $R_{\mathrm{mag}} = 2.5\,\mathrm{mm}$ and a distance of $\Delta = 0.2\,\mathrm{mm}$ to the bottom boundary of the domain. The cylindrical magnet of finite length has a length of $L_{\mathrm{mag}} = 5.0\,\mathrm{mm}$, as used in the previous examples. For simplicity, we here assume that $f(|\boldsymbol{H}|) = 1.0 = \mathrm{const}$ in both cases.

Fig. 3.12 shows the magnetic force and the resulting nanoparticle distribution for the magnet of infinite length compared to the finite-length magnet. As is also evident in Fig. 3.9, the magnetic force of the finite-length magnet varies along the longitudinal axis of the magnet, and so we compare the force in different slices along the longitudinal axis, in this case the y-axis (but the z-axis in Fig. 3.9). As evident in Fig. 3.12, the direction of the magnetic force is the same in all cases, but the magnitude is significantly different. For the cylindrical magnet of infinite length, the maximum force in the domain is 0.72 pN. For the finite-length magnet, the maximum force varies considerably depending on the position of the slice: the maximum magnitude is 0.06 pN, 0.09 pN, 1.02 pN and 1.65 pN for the slices at $y = 0.0\,\mathrm{mm}$, $1.0\,\mathrm{mm}$, $2.3\,\mathrm{mm}$ and $2.5\,\mathrm{mm}$, respectively. Accordingly, the nanoparticle distributions are also markedly different: the nanoparticles accumulate in a higher mass fraction above the ends of the finite-length magnet than along the infinitely long magnet.

In sum, one has to be aware that the assumption of an infinitely long magnet leads to significantly different results than a finite-length magnet. The analytical solution for the finite-length magnet provides a simple and computationally efficient way to investigate the transport of nanoparticles in a more realistic setup.

3.2.3.3 In-flow nanoparticle capture with a tumour spheroid

We now investigate the motivational example sketched in Fig. 3.6B: we study the capture of magnetic nanoparticles in the flow chamber with a tumour spheroid. This example was published in B. Wirthl, C. Janko, S. Lyer, B. A. Schrefler, C. Alexiou and W. A. Wall. 'An in silico model of the capturing of magnetic nanoparticles in tumour spheroids in the presence of flow'. *Biomedical Microdevices* 26.1 (2024) [60], which is licensed under CC BY 4.0.

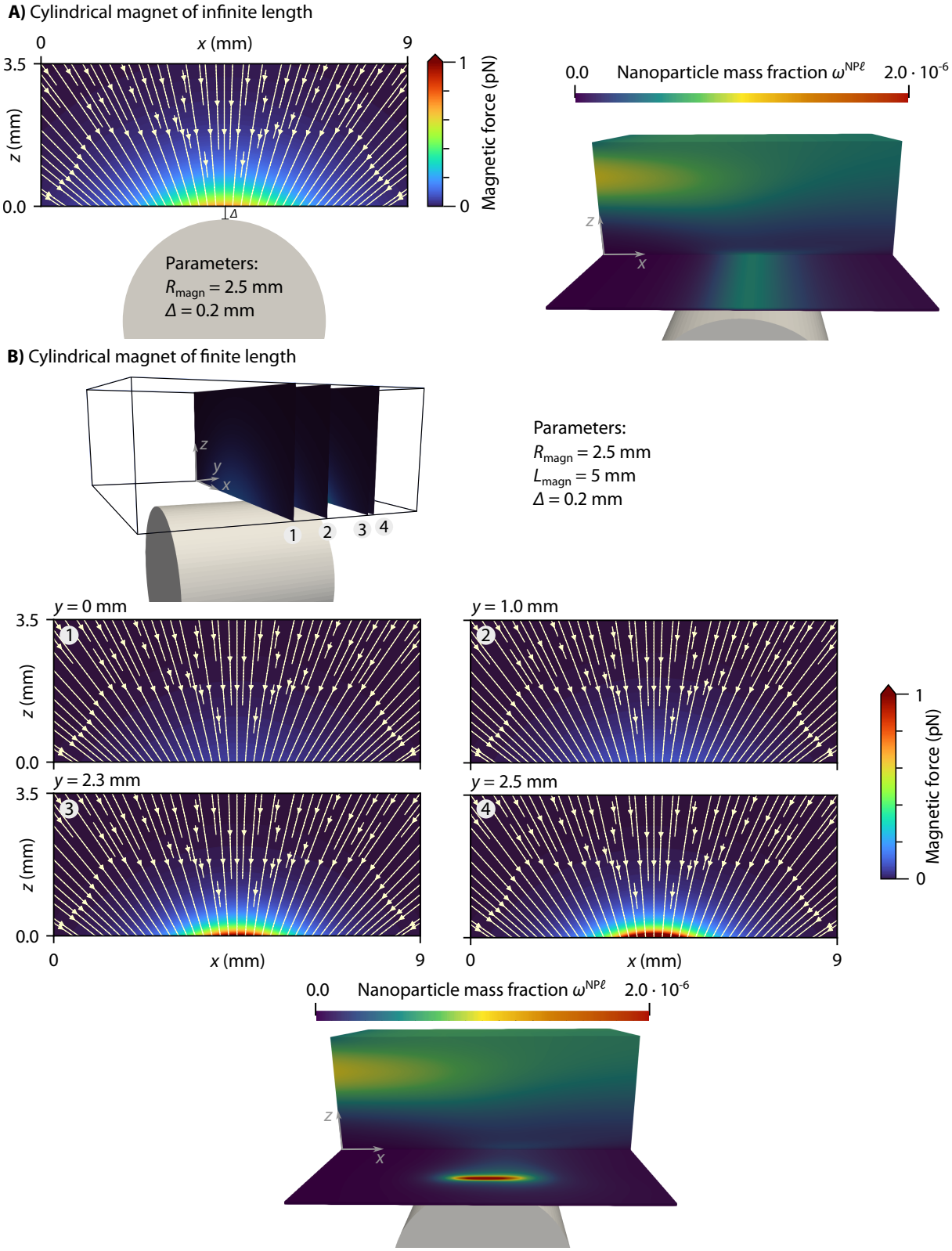

Figure 3.12 Comparison of the magnetic force and the resulting nanoparticle distribution for a cylindrical magnet of A) infinite length and B) finite length with $L_{\text{mag}} = 5.0\,\text{mm}$. This figure is reprinted with permission from [59], where it is copyrighted by the American Physical Society.

Table 3.4 Parameters for the magnetic nanoparticles, the cylindrical magnet, and the fluid phases.

Symbol	Parameter	Value	Units	Ref.
Magnetic nanoparticles				
R^{NP}	Radius of the nanoparticles	100	nm	[205]
D^{NP}	Diffusion coefficient	2.5×10^{-10}	$\mathrm{m^2\,s^{-1}}$	[250]
M_{sp}	Saturation magnetisation	4.78×10^5	$\mathrm{A\,m^{-1}}$	[205]
Cylindrical magnet				
R_{mag}	Radius of the magnet	0.5	mm	Assumed
L_{mag}	Length of the magnet	1.0	mm	Assumed
M_s	Magnetisation of the magnet	1×10^6	$\mathrm{A\,m^{-1}}$	[205]
Fluid phases				
ρ^ℓ, ρ^t	Density of the medium and the cells	1×10^3	$\mathrm{kg\,m^{-3}}$	Known
μ^ℓ	Dynamic viscosity of the medium	1×10^{-3}	Pa s	Known
μ^t	Dynamic viscosity of the cells	20	Pa s	[33]
k	Intrinsic permeability of the ECM	1×10^{-9}	$\mathrm{mm^2}$	[62]
A_ℓ	Relative permeability exponent of the medium	4	–	[67]
A_t	Relative permeability exponent of the cells	2	–	[72]

We analyse four different configurations of the tumour spheroid: two different tumour spheroid sizes ($R^t_{\mathrm{small}} \approx 200\,\mu\mathrm{m}$ and $R^t_{\mathrm{large}} \approx 340\,\mu\mathrm{m}$) and two different positions (centred or lying at the bottom of the chamber). The tumour spheroid placed at the bottom of the chamber mimics our experimental test setup. The tumour spheroid in the centre of the chamber assumes that the tumour spheroid is placed into an insert, fitting the flow chamber [249]. The entire computational domain has a size of $2\,\mathrm{mm} \times 1\,\mathrm{mm} \times 1\,\mathrm{mm}$ discretized with $\sim 2 \times 10^6$ linear hexahedral elements. This fine discretisation is required to resolve the sharp gradients in the primary variables of the fluid field at the edge of the tumour spheroid: the porosity is 1.0 outside and 0.8 inside the tumour spheroid, and the culture medium only occupies a volume fraction of $\varepsilon^\ell = \varepsilon S^\ell = 0.12$ inside the tumour spheroid, with the ECM and tumour cells sharing in remaining volume. We apply the pressure of the fluid as Dirichlet boundary condition at the inflow and outflow such that the pressure difference together with the tensor $\boldsymbol{K}$ results in an average velocity of $0.25\,\mathrm{mm\,s^{-1}}$ in Ω^ℓ, as given by Eq. (3.13). Table 3.4 summarises the employed parameters for the magnetic nanoparticles, the cylindrical magnet and the fluid phases: all values are based on experimental results or previous computational studies in the literature.

Fluid flow. We first analyse the fluid flow around and through the tumour spheroid for the four different configurations. Fig. 3.13 depicts the results: the flow around the tumour spheroid resembles the classical Stokes flow around a sphere. The velocity is zero at the impenetrable wall at the bottom of the flow chamber, and the highest velocities occur at the top edge of the tumour spheroid. The bulk of the fluid flows around the tumour, and the velocities inside the tumour are much smaller. Nevertheless, the fluid in the tumour is not stagnant: the fluid velocities are of the order of $\mathrm{nm\,s^{-1}}$.

We employ a one-domain approach due to its simplicity while retaining essential physics. If more complex flow patterns around the tumour spheroid are of interest, such as transitional flow with vortices or turbulent flow, one can solve the Navier–Stokes equations in Ω^ℓ. Based on a two-domain

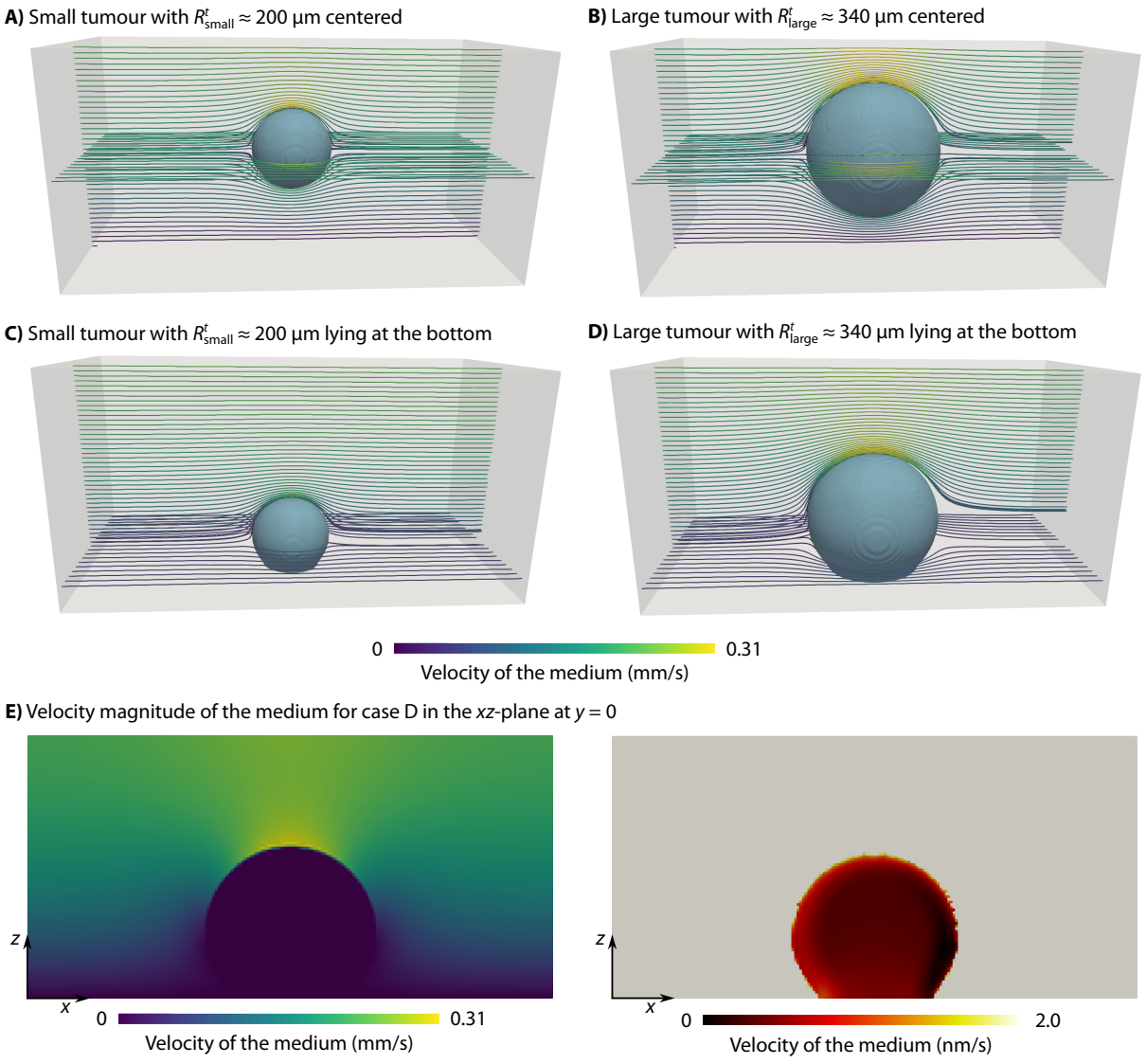

Figure 3.13 Velocities in the flow chamber for different tumour spheroid sizes and positions. A) Small tumour spheroid centred in the flow chamber. B) Large tumour spheroid centred in the flow chamber. C) Small tumour spheroid lying at the bottom of the flow chamber. D) Large tumour spheroid lying at the bottom of the flow chamber. E) Velocity magnitude for the large tumour spheroid lying at the bottom of the flow chamber (case D): velocity magnitude in the free fluid (left) in $\mathrm{mm/s}$ and in the tumour spheroid (right) in $\mathrm{nm/s}$. This figure is taken from [60], where it is licensed under CC BY 4.0.

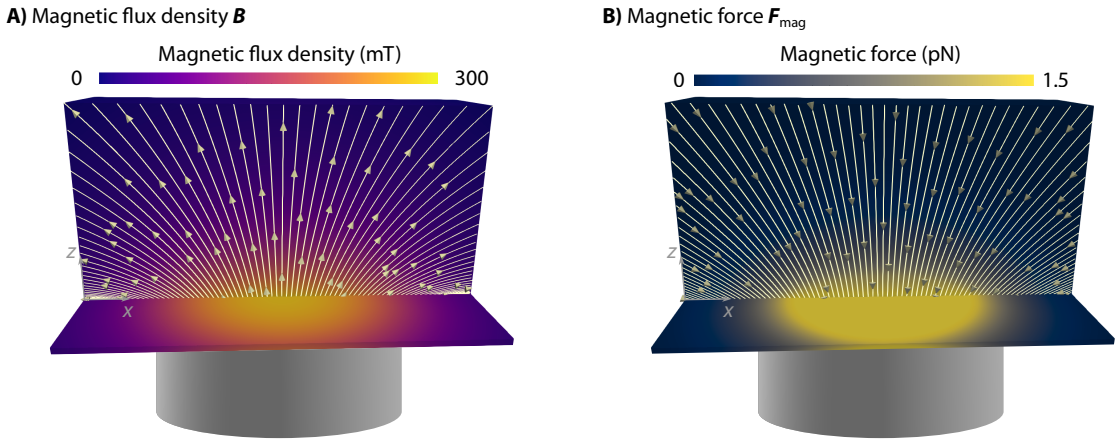

Figure 3.14 Magnetic flux density and force for the cylindrical magnet vertically positioned below the flow chamber at a distance of 0.25 mm from the bottom of the domain. The magnet has a radius of 0.5 mm and a length of 1 mm. A) Magnetic flux density $\boldsymbol{B}$. B) Magnetic force $\boldsymbol{F}_{\text{mag}}$. This figure is taken from [60], where it is licensed under CC BY 4.0.

approach, the free fluid is described by the Navier–Stokes equations and coupled to the solid structure or the porous medium via interface conditions, for example [251–253].

Nanoparticle distribution. We now investigate the distribution of the nanoparticles for the four different configurations. For all configurations, the nanoparticles are injected in the upper half of the inflow boundary with a mass fraction of $\omega_D^{\text{NP}\ell} = 1.0 \times 10^{-6}$. The cylindrical magnet has a radius of $R_{\text{mag}} = 0.5\,\text{mm}$ and a length of $L_{\text{mag}} = 1\,\text{mm}$. The centre of the magnet is positioned at $x = 1.0\,\text{mm}$, centred in the y-direction with a vertical distance of 0.25 mm to the bottom of the domain.

The resulting magnetic flux density $\boldsymbol{B}$ and magnetic force $\boldsymbol{F}_{\text{mag}}$ in the computational domain are presented in Fig. 3.14. Both the magnetic flux density and the magnetic force are highest directly at the edge of the magnet but rapidly decrease with distance. The smaller the magnet, the harder it is to capture nanoparticles at the top of the domain. The maximum magnetic flux density is $|\boldsymbol{B}|_{\text{max}} = \mu_0 |\boldsymbol{H}|_{\text{max}} = 300\,\text{mT}$, which is of the same order of magnitude as the magnetic flux density in our experimental setup [200, 254]. The maximum magnetic force in the domain is of the order of pN, which is larger than the values estimated in [215] but on a similar order of magnitude.

Fig. 3.15 depicts the nanoparticle distribution at $t = 20\,\text{s}$ for the four different configurations. The nanoparticles accumulate just above where the magnet is positioned. More nanoparticles accumulate at the left side of the magnet due to the flow direction and the fact that the velocity in the lower part of the domain is decreasing because of the no-slip condition at the bottom wall. In cases C and D, where the tumour spheroid is positioned at the bottom of the domain, the nanoparticles form a ring-like structure around the edge of the tumour spheroid.

The results in Fig. 3.15 further show that the nanoparticles have not yet fully penetrated the tumour spheroid after 20 s but are located close to the surface, similar to what has been observed experimentally [255, 256]. The penetration of the nanoparticles into the tumour spheroid is a complex process, which we do not study in further detail here. Dai *et al.* [21] quantified that only 0.0014% of the intravenously injected nanoparticles reach the tumour cells, and He *et al.* [152]

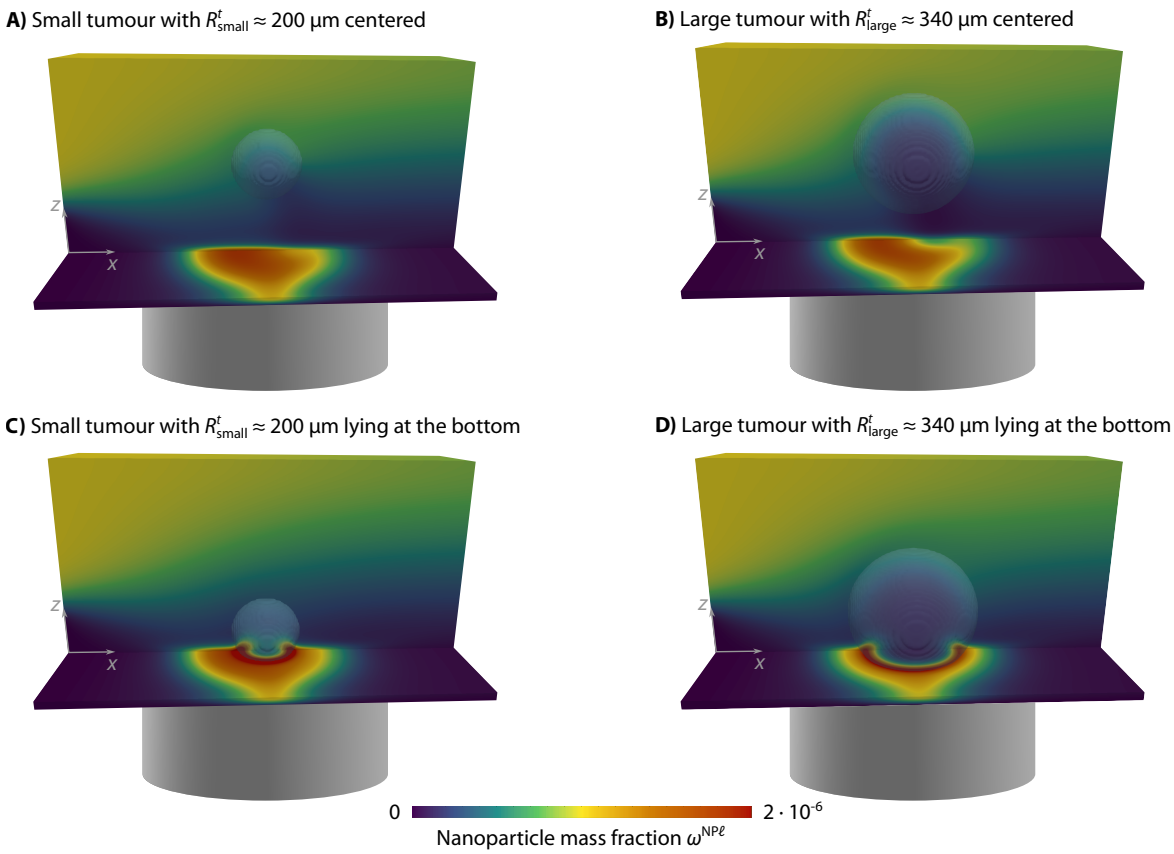

Figure 3.15 Results for the nanoparticle mass fractions $\omega^{\mathrm{NP}\ell}$ at $t = 20\,\mathrm{s}$ for different tumour spheroid sizes and positions. This figure is taken from [60], where it is licensed under CC BY 4.0.

discussed the ECM as the main steric obstacle for nanoparticle diffusion in the tumour. However, the underlying mechanisms remain largely unexplored. Experimental measurements of the diffusion coefficient of nanoparticles in the tumour vary significantly and indicate that the diffusion coefficient depends on the physicochemical properties of the nanoparticles, the tumour type, and the tumour microenvironment [21]. A more detailed study of nanoparticle transport in the tumour spheroid is consequently required, both experimentally and computationally, to overcome this transport barrier and improve the efficacy of nanoparticle-based drug delivery systems.

Here, we only consider the force exerted by the external magnetic field. However, the magnetised nanoparticles also exert forces on each other when they are close. We neglect these inter-particle forces, similar to [257]. According to [205, 232–235, 258], the inter-particle forces are negligible when the nanoparticles have a distance of more than three particle diameters, which we assume to be the case and thus neglect the inter-particle forces. However, nanoparticles are known to form aggregates, e.g., chains [259], and in such cases, the inter-particle forces indeed play a significant role. In this context, [260, 261] studied nanoparticle agglomeration with a particle-based approach, including the inter-particle forces for a small number of particles (up to 25). By contrast, Pálovics *et al.* [259] presented a continuum model capable of modelling the aggregation of the nanoparticles: they first simulated the aggregate formation at the microscale based on a discrete particle method and then transferred the results to the continuum approach at the macroscale by adapting the viscosity.

Finally, we only study a simplified model in the experimental test setup and the computational model: we consider the tumour spheroid with the ECM and the flow in the flow chamber, but such a setup does not include the blood vessels and the surrounding tissue, which are important for the translation of the results to *in vivo* scenarios and clinical practice. Accordingly, Stillman *et al.* [24] argued that circulation and extravasation are major transport barriers, which *in silco* models should include. The approach we present here is readily extendable to the vascular version of our tumour growth model, which includes the vasculature, angiogenesis, and the surrounding host tissue [58, 72–74]. This then allows for integrating the results of magnetic nanoparticle capture in blood vessels [205–207] with the results of nanoparticle transport in the tumour spheroid presented here.

3.2.3.4 Comparison of the force exerted by the permanent magnet to the inter-particle forces

In the preceding examples, we only considered the external magnetic force the permanent magnet exerts on the nanoparticles. However, the nanoparticles also exert forces on each other, and thus the question arises when these inter-particle forces are negligible compared to the force exerted by the permanent magnet. So far, we have assumed that the low mass fraction of nanoparticles ensures that the inter-particle distance is large enough for the inter-particle forces to be negligible, similar to [205, 232–235]. In general, the cut-off length of dipole-dipole interactions in nanoparticle assemblies is about three particle diameters [258]. Assuming that the nanoparticles are more than three particle diameters apart seems reasonable for the nanoparticles dissolved in the flowing fluid in our previous examples. However, when the nanoparticles accumulate at the bottom of the domain, they come very close to each other, and thus the inter-particle forces might become relevant there. Therefore, we compare the external magnetic force to the inter-particle forces.

This example was published in B. Wirthl, V. Wirthl and W. A. Wall. 'Efficient Computational Model of the In-Flow Capturing of Magnetic Nanoparticles by a Cylindrical Magnet for Cancer Nanomedicine'. *Physical Review E* 109.6 (2024), 065309 [59], where it is copyrighted by the American Physical Society. It is reused here with permission from the American Physical Society.

We use our analytical expressions for the magnetic field and the external magnetic force and build on the force comparison presented by Pálovics and Rencz [215], who investigated a similar setup. We analyse a simplified example shown in Fig. 3.16A: we consider two nanoparticles with a diameter of $d^{\mathrm{NP}} = 200\,\mathrm{nm}$ and a distance $\boldsymbol{r}$ between their centres. The cylindrical magnet is positioned vertically below the domain (see previous example Fig. 3.11A). We assume that the two nanoparticles are aligned with the magnetic field $\boldsymbol{H}$ such that $\boldsymbol{r}$ is parallel to $\boldsymbol{H}$. We again assume $f(|\boldsymbol{H}|) = 1.0 = \mathrm{const}$ for simplicity.

In the following, the non-bold symbols denote the magnitudes of the vectors, e.g., $r = |\boldsymbol{r}|$, and a hat denotes the unit vector in the given direction, e.g., $\hat{\boldsymbol{r}} = \boldsymbol{r}/r$.

As discussed in Section 3.2.2.3, the nanoparticles are modelled as point dipoles, with the magnetic moment $\boldsymbol{m}_1$ of nanoparticle ① given by

$$\boldsymbol{m}_1 = V^{\mathrm{NP}} \boldsymbol{H}. \tag{3.51}$$

Thus, the magnetic moment of the nanoparticle is aligned with the applied magnetic field. Since the nanoparticles are much smaller than the computational domain, we assume that $\boldsymbol{H}(\boldsymbol{x}_1) = \boldsymbol{H}(\boldsymbol{x}_2)$ and hence $\boldsymbol{m}_1 = \boldsymbol{m}_2$. The magnetised nanoparticle ① generates a magnetic field $\boldsymbol{H}_1$ at the position $\boldsymbol{r}$ of nanoparticle ②, which based on Jackson [237] is given by

$$\boldsymbol{H}_1 = \frac{1}{4\pi r^3} \left[3(\boldsymbol{m}_1 \hat{\boldsymbol{r}}) \hat{\boldsymbol{r}} - \boldsymbol{m}_1 \right]. \tag{3.52}$$

In our case, $\boldsymbol{m}_1 \parallel \boldsymbol{r}$ and Eq. (3.52) simplifies to

$$\boldsymbol{H}_1 = \frac{1}{2\pi r^3} \boldsymbol{m}_1. \tag{3.53}$$

Hence, the total magnetic field $\boldsymbol{H}_2^*$ at the position $\boldsymbol{r}$ of nanoparticle ② is given by

$$\boldsymbol{H}_2^* = \boldsymbol{H} + \boldsymbol{H}_1 \tag{3.54}$$

and accordingly, the magnetic moment of nanoparticle ② also changes to

$$\boldsymbol{m}_2^* = V^{\mathrm{NP}} \boldsymbol{H}_2^*. \tag{3.55}$$

The magnetic moments of both particles increase due to the cross-effects. The new values for the magnetic moments can be substituted back into the previous equations to calculate a second correction of the magnetic field and magnetic moments. In practice, this is not necessary, and we omit it [215, 234].

The force $\boldsymbol{F}_{12}$ between the two particles, i.e., the inter-particle force, based on Griffiths [262] is given by

$$\boldsymbol{F}_{12} = \frac{3\mu_0 m_1^* m_2^*}{4\pi r^4}\left[\hat{\boldsymbol{r}}\left(\hat{\boldsymbol{m}}_1^*\hat{\boldsymbol{m}}_2^*\right) + \hat{\boldsymbol{m}}_1^*\left(\hat{\boldsymbol{r}}\hat{\boldsymbol{m}}_2^*\right) + \hat{\boldsymbol{m}}_2^*\left(\hat{\boldsymbol{r}}\hat{\boldsymbol{m}}_1^*\right) - 5\hat{\boldsymbol{r}}\left(\hat{\boldsymbol{r}}\hat{\boldsymbol{m}}_1^*\right)\left(\hat{\boldsymbol{r}}\hat{\boldsymbol{m}}_2^*\right)\right] = -\frac{3\mu_0 m_1^* m_2^*}{2\pi r^4}\hat{\boldsymbol{r}}. \quad (3.56)$$

We evaluate the inter-particle force $\boldsymbol{F}_{12}$ for different distances r between the two nanoparticles: $r \in \left\{5d^{\mathrm{NP}}, 3d^{\mathrm{NP}}, 2d^{\mathrm{NP}}, d^{\mathrm{NP}}\right\}$. Fig. 3.16B shows the force $\boldsymbol{F}_{\mathrm{mag}}$ exerted by the external magnet and Fig. 3.16C the inter-particle force $\boldsymbol{F}_{12}$. For a distance of five particle diameters, the forces are on the same order of magnitude, namely pN. However, the inter-particle force strongly increases for smaller distances: for a distance of one particle diameter, it is about three orders of magnitude larger than the force of the external magnet, especially for the particles at the bottom of the domain. This is in good agreement with the results of Pálovics and Rencz [215].

These results underline that one cannot simply assume that the inter-particle forces are negligible but must carefully assess whether they are relevant in the configuration studied with the assumptions made.

3.2.4 Conclusion

Motivated by a recent experimental test setup [200], we presented a computational model for the magnetic capture of nanoparticles in a flow chamber with a tumour spheroid. Our continuum approach for the transport of the nanoparticles based on the Smoluchowski advection-diffusion equation includes the advection by the fluid flow and the magnetophoresis by the external magnetic field. Based on a multiphase porous-media approach, our model further couples the flow of the free fluid to the flow in the tumour spheroid. We include a simple and numerically stable way to consider an impenetrable boundary at the wall where the nanoparticles are captured. Further, the analytical expression for the magnetic force of a cylindrical magnet of finite length on the magnetic nanoparticles, which we derived, provides an efficient way to model the capture of magnetic nanoparticles in a more realistic setup in three dimensions. Investigating the capturing of magnetic nanoparticles in a controlled flow environment, both *in vitro* and *in silico*, forms the basis for further studies in more complex scenarios, e.g., in a vascular *in vivo* model.

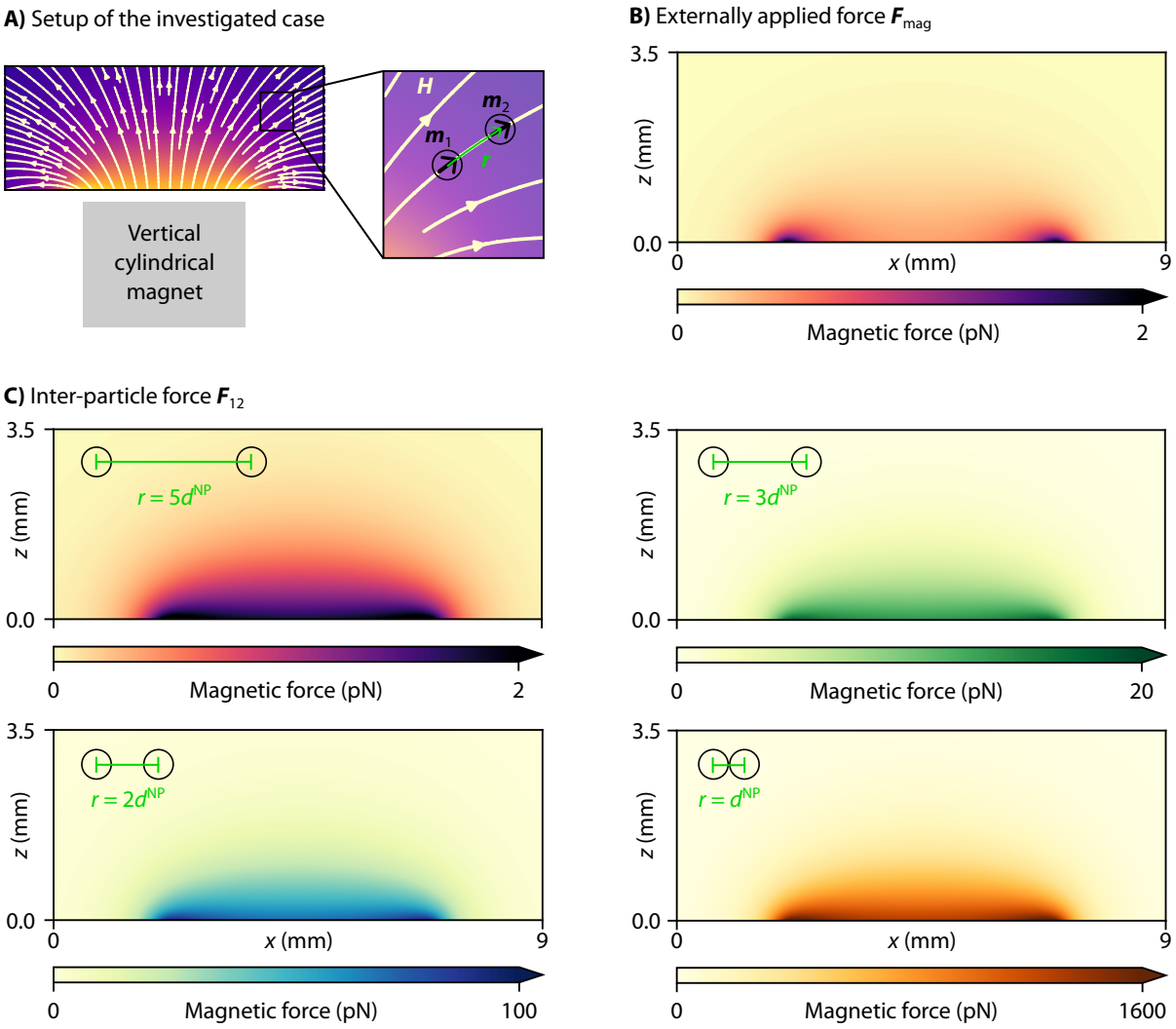

Figure 3.16 Comparison of the force exerted by the permanent magnet to the inter-particle forces. A) Setup of the investigated case. B) Externally applied force $\boldsymbol{F}_{\text{mag}}$. C) Inter-particle force $\boldsymbol{F}_{12}$ between two nanoparticles with a distance r between their centres. Note the different orders of magnitude of the forces, which are represented by the different colourmaps used in the subfigures. This figure is reprinted with permission from [59], where it is copyrighted by the American Physical Society.

4 Global sensitivity analysis with Gaussian-process metamodelling

The following Sections 4.1, 4.2, 4.3 and 4.5 are largely based on the author's publication B. Wirthl, S. Brandstaeter, J. Nitzler, B. A. Schrefler and W. A. Wall. 'Global Sensitivity Analysis Based on Gaussian-process Metamodelling for Complex Biomechanical Problems'. *International Journal for Numerical Methods in Biomedical Engineering* 39.3 (2023), e3675 [61], which is licensed under CC BY 4.0.

4.1 Introduction

Over the past few decades, computational biomechanical models have become an essential tool in cancer research. The goal of these models is to allow predictions so as to better understand the underlying mechanisms or to support decision-making in a medical context, e.g., to choose the most efficient therapy for a specific patient. Nevertheless, the output of such models is inherently subject to uncertainty for various reasons. First, the underlying biological process is stochastic—which is particularly true for oncophysics and cancer treatment models (for example, branching process models for cancer [263, 264], or stochastic models for immunotherapy of cancer [265]). Second, the experimental data used to calibrate models is uncertain [266]. Third, the computational model itself includes sources of uncertainty, including the assumptions made to set up the model, other simplifications, or the input parameters [50].

When analysing the uncertainty of the model output, we distinguish uncertainty analysis from sensitivity analysis [50]. Uncertainty analysis quantifies the uncertainty in the model output by propagating input uncertainties—via the model—onto the output [44]. Sensitivity analysis, on the other hand, apportions the uncertainty in the model output to different sources of uncertainty in the model input [47]. Inputs of interest can generally include not only model parameters but also boundary and initial conditions, assumptions, and constraints [267]. In the context of sensitivity analysis, those inputs of interest are commonly referred to as *factors*. Here, we only consider model parameters as sources of uncertainty and refer to those as *input parameters*. The goal of senstivity analysis is threefold:

1. Identify the most influential parameters on which further experimental estimation should focus (called factor prioritisation or ranking).

2. Identify parameters with little or no effect, which can thus be set to fixed values within their range (called factor fixing or screening).
3. Identify and quantify the interaction between parameters.

This knowledge expedites the efficient design of future computational and experimental studies while avoiding wasting resources on determining non-influential parameters.

We propose applying a specific type of sensitivity analysis to achieve the goals just described. One way of quantifying the sensitivity of the model output Y on the input parameter X_i is to calculate the partial derivative $\partial Y/\partial X_i$, which involves choosing a base point $\boldsymbol{X}^*$ and then perturbing one factor at a time while keeping all remaining factors fixed. This results in a local sensitivity measure at the base point $\boldsymbol{X}^*$, which only explores one point of the input space and thus results in a deficient sensitivity analysis [50]. In contrast, the Elementary Effects method (also called Morris method [268]) is not limited to one single point but explores the whole input space. It thereby overcomes the major limitation of local methods while only requiring a relatively small number of model evaluations. While the Elementary Effects method is a global sensitivity analysis method, it only provides semi-quantitative information and is typically used for factor fixing [44, 47]. However, it cannot detect and quantify interactions between parameters and nonlinearities [269]. In the case of complex biomechanical problems, like the tumour growth model, interactions between parameters can be expected. Therefore, we need a global method that can provide more detailed information.

Our method of choice is the Sobol[8] method [48, 49], which is a variance-based global sensitivity analysis method that decomposes the output variance into portions attributed to the input parameters (see Fig. 4.1). The downside is that it requires many model evaluations, which quickly becomes computationally prohibitive in the case of complex models. We propose to introduce Gaussian processes [51] as a metamodel for the full model to mitigate the problem of computationally expensive model evaluations. Since the use of a metamodel introduces a further source of uncertainty in the sensitivity analysis, we estimate the uncertainty following the approach presented by Le Gratiet *et al.* [52]. After the full biomechanical model is substituted by the metamodel, we can calculate the Sobol indices based on Monte Carlo integration. The uncertainty related to metamodelling and the uncertainty related to Monte Carlo integration are analysed both separately and in total.

So far, the approach suggested by Le Gratiet *et al.* [52] has been applied to different computational models: an individual-based model simulation of microbial communities [270], a mathematical model of renal fibrosis [271], climate change simulations [272], and numerical wind-turbine models [273]. Moreover, Sahli Costabal *et al.* [274] applied the same idea to the calculation of Elementary Effects of a heart model. In [270–272, 274], the authors state that they used the method, but no analysis of the associated uncertainties was presented. Only Hirvoas *et al.* [273] quantified the uncertainty related to the metamodel and the uncertainty related to Monte Carlo integration separately.

The goal of this chapter is to present the complete workflow of estimating Sobol indices based on Gaussian processes as a metamodel, including the uncertainties: we demonstrate how to apply the approach suggested by Le Gratiet *et al.* [52] to the tumour growth model and compare the results to

[8] The Sobol method was proposed by and is named after Ilya Meyerovich Sobol' (Russian: *Илья Меерович Соболь*) to whose last name an apostrophe is appended in English to transliterate the Russian letter ь. To avoid confusion with the apostrophe used in English grammar, we omit the apostrophe when referring to the Sobol method.

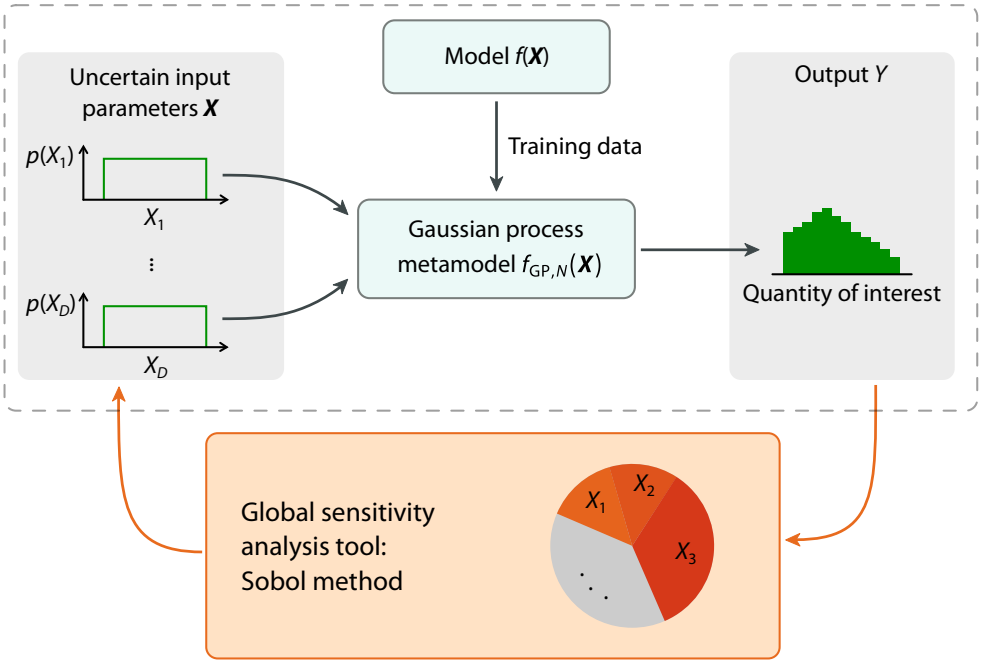

Figure 4.1 Overview of sensitivity analysis with a Gaussian process metamodel. The Gaussian-process metamodel $f_{\mathrm{GP},N}(\boldsymbol{X})$ is trained on a data set generated by the full model $f(\boldsymbol{X})$. Uncertain input parameters X_i are propagated via the metamodel and result in an uncertain output Y. The Sobol method, as an example of a global sensitivity analysis tool, decomposes the output variance into portions attributed to the input parameters. This figure is taken from [61], where it is licensed under CC BY 4.0.

other complex models in the context of biomechanics and beyond. We also assess the performance of the method when applied to such complex examples.

The following chapter is structured as follows: we first introduce the Sobol method and Gaussian processes in general. The Gaussian-process metamodel is then used to estimate the Sobol indices, including separate estimates for uncertainty related to Monte Carlo integration and uncertainty related to the metamodel based on Le Gratiet *et al.* [52]. As an example, we subsequently demonstrate how to apply this approach to our tumour growth model and assess its performance in detail. Finally, we conclude with an outlook on different complex models in the context of biomechanics and beyond, to which the approach can be applied.

4.2 Methods

4.2.1 The Sobol method

In its most general form, a model f is a functional representation of the relevant physical process. The model calculates an output $y = f(\boldsymbol{x}) \in \mathbb{R}$ for any given realisation $\boldsymbol{x} \in \mathbb{R}^D$ of the uncertain input parameters $\boldsymbol{X}$, with D being the number of parameters (see upper left side of Fig. 4.1). We assume that the random vector $\boldsymbol{X}$ summarises the input parameters $X_1, \ldots, X_D$, which are independent random variables. The probability distribution of $\boldsymbol{X}$ is described by the probability density function

$p(\boldsymbol{x})$. In the following, we assume that the input parameters are uniformly distributed, with no loss of generality. Common alternatives are the normal distribution or the log-normal distribution, among many others.

Our goal is to investigate the sensitivity of the model output to the uncertain input parameters $\boldsymbol{X}$. Because of the randomness in the input parameters, the model output Y is also a random variable defined as

$$Y = f(\boldsymbol{X}) = f(X_1, X_2, \ldots, X_D) \tag{4.1}$$

(see upper right side of Fig. 4.1). The output distribution can (partially) be described by its first two moments: the expected value $\mathbb{E}[Y]$, given by

$$\mathbb{E}[Y] = \int Y \; p(\boldsymbol{x}) \, \mathrm{d}\boldsymbol{x}, \tag{4.2}$$

with $\mathbb{E}[\cdot]$ denoting the expectation operator, and the variance $\sigma_Y^2 = \mathbb{V}[Y]$, given by

$$\sigma_Y^2 = \mathbb{V}[Y] = \int (Y - \mathbb{E}[Y])^2 \, p(\boldsymbol{x}) \, \mathrm{d}\boldsymbol{x} \tag{4.3}$$

with $\mathbb{V}[\cdot]$ denoting the variance operator and σ_Y the standard deviation.

One way of characterising sensitivity is to decompose the variance of the output $\mathbb{V}[Y]$ into portions ascribed to the individual input parameters. A common sensitivity analysis method based on variance decomposition is the Sobol method [275]. The core idea is to decompose the output variance $\mathbb{V}[Y]$ as

$$\mathbb{V}[Y] = \sum_{i=1}^{D} V_i + \sum_{i=1}^{D-1} \sum_{j>i}^{D} V_{ij} + \cdots + V_{12\ldots D} \tag{4.4}$$

with the conditional variances given by

$$\begin{aligned}
V_i &= \mathbb{V}_{X_i}\left[\mathbb{E}_{\boldsymbol{X}_{\sim i}}[Y|X_i]\right] \\
V_{ij} &= \mathbb{V}_{X_i,X_j}\left[\mathbb{E}_{\boldsymbol{X}_{\sim i,j}}\left[Y|X_i,X_j\right]\right] - V_i - V_j \\
V_{ijk} &= \mathbb{V}_{X_i,X_j,X_k}\left[\mathbb{E}_{\boldsymbol{X}_{\sim i,j,k}}\left[Y|X_i,X_j,X_k\right]\right] - V_{ij} - V_{ik} - V_{jk} - V_i - V_j - V_k \\
&\ldots
\end{aligned}$$

where $\boldsymbol{X}_{\sim i}$ denotes the vector of all input parameters except X_i. Thus, the output variance $\mathbb{V}[Y]$ is the sum of variances contributed by input parameter X_i, including interactions with other parameters. The idea now is to attribute the total variance to the individual input parameters according to their variance contribution. Note that V_{ij} is the variance contributed by the input parameters X_i and X_j but not expressed in V_i nor V_j and is called the interaction of parameters X_i and X_j. Note that this decomposition assumes statistical independence of the input parameters X_i.

Because $\mathbb{V}_{X_i}[\mathbb{E}_{\boldsymbol{X}_{\sim i}}[Y|X_i]]$ is the portion of the output variance ascribed to input parameter X_i, we define the first-order Sobol index S^i as

$$S^i = \frac{\mathbb{V}_{X_i}[\mathbb{E}_{\boldsymbol{X}_{\sim i}}[Y|X_i]]}{\mathbb{V}[Y]}. \tag{4.5}$$

The numerator $\mathbb{V}_{X_i}\left[\mathbb{E}_{\boldsymbol{X}_{\sim i}}\left[Y|X_i\right]\right]$ describes the extent to which the output variance $\mathbb{V}\left[Y\right]$ would be reduced if the parameter X_i was fixed. A parameter X_i with a high first-order index S^i should, hence, have priority when determining parameters based on experiments so as to efficiently reduce the overall uncertainty of the model. The first-order Sobol index is typically used to identify the most influential parameters, which is our first goal. Moreover, a parameter with a high first-order index S^i is more likely to be identifiable from experiments but can still be non-identifiable [267]: to decide whether a parameter is identifiable or not, an identifiability analysis is required, which complements the sensitivity analysis (see [276] for an overview of identifiability analysis).

The question now arises as to whether $S^i = 0$ is also sufficient to conclude that a parameter has no influence. In fact, this is not the case because the parameter might be involved in interactions with other parameters. A parameter may have no effect if it is varied alone; however, this may be different when it is varied in combination with another parameter or even with several other parameters. An additional sensitivity measure that includes higher-order interaction effects is needed to identify non-influential parameters. The total-order Sobol index is therefore defined as

$$S^{Ti} = \frac{\mathbb{E}_{\boldsymbol{X}_{\sim i}}\left[\mathbb{V}_{X_i}\left[Y|\boldsymbol{X}_{\sim i}\right]\right]}{\mathbb{V}\left[Y\right]} = 1 - \frac{\mathbb{V}_{\boldsymbol{X}_{\sim i}}\left[\mathbb{E}_{X_i}\left[Y|\boldsymbol{X}_{\sim i}\right]\right]}{\mathbb{V}\left[Y\right]}. \tag{4.6}$$

In this case, the numerator $\mathbb{E}_{\boldsymbol{X}_{\sim i}}\left[\mathbb{V}_{X_i}\left[Y|\boldsymbol{X}_{\sim i}\right]\right]$ describes the expected output variance that would be left if all parameters but X_i were to be determined [269]. If—and only if—this expected output variance is close to zero, is the parameter X_i non-influential. The total-order index describes the total contribution of the parameter X_i to the output Y: this includes the first-order effect plus any higher-order effects that arise from interactions. The difference $S^{Ti} - S^i$ then indicates interaction effects between factor X_i and any other factor [44]. As mentioned above, the total-order index is particularly helpful in the context of factor fixing: if $S^{Ti} = 0$ (or is in practice sufficiently small), the parameter X_i is non-influential and can be fixed anywhere in its input range without affecting the output variance.

So, the first-order and the total-order Sobol indices serve our first two goals: identify the most influential and the non-influential parameters. To additionally identify interactions between two specific parameters X_i and X_j—which is our third goal—we define the second-order Sobol index as

$$S^{ij} = \frac{\mathbb{V}_{X_i,X_j}\left[\mathbb{E}_{\boldsymbol{X}_{\sim i,j}}\left[Y|X_i,X_j\right]\right]}{\mathbb{V}\left[Y\right]} - S^i - S^j. \tag{4.7}$$

Finally, dividing Eq. (4.4) by $\mathbb{V}\left[Y\right]$ and inserting Eqs. (4.5) and (4.7) leads to

$$\sum_{i=1}^{D} S^i + \sum_{i=1}^{D-1}\sum_{j>i}^{D} S^{ij} + \ldots + S^{12\ldots D} = 1. \tag{4.8}$$

All sensitivity indices thus sum up to one; furthermore, they are non-negative. This leads to an interesting implication which is worth noting: even when we have a large number of parameters, we cannot have a large number of influential parameters. If all D parameters are equally influential, each can only contribute $1/D$ of the variance. If however a few parameters have a strong influence

on the output Y, the remaining parameters can contribute even less [44]. As Box and Meyer [277] stated: only a small subset of parameters significantly influences one specific system output (*sparsity of factors* principle). It should also be noted that the total-order indices S^{Ti} do not, in general, sum up to one.

4.2.2 Numerical approximation of Sobol indices

To estimate the Sobol indices according to Eqs. (4.5), (4.6) and (4.7), we need to compute conditional variances, e.g., $\mathbb{V}_{X_i}\left[\mathbb{E}_{\boldsymbol{X}_{\sim i}}\left[Y|X_i\right]\right]$, which involves evaluating multidimensional integrals in the space of the input parameters $\mathbb{R}^D$. Numerical integration based on quadrature rules becomes prohibitively expensive as the number of input space dimensions increases. This is why Monte Carlo integration is employed, the accuracy of which is independent of the number of input space dimensions [278]. Monte Carlo integration is a numerical integration technique based on random sampling. We independently draw M input samples $\mathscr{X} = \{\boldsymbol{x}^{(1)}, \ldots, \boldsymbol{x}^{(M)}\}$ from the input distribution and compute the corresponding responses $\mathscr{Y} = \{y^{(1)}, \ldots, y^{(M)}\}$. Thus, $y^{(m)} = f(\boldsymbol{x}^{(m)})$ are realisations of the random variable Y, for $m = 1, \ldots, M$. The Monte Carlo estimate of the expected value, given in Eq. (4.2), then is

$$\mathbb{E}\left[Y\right] = \frac{1}{M}\sum_{m=1}^{M} y^{(m)}. \tag{4.9}$$

Monte Carlo estimates have a convergence rate of $\mathcal{O}(1/\sqrt{M})$, which is independent of the input dimension. Therefore, Monte Carlo integration is especially suitable for high-dimensional problems.

For each single integral, Monte Carlo integration involves evaluating M Monte Carlo samples: to compute, for example, $\mathbb{V}_{X_i}\left[\mathbb{E}_{\boldsymbol{X}_{\sim i}}\left[Y|X_i\right]\right]$ one would need M samples to calculate the inner expectation and then repeat this M times to calculate the outer variance, resulting in a computational cost of $\mathcal{O}(M^2)$ [44]. Since M usually has to be large[9], this is impractical, especially considering that we would need to evaluate the full model f for each Monte Carlo sample. To make the estimation of Sobol indices more efficient, Ishigami and Homma [279] rewrote the multidimensional integral so that it can be computed using a single Monte Carlo loop. For the first-order index, we rewrite

$$\mathbb{V}_{X_i}\left[\mathbb{E}_{\boldsymbol{X}_{\sim i}}\left[Y|X_i\right]\right] = \mathbb{E}_{X_i}\left[\mathbb{E}^2_{\boldsymbol{X}_{\sim i}}\left[Y|X_i\right]\right] - \left(\mathbb{E}_{X_i}\left[\mathbb{E}_{\boldsymbol{X}_{\sim i}}\left[Y|X_i\right]\right]\right)^2 \tag{4.10}$$

$$= \int \mathbb{E}^2_{\boldsymbol{X}_{\sim i}}\left[Y|X_i\right] \mathrm{d}x_i - \left(\int \mathbb{E}_{\boldsymbol{X}_{\sim i}}\left[Y|X_i\right] \mathrm{d}x_i\right)^2. \tag{4.11}$$

The latter integral is $\left(\mathbb{E}\left[Y\right]\right)^2$ since

$$\int \mathbb{E}_{\boldsymbol{X}_{\sim i}}\left[Y|X_i\right] \mathrm{d}x_i = \iint Y \,\mathrm{d}x_i \,\mathrm{d}\boldsymbol{x}_{\sim i} = \int Y \,\mathrm{d}\boldsymbol{x}. \tag{4.12}$$

However, the former integral in Eq. (4.11) is computationally impractical: in a Monte Carlo frame, such terms imply a double loop and thus a computational cost of M^2. Ishigami and Homma [279]

rewrote this integral as

$$\int \mathbb{E}^2_{\boldsymbol{X}_{\sim i}}[Y|X_i]\,\mathrm{d}x_i = \iiint f(X_1,\ldots,X_D)\cdot f(X'_1,\ldots,X_i,\ldots,X'_D)\,\mathrm{d}\boldsymbol{x}_{\sim i}\,\mathrm{d}\boldsymbol{x}'_{\sim i}\,\mathrm{d}x_i \tag{4.13}$$

$$= \iint f(X_1,\ldots,X_D)\cdot f(X'_1,\ldots,X_i,\ldots,X'_D)\,\mathrm{d}\boldsymbol{x}\,\mathrm{d}\boldsymbol{x}'_{\sim i}, \tag{4.14}$$

where the last line is equal to the expected value of

$$F(X_1,\ldots,X_D,X'_1,\ldots,X_i,\ldots,X'_D) = f(X_1,\ldots,X_D)\cdot f(X'_1,\ldots,X_i,\ldots,X'_D), \tag{4.15}$$

and it hence can be computed using a single Monte Carlo loop.

To make the best use of the model evaluations, we employ the efficient algorithms suggested by Saltelli [281]: to estimate the first and the total-order indices, we generate M samples row-wise concatenated as a matrix $\boldsymbol{A}$ and further M samples concatenated as a matrix $\boldsymbol{B}$

$$\boldsymbol{A} = \begin{pmatrix} x_{11} & x_{12} & \ldots & x_{1i} & \ldots & x_{1D} \\ x_{21} & x_{22} & \ldots & x_{2i} & \ldots & x_{2D} \\ \ldots & & & & & \\ x_{M1} & x_{M2} & \ldots & x_{Mi} & \ldots & x_{MD} \end{pmatrix} \text{ and } \boldsymbol{B} = \begin{pmatrix} x'_{11} & x'_{12} & \ldots & x'_{1i} & \ldots & x'_{1D} \\ x'_{21} & x'_{22} & \ldots & x'_{2i} & \ldots & x'_{2D} \\ \ldots & & & & & \\ x'_{M1} & x'_{M2} & \ldots & x'_{Mi} & \ldots & x'_{MD} \end{pmatrix}, \tag{4.16}$$

resulting in two independent $M \times D$ matrices. We write x_{ji} as a generic element: the index j is the row index running from 1 to M, the number of Monte Carlo samples, and similar the index i is the column index running from 1 to D, the number of input space dimensions. We now introduce a third matrix $\boldsymbol{A}_{\boldsymbol{B}}^{(i)}$ as

$$\boldsymbol{A}_{\boldsymbol{B}}^{(i)} = \begin{pmatrix} x_{11} & x_{12} & \ldots & x'_{1i} & \ldots & x_{1D} \\ x_{21} & x_{22} & \ldots & x'_{2i} & \ldots & x_{2D} \\ \ldots & & & & & \\ x_{M1} & x_{M2} & \ldots & x'_{Mi} & \ldots & x_{MD} \end{pmatrix}, \tag{4.17}$$

where all columns are taken from matrix $\boldsymbol{A}$ apart from the i-th column which is taken from matrix $\boldsymbol{B}$. One sample j in $\boldsymbol{B}$ and the corresponding sample j in $\boldsymbol{A}_{\boldsymbol{B}}^{(i)}$ have in common x'_{ji} but differ in all other parameters $\boldsymbol{x}_{\sim i}$.

To calculate the first-order index, we then use the estimator proposed by Saltelli *et al.* [282]

$$\mathbb{V}_{X_i}\left[\mathbb{E}_{\boldsymbol{X}_{\sim i}}[Y|X_i]\right] \approx \frac{1}{M}\sum_{m=1}^{M} f(\boldsymbol{B})_m \left(f(\boldsymbol{A}_{\boldsymbol{B}}^{(i)})_m - f(\boldsymbol{A})_m\right), \tag{4.18}$$

and for the total-order index, we use the estimator proposed by Jansen [283]:

$$\mathbb{E}_{\boldsymbol{X}_{\sim i}}\left[\mathbb{V}_{X_i}[Y|\boldsymbol{X}_{\sim i}]\right] \approx \frac{1}{2M}\sum_{m=1}^{M}\left(f(\boldsymbol{A})_m - f(\boldsymbol{A}_{\boldsymbol{B}}^{(i)})_m\right)^2. \tag{4.19}$$

[9] The error of the Monte Carlo estimate for the expectation is proportional to $\frac{\sqrt{\mathbb{V}[g]}}{\sqrt{M}}$, with g denoting the integrand. If we assume $\mathbb{V}[g]$ to be fixed, we have to increase the number of Monte Carlo samples M, and the error of the estimate thus decreases by $\frac{1}{\sqrt{M}}$ [280].

Alternative forms were presented in [48, 283–285], among others. The denominator is estimated as

$$\mathbb{V}[Y] \approx \mathcal{V}[f([\boldsymbol{A}\ \boldsymbol{B}])], \tag{4.20}$$

where we estimate the variance of the output as the sample variance $\mathcal{V}$ of evaluations of all samples $\boldsymbol{A}$ and $\boldsymbol{B}$. This yields better results, i.e., an estimator with lower variance, compared to $\mathbb{V}[Y] \approx \mathcal{V}[f(\boldsymbol{A})]$ alone [281].

In addition to the first- and total-order indices, we estimate the second-order indices as proposed by Saltelli [281]:

$$\mathbb{V}_{X_i,X_j}\left[\mathbb{E}_{\boldsymbol{X}_{\sim i,j}}\left[Y|X_i,X_j\right]\right] \approx \frac{1}{M}\sum_{m=1}^{M} f(\boldsymbol{B}_{\boldsymbol{A}}^{(i)})_m\, f(\boldsymbol{A}_{\boldsymbol{B}}^{(j)})_m - f(\boldsymbol{A})_m\, f(\boldsymbol{B})_m \tag{4.21}$$

where the matrix $\boldsymbol{B}_{\boldsymbol{A}}^{(i)}$ is built similar to $\boldsymbol{A}_{\boldsymbol{B}}^{(i)}$. More details on different sensitivity-index estimators can be found in [281, 282], among others.

We hence have to evaluate our model f at all samples of the triplet $\boldsymbol{A}$, $\boldsymbol{B}$ and $\boldsymbol{A}_{\boldsymbol{B}}^{(i)}$ (and additionally $\boldsymbol{B}_{\boldsymbol{A}}^{(i)}$ if second-order indices are included). This means $2M$ simulations are needed for computing $f(\boldsymbol{A})$ and $f(\boldsymbol{B})$ plus $D \cdot M$ simulations needed for computing $f(\boldsymbol{A}_{\boldsymbol{B}}^{(i)})$ for $i = 1, \ldots, D$. The cost of first- and total-order indices is hence $M(D+2)$ simulations. If second-order indices are included, we need an additional $D \cdot M$ simulations for $f(\boldsymbol{B}_{\boldsymbol{A}}^{(i)})$, resulting in $M(2D+2)$ simulations in total (for more details, see the original publication by Saltelli [281]). In practice, Quasi–Monte Carlo (QMC) integration is often used to generate the samples because of its superior convergence rate compared to Monte Carlo integration [286].

4.2.3 Gaussian process metamodels

As just described, Monte Carlo integration to estimate the Sobol indices requires a large number of sample evaluations and is thus computationally prohibitive if the evaluation of the underlying model is expensive. We therefore use a metamodel (also known as surrogate model or emulator) as an approximation of the full model. Classically used metamodels include polynomials, splines, neural networks, polynomial chaos expansion, support vector regression, and Gaussian processes (GPs), among others [287, 288]. Before a metamodel can be used for a sensitivity analysis, for example, it has to be trained to later ensure that it is a good approximation of the full model.

This process consists of three steps, which we first summarise (see Fig. 4.2) and then explain in more detail below:

1. Generate N training samples summarised in $\boldsymbol{\mathcal{X}}$ (resulting in an $N \times D$ matrix).
2. Evaluate the full model at the training samples to obtain the corresponding response: $\boldsymbol{\mathcal{Y}} = f(\boldsymbol{\mathcal{X}})$ (resulting in an $N \times 1$ vector).
3. Form and train the metamodel.

First, we generate N training samples that are summarised in the matrix $\boldsymbol{\mathcal{X}}$ ($N \times D$ matrix). The choice of training samples has to provide a good coverage of the input space to later ensure a good

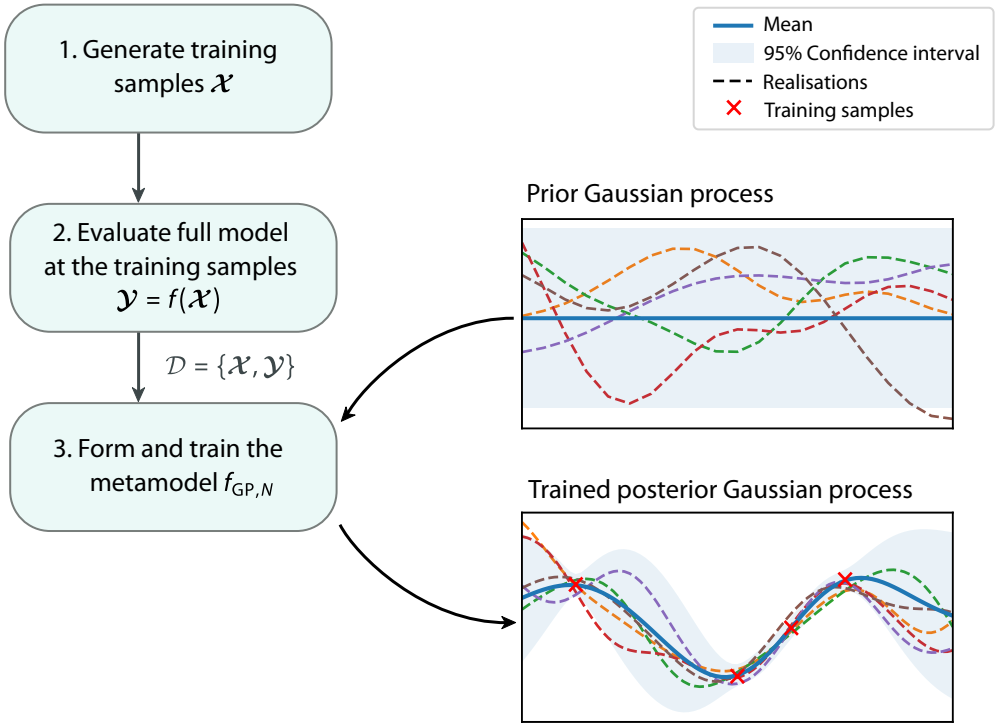

Figure 4.2 Schematic overview of the steps involved in training the Gaussian process metamodel. Conditioning the prior Gaussian process on the training samples results in the posterior Gaussian process. This figure is taken from [61], where it is licensed under CC BY 4.0.

predictive quality of the metamodel. To this end, we use a QMC approach based on Sobol sequences [289] to generate the training samples.

Remark (Sequential design)**.** *A commonly used alternative to a QMC approach is Latin Hypercube Sampling (LHS) [290]. Iooss* et al. *[287] state that optimised LHS is particularly well-suited for metamodel fitting. However, sequential design is also important in the context of metamodelling: if the original number of training samples is not sufficient to achieve a good predictive quality of the metamodel, additional samples can be added while still making use of the original training samples. Since only advanced LHS methods [291, 292] enable sequentially adding new points, while this is straightforward with QMC schemes [293], we use a QMC approach.*

Subsequently, we evaluate the full model at each training sample: $\mathcal{Y} = f(\mathcal{X})$ with $\mathcal{Y}$ hence being an $N \times 1$ vector. This results in the training data set

$$\mathcal{D} = \{\mathcal{X}, \mathcal{Y}\}, \tag{4.22}$$

where each row corresponds to one training point.

Finally, we have to *train* the metamodel. We use a GP f_{GP} as a metamodel similar to [52, 294, 295] and summarise what training means for GPs below. Note that we only include a compact overview of the most relevant concepts used in this paper. For more details, the reader is referred, e.g., to Rasmussen and Williams [51].

A GP defines a distribution over functions such that any finite set of function values $f_{\mathrm{GP}}(\boldsymbol{x}^{(1)})$, $f_{\mathrm{GP}}(\boldsymbol{x}^{(2)}), \ldots, f_{\mathrm{GP}}(\boldsymbol{x}^{(n)})$ has a joint Gaussian distribution [51, 296]. From a Bayesian point of view, we distinguish between prior and posterior: the prior GP reflects our beliefs about the metamodel before seeing any (training) data, and the posterior GP is then conditioned on the (training) data, i.e., includes the knowledge from the data (see Fig. 4.2). This conditioning on the data is what we refer to as *training*.

The prior GP $f_{\mathrm{GP}}(\boldsymbol{X})$ is given by

$$f_{\mathrm{GP}}(\boldsymbol{X}) \sim \mathrm{GP}(m_{\mathrm{GP}}(\boldsymbol{X}), k(\boldsymbol{X}, \boldsymbol{X}')) \tag{4.23}$$

and is completely specified by its mean function $m_{\mathrm{GP}}(\boldsymbol{X})$ and its covariance function $k(\boldsymbol{X}, \boldsymbol{X}')$ between all possible pairs $(\boldsymbol{X}, \boldsymbol{X}')$. The covariance function is a positive definite kernel, e.g., the squared exponential covariance function (also called radial basis function)

$$k(\boldsymbol{X}, \boldsymbol{X}') = \sigma_f^2 \exp\left(-\frac{1}{2\ell^2}||\boldsymbol{X} - \boldsymbol{X}'||^2\right) \tag{4.24}$$

with the characteristic length scale ℓ, variance parameter σ_f and $||\cdot||$ denoting the Euclidean L2-norm. We assume that the prior mean function is zero: $m_{\mathrm{GP}}(\boldsymbol{X}) = \boldsymbol{0}$, which is common practice and does not limit the GP model, as any uncertainty about the mean function can be included in the choice of a covariance function [296]. Different covariance functions exist and can be combined, for example, through multiplication or addition. Duvenaud [296] presents a concise overview of different covariance functions for GPs and how to use them to express the structure of the data. The choice of a suitable covariance function is essential since the more a-priori knowledge goes into choosing the covariance function, the less data we need to train the metamodel [297].

As described above, we observe the output at N training points. The goal then is to predict the output at N_* new points summarised in $\boldsymbol{\mathcal{X}}_*$; in our case, those new points (where we predict the output) will be the Monte Carlo samples for estimating the Sobol indices.

Remember that Eq. (4.23) is only the prior distribution and does not yet incorporate our knowledge from the training data. To obtain the posterior, we now condition the prior GP on our set of N training data points. This conditioning results in the key predictive equations

$$f_{\mathrm{GP},N}(\boldsymbol{\mathcal{X}}_*) \sim \mathrm{GP}(m_{\mathrm{GP},N}(\boldsymbol{\mathcal{X}}_*), k_N(\boldsymbol{\mathcal{X}}_*, \boldsymbol{\mathcal{X}}_*)) \tag{4.25}$$

with

$$m_{\mathrm{GP},N}(\boldsymbol{\mathcal{X}}_*) = \boldsymbol{K}_*^{\mathrm{T}} \boldsymbol{K}_\varepsilon^{-1} \boldsymbol{\mathcal{Y}}, \tag{4.26}$$

$$k_N(\boldsymbol{\mathcal{X}}_*, \boldsymbol{\mathcal{X}}_*) = \boldsymbol{K}_{**} - \boldsymbol{K}_*^{\mathrm{T}} \boldsymbol{K}_\varepsilon^{-1} \boldsymbol{K}_*. \tag{4.27}$$

In Eqs. (4.26) and (4.27), $\boldsymbol{K}_\varepsilon = \boldsymbol{K} + \sigma_y^2 \boldsymbol{I}$, where $\boldsymbol{K} = k(\boldsymbol{\mathcal{X}}, \boldsymbol{\mathcal{X}})$ denotes the $N \times N$ matrix we obtain when evaluating the covariance function (given in Eq. (4.24)) for all pairs of training points, similarly for $\boldsymbol{K}_* = k(\boldsymbol{\mathcal{X}}, \boldsymbol{\mathcal{X}}_*)$ and $\boldsymbol{K}_{**} = k(\boldsymbol{\mathcal{X}}_*, \boldsymbol{\mathcal{X}}_*)$. We use σ_y^2 as an artificially introduced variable nugget term to alleviate numerical problems [298, 299]. The hyperparameters $\boldsymbol{\theta} = (\sigma_f, \ell)$ are optimised

by maximising the log marginal likelihood using a gradient-based optimiser. The log marginal likelihood is given by

$$\log p(\mathcal{Y}|\mathcal{X}) = -\frac{1}{2}\mathcal{Y}^{\mathrm{T}}\boldsymbol{K}_{\varepsilon}^{-1}\mathcal{Y} - \frac{1}{2}\log|\boldsymbol{K}_{\varepsilon}| - \frac{N}{2}\log 2\pi \tag{4.28}$$

with $|\cdot|$ denoting the determinant. Maximising the log marginal likelihood given by Eq. (4.28) with respect to the hyperparameters $\boldsymbol{\theta}$ automatically incorporates a trade-off between model fit and model complexity: the first term in Eq. (4.28) penalises the model's failure to describe the data, while the second term penalises high model complexity. Thus, this favours the least complex model that is able to explain the data [51].

One advantage of employing GPs as a metamodel is that predictions can be computed exactly in a closed form [296] and that GPs inherently provide uncertainty measures over the predictions. Moreover, one can incorporate a wide range of modelling assumptions into the choice of the covariance function. However, note that computing the inverse in the first term in Eq. (4.28) (and the determinant in the second term) is computationally expensive, i.e., on the order $\mathcal{O}(N^3)$. This cubic complexity results in slow inference as the number of training samples increases. One further challenge of using GPs as a metamodel is that they are susceptible to the curse of dimensionality: as the dimensionality of the input space increases, the number of training samples required to train the metamodel grows exponentially [300, 301] and the optimisation of hyperparameters $\boldsymbol{\theta}$ becomes impractical.

Remark (Advanced GPs)**.** *In case of large numbers of training samples and/or input space dimensions, various advanced GP metamodels are available: Liu* et al. *[302] reviewed approaches to improve the scalability of GPs to large data sets, e.g., by using stochastic variational inference [303]; Tripathy* et al. *[301] presented an approach with built-in dimensionality reduction.*

4.2.4 Estimation of Sobol indices and their uncertainty

To estimate the Sobol indices, we now use the estimators given by Eqs. (4.18), (4.19) and (4.21) and substitute the realisations of the full model f with those of the trained GP metamodel $f_{\mathrm{GP},N}$, as suggested by [52]:

$$\hat{S}^{i} = \frac{\frac{1}{M}\sum_{m=1}^{M} f_{\mathrm{GP},N}(\boldsymbol{B})_m \left(f_{\mathrm{GP},N}(\boldsymbol{A}_{\boldsymbol{B}}^{(i)})_m - f_{\mathrm{GP},N}(\boldsymbol{A})_m\right)}{\mathcal{V}[f_{\mathrm{GP},N}([\boldsymbol{A}\ \boldsymbol{B}])]}, \tag{4.29}$$

$$\hat{S}^{Ti} = \frac{\frac{1}{2M}\sum_{m=1}^{M}\left(f_{\mathrm{GP},N}(\boldsymbol{A})_m - f_{\mathrm{GP},N}(\boldsymbol{A}_{\boldsymbol{B}}^{(i)})_m\right)^2}{\mathcal{V}[f_{\mathrm{GP},N}([\boldsymbol{A}\ \boldsymbol{B}])]}, \tag{4.30}$$

$$\hat{S}^{ij} = \frac{\frac{1}{M}\sum_{m=1}^{M} f_{\mathrm{GP},N}(\boldsymbol{B}_{\boldsymbol{A}}^{(i)})_m\, f_{\mathrm{GP},N}(\boldsymbol{A}_{\boldsymbol{B}}^{(j)})_m - f_{\mathrm{GP},N}(\boldsymbol{A})_m\, f_{\mathrm{GP},N}(\boldsymbol{B})_m}{\mathcal{V}[f_{\mathrm{GP},N}([\boldsymbol{A}\ \boldsymbol{B}])]} - \hat{S}^{i} - \hat{S}^{j}, \tag{4.31}$$

with M again being the number of Monte Carlo samples. We summarise the estimates as $\hat{S}^{\diamond}$ with $\diamond \in \{i, Ti, ij\}$ for the first-, total-, or second-order index estimates, respectively. Remember that we now evaluate the Monte Carlo samples with the metamodel instead of the full model. We can

therefore afford considerably larger numbers of Monte Carlo samples. Since we sample realisations of the GP metamodel $f_{\mathrm{GP},N}$, the resulting estimates $\hat{S}^\diamond$ are again random variables. These include two sources of uncertainty: one related to the metamodel approximation and one related to the Monte Carlo integration. To estimate those uncertainties, and additionally the total uncertainty, we employ the algorithm suggested by [52]. The steps described in the following can equally be applied to all indices of different order.

We visually summarise the approach in Fig. 4.3; a more detailed version is included in the Supplement A.4 of [61]. The core idea is to sample N_{GP} realisations of the GP metamodel and subsequently resample each realisation B times using the bootstrap technique [304]. This results in $N_{\mathrm{GP}} \times B$ estimates $\hat{S}^\diamond_{k,b}$ of the respective Sobol index. We then calculate the mean as

$$\bar{S}^\diamond = \frac{1}{N_{\mathrm{GP}} B} \sum_{k=1}^{N_{\mathrm{GP}}} \sum_{b=1}^{B} \hat{S}^\diamond_{k,b} \tag{4.32}$$

and the total variance as

$$\hat{\sigma}^2(S^\diamond) = \frac{1}{N_{\mathrm{GP}} B - 1} \sum_{k=1}^{N_{\mathrm{GP}}} \sum_{b=1}^{B} \left(\hat{S}^\diamond_{k,b} - \bar{S}^\diamond\right)^2 . \tag{4.33}$$

Since this estimator includes two sources of uncertainty (one related to the metamodel approximation and one related to the Monte Carlo integration), we decompose the variance of $S^\diamond$ as

$$\hat{\sigma}^2(S^\diamond) = \underbrace{\hat{\sigma}^2_{\mathrm{GP}}(S^\diamond)}_{\text{Metamodel}} + \underbrace{\hat{\sigma}^2_{\mathrm{MC}}(S^\diamond)}_{\text{Monte Carlo}} . \tag{4.34}$$

Sampling realisations of the metamodel $f_{\mathrm{GP},N}(\boldsymbol{X})$ as opposed to using only the predictive mean $m_{\mathrm{GP},N}(\boldsymbol{X})$ allows us to take into account the covariance structure of the metamodel. The part of the variance related to the metamodel approximation can be estimated as

$$\hat{\sigma}^2_{\mathrm{GP}}(S^\diamond) = \frac{1}{B} \sum_{b=1}^{B} \frac{1}{N_{\mathrm{GP}} - 1} \sum_{k=1}^{N_{\mathrm{GP}}} \left(\hat{S}^\diamond_{k,b} - \bar{\hat{S}}^\diamond_b\right)^2 \quad \text{with} \quad \bar{\hat{S}}^\diamond_b = \frac{1}{N_{\mathrm{GP}}} \sum_{k=1}^{N_{\mathrm{GP}}} \hat{S}^\diamond_{k,b}. \tag{4.35}$$

Alternatively, Janon *et al.* [305] present an approach to estimate an upper bound for the metamodel error based directly on the covariance function of the GP, but their approach only provides a rough upper bound [52]. In addition, Panin [306] present an approach to investigate the accuracy of Sobol indices based on a general relation between the accuracy of an arbitrary metamodel and the error of the estimated indices.

To estimate the uncertainty related to Monte Carlo integration, we use the bootstrap technique [304]. The Monte Carlo samples $\boldsymbol{A}$, $\boldsymbol{B}$, $\boldsymbol{A}_{\boldsymbol{B}}^{(i)}$ and $\boldsymbol{B}_{\boldsymbol{A}}^{(i)}$ are resampled (i.e., sampled with replacement) B times as depicted in Fig. 4.3. We then calculate $\hat{S}^\diamond$ according to Eqs. (4.29), (4.30) and (4.31) for each bootstrap sample, resulting in B estimates for the Sobol index for each realisation k of the metamodel.

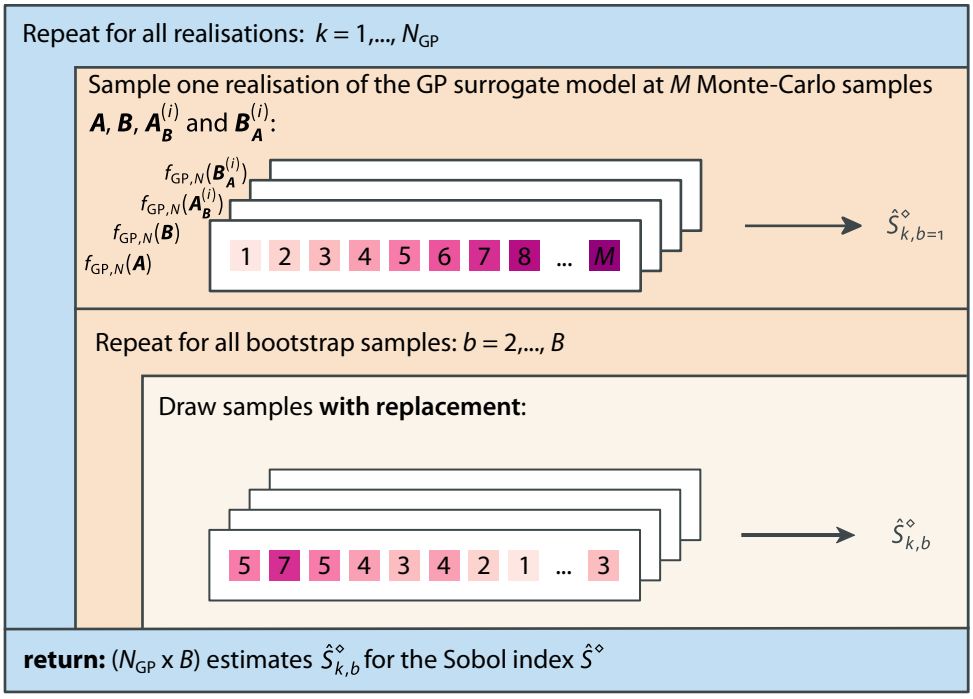

Figure 4.3 Calculation of $(N_{GP} \times B)$ estimates $\hat{S}^{\diamond}_{k,b}$ of the Sobol index. We sample N_{GP} realisations of the GP metamodel and subsequently resample each realisation B times using the bootstrap technique as suggested by Le Gratiet *et al.* [52]. This figure is taken from [61], where it is licensed under CC BY 4.0.

The part of the variance related to the Monte Carlo integration is given by

$$\hat{\sigma}^2_{MC}(S^{\diamond}) = \frac{1}{N_{GP}} \sum_{k=1}^{N_{GP}} \frac{1}{B-1} \sum_{b=1}^{B} \left(\hat{S}^{\diamond}_{k,b} - \bar{\hat{S}}^{\diamond}_{k} \right)^2 \quad \text{with} \quad \bar{\hat{S}}^{\diamond}_{k} = \frac{1}{B} \sum_{b=1}^{B} \hat{S}^{\diamond}_{k,b}. \tag{4.36}$$

The bootstrap technique is based on the fact that sampling with replacement from a set of independent, identically distributed data equals sampling from the empirical distribution function of the data [307]. It is important to note that bootstrapping does not require further model evaluations. For a general introduction to the bootstrap technique, the reader is referred to [308] or [309].

4.3 Application to nanoparticle-mediated drug delivery

To demonstrate the proposed approach, we apply it to nanoparticle-mediated drug delivery in our multiphase tumour growth model, as presented and discussed in Section 3.1. All challenging, motivating arguments for our approach to sensitivity analysis are present in this example, including a complex, costly model and a large number of parameters.

4.3.1 Computational setup

We include the transport of the nanoparticles as presented and discussed in Section 3.1, including the interendothelial and the transendothelial pathway, the transport in the interstitial fluid, and the lymphatic drainage. We now additionally assume that the nanoparticles transport and release anti-cancer drugs. Those kill tumour cells and thus increase the mass fraction of necrotic tumour cells ω^{Nt}. At the same time, those drugs have adverse side effects and kill host cells. This additionally increases the mass fraction of necrotic host cells ω^{Nh}. For the sake of simplicity, we assume that the mass fraction of killed cells is directly proportional to the mass fraction of nanoparticles present in the interstitial fluid at a certain position. We introduce intra-phase reaction terms that increase the mass fraction of necrotic tumour cells and host cells according to

$$r_{\text{kill}}^{Nt} = \gamma_{\text{kill}}^{t} \omega^{\text{NP}\ell} (1 - \omega^{Nt}) \quad \text{and} \quad r_{\text{kill}}^{Nh} = \gamma_{\text{kill}}^{h} \omega^{\text{NP}\ell} (1 - \omega^{Nh}), \tag{4.37}$$

where γ_{kill}^{t} and γ_{kill}^{h} characterise the strength of the drug.

As the quantity of interest for the sensitivity analysis, we consider the mean of the necrotic fraction of tumour cells given by

$$\bar{\omega}^{Nt} = \frac{1}{A^t} \int \omega^{Nt} \, \mathrm{d}\Omega, \tag{4.38}$$

where the tumour size is defined as $A^t = \int \mathcal{H}(S^t - 0.1) \, \mathrm{d}\Omega$ with the Heaviside function $\mathcal{H}(\cdot)$. We define the tumour as the part of the domain where $S^t > 0.1$.

In the context of sensitivity analysis, it is crucial to choose the quantity of interest carefully and to bear in mind that a parameter that is non-influential under one particular investigated condition, e.g., one particular quantity of interest, might be highly influential under a new condition [267].

The computational setup is similar to the ones presented and discussed in Sections 2.2.2 and 3.1.2. The transport of nanoparticles, and thus the question of which regions nanoparticles reach and where drugs can kill cells, essentially depends on the tumour microenvironment. Solid tumours exhibit typical features relevant in this context: a necrotic core with collapsed blood vessels as well as an increased interstitial pressure, which experimental research has also observed [122, 126, 127, 129]. We analyse a time interval of 20 min of nanoparticle transport and killing of cells based on examples by [158, 174]. Assuming the intravenous infusion of nanoparticles, we prescribe a constant value of $\omega_D^{\text{NP}v} = 2.0 \times 10^{-3}$ for the mass fraction of nanoparticles in the vasculature.

Table 4.1 summarises the six uncertain input parameters included in the sensitivity analysis. We assume that all input parameters are distributed uniformly within the given ranges, which are based on experimental data (see references in Table 4.1). The uniform distribution is chosen because we lack more specific information about the input parameters: given only the range of the input parameters (and no further information such as mean or variance), uniform distributions maximise the information entropy and hence minimise the introduced bias [310, 311]. Note that the killing coefficient of host cells γ_{kill}^{h} has no influence on our quantity of interest, the mean of the necrotic fraction of tumour cells—neither directly nor indirectly through coupling terms. We nevertheless include the killing coefficient of host cells γ_{kill}^{h} in the sensitivity analysis to investigate how reliably we can identify a non-influential input parameter as such.

Table 4.1 Probability distributions of the uncertain input parameters. We assume that all parameters are distributed uniformly within the given range.

Symbol	Parameter	Range	Units	Source
L_p^v	Hydraulic conductivity of blood-vessel wall*	$[7.8;\ 125] \cdot 10^{-8}$	mm/(Pa s)	[107]
P^v	Blood-vessel wall permeability	$[3.2;\ 128] \cdot 10^{-5}$	mm/s	[175–177]
$D^{\mathrm{NP}\ell}$	Diffusivity of nanoparticles	$[0.26;\ 30.83]$	$\mu m^3/s$	[177]
$\left(L_p \frac{S}{V}\right)^{\mathrm{ly}}$	Lymphatic filtration coefficient	$[0;\ 5.2] \cdot 10^{-4}$	$Pa^{-1}\,s^{-1}$	[58]
γ_{kill}^t	Killing coefficient of tumour cells	$[5;\ 10] \cdot 10^{-4}$	$g/(mm^3\,s)$	–
γ_{kill}^h	Killing coefficient of host cells	$[2;\ 7] \cdot 10^{-4}$	$g/(mm^3\,s)$	–

* The given values for the hydraulic conductivity of the blood-vessel wall correspond to a pore radius of $r_0 = [50;\ 200]$ nm as used in Section 3.1.2 and Wirthl *et al.* [58].

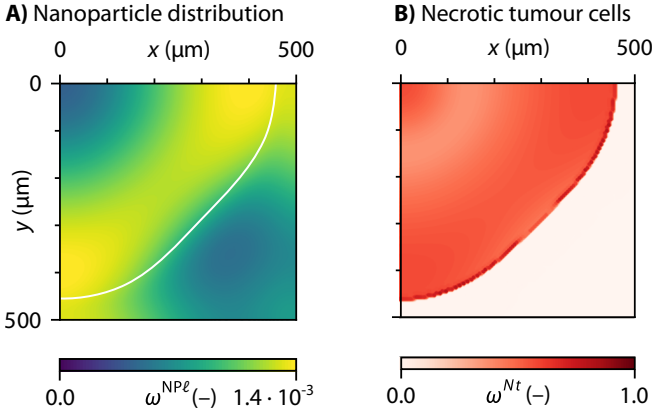

Figure 4.4 Distribution of nanoparticles and necrotic tumour cells in the tumour microenvironment for the mean values of the uncertain input parameters. A) Mass fraction of nanoparticles in the interstitial fluid $\omega^{\mathrm{NP}\ell}$. B) Mass fraction of necrotic tumour cells ω^{Nt}. This figure is adapted from [61], where it is licensed under CC BY 4.0.

Fig. 4.4 presents a result for the distribution of nanoparticles in the interstitial fluid and the mass fraction of necrotic tumour cells: for this example, we used the mean values of the six uncertain input parameters given in Table 4.1. Most nanoparticles accumulate at the edge of the tumour, while lymphatic drainage removes most particles outside the tumour area, and roughly 50% of the tumour cells are necrotic.

4.3.2 Predictive quality of the metamodel

Since we use a GP metamodel to estimate the Sobol indices, we first assess its predictive quality. To this end, we investigate the quality of the metamodel predictions for two different covariance functions $k(\boldsymbol{X}, \boldsymbol{X}')$ used for the GP: we compare a tensorised, squared, exponential covariance function to a tensorised 5/2-Matérn covariance function (with $\nu = 5/2$) [51, 312, 313]. A tensorised covariance function has the form $k(\boldsymbol{X}, \boldsymbol{X}') = k_1(X_1, X_1') \cdot k_2(X_2, X_2') \cdot \ldots \cdot k_D(X_D, X_D')$ and as such includes a set of hyperparameters $\boldsymbol{\theta} = (\sigma_{fi}, \ell_i)_{i=1,\ldots,D}$ for all input space dimensions, which we optimise by maximising the log marginal likelihood.

For this comparison, we consider different sizes of training sample sets $N = [10, 15, 20, 25, 30, 40, 60, 80, 100, 150, 200]$, which we generate based on Sobol sequences. Additionally, we generate a set $\mathcal{T}$ of $N_T = 1000$ testing samples disjoint of the training samples. Based on the training samples and the testing samples, we calculate the Nash–Sutcliffe efficiency Q^2 [314] given by

$$Q^2 = 1 - \frac{\sum_{\boldsymbol{X}\in\mathcal{T}} \left(m_{\mathrm{GP},N}(\boldsymbol{X}) - f(\boldsymbol{X})\right)^2}{\sum_{\boldsymbol{X}\in\mathcal{T}} \left(m_{\mathrm{GP},N}(\boldsymbol{X}) - \bar{f}\right)^2} \quad \text{with} \quad \bar{f} = \frac{1}{N_T} \sum_{\boldsymbol{X}\in\mathcal{T}} f(\boldsymbol{X}) \tag{4.39}$$

similar to [52]. This is based on the predictive posterior mean $m_{\mathrm{GP},N}(\boldsymbol{X})$ of the GP with optimised hyperparameters, and thus compares the mean prediction of the posterior GP to the actual output of the full model f. A Nash–Sutcliffe efficiency close to one indicates good agreement and hence reliable predictions. Fig. 4.5 shows good convergence of the Nash–Sutcliffe efficiency for both covariance functions with values close to one, even for smaller training sample set sizes. If the number of training samples is restricted due to the computational cost, Van Steenkiste *et al.* [315] suggest an algorithm to improve the metamodelling accuracy and efficiency based on sequential sampling.

Note that we use a set of testing samples here that is disjoint of our set of training samples; this means that we also evaluate our full model N_T times, which might be infeasible if the model is computationally more expensive. In those cases, one can use cross-validation methods, such as those explained in [51], where the training set itself is split into two disjoint sets: one is actually used for training and the other for validation.

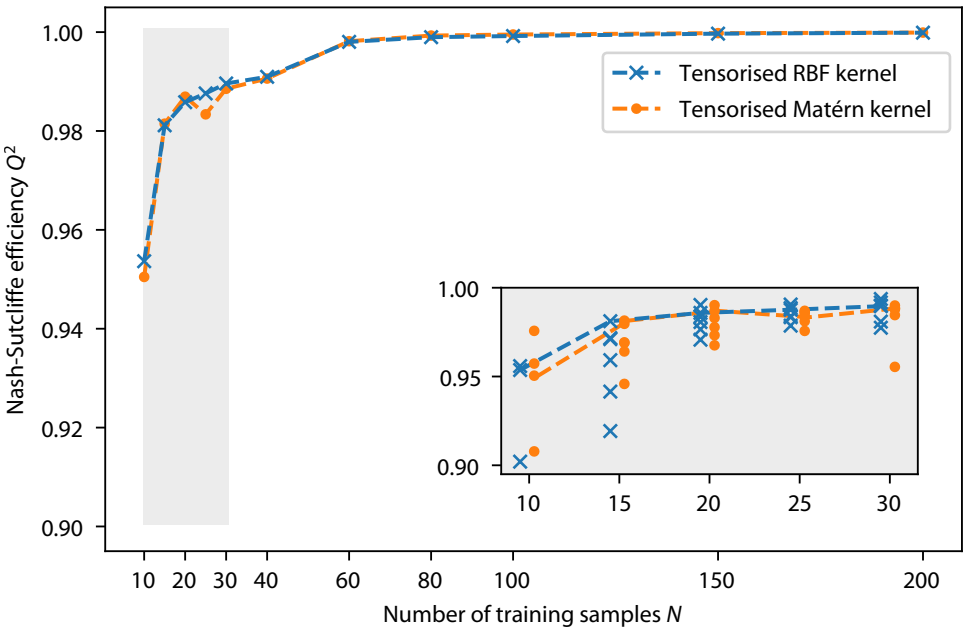

Figure 4.5 Nash–Sutcliffe efficiency Q^2 for different training sample set sizes with a tensorised, squared, exponential covariance function and a tensorised Matérn covariance function. N training samples were randomly generated for the main plot. For the detail plot, we repeated the process five times with different training sample sets of sizes $N = [10, 15, 20, 25, 30]$. For reference, the dashed lines in the detail plot are identical to the dashed lines in the main plot. This figure is taken from [61], where it is licensed under CC BY 4.0.

Both covariance functions yield a very similar predictive quality. In the following, we only use the tensorised, squared, exponential covariance function because it is the default choice in most applications of GPs [296] and because it is a universal covariance function [316].

Remark (Randomness of metamodel training). *In Fig. 4.5, we notice a slight kink in the Nash–Sutcliffe efficiency for $N = 25$ in the case of the Matérn covariance function. Therefore, we repeat the training of the GP with other randomly chosen training sample sets for $N = [10, 15, 20, 25, 30]$ to check whether the original training sets happen to perform exceptionally well. The grey detail plot in Fig. 4.5 presents the results: while the Nash–Sutcliffe efficiency is still above 0.90 in all cases, we notice that some training sample sets result in slightly worse efficiencies than others for those smaller sample sizes. This is precisely the case for the Matérn covariance function with $N = 25$ in the main plot. Moreover, the two different covariance functions lead to slightly different efficiencies.*

One possible reason for such behaviour may be the convergence of the optimiser used to optimise the hyperparameters according to Eq. (4.28). As with all gradient-based optimisers, the optimisation may get stuck in a local minimum. To avoid ending the optimisation in a local minimum, one can repeat the optimisation multiple times from random initial points [301], as provided by the package GPy [317], for example, or use stochastic optimisation, such as Adam optimisation [318].

Further, we take a closer look at the underlying GP, which is depicted in Fig. 4.6 for 20 training samples. The projection of the GP into the input-space dimensions reveals a linear relation in most dimensions. We only see considerable nonlinearity for the blood-vessel wall permeability P^v. Those characteristics make it much easier to train the GP based on a small number of training samples.

Remark (Projection of the D-dimensional Gaussian process). *The projection $m_{GPi}(X_i)$ of the D-dimensional posterior mean $m_{GP,N}(\boldsymbol{X})$ into the input space dimension X_i (as presented in Fig. 4.6) is calculated as follows. First, we uniformly sample discrete values of the posterior mean $m_{GP,N}(\boldsymbol{X})$ in the D-dimensional input space. Second, we project those values over the input space dimension X_i. Third, the results are binned in the X_i-direction, and we calculate the mean and confidence interval for each bin. Note that we only project the posterior mean $m_{GP,N}(\boldsymbol{X})$ and neglect the covariance function k_N here.*

Plotting the model output over a specific input in the form of scatterplots—as done with the training samples in Fig. 4.6—helps us gain a general understanding of the magnitude of the underlying sensitivity [269]. Saltelli [44, Sec. 1.2.7] offers a compelling interpretation of scatterplots in relation to the first-order Sobol index: if the conditional expectation $\mathbb{E}_{X_{\sim i}}[Y|X_i]$—here represented by the projection of the mean $m_{\mathsf{GP}i}$ of the GP—has a large variation across X_i, the corresponding input parameter has a high first-order Sobol index. Fig. 4.6 reveals that the projection of the mean $m_{\mathsf{GP}i}$ is almost constant for the diffusivity of nanoparticles $D^{\mathsf{NP}\ell}$, the lymphatic filtration coefficient $\left(L_p \frac{S}{V}\right)^{\mathsf{ly}}$, and the killing coefficient of host cells γ^h_{kill}. In contrast, the variation of the projection of the mean $m_{\mathsf{GP}i}$ is larger for the blood-vessel wall L^v_p, the vascular permeability P^v, and the killing coefficient γ^t_{kill}, and we therefore expect the output to be highly sensitive to those parameters.

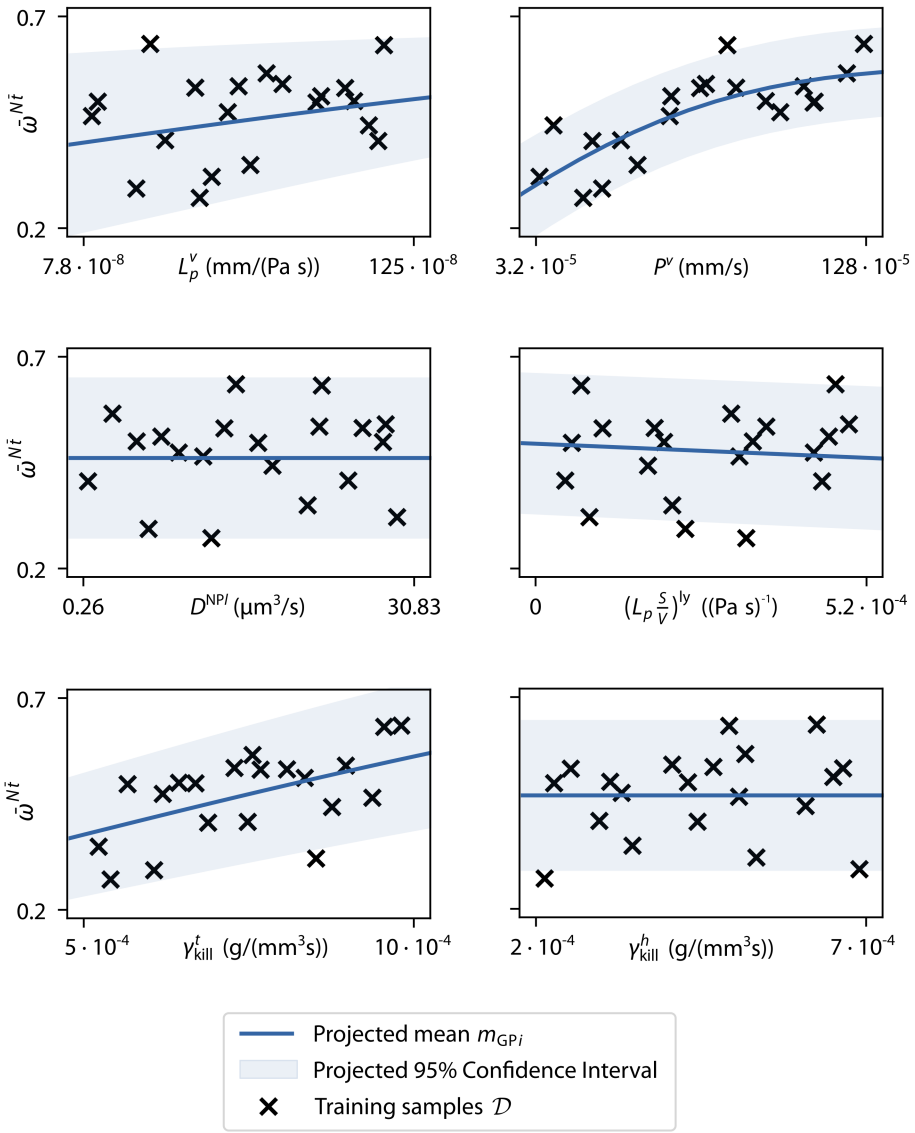

Figure 4.6 Gaussian process for $N = 20$ with a tensorised, squared, exponential covariance function. Projected mean $m_{GPi}(X_i)$, projected 95% confidence interval (CI) and training samples $\mathcal{D}$ for the mean of the necrotic fraction of tumour cells $\bar{\omega}^{N\bar{t}}$ (the y-axis labels apply to both figures). This figure is taken from [61], where it is licensed under CC BY 4.0.

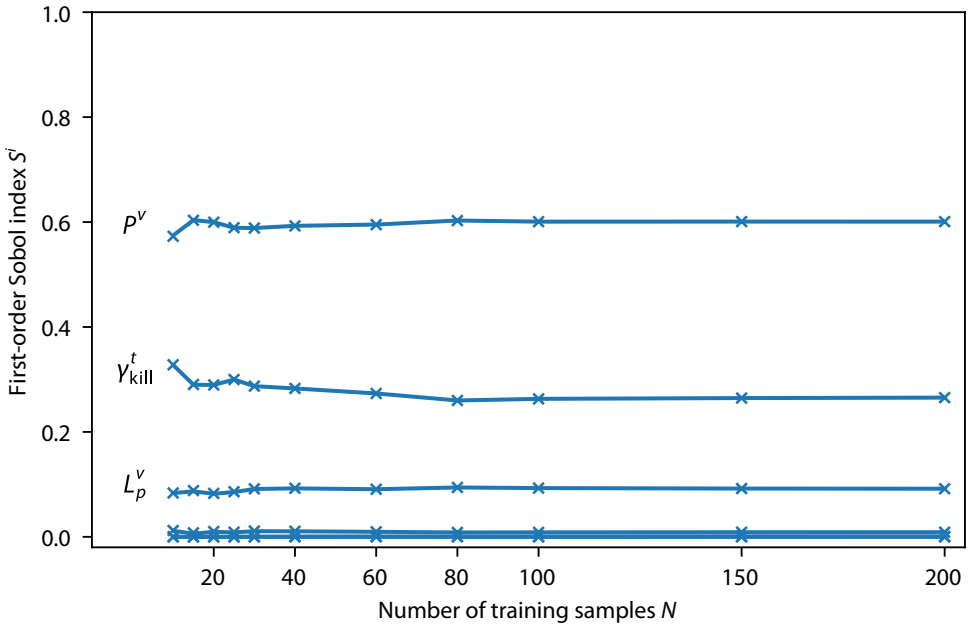

Figure 4.7 Convergence of first-order Sobol index estimate for increasing training sample set size. We use $M = 10\,000$ Monte Carlo samples and $N_{\text{GP}} = 500$ realisations of the Gaussian process. This figure is taken from [61], where it is licensed under CC BY 4.0.

4.3.3 First-order Sobol index estimates

We now assess the convergence of the first-order Sobol index estimates for increasing numbers of training samples. To calculate the mean $\bar{S}^i$ based on Eq. (4.32), we use $N_{\text{GP}} = 500$ metamodel realisations, and the number of Monte Carlo samples is set to $M = 10\,000$. We do not include bootstrapping here. The uncertainties in the estimates will be studied in the next section.

Fig. 4.7 presents the results for training sample set sizes $N = [10, \ldots, 200]$. The result confirms what we expected based on the scatterplots in the previous section: three parameters—namely the vascular permeability P^v, the killing coefficient γ^t_{kill}, and the hydraulic conductivity of the blood-vessel wall L^v_p—have considerably higher first-order Sobol indices than the remaining three parameters. Fig. 4.7 also allows to assess the convergence of the Sobol indices for an increasing number of training samples: even small sizes of training sample sets yield values close to the value based on $N = 200$. This is due to the high values of the respective Nash–Sutcliffe efficiency, as discussed in the previous section. Those results are promising, in particular for models that are computationally very expensive, and thus do not allow a large number of evaluations of the full model: the computational cost of the demonstrated approach is considerably reduced compared to an analysis based directly on evaluations of the full model, as for example presented in [31, 319] for tumour growth models.

We assessed convergence visually based on Fig. 4.7. In addition, [320] present a thorough definition of convergence criteria for global sensitivity analysis results. Nevertheless, the computationally limiting factor is usually the number of Monte Carlo samples. Since we evaluate the Monte Carlo samples on the GP metamodel, this limitation is less critical in the presented workflow. If sampling

Table 4.2 First and total-order Sobol indices based on 200 training samples. We use $M = 10\,000$ Monte Carlo samples, $N_{\mathrm{GP}} = 500$ realisations of the Gaussian process, and $B = 300$ bootstrap samples.

Parameter	S^i	S^{Ti}
L_p^v	0.092	0.121
P^v	0.600	0.632
$D^{\mathrm{NP}\ell}$	0.001	0.004
$\left(L_p \frac{S}{V}\right)^{\mathrm{ly}}$	0.009	0.011
γ_{kill}^t	0.265	0.270
γ_{kill}^h	0.000	0.000
Sum	**0.967**	

the realisations of the metamodel for very large numbers of Monte Carlo samples becomes an issue, Le Gratiet *et al.* [52] include an efficient approach based on conditional GPs.

4.3.4 Uncertainties of Sobol index estimation

We now go on to not only estimate the mean $\bar{S}^i$ but also include the uncertainty related to the metamodel and to the Monte Carlo integration given by Eqs. (4.35) and (4.36). In addition to the first-order index S^i, we also include the total-order Sobol index S^{Ti}. Again, we use different training sample set sizes $N = [10, \ldots, 200]$ and a tensorised, squared, exponential covariance function with hyperparameters optimised based on maximising the log marginal likelihood of the GP. We draw $N_{\mathrm{GP}} = 500$ realisations of the GP, $B = 300$ bootstrap samples, and $M = 10\,000$ Monte Carlo samples. We calculate 95% confidence intervals on the basis of the variance related to the metamodel $\hat{\sigma}^2_{\mathrm{GP}}$ and the variance related to Monte Carlo integration $\hat{\sigma}^2_{\mathrm{MC}}$.

Fig. 4.8A presents the results for all six input parameters. Note the different scaling on the vertical axes. We first take a look at the results for the indices themselves. Fig. 4.8A again confirms that even for small numbers of training samples, the estimates for first and the total-order Sobol indices rapidly converge. As mentioned above, we do not expect any influence of the parameter γ_{kill}^h on the quantity of interest. Fig. 4.8A shows that we can identify this non-influential parameter as such even for small numbers of training samples. The parameter $D^{\mathrm{NP}\ell}$ also leads to Sobol indices close to zero for $N < 60$. For larger training sample set sizes however we get a slightly higher total-order Sobol index, which is nevertheless small. Hence, we can clearly separate the three most influential parameters from the three non-influential parameters.

Moreover, the total-order index is higher than the first-order index, in particular for the hydraulic conductivity of the blood-vessel wall L_p^v and the vessel wall permeability P^v. This leads to the conclusion that higher-order effects are indeed present. We will therefore analyse the second-order Sobol indices in the next section. In addition, Table 4.2 summarises the values for the first and the total-order indices for 200 training samples: the sum of all first-order Sobol indices is 0.967. Since this is close to one, we conclude that higher-order effects are present, but only play a minor role. The largest part of the output variance is covered by the first-order indices.

We now focus on the uncertainties: we assess the uncertainty related to the GP metamodel and the total uncertainty, where the latter includes both sources of uncertainty (related to Monte Carlo integration and related to the metamodel). For small training sample set sizes, we see considerable uncertainty related to the metamodel (depicted in light blue/orange in Fig. 4.8A). However, the uncertainty related to Monte Carlo integration dominates for $N > 40$. We therefore present the uncertainty related to the metamodel in detail in Fig. 4.8B: the uncertainty rapidly decreases as the number of training samples increases for both the first-order and the total-order index and becomes one order of magnitude smaller than the uncertainty related to Monte Carlo integration. Hirvoas *et al.* [273] also found the uncertainty related to the GP metamodel to be much smaller than the uncertainty related to Monte Carlo integration in their example. The total uncertainty (depicted in grey) could be reduced even further by increasing the number of Monte Carlo samples.

Based on these results, we conclude that including the uncertainty related to the metamodel is not absolutely necessary in our example. However, the example presented in the outlook and the example presented by Le Gratiet *et al.* [52] illustrate that this is not always the case: only taking into account the Monte Carlo uncertainty might then underestimate the confidence interval. In such cases, it is essential to consider the uncertainty related to the metamodel. Hence, this largely depends on the model, the input parameters, and the quantity of interest, and no *one-size-fits-all* rule can be given.

Nevertheless, even taking into account the metamodel and the Monte Carlo uncertainty may incorrectly estimate the confidence intervals: poor optimisation of the hyperparameters may result in underestimated or overestimated confidence intervals. In such cases, one could additionally consider the uncertainty related to the estimation of the hyperparameters of the GP covariance function by using a full-Bayesian approach with hyperpriors [52].

To sum up, the demonstrated workflow not only identifies parameters with a high first-order Sobol index (necessary for factor prioritisation) but also parameters with a small total-order Sobol index (necessary for factor fixing). In both cases, small numbers of training samples suffice in our example.

4.3.5 Second-order Sobol index estimation

Since we concluded from the results in the previous sections that higher-order effects are indeed present in our example, the goal now is to estimate the second-order Sobol indices, and thereby identify interaction effects between the input parameters. The results in the previous section show that the uncertainty related to Monte Carlo integration is dominant, and the uncertainty related to the GP metamodel is much smaller. We therefore estimate the second-order indices based on the predictive mean $m_{\mathrm{GP},N}(\boldsymbol{X})$ of the GP and do not take into account the uncertainty related to the metamodel. Thus, we estimate the second-order Sobol indices as

$$\hat{S}^{ij} = \frac{\frac{1}{M}\sum_{m=1}^{M} m_{\mathrm{GP},N}(\boldsymbol{B}_{\boldsymbol{A}}^{(i)})_m \, m_{\mathrm{GP},N}(\boldsymbol{A}_{\boldsymbol{B}}^{(j)})_m - m_{\mathrm{GP},N}(\boldsymbol{A})_m \, m_{\mathrm{GP},N}(\boldsymbol{B})_m}{\mathcal{V}[m_{\mathrm{GP},N}([\boldsymbol{A}\ \boldsymbol{B}])]} - \hat{S}^i - \hat{S}^j, \tag{4.40}$$

which includes estimating the first-order effects $\hat{S}^i$ and $\hat{S}^j$ also based on the mean of the GP only.

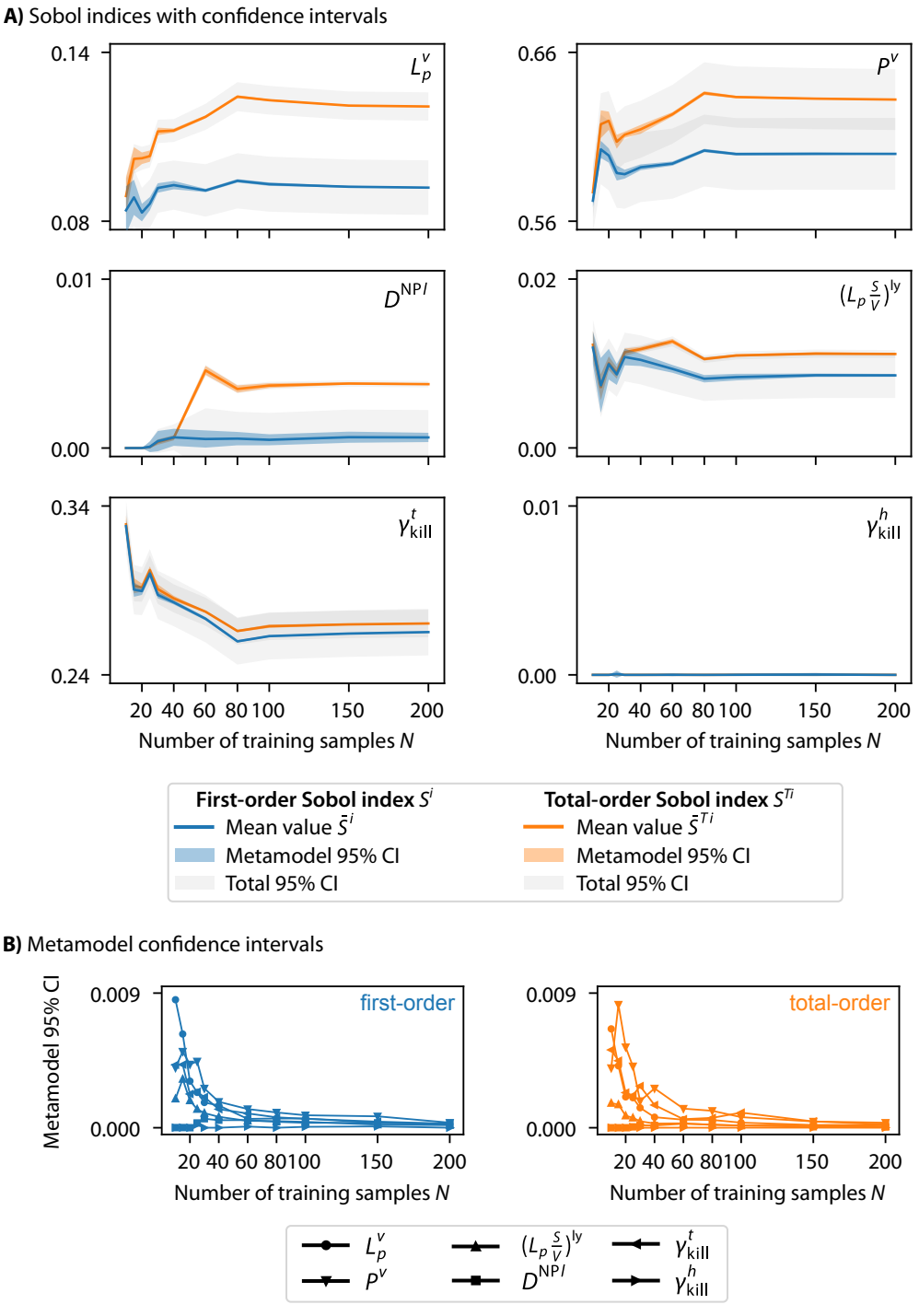

Figure 4.8 First-order and total-order Sobol indices and 95% confidence intervals (CI) for an increasing number of training samples. We use $M = 10\,000$ Monte Carlo samples, $N_{GP} = 500$ realisations of the Gaussian process, and $B = 300$ bootstrap samples. A) Sobol indices with metamodel CI and the sum of metamodel and Monte Carlo CI for the six input parameters separately. Monte Carlo abbreviates as MC. B) Detailed view of the metamodel CI. This figure is taken from [61], where it is licensed under CC BY 4.0.

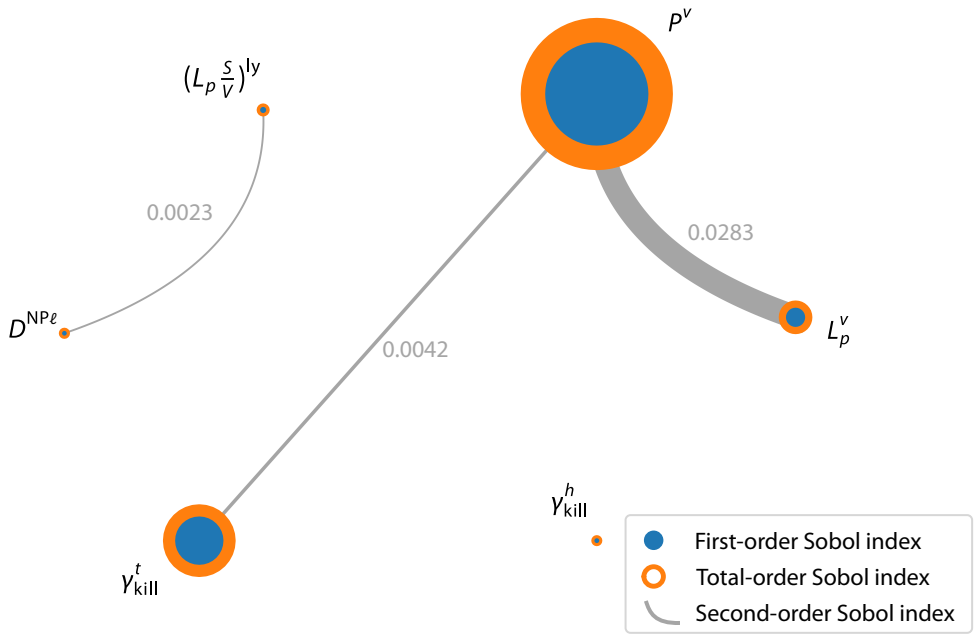

Figure 4.9 Second-order Sobol indices $\hat{S}^{ij}$ for $M = 1\,000\,000$ Monte Carlo samples and $B = 300$ bootstrap samples. The blue circles represent the first-order Sobol indices. The orange surrounds represent the total-order Sobol indices. The grey areas connecting the nodes represent the second-order Sobol indices. All other second-order indices are $\hat{S}^{ij} < 0.001$. This figure is taken from [61], where it is licensed under CC BY 4.0.

Table 4.3 Second-order Sobol indices for $B = 300$ bootstrap samples. All other second-order indices are $S^{ij} < 0.001$.

Parameter i	**Parameter** j	$M = 10\,000$		$M = 1\,000\,000$	
		S^{ij}	95% CI	S^{ij}	95% CI
L_p^v	P^v	0.0276	0.0198	0.0283	0.0021
L_p^v	$D^{\text{NP}\ell}$	−0.0009	0.0136	0.0003	0.0016
L_p^v	γ_{kill}^t	−0.0004	0.0142	0.0007	0.0017
P^v	γ_{kill}^t	0.0036	0.0312	0.0042	0.0030
$(L_p \frac{S}{V})^{\text{ly}}$	$D^{\text{NP}\ell}$	0.0021	0.0037	0.0023	0.0004

Using the same number of Monte Carlo samples as before ($M = 10\,000$), however, results in a 95% confidence interval with the same order of magnitude as the indices themselves and even leads to negative values for the Sobol indices (as given in Table 4.3). Therefore, we increase the number of Monte Carlo samples to $M = 1\,000\,000$ to obtain reasonably small confidence intervals.

Table 4.3 and Fig. 4.9 summarise the results for the second-order Sobol indices: the highest interaction is present between P^v and L_p^v, as we already expected based on the results presented in Fig. 4.8. Summing up all first- and second-order Sobol indices results in 0.999. We thus (almost) completely apportioned the variance in the output to the input parameters, including interaction effects.

The large number of Monte Carlo samples necessary to estimate the second-order Sobol indices highlights the relevance of metamodel-based estimation approaches. Evaluating the full model f

several million times is computationally prohibitive for most models. Without using a metamodel, estimating higher-order Sobol indices is thus impossible in most cases.

4.4 Outlook to other complex models in the context of biomechanics and beyond

In the previous sections, we assessed the performance of the workflow as applied to a model of nanoparticle-mediated drug delivery in great detail: even small numbers of training samples result in reliable estimates of the Sobol indices and a small uncertainty related to the GP metamodel. To give an outlook, we now apply the workflow to other complex models in the context of biomechanics and beyond.

Arterial growth and remodelling. As a first example, we consider a homogenised, constrained mixture model of arterial growth and remodelling [321–323]. This example was published as part of the author's publication [61].

Brandstaeter *et al.* [324] performed an exhaustive global sensitivity analysis, where they estimated the first- and total-order Sobol indices by evaluating the full model for all Monte Carlo samples. However, this entails a large computational burden (> 70 000 model evaluations). Therefore, the question arises as to whether we can reduce this computational cost by using a GP metamodel and still get reliable Sobol index estimates, including reliable uncertainty estimates.

For this comparison, we investigate *Case 2* of the original publication [324], where the maximum diameter of an idealised cylindrical abdominal aorta was studied 15 years after spontaneous damage to elastin. In this case, the majority of samples lead to minor dilatation of the vessel $d_{\text{max}} < 3$ cm. In contrast, a considerable number of samples do not stabilise and keep enlarging, leading to aneurysms with a much larger diameter $d_{\text{max}} >> 3$ cm (see Fig. 4b in [324]). We use the original results from [324] as a reference and compare them to our results based on the metamodel approach.

First, we look at the GP metamodel's predictive quality. Once again, we use a tensorised, squared, exponential covariance function and compare the results for different numbers of training samples, $N = [40, 60, 80, 100, 150, 200, 300, 500]$ in this case. As an example, Fig. 4.10A presents the training samples for $N = 300$ for two parameters. The results for the remaining parameters are included in the Supplement of [61]. We see that the majority of samples result in a small dilatation in contrast to the fewer aneurysmatic samples with a very large diameter of up to 8 cm. This bimodal structure of the data makes training the GP metamodel more difficult compared to our previous example.

Second, we calculate the first- and total-order Sobol indices and respective uncertainties for different numbers of training samples. To this end, we use $M = 10\,000$ Monte Carlo samples, $N_{\text{GP}} = 500$ realisations of the GP metamodel, and $B = 300$ bootstrap samples. By way of example, we present the results for two parameters, the gain parameter $\bar{k}_\sigma$ and the initial volume fraction of elastin $\phi^{\text{el}}_{t_0}$, in Fig. 4.10C. For the gain parameter $\bar{k}_\sigma$, the estimates based on the metamodel converge to the reference values from [324] for both the first- and the total-order Sobol index. For the initial volume fraction of elastin $\phi^{\text{el}}_{t_0}$, the reference values for the Sobol indices are very small (0.01 or smaller). In

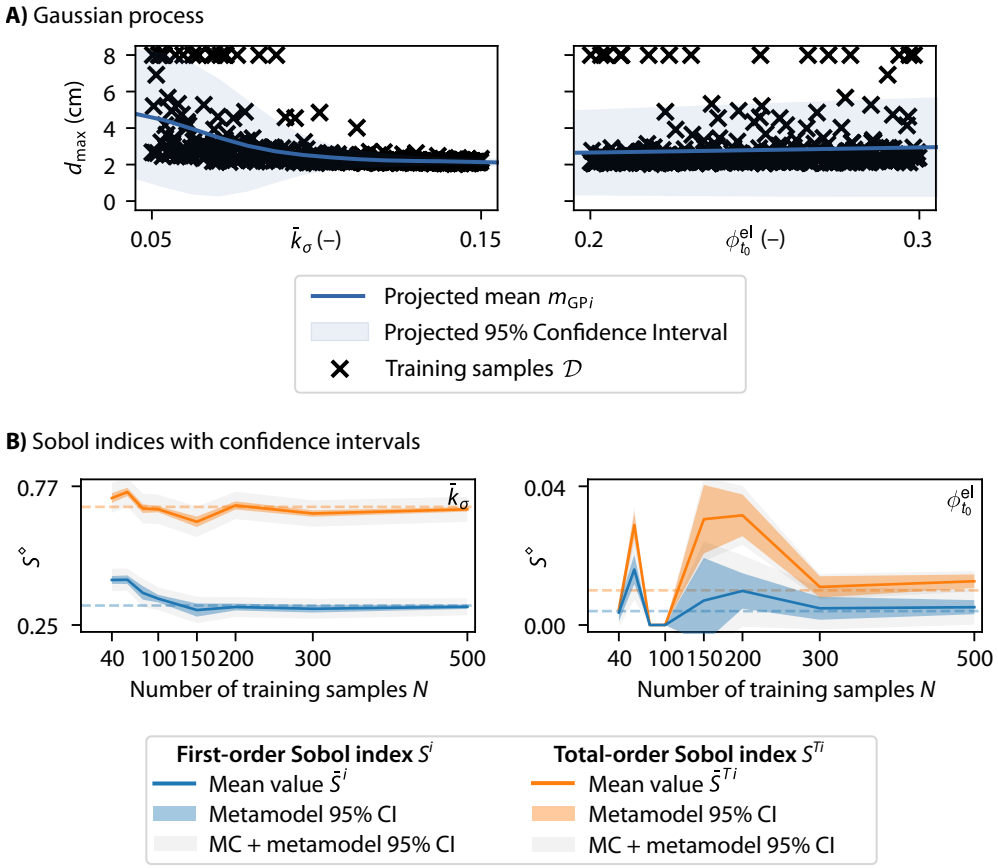

Figure 4.10 Arterial growth and remodelling model example. A) Gaussian process. Projected mean $m_{GPi}(X_i)$, projected 95% confidence interval (CI) and training samples $\mathcal{D}$ for the diameter d_{max} (the y-axis labels apply to both figures). B) First-order and total-order Sobol indices and 95% confidence intervals (CI) for an increasing number of training samples. Monte Carlo abbreviates as MC. This figure is taken from [61], where it is licensed under CC BY 4.0.

this case, exact estimates based on the metamodel approach are much harder to achieve: for $N \leq 300$ training samples the estimates only stabilise. Nevertheless, we can still reliably separate the three most influential parameters from the non-influential parameters, even for small numbers of training samples (see the Supplement of [61]). One further detail should be mentioned as an example: the plot for $\phi^{\mathrm{el}}_{t_0}$ reveals problems in estimating the first and total-order Sobol indices for $N = 80$ or 100. The Sobol indices and the uncertainties are all close to zero. For $N < 300$, the GP has not yet converged and hence does not capture all features of the quantity of interest. Furthermore, we note that the uncertainty related to the metamodel is much higher and in some cases even dominates the total uncertainty in this example, while the uncertainty related to Monte Carlo integration dominated the previous example. It is therefore important to include the uncertainty related to the metamodel because considering only the uncertainty related to Monte Carlo integration would underestimate the total uncertainty in the Sobol index estimate.

Finally, the computation of higher-order indices was not feasible with the approach chosen in the original contribution [324]. In contrast, the following will show that the metamodel-based approach enables their computation. As an example, we again consider the gain parameter $\bar{k}_\sigma$: a closer look at Fig. 4.10C reveals that the total-order index is considerably higher than the first-order index: $S^{T\bar{k}_\sigma} - S^{\bar{k}_\sigma} = 0.34$. This delta indicates interactions with other parameters, and thus estimating the second-order indices is of particular interest for this example. Since we see in Fig. 4.10C that the metamodel contributes significantly to the total uncertainty, we include uncertainty estimates for the metamodel (as opposed to relying solely on the predictive mean, as in the previous second-order estimates). The estimates indeed show interaction with two parameters: the turnover time[10] τ and the constitutive parameter k_2 ($S^{\bar{k}_\sigma \tau} = 0.19$ and $S^{\bar{k}_\sigma k_2} = 0.06$). However, the sum of all second-order indices ($S^{\bar{k}_\sigma j} = 0.25$) still does not cover the delta between the first and total-order index. Hence, we specifically estimate the third-order Sobol index for the three most influential parameters, $\bar{k}_\sigma$, τ, and k_2, resulting in considerable third-order interaction: $S^{\bar{k}_\sigma \tau k_2} = 0.06$.

Thus, we can identify influential parameters for factor prioritisation based on the metamodel approach with small numbers of training samples, and we can also separate the influential parameters from the non-influential ones. Hence, the metamodel-based approach provides the same results as the approach based directly on the full model in the original publication [324]. The computational cost, i.e., the number of evaluations of the full model, however, is much lower when using a metamodel. Additionally, we can quantify higher-order indices, which is infeasible based on evaluations of the full model.

Reduced-dimensional lung. We further apply the metamodel-based sensitivity analysis workflow to a reduced-dimensional lung model, including alveolar recruitment/derecruitment dynamics. This work was part of a student term paper by D. Rudlstorfer [325], co-supervised by the author of this thesis together with C. Geitner.

Based on Geitner *et al.* [326], we investigate alveolar recruitment/derecruitment based on the pressure- and time-dependent variation of the stress-free reference volume to capture fully collapsed, poorly aerated and normally ventilated terminal units. The alveolar recruitment/derecruitment

[10] The turnover time was denoted by T in the original publication [324].

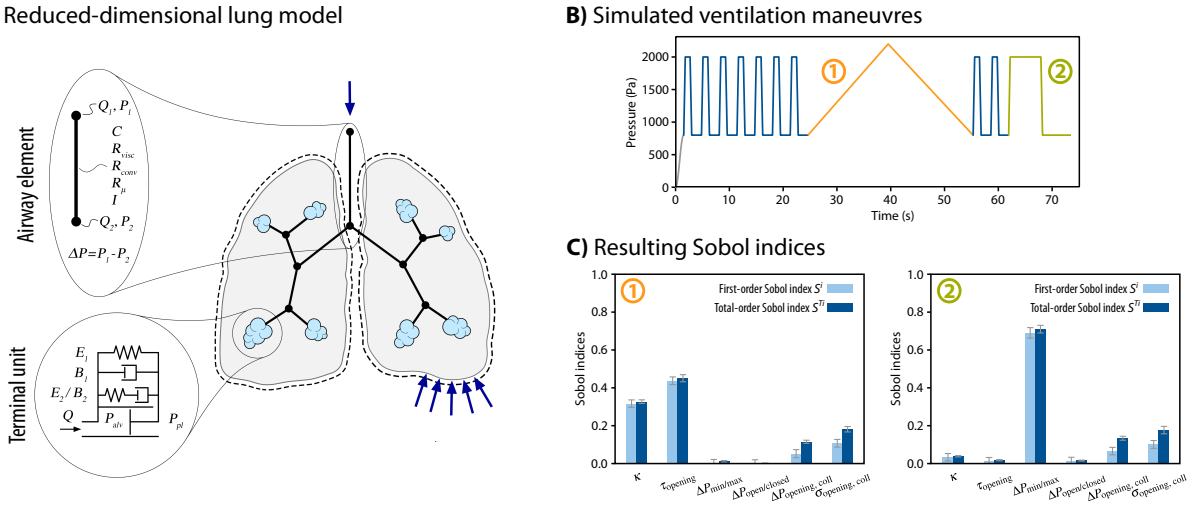

Figure 4.11 Reduced-dimensional lung model example. A) Schematic overview of the reduced-dimensional lung model. B) Simulated ventilation maneuvres, including the quasi-static inflation manoeuvre (orange) and the inspiratory hold manoeuvre (green). C) First-order and total-order Sobol indices and 95% confidence intervals for the volume increase during a quasi-static inflation manoeuvre (1) and the volume increase during an inspiratory hold manoeuvre (2). The subfigures are adapted from [325].

model is included in a comprehensive multi-compartment reduced-dimensional model of an injured human lung, depicted schematically in Fig. 4.11A. To use this model in a clinical setting, we need to be able to determine the model parameters based on patient-specific clinical data, e.g., medical image data or artificial ventilation data. Since this parametrisation should be feasible with a reasonable effort, this presents a classical scenario for sensitivity analysis: we need to identify the most influential parameters, which need to be determined patient-specifically, and separate them from the non-influential parameters, which can be set to population average values.

We consider six uncertain input parameters and two quantities of interest: the volume increase during a quasi-static inflation manoeuvre and during an inspiratory hold manoeuvre (see Fig. 4.11B). Similar to the tumour example in the previous sections, a relatively small number of training samples ($N = 100$) is sufficient to obtain a good predictive quality of the Gaussian process, i.e., a Nash–Sutcliffe efficiency of $Q^2 > 0.9$ for both quantities of interest. Interestingly, the most influential parameters of the quasi-static inflation manoeuvre are non-influential during the inspiratory hold manoeuvre and vice versa (see Fig. 4.11C)—a valuable insight for the parametrisation of the model.

When manually calibrating the model, as presented in [326], difficulties are often encountered when trying to fit a quasi-static inflation manoeuvre and an inspiratory hold manoeuvre simultaneously. The sensitivity analysis results suggest that fitting to both maneuvres is indeed necessary to obtain the best patient-specific fit. However, the parameters can be fitted separately to the two maneuvres.

Beyond biomechanics: Powder bed fusion additive manufacturing. To further demonstrate that a carefully performed global sensitivity analysis is generally an integral part to ensure the high quality of any model development, we apply a global sensitivity analysis to a model of powder bed fusion

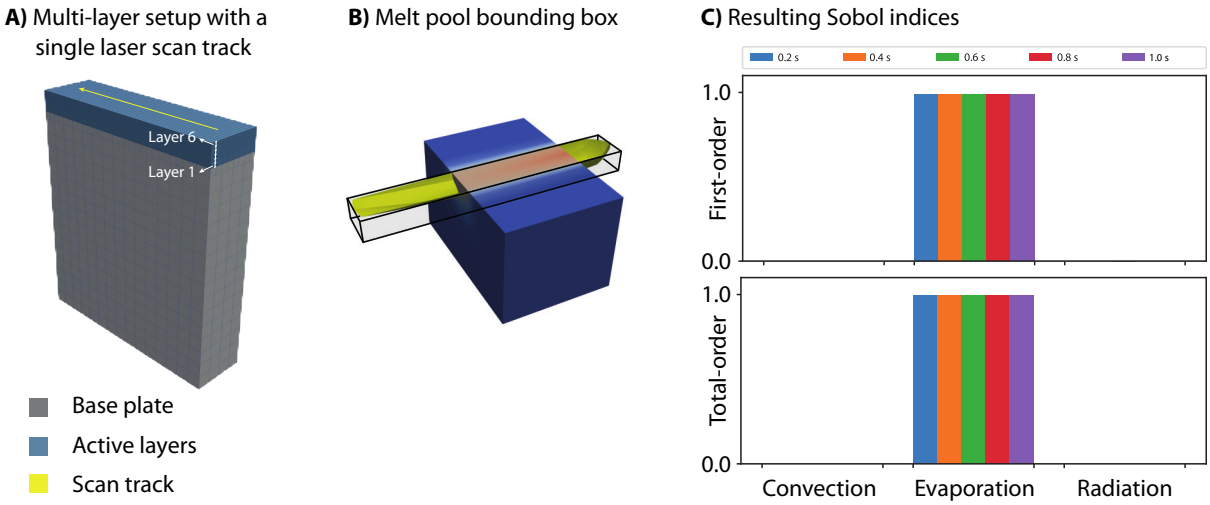

Figure 4.12 Powder bed fusion additive manufacturing (PBFAM) model example. A) Multi-layer PBFAM setup with a single laser scan track. B) Melt pool bounding box volume used as the quantity of interest. C) First- and total-order Sobol indices. The subfigures are adapted from [327].

additive manufacturing (PBFAM). This work was part of the Bachelor's thesis by M. Waldmann [327], co-supervised by the author of this thesis together with S. Proell.

Proell *et al.* [328] developed a highly efficient computational approach to predict the temperature field during PBFAM and assumed that a convection boundary condition has a negligible influence on the temperature field compared to the radiation and the evaporation boundary conditions. This assumption was based on qualitative observations and experience with the model. Therefore, we perform a global sensitivity analysis to quantify the influence of the convection boundary condition. As depicted in Fig. 4.12A, we consider a simplified setup with a single laser scan track repeated on six powder layers. The base plate serves as a main heat sink for the energy input by the laser needed to melt the powder. The quantity of interest is chosen as the melt pool bounding box volume, as depicted in Fig. 4.12B. Notably, the highly efficient approach presented by Proell *et al.* [328] enables the estimation of the Sobol indices based on the full model, i.e., without using a metamodel.

The estimated Sobol indices indeed confirm that the convection boundary condition has a negligible influence on the melt pool bounding box volume in the investigated parameter range and considered setup, as shown in Fig. 4.12C. In addition, the results also reveal that the radiation boundary condition has a negligible influence on the melt pool bounding box volume and that (almost) the entire variance in the melt pool bounding box volume is due to the evaporation boundary condition alone. We expected the other two boundary conditions to increase in importance for bigger setups. However, all setups considered in [327] are highly dominated by the evaporation boundary condition. Possible hypotheses that could explain this unexpected result include the following: the investigated setup might be too small and should be increased in size (up to 1000 layers); or the melt pool bounding box volume might not be the most expressive quantity of interest to investigate the influence of the boundary conditions, or the model indeed behaves differently than expected or does not capture the influence of the boundary conditions correctly. This insight highlights the relevance

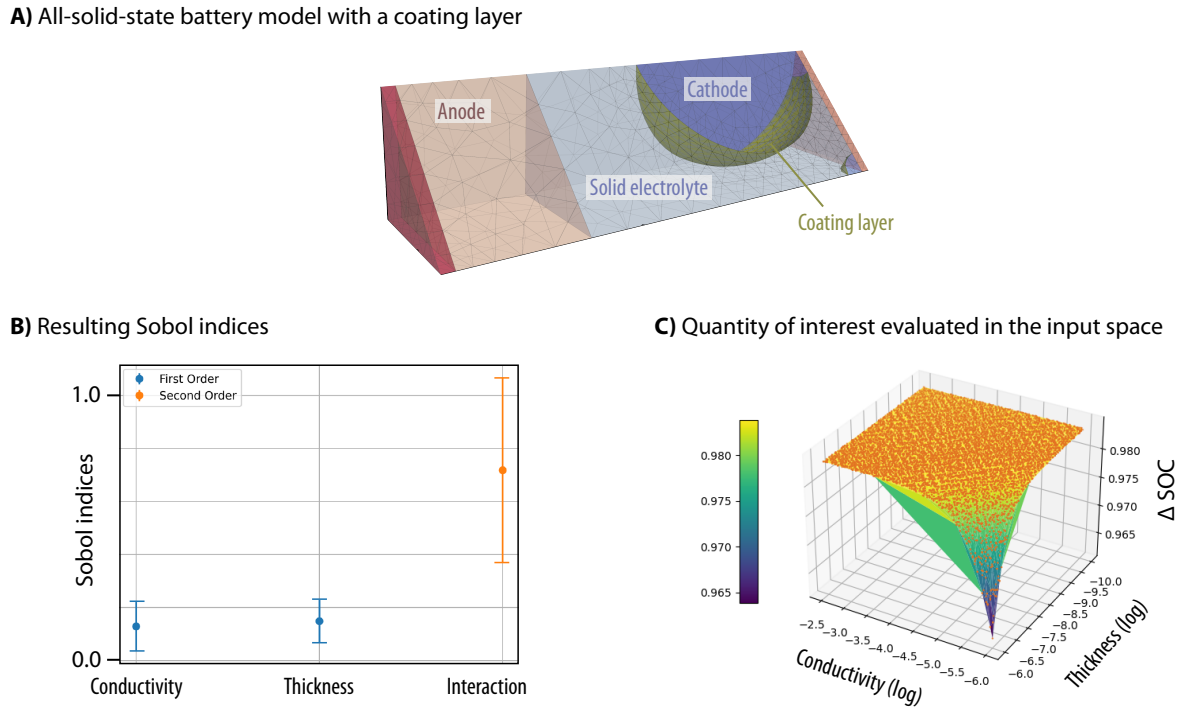

Figure 4.13 All-solid-state battery model example. A) Simplified geometric representation of a microstructure of a battery cell. B) First- and second-order Sobol indices and 95% confidence intervals. C) Quantity of interest ΔSOC evaluated in the input space. The subfigures are adapted from [329].

of a global sensitivity analysis to guide further model development and contribute to an improved understanding of the model and underlying physics.

Beyond biomechanics: All-solid-state batteries. Finally, we apply a global sensitivity analysis to an electrochemo-mechanical model for all-solid-state batteries (ASSBs). This work was part of a student term paper by A. Wendl [329], co-supervised by the author of this thesis together with S. Sinzig.

Sinzig *et al.* [330] developed a novel approach to capture ion transport in the coating layer of active material particles in ASSBs embedded into a three-dimensional electrochemo-mechanical continuum model. The question is how the thickness and ionic conductivity of the coating layer influence the usable capacity of the battery (ΔSOC, with SOC abbreviating *state of charge*). To this end, we perform a global sensitivity analysis on a simplified geometry, as depicted in Fig. 4.13A. Again, we do not use a metamodel and estimate the Sobol indices based on the full model.

The results of the sensitivity analysis, presented in Fig. 4.13B, reveal that the interaction between the thickness and ionic conductivity dominates, i.e., the second-order index is considerably higher than the first-order indices of both parameters. However, the confidence interval of the second-order index is large. It could be reduced by increasing the number of Monte Carlo samples—which is computationally prohibitive in this case, especially considering the convergence rate of Monte Carlo integration being $\mathcal{O}(1/\sqrt{N})$ and the fact that the current geometry is already highly simplified. Hence,

this presents an example where a metamodel-based approach would be beneficial to overcome the computational limitation. However, a closer look at the quantity of interest ΔSOC in the parameter space, shown in Fig. 4.13C, reveals a highly non-linear behaviour, which makes training a Gaussian process more complex compared to the previous example in Section 4.3.

4.5 Conclusion

Since a global sensitivity analysis is computationally expensive, modellers often rely on local methods alone, which may be inadequate [50]. The use of a metamodel-based approach, however, allows a global variance-based sensitivity analysis to be performed, even for computationally expensive biomechanical models with a moderate number of input space dimensions at a manageable computational cost. The number of training samples required to obtain reliable estimates for the Sobol indices depends largely on the problem set-up itself: our results demonstrate that we can identify the most influential input parameters and separate them from non-influential parameters with small numbers of training samples. However, quantifying the exact value of the Sobol indices requires more training samples. Moreover, the approach is able to quantify the uncertainty related to the metamodel: including this uncertainty is important, because considering only the uncertainty related to Monte Carlo integration could underestimate the total uncertainty in the Sobol index estimates. The metamodel-based approach also allows an estimation of higher-order Sobol indices, and thus a quantification of interaction effects, which is not feasible without a metamodel due to the computational costs involved. While there is no *one-size-fits-all* rule, the approach is general and efficient enough to allow a study of different aspects of sensitivity analysis, including a transparent declaration of the uncertainties involved in the estimation process.

We demonstrated how a rigorous global sensitivity analysis can be applied to complex, computationally expensive problems. A carefully performed sensitivity analysis is generally an integral part to ensure the high quality of any model development [50]. By demonstrating the workflow and its application for biomechanical problems, we contribute to closing the gap between proposals of new sensitivity analysis methods and application papers [267]. We hereby encourage sensitivity analysis in general and the metamodel-based approach in particular in the biomechanics community. In the big picture of model development, the presented workflow can be a building block towards inverse analysis, or it can be a valuable tool to better understand the model itself.

5 Bayesian inverse analysis

The following Sections 5.1, 5.2, 5.3, 5.4 and 5.6 are largely based on the author's publication S. Hervas-Raluy*, B. Wirthl*, P. E. Guerrero, G. Robalo Rei, J. Nitzler, E. Coronado, J. F. de Mora Sainz, B. A. Schrefler, M. J. Gomez-Benito, J. M. García-Aznar and W. A. Wall. 'Tumour Growth: An Approach to Calibrate Parameters of a Multiphase Porous Media Model Based on in Vitro Observations of Neuroblastoma Spheroid Growth in a Hydrogel Microenvironment'. *Computers in Biology and Medicine* 159 (2023), 106895 [62], which is licensed under CC BY-NC-ND 4.0. *Co-first authorship

5.1 Introduction

The synergy between experimental and computational tools provides powerful opportunities: *in silico* models are a helpful tool for simulating complex experiments, improving our understanding of *in vitro* scenarios, and trialling new ideas in the computational environment prior to *in vitro* experiments. Indeed, the calibration and validation of mechanical models based on experimental data and the quantification of the associated uncertainties are integral to scientific activity, especially in a medical context. While computational models have widened their horizons dramatically in recent years, it is crucial to be able to calibrate these models so that relevant patient-specific predictions can be made. In order to do this, the model parameters have to be determined. Some parameters can be measured directly. Since however a direct measurement of most parameters is not possible, they have to be estimated by inverse analysis. There are two general approaches to solving the inverse problem: deterministic and probabilistic. While deterministic optimisation techniques yield a point estimate for the best fit, Bayesian methods infer the entire probability distribution, including the uncertainty, which is especially important in a medical setting. Since most models contain a large number of uncertain parameters, which have to be calibrated, it is first necessary to identify the most influential parameters and to distinguish them from non-influential parameters using sensitivity analysis.

Subsequent calibration then focuses on the most relevant parameters. In the context of tumour-growth modelling, several groups have made some advances in this direction. Hawkins-Daarud *et al.* [331] laid out a Bayesian framework for calibration, validation and uncertainty quantification of tumour-growth models considering synthetic data, and Collis *et al.* [332] presented the Bayesian calibration of a simple Gompertzian tumour-growth model as a tutorial. Furthermore, Urcun *et al.* [333] used a similar methodology to analyse the effect of mechanical forces on tumour growth,

and Lima *et al.* [334] performed a Bayesian calibration of a stochastic, multiscale agent-based model based on two-dimensional (2D) cell cultures of human breast carcinoma cells.

So far, the tumour growth model presented in this thesis has been very generic and has not been adapted to a specific tumour type. This chapter now focuses on a specific tumour type: neuroblastoma, literally defined as an immature (*blast*) tumour (*oma*) of the nervous system (*neuro*) [335]. Neuroblastomas typically occur in very young children and are rare in adults; the median age of diagnosis is 17 months [336]. Neuroblastoma is by far the most common cancer of infancy (age <12 months): the incidence rate is almost twice that of leukaemia, the second most common malignancy in the first year of life [335, 337–339]. The primary tumour is usually located in the adrenal glands, inside the abdominal cavity, with metastasis frequently appearing in bone and bone marrow, liver, lymphatic nodes, and, in very infants, even in the eyes or skin [335, 340]. Neuroblastomas exhibit unique clinical features, including spontaneous regression, but also a high frequency of metastatic disease at diagnosis. In fact, in 60–70% of cases, the tumour has already metastasised at the time of diagnosis [341]. While infants with low-risk diseases typically have a favourable prognosis of >90% survival, the 5-year survival rate of patients with high-risk diseases is below 40%, despite aggressive treatment [342, 343].

To mimic the morphological and functional features of *in vivo* neuroblastomas within a controlled environment, multicellular tumour spheroids are grown *in vitro* [344]. To create a three-dimensional (3D) microenvironment, we use collagen-based hydrogels: these collagen gels make it possible to produce matrices with different mechanical properties depending on their composition and preparation methods. There have been several recent attempts to replicate the first stages of tumour formation [344–347]. Microfluidic techniques enable such miniaturisation of tumour growth [348]. Constraining the system to a small scale ensures better control of the environmental conditions. The main advantage of this approach is its ability to recreate more realistic biological environments than traditional *in vitro* 2D cell cultures [348–350]. 3D cell culture models are able to reproduce features such as tumour architecture and metabolism, unlike 2D cultures.

In this chapter, we perform a Bayesian calibration of 3D neuroblastoma spheroid growth based on our multiphase porous-media model and experimental data (see Fig. 5.1). The main contribution to the state-of-the-art is the combination and integration of experimental and computational techniques to achieve a validated model of tumour growth, which is an essential area for future progress in the field but, so far, only sparsely covered. To this end, we combine *in-vitro* experiments of spheroid growth in a 3D collagen-based porous hydrogel with a matching multiphase porous-media model setup so that both adequately include the interaction of the tumour with its microenvironment. The integration of both models is built on a unique approach based on a Bayesian calibration process, which naturally incorporates the uncertainties associated with the calibration process.

In Section 5.2.1, we summarise the 3D neuroblastoma spheroids experiments performed in microfluidic devices. Next, as introduced in Section 5.2.2, we perform a time-dependent global sensitivity analysis to identify the relative importance of the model parameters, where we again use the Sobol method [48, 49] combined with a Gaussian process as a metamodel, as presented in Chapter 4. We then feed the results of the sensitivity analysis into a Bayesian calibration process based on sequential Monte Carlo (SMC) methods [55, 351] to infer the posterior density of the most

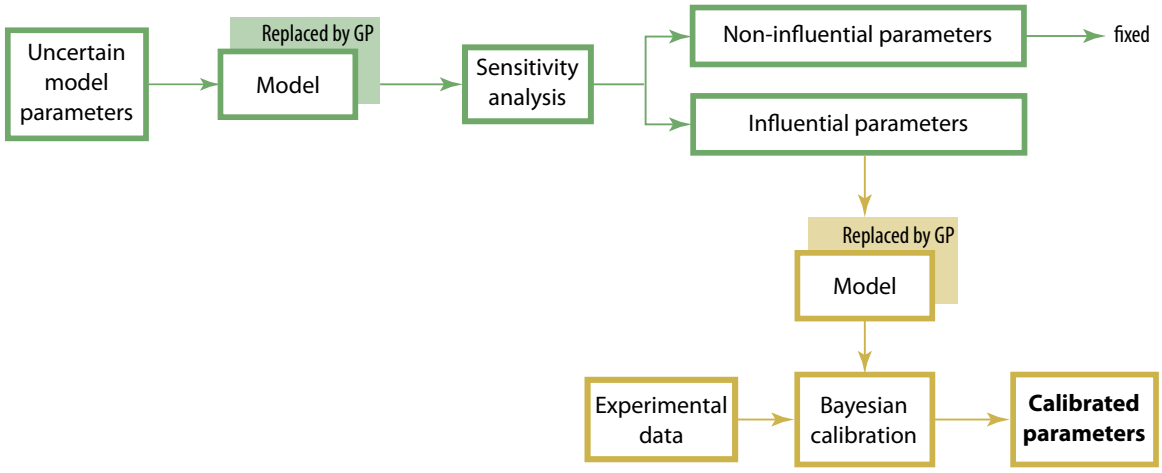

Figure 5.1 Workflow to calibrate the uncertain model parameters based on experimental data. The uncertain model parameters are first analysed by a global sensitivity analysis, where the model is replaced by a Gaussian process (GP). The sensitivity analysis determines which parameters are non-influential and which have a significant influence on the selected quantity of interest, in this case the spheroid volume. The non-influential parameters are fixed, whereas the influential ones are further calibrated by the Bayesian framework. In this part, the model is again replaced by a Gaussian process, and the influential parameters are calibrated together with the experimental behaviour observed in the microfluidic devices. This picture is taken from [62], where it is licensed under CC BY-NC-ND 4.0.

influential parameters from the experimental data (see Section 5.2.3). The findings of the study are summarised in Section 5.3 and discussed in Section 5.4. Finally, we give an outlook on coupled multi-physics observations in Section 5.5 and draw a conclusion in Section 5.6.

5.2 Methods

5.2.1 Experimental setup

In the following, we concisely summarise the experimental setup. The experiments were performed by our collaborators at the University of Zaragoza (Spain) and are described in more detail in [62].

Neuroblastoma primary culture was obtained from a patient's tumour at La Fe University and Polytechnic Hospital (Valencia, Spain), with the approval of the Ethics Committee of the hospital. The pathology department of the University of Valencia had diagnosed the patient with a poorly differentiated neuroblastoma with a deletion in chromosome 11q. The differentiation of a tumour describes the extent to which the tumour cells resemble their normal counterparts: while well-differentiated tumours resemble normal cells and are considered less aggressive, poorly differentiated tumours exhibit abnormal and immature cell features, making it difficult to determine the tumour's tissue of origin [352]. Often, poorly differentiated tumours are more aggressive and have a worse prognosis than well-differentiated tumours [335]. The deletion in chromosome 11q is a genetic alteration that is associated with a poor prognosis in neuroblastoma patients [353]. The tumour was surgically removed, and the remaining material was used for the preparation of the primary culture.

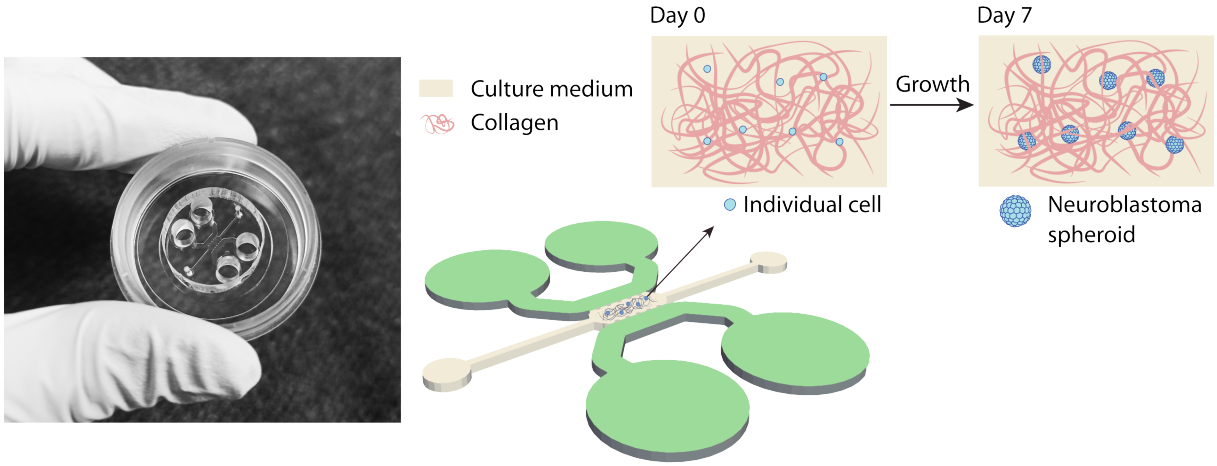

Figure 5.2 Microfluidic devices used for the analysis of 3D neuroblastoma spheroids. The image on the left shows the microfluidic device bonded to a glass plate. On the right is a 3D visualisation of the microfluidic chip system. Collagen hydrogel was loaded in the central chamber (light beige). The setup included two side media channels (green) to supply the culture media and ensure the hydration and transport of nutrients and other chemical factors throughout the hydrogel. Individual cells were seeded in the chamber and cultured for up to seven days. This figure is taken from [62], where it is licensed under CC BY-NC-ND 4.0.

The neuroblastoma cells were cultured in a 3D collagen-based hydrogel in microfluidic devices. The polydimethylsiloxane (PDMS)-based microfluidic devices were produced using the method described by Shin *et al.* [349]. The device geometry is illustrated in Fig. 5.2 and described in detail in Plou *et al.* [344]. The central chamber was filled with the hydrogel, prepared based on [349], and the device additionally included two side channels (each with two media reservoirs, marked in green in Fig. 5.2) for hydration and medium replacement to ensure the transport of nutrients and other chemical factors throughout the hydrogel. Individual tumour cells were homogeneously embedded in the 3D hydrogel in the chamber and cultured for up to seven days. The spheroid formation and growth were visualised and recorded every 24 hours.

5.2.2 Global sensitivity analysis

The sensitivity analysis aims to separate the (most) influential uncertain input parameters from the non-influential ones. We employ the workflow presented in Chapter 4 and again estimate the first- and the total-order Sobol indices using a Gaussian process as a metamodel.

The computational setup is the same as in Section 2.2.1. The quantity of interest is the volume V^t of the tumour spheroid over time, given by

$$V^t = \int \mathcal{H}(S^t - 0.1)\,\mathrm{d}\Omega, \tag{5.1}$$

where the tumour is defined as the part of the domain where the saturation of tumour cells is greater than 0.1 ($S^t > 0.1$). As the neuroblastoma spheroids observed in the experimental tests grow in tightly packed aggregates, we assume that a threshold of 0.1 is indicative of these particular experiments.

Table 5.1 Probability distributions of the uncertain input parameters. We assume that all parameters are distributed uniformly within the given range.

Symbol	Parameter	Range	Units	Ref.
k	Intrinsic permeability of the ECM	$[0.5;\ 1.5] \cdot 10^{-9}$	mm^2	[72, 354, 355]
ν	Poisson's ratio of the ECM	$[0.35;\ 0.48]$	–	[67, 356, 357]
G	Shear modulus of the ECM	$[120;\ 710]$	Pa	[89, 354, 358–361]
μ^s	Dynamic viscosity of the ECM	$[10;\ 35]$	Pa s	[89, 362, 363]
μ^t	Dynamic viscosity of the TC*	$[10;\ 1000]$	Pa s	[33, 364–370]
$\sigma_{t\ell}$	Interfacial tension	$[2;\ 50]$	Pa	[67, 371]
A_t	Rel. permeability exponent for TC	$[1;\ 10]$	–	[72]
A_ℓ	Rel. permeability exponent for medium	$[1;\ 7]$	–	[72]
γ^t_{growth}	Tumour-growth coefficient	$[0.1;\ 2.0] \cdot 10^{-8}$	$g/(mm^3 s)$	[67, 72, 171]
$\gamma^t_{\text{necrosis}}$	Necrosis coefficient of TC	$[1;\ 10] \cdot 10^{-9}$	$g/(mm^3 s)$	[67, 72, 171]
$\gamma^{nt}_{\text{growth}}$	Oxygen consumption due to growth	$[1;\ 5] \cdot 10^{-10}$	$g/(mm^3 s)$	[67, 72, 171]

* TC denotes the tumour cell phase.

From the myriad of model parameters, we identify those parameters whose values are known *a priori*, e.g., from the literature, experimental measurements, previous *in silico* studies, or expert knowledge: the initial tumour radius r_0 is obtained from the experimental images; the densities of the fluid phases (ρ^t and ρ^ℓ) and the ECM (ρ^s) are assumed to be equal to the density of water. In the experiments, nutrients are supplied daily to ensure they are available in sufficient concentration throughout the assay. In the computational model, we include oxygen as the only nutrient and assume that oxygen-related parameters ($\omega^{n\ell}_{\text{crit}}$, $\omega^{n\ell}_{\text{env}}$, $D^{n\ell}_0$ and δ) are known. All *a priori* known parameters are listed in Table A.1.

The remaining parameters are considered uncertain, and we estimate their influence on the quantity of interest V^t. Table 5.1 lists the eleven uncertain parameters: we assume a uniform distribution for all parameters and define the ranges based on values obtained from the literature. In particular, the ranges of the initial porosity ε_0 and the properties of the ECM (intrinsic permeability k, shear modulus G, Poisson's ratio ν and dynamic viscosity μ^s) are based on experimental results, where the role of the ECM was investigated [67, 72, 89, 354–363], and the dynamic viscosity of the tumour cell phase μ^t has been measured in numerous studies, producing values that vary over several orders of magnitude [33, 364–370].

5.2.3 Bayesian calibration

We favour a Bayesian approach to parameterise our computational tumour-growth model for several reasons. As stated above, the model contains uncertain input parameters for which we do not know the true value. Additionally, the true value itself may be uncertain, e.g., due to randomness in the underlying processes: probability distributions then characterise the uncertain input parameters instead of a single (fixed) value. When working with experimental data of biological systems, assuming that a certain degree of uncertainty is present (such as measurement error, model error or intrinsic variability) is necessary. Otherwise, the solution is overconfident or incorrect. Indeed,

uncertainty can also be found in computational modelling, e.g., by simplifying assumptions in the model formulation. Therefore, Bayesian techniques are deemed the most appropriate for performing model calibration since the approaches used are intrinsically able to characterise uncertainty [25].

Based on Bayes' rule [372], *a priori* knowledge about the uncertain parameters $\boldsymbol{\theta}$ of a model f is updated in the presence of the experimental data $\boldsymbol{y}_{\text{obs}}$ resulting in a posterior distribution $p(\boldsymbol{\theta}|\boldsymbol{y}_{\text{obs}})$ of the parameters as

$$p(\boldsymbol{\theta}|\boldsymbol{y}_{\text{obs}}) \propto p(\boldsymbol{y}_{\text{obs}}|\boldsymbol{f}(\boldsymbol{\theta}))\, p(\boldsymbol{\theta}), \tag{5.2}$$

where $p(\boldsymbol{\theta})$ is the prior distribution and $p(\boldsymbol{y}_{\text{obs}}|\boldsymbol{f}(\boldsymbol{\theta}))$ is the likelihood function.

The observations $\boldsymbol{y}_{\text{obs}}$ are the tumour-spheroid volumes obtained by the *in vitro* experiments over time. Here, we use N conditionally independent observations $\boldsymbol{y}_{\text{obs}} = \{\boldsymbol{y}_{\text{obs},i}\}_{i=1}^{N}$, with N being the number of observed tumour spheroids[11]. We assume an additive Gaussian noise $\boldsymbol{\epsilon}$ such that

$$\boldsymbol{y}_{\text{obs}} = \boldsymbol{f}(\boldsymbol{\theta}) + \sigma_N \cdot \boldsymbol{\epsilon} \quad \text{with} \quad \boldsymbol{\epsilon} \sim \mathcal{N}(\mathbf{0}, \mathbf{1}), \tag{5.3}$$

where $\mathcal{N}$ denotes the Gaussian distribution and σ_N the standard deviation [373].

Further, the *prior* distribution $p(\boldsymbol{\theta})$ encodes the uncertainty about the parameters before observing the data. The prior distribution is specified beforehand and represents the parameter information that we wish to include in the model calibration. It might represent the ignorance of a parameter or introduce a strong subjective belief [332]. As the prior distribution, we use the same distribution as in the global sensitivity analysis, i.e., a uniform distribution with the ranges given in Table 5.1.

The *likelihood* function $p(\boldsymbol{y}_{\text{obs}}|\boldsymbol{f}(\boldsymbol{\theta}))$ is a true probability density for the observations $\boldsymbol{y}_{\text{obs}}$, conditionally dependent on the parameters $\boldsymbol{\theta}$: it connects the experimental data to the computational model. In the context of Bayesian calibration, the likelihood function can be interpreted as a goodness-of-fit measure, i.e., how well the model output fits the experimental data, given a particular value for the input parameters [374]. Based on the additive Gaussian noise assumption (see Eq. (5.3)), the likelihood is given by

$$\begin{aligned} p(\boldsymbol{y}_{\text{obs}}|\boldsymbol{f}(\boldsymbol{\theta})) = \prod_{i=1}^{N} \mathcal{N}(\boldsymbol{y}_{\text{obs},i}|\boldsymbol{f}(\boldsymbol{\theta}), \sigma_N) = \\ \prod_{i=1}^{N} \frac{1}{\sqrt{2\pi}\sigma_N} \exp\left(-\frac{1}{2\sigma_N^2} \|\boldsymbol{y}_{\text{obs},i} - \boldsymbol{f}(\boldsymbol{\theta})\|^2\right), \end{aligned} \tag{5.4}$$

with $\|\cdot\|$ denoting the Euclidean L2-norm.

Finally, the *posterior* distribution $p(\boldsymbol{\theta}|\boldsymbol{y}_{\text{obs}})$ characterises the knowledge of the model parameters, having now observed the data. It is defined as a conditional distribution of the parameters $\boldsymbol{\theta}$, given the data $\boldsymbol{y}_{\text{obs}}$. The aim of this Bayesian calibration is to obtain the posterior distribution of the most influential uncertain model parameters.

[11] To avoid cluttered notation, the output of $\boldsymbol{f}(\boldsymbol{\theta})$ is a vector containing the tumour-spheroid volumes at different discrete time points. Similarly, $\boldsymbol{y}_{\text{obs},i}$ contains the experimentally observed volume of one tumour spheroid i at different discrete time points, and $\boldsymbol{y}_{\text{obs}}$ concatenates the tumour-spheroid volumes for all time points and all observed spheroids.

Due to the implicit dependency on the forward solver, the posterior distribution is analytically intractable, and we approximate it using sampling techniques [25]. However, sampling from the posterior distribution involves numerous evaluations of the forward model f, which results in a tremendous computational burden for complex models, such as our tumour-growth model. Therefore, the forward model f is again replaced by a Gaussian process f_{GP} as a metamodel (see Section 4.2.3): we use a single-surface approximation [375] based on the mean of the Gaussian process. If including the uncertainty introduced by using the Gaussian process metamodel instead of the forward model is of interest, Bilionis and Zabaras [375] propose different approaches to capture this additional uncertainty.

As sampling technique, we use a sequential Monte Carlo (SMC) approach [55–57, 351], in which the posterior distribution is approximated by a large collection of $M \gg 1$ weighted particles [376], such that

$$p(\boldsymbol{\theta}|\boldsymbol{y}_{\mathrm{obs}}) \approx \sum_{i=0}^{M} W^{(i)} \delta_{\theta^{(i)}}(\boldsymbol{\theta}) \quad \text{with} \quad \sum_{i=0}^{M} W^{(i)} = 1 \tag{5.5}$$

where M is the number of particles, $\{W^{(i)}\}_{i=1}^{M}$ are weights, $\{\boldsymbol{\theta}^{(i)}\}_{i=1}^{M}$ is the ensemble of particles and $\delta(\cdot)$ represents the Dirac delta. The key idea of SMC is to start from a particle representation of the prior distribution and sequentially blend over to the target, i.e., posterior distribution [56]. The SMC method has gained considerable attention due to its superior efficiency and algorithmic robustness compared to Markov Chain Monte Carlo methods [55, 56, 351, 377]. SMC comprises numerous steps, such as reweighting, resampling and MCMC-based rejuvenation[12]. The technical details of SMC can be found in [55, 56, 351, 378, 379].

5.3 Results

In this section, we first present the results of the experiment, that is, the evolution of the tumour spheroid. We then move on to consider the outcome of the global sensitivity analysis and determine which model parameters are the most influential. Finally, we calibrate the relevant parameters of the multiphase model in such a way that they mimic the experimental results.

5.3.1 Growth of neuroblastoma spheroids in the microfluidic devices

The bright-field microscopy images in Fig. 5.3A show the growth of the spheroids in the collagen hydrogel in the microfluidic device from day zero (single cells) to day seven. The size of the spheroids is measured as the cell area of the spheroids: the size increases from 381(154) µm² at day 0 up to 10 199(2384) µm² at day seven, as shown in Fig. 5.3B.

An examination of the spheroid populations reveals a narrow morphology spectrum: most spheroids form circular structures without elongations or protrusions on their surface. Measuring

[12] In the rejuvenation step, we use a random walk Metropolis kernel as the MCMC transition kernel, where the covariance matrix of the proposal distribution is set proportionally to the empirical variance of the particles [57]. Further, an adaptive tempering scheme [57] is employed such that the ratio between two subsequent tempering exponents equals 0.95.

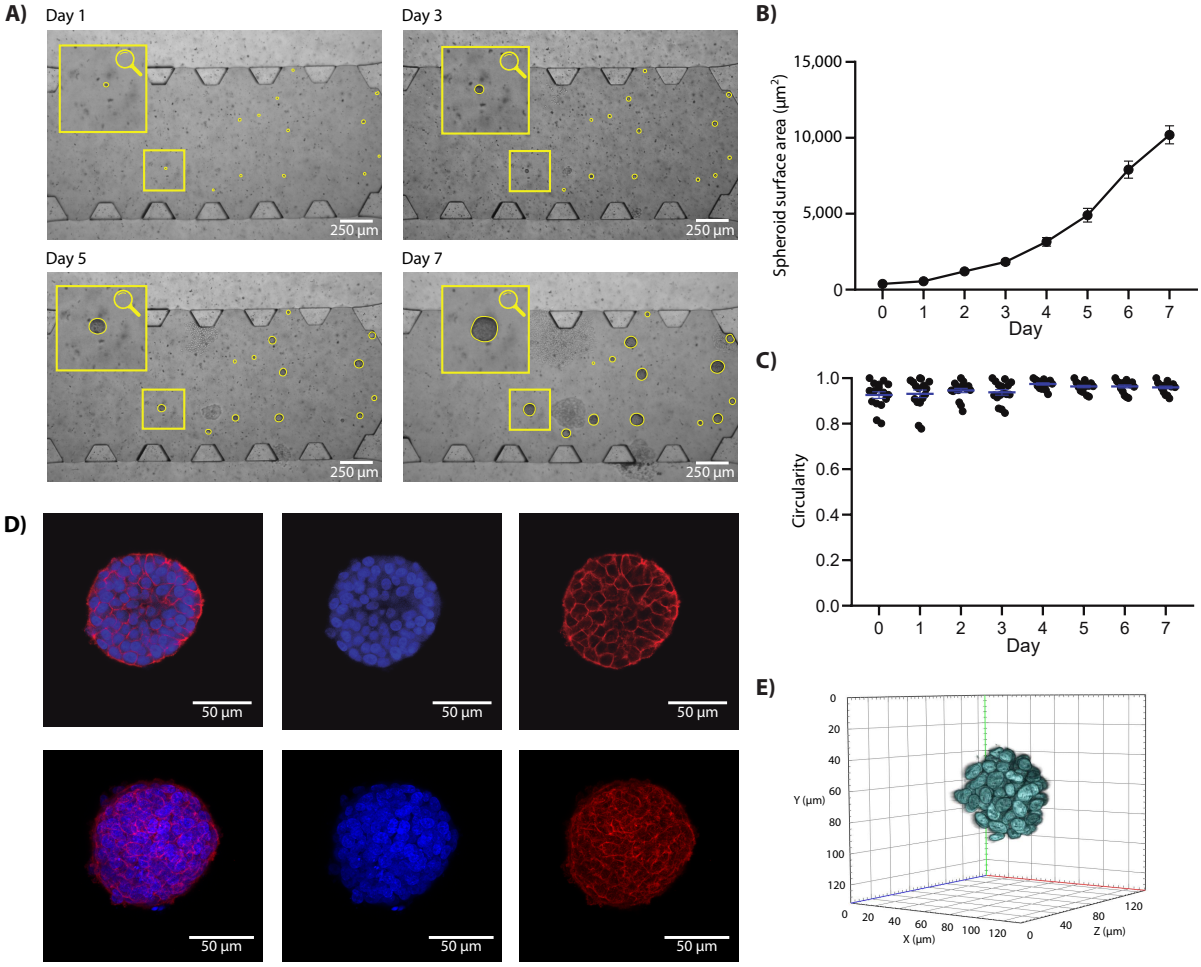

Figure 5.3 Growth of neuroblastoma spheroids in the collagen hydrogel in the microfluidic device. A) Representative bright-field time-lapse images showing the formation of neuroblastoma spheroids on days 1, 3, 5, and 7. B) Evolution of the spheroid area of individual spheroids over time. Data is expressed as mean ± SEM (standard error of the mean). C) Evolution of the spheroid circularity of individual spheroids over time. Data is expressed as mean ± SD (standard deviation). D) Confocal images as Z-stack[13] (upper row) and orthogonal projection (bottom row) on day 7. E) 3D reconstruction of a neuroblastoma spheroid on day 7. This figure is taken from [62], where it is licensed under CC BY-NC-ND 4.0.

[13] Z-stacking is a digital imaging technique that combines multiple images taken at different focal lengths to create a composite image with greater depth [380].

the circularity over time reveals high circularity values, i.e., high circularities of the projected area of the spheroids (with the median values ranging from 0.92 to 0.97 at various time points, see Fig. 5.3C), confirming the predominance of a single spheroid phenotype. The lower circularity values during the first days may be due to a small inherent error in measuring the size of small pixelated objects or the lack of total compactness at the beginning of the spheroid formation. The observation of a single phenotype is confirmed by confocal imaging and 3D reconstruction of the spheroids on day seven (Fig. 5.3D and E): again, most spheroids have a round shape with a highly compacted cytoskeleton, few protrusions, and a smooth surface. This phenotype is typically associated with high cell-cell adhesion due to the high compressive forces acting on the spheroids in the 3D hydrogel. Both cell spreading and tumour invasion are greatly reduced, and most of the cells remain as dense and isolated aggregates, with minor motility through the collagen gel compared with previously studied cancer types [344].

5.3.2 Global sensitivity analysis

We estimate the Sobol indices separately for each time point in the experimental measurements, i.e., from day zero to day seven. For this purpose, we train a Gaussian process in which the scalar quantity of interest is the tumour volume at the corresponding time point. The training is based on 460 training samples and results in a Nash–Sutcliffe efficiency (see Eq. (4.39)) of $Q^2 > 0.96$ for all cases. First- and total-order Sobol indices are estimated for 1, 3, 5, and 7 days of growth. The estimation is based on 100 000 Monte Carlo samples, 300 bootstrap samples, and 500 realisations of the trained Gaussian process metamodel.

Only five input parameters have a major impact on the tumour volume, these being the interfacial tension ($\sigma_{t\ell}$), the dynamic viscosity of the tumour cell phase (μ^t), the relative permeability exponent of the tumour cell phase (A_t), the tumour-growth coefficient (γ^t_{growth}), and the intrinsic permeability of the ECM (k). The remaining six parameters have a first- and total-order Sobol index of less than 0.01 (see Table 5.2). We thus conclude that these parameters are non-influential in the given setup and can be fixed at any value within the studied ranges.

The Sobol index estimates for the most influential parameters are shown in Fig. 5.4: for all five of the most influential parameters, the total-order Sobol index is considerably higher than the first-order index, indicating higher-order interaction effects. Therefore, we estimate the second-order Sobol indices for the influential parameters: the results confirm that interactions are indeed present, particularly an interaction of the dynamic viscosity μ^t and the growth coefficient γ^t_{growth} (see Table 5.3).

Comparing the estimated Sobol indices for the various time points reveals that while the total-order Sobol index of the growth coefficient γ^t_{growth} dominates the global sensitivity analysis, the corresponding first-order Sobol index decreases over time. At the same time, the influence of the dynamic viscosity μ^t of the tumour cell phase increases, in particular the total-order Sobol index. This could be because the cells are initially more independent as they are separated from each other. In contrast, once the spheroid has grown, cells behave like a cluster and no longer as individual entities. Our results highlight the increasing influence of the mechanical properties of the tumour cell

Table 5.2 First- and total-order Sobol indices. All values are rounded to three decimal places.

Parameter	Day 1		Day 3		Day 5		Day 7	
	S^i	S^{Ti}	S^i	S^{Ti}	S^i	S^{Ti}	S^i	S^{Ti}
k	0.003	0.015	0.009	0.023	0.008	0.027	0.007	0.027
ν	0.001	0.003	0.000	0.000	0.000	0.001	0.000	0.001
G	0.001	0.004	0.000	0.001	0.000	0.004	0.0	0.005
μ^s	0.000	0.000	0.000	0.000	0.000	0.000	0.000	0.000
μ^t	0.055	0.238	0.112	0.274	0.152	0.436	0.175	0.532
$\sigma_{t\ell}$	0.014	0.040	0.038	0.091	0.035	0.105	0.032	0.110
A_t	0.087	0.251	0.061	0.154	0.059	0.213	0.062	0.269
A_ℓ	0.000	0.0 00	0.000	0.0 00	0.000	0.000	0.000	0.000
γ^t_{growth}	0.632	0.679	0.521	0.739	0.344	0.665	0.250	0.605
$\gamma^t_{\text{necrosis}}$	0.000	0.000	0.000	0.000	0.001	0.001	0.001	0.001
$\gamma^{nt}_{\text{growth}}$	0.000	0.000	0.000	0.001	0.000	0.002	0.000	0.001

Table 5.3 Second-order Sobol indices for day 7 rounded to three decimal places.

Parameter	μ^t	A_t	γ^t_{growth}	k
$\sigma_{t\ell}$	0.014	0.009	0.032	0.003
μ^t		0.067	**0.188**	0.007
A_t			0.059	0.0
γ^t_{growth}				0.004

phase (in this case, its dynamic viscosity) the longer the tumour grows. Moreover, the influence of interactions of different parameters also increases over time. On the one side, these results emphasise the importance of using a proper global method for sensitivity analysis, such as the Sobol method used here, which gives such detailed insights as opposed to local estimates. On the other side, further experiments should build on this knowledge and not only investigate single mechanical properties of tumours but also consider the interactions by changing more than one parameter at a time.

We also include the uncertainty of the Sobol index estimates based on the workflow presented in Chapter 4: the total uncertainty in the Sobol index estimates, included as 99% confidence intervals in Fig. 5.4, is reasonably small compared to the value of the Sobol indices. Neither the uncertainty due to Monte Carlo integration nor the uncertainty due to the use of the Gaussian process metamodel is dominating (see Table 5.4).

The results of the global sensitivity analysis show that six out of the eleven uncertain input parameters have a total-order Sobol index close to zero. This suggests that these parameters are non-influential with respect to the quantity of interest, i.e., the tumour volume, and can hence be fixed anywhere with the range given in Table 5.1. As a result, the number of input space dimensions that must be included in the subsequent calibration can be reduced to the number of influential parameters. To validate this assumption, we fix the non-influential parameters at the mean value of the corresponding probability distributions and compare the resulting PDFs of the tumour volume to the original PDF with all eleven uncertain input parameters: the resulting distributions show very good agreement for all time points (see Fig. 5.5), and we conclude that fixing the six non-influential parameters is justified.

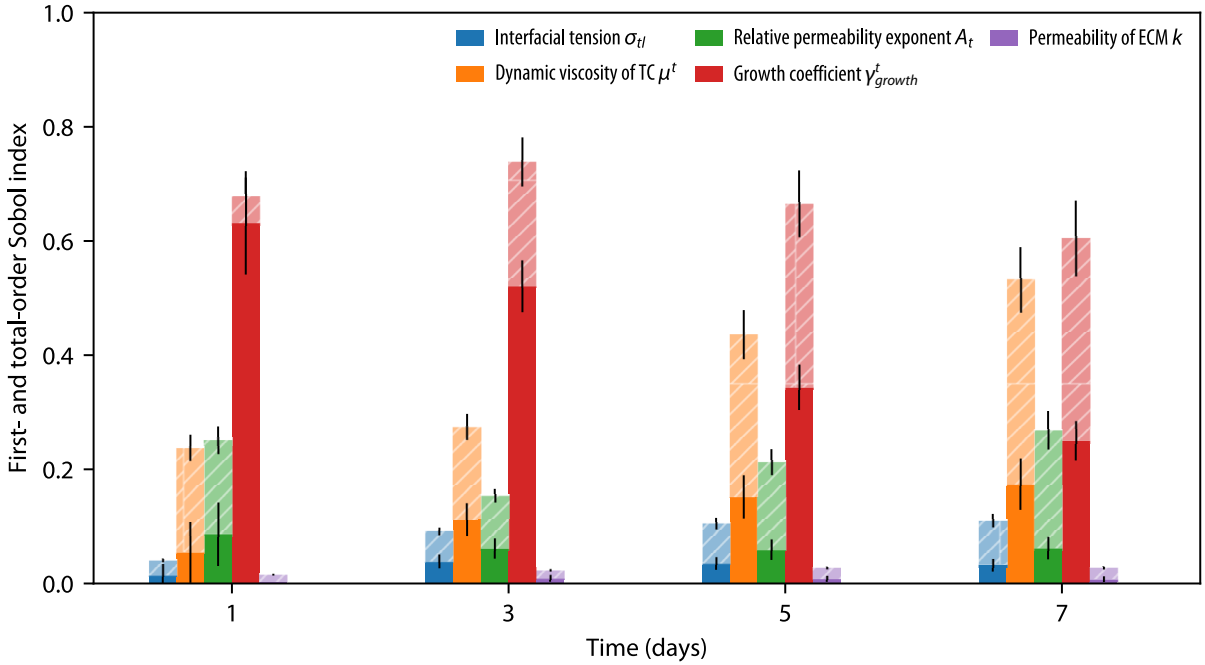

Figure 5.4 First- and total-order Sobol indices for 1, 3, 5, and 7 days of growth. First-order Sobol indices are shown as bold bars, while total-order Sobol indices are shown as dashed bars in the background. The error bars indicate the 99% confidence intervals for the corresponding Sobol index estimates.

Table 5.4 Total-order Sobol indices with the 99% confidence intervals (CI) due to Monte Carlo (MC) integration and the use of the Gaussian process (GP) metamodel for day 7. All values are rounded to four decimal places.

Parameter	S^{Ti}	CI due to MC integration	CI due to the GP
k	0.0269	0.0030	0.0007
ν	0.0012	0.0001	0.0001
G	0.0051	0.0005	0.0003
μ^t	0.5322	0.0570	0.0062
μ^s	0.0000	0.0000	0.0000
$\sigma_{t\ell}$	0.1102	0.0116	0.0020
A_t	0.2687	0.0334	0.0040
A_ℓ	0.0000	0.0000	0.0000
γ^t_{growth}	0.6049	0.0658	0.0057
$\gamma^t_{\text{necrosis}}$	0.0015	0.0001	0.0001
$\gamma^{nt}_{\text{growth}}$	0.0014	0.0001	0.0001

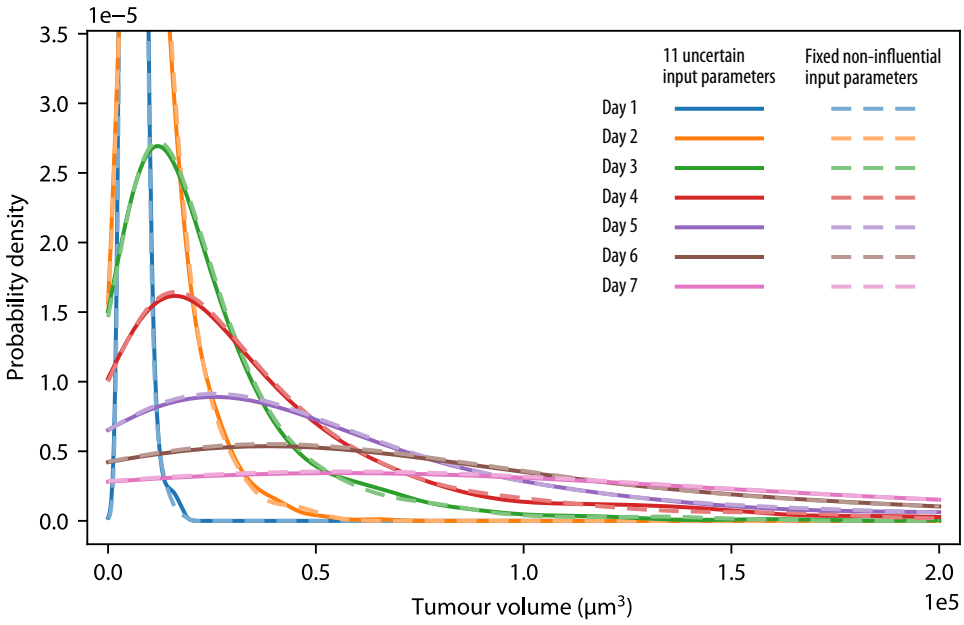

Figure 5.5 Probability density functions (PDFs) for different numbers of uncertain input parameters. The solid lines show the distributions with all 11 uncertain input parameters as listed in Table 5.1. The dashed lines represent the distributions with the six non-influential parameters fixed at their mean values. This figure is taken from [62], where it is licensed under CC BY-NC-ND 4.0.

5.3.3 Bayesian calibration

Based on the results of the global sensitivity analysis, only the most influential parameters are included in the Bayesian calibration:

$$\hat{\boldsymbol{\theta}} = [\sigma_{t\ell},\ \mu^t,\ A_t,\ k,\ \gamma^t_{\text{growth}}]. \tag{5.6}$$

We define the priors of each parameter as uniform distributions, following the ranges used in the global sensitivity analysis (see Table 5.1). The observations are the tumour volumes measured at the eight different time points in the *in vitro* spheroid experiments, as described in Section 5.2.1. The physics-based tumour model is replaced by the posterior mean of a Gaussian metamodel trained on the following data set: the time is used as an additional input space dimension, and 536 training samples, each taken at eight time points, hence from a training data set of 4288 data points. We use a sparse variational Gaussian process to reduce computational complexity and storage demands [303]. This results in a Nash–Sutcliffe efficiency of $Q^2 > 0.98$ for the metamodel. The posterior distribution is approximated with 20 000 particles and 5 SMC rejuvenation steps, using a fixed noise variance of $\sigma_N^2 = 1 \times 10^{12}\ \mu\text{m}^6$ (see Eq. (5.3)).

In the following, we consider the results of the Bayesian calibration from two perspectives. First, we analyse the output distribution of the calibrated model $p(V^t|\boldsymbol{y}_{\text{obs}})$ (in the output space, i.e., the tumour volume). This allows us to compare the remaining uncertainty in the tumour volume V^t with

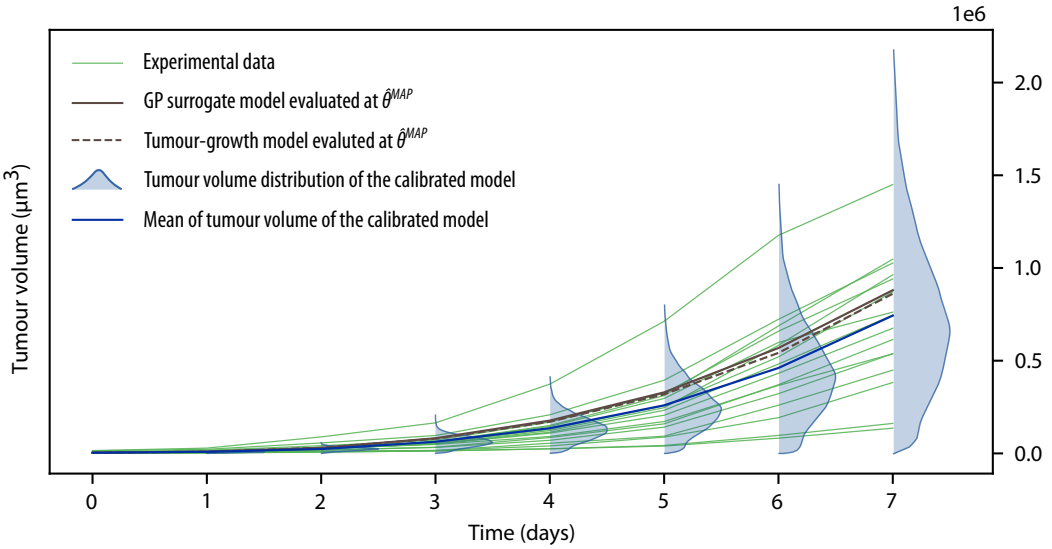

Figure 5.6 Spheroid tumour volume over time. In green solid lines, the growth of each spheroid from the experimental data set is plotted. The outcome of the metamodel evaluated at $\hat{\theta}^{\text{MAP}}$ is plotted in brown, and the outcome of the forward model in dashed brown line using the same point estimate $\hat{\theta}^{\text{MAP}}$. The distribution of the tumour volume $p(V^t|\boldsymbol{y}_{\text{obs}})$ of the calibrated model is evaluated at each experimental time point and shown in light blue. The mean of the tumour volume of the calibrated model is plotted in dark blue. This figure is taken from [62], where it is licensed under CC BY-NC-ND 4.0.

the experimental data. We then analyse the posterior distribution $p(\hat{\boldsymbol{\theta}}|\boldsymbol{y}_{\text{obs}})$ of the input parameters themselves (in the input parameter space).

The results of the Bayesian calibration in the output space are shown in Fig. 5.6 together with the experimental data. We evaluate the maximum a posteriori density estimate (MAP)[14] in both the tumour-growth model f and the mean of the Gaussian process metamodel m_{GP}, and the corresponding results are depicted as brown dashed and continuous lines, respectively. These plots confirm that the Gaussian process metamodel emulates the tumour-growth model reasonably well. We also exploit the capacity of the Bayesian approach to represent uncertainty in the output space. The probability distribution of the tumour volume $p(V^t|\boldsymbol{y}_{\text{obs}})$ that emerges from a forward uncertainty quantification using the posterior distribution is plotted in light blue. It estimates the probability density function of the spheroid volume over time. The mean tumour volume $\mathbb{E}_{p(\hat{\boldsymbol{\theta}}|\boldsymbol{y}_{\text{obs}})}[V^t(\hat{\boldsymbol{\theta}})]$ of the calibrated model is plotted in dark blue. It is noteworthy that the results of the Bayesian calibration match the experimental variability.

To gain a better understanding of the five calibrated parameters, we consider the posterior distribution $p(\hat{\boldsymbol{\theta}}|\boldsymbol{y}_{\text{obs}})$ in the input parameter space. Since we are interested in the implications for each individual parameter, we first focus on 1D marginal posteriors $p(\theta_i|\boldsymbol{y}_{\text{obs}})$. We will then analyse the 2D marginal posteriors for parameter pairs, as the global sensitivity analysis indicates the presence of interactions between the input parameters. The overall results are shown in Fig. 5.7.

[14] The combination of parameters that results in the MAP density estimate is $\hat{\boldsymbol{\theta}}^{\text{MAP}}$: $\sigma_{t\ell} = 49.898\,\text{mN}\,\text{m}^{-1}$, $\mu^t = 706.56\,\text{Pa}\,\text{s}$, $A_t = 2.5259$, $k = 0.8201 \times 10^{-9}\,\text{mm}^2$, $\gamma^t_{\text{growth}} = 1.7919 \times 10^{-8}\,\text{g}\,\text{mm}^{-3}\,\text{s}^{-1}$.

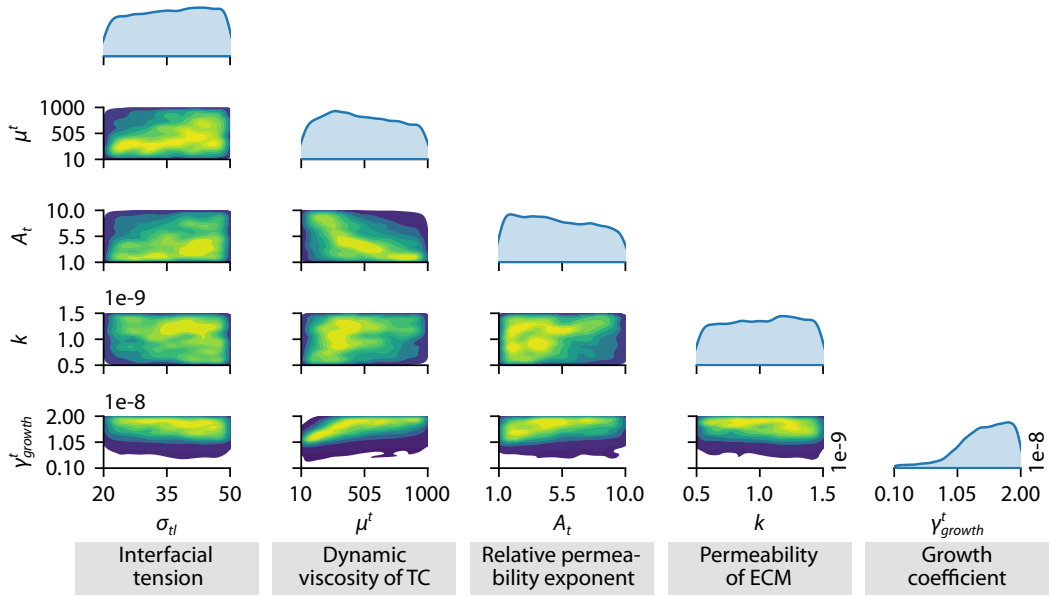

Figure 5.7 Marginal posterior PDF projected to 1D and 2D. Yellow colours indicate high values of the posterior densities, whereas purple colours indicate small values. The diagonal, in light blue, shows the 1D marginal posterior distribution for a single parameter. This figure is taken from [62], where it is licensed under CC BY-NC-ND 4.0.

It should be borne in mind that the 1D and 2D marginal distributions all are projections of the five-dimensional posterior distribution $p(\hat{\boldsymbol{\theta}}|\boldsymbol{y}_{obs})$ to lower dimensions.

The marginal posterior of the growth coefficient γ^t_{growth} has a higher probability mass clustered around the value $2 \times 10^{-8}\,\text{g}\,\text{mm}^{-3}\,\text{s}^{-1}$. Therefore, we conclude that the lower values obtained from the literature are unlikely to fit the experimental neuroblastoma spheroid growth. The marginal posterior of the growth coefficient is significantly different from the other four ($\sigma_{t\ell}$, μ^t, A_t and k). This is in agreement with the global sensitivity analysis, which indicates that the growth coefficient is the most influential parameter. Thus, we consider that the identification of a more probable range of values for this parameter is a solid outcome of the Bayesian calibration. Nevertheless, the plot does not reveal a clear peak at any certain value, presumably due to the need to explain the high variability of the experimental data.

Fig. 5.7 further shows that the 1D marginal posterior distributions for the interfacial tension $\sigma_{t\ell}$ and permeability k of the ECM are uninformative. This finding is in agreement with the output of the global sensitivity analysis, in which both parameters are the least influential of the five parameters selected for the Bayesian calibration. The flat marginal posteriors indicate that no information about the effect of each individual parameter can be extracted separately from the available data. This is assumed to be due to the small influence of these parameters on the resulting tumour volume. Also, the forward model may allow for a wide range of parameters without resulting in a drastic change in the outcome. A further hypothesis is that this is due to the low data regime, which comprises only eleven spheroid data points per time step. The 1D marginal posterior distribution of the dynamic viscosity μ^t reveals a slightly higher probability mass for values below 500 Pa s.

We now consider the 2D marginal posteriors. Figure 5.7 reveals that the dynamic viscosity μ^t has a negative correlation to the relative permeability exponent A_t; in other words, that large μ^t values have a high density in combination with small values for A_t. Apart from that, the 2D marginal posteriors are relatively flat.

To conclude the Bayesian calibration results, we relate them back to the theoretical framework of our computational model. In the TCAT framework, the interfacial tension (together with the interfacial curvature) causes the pressure difference between the cell phase and the surrounding medium at the microscale. However, at the macroscale, which is where all model equations are formulated, the use of Eqs. (2.31) and (2.32) are only heuristically proposed relations [65]. The interfacial tension influences the density of the tumour. Here, we only used the tumour volume for the Bayesian calibration, which is why it is not possible to distinguish between two spheroids of the same volume but with different densities. This might explain why the marginal posterior for the interfacial tension does not show a clear peak. With the inclusion of additional data, such as cell count, tumour mass or density, a more pronounced posterior may be possible. Similarly, Eq. (2.30) is also a heuristical relation to include interaction forces between the cell phase and the surrounding medium at the macroscale [65], which again is not consistent with the TCAT framework. Further experimental analyses of how tumour cells interact with their surroundings (ECM and other phases) are clearly necessary. From the mathematical side, Miller *et al.* [82] have already proposed a theoretically sound version which considers the interfaces between the phases.

5.4 Discussion

We combined *in vitro* experiments with computational modelling to investigate the growth of tumour spheroids subject to regulation by their microenvironment. Our methodology goes one step beyond those presented in the literature [331–334].

Employing 3D experiments with microfluidic chips allows us to better reproduce the spatial organisation of cells, control the microenvironmental conditions and present a low-cost and accessible method for rapidly characterising 3D cell clusterisation. The potential impact of 3D cultures has strongly been emphasised in recent year, and authors have provided a variety of techniques for 3D culture systems to attain more reliable and comprehensive results [381], also for neuroblastoma [382–386]. Traditionally, the hanging drop method has been used to study spheroid growth: the cells are deposited by gravity at the bottom of the hanging droplets, gradually forming a spheroid. However, as no scaffold provides support, the natural tumour microenvironment is missing, which makes this approach unsuitable for reproducing *in vivo* tumour formation. Employing a collagen hydrogel enhances the study of 3D growth models in a more reliable approach, and its usefulness for the study and characterisation of different tumours has been widely reported [359, 387]. Previous studies have also reviewed the role of ECM in neuroblastoma progression, evidencing that alterations of the ECM mediate cancer progression [361, 388]: the ECM stiffness regulates the neuroblastoma dynamics and behaviour [359, 389] as well as the chemotherapeutic distribution and efficacy [384].

The main limitation of spheroids is that they are formed from a single cell. Although culturing them from single cells embedded in hydrogels allows us to produce spheroids without aggregation

techniques, they are still a simplified model. Spheroids lag behind other more complex models where multiple cell types interact and where physiological functions are more clearly defined, e.g., in organotypic cultures. The combination of long-term 3D culture and microfluidic devices paves the way to a better understanding of tumour spheroid formation, offering a refined methodology to feed the computational models. Additionally, to create a tumour-on-a-chip platform which closely recreates *in vivo* tumour growth, the flow has to be incorporated into the microfluidic devices [345, 390, 391]. On the computational side, models must then replicate the complex tumour structure, integrating the vascular network to simulate *in vivo* dynamic flow and drug transport in the tumour microenvironment. This is directly enabled by our modelling approach [58, 73].

A multiphase porous-media model based on porous media is chosen for the simulation of spheroid growth to better account for the features of the experimental setup. A wide range of models is presented in the literature, e.g., [31, 392–395]. Hydrogels are network polymeric materials with highly hydrophilic polymeric chains and are hence associated with large quantities of water, which accounts for their biocompatibility. As with most polymers, the hydrogels exhibit time-dependent mechanical behaviour due to the intrinsic viscoelasticity of the polymeric network. Our modelling approach offers the advantage of seamlessly incorporating recent scientific findings on the importance of hydrogel viscoelasticity [396, 397] by applying a viscoelastic material law for the scaffold. To better characterise the multiphase nature of hydrated materials (like the collagen hydrogels of these spheroids), porous-media approaches are seen as the best solution [398]. A further advantage is that the multiphase model presented here allows us to replicate the experimental setup, as the biophysical properties of the hydrogel scaffold (i.e., stiffness, porosity and permeability) are valuable inputs in the model. A current limitation is that we do not include the fibre orientation of the collagen gels and the ECM deposition, which could be the subject of potential future research. Finally, studying tumour growth in a heterogeneous microenvironment (asymmetric as opposed to spherical growth) is a further area in which the experimental and computational models complement each other in a feedback loop.

Combining the experimental activity with the multiphase porous-media model is crucial to improving our understanding of the biological processes, i.e., the onset, formation, and growth of tumour spheroids. To do this, we first assess the model's parameter sensitivity towards the relevant output quantity over time, i.e., the tumour volume. This reveals an overall dominant effect of the input parameter accounting for growth. The other influential input parameters concern the biophysical properties of the tumour cells and their interaction with the microenvironment—a fact that confirms the importance of understanding the links between cancer biophysics and biology [9]. These findings emphasise the advantage of a genuinely global method of sensitivity analysis, such as the Sobol method, which enables detailed insights rather than local estimates.

We then estimate the model parameters using Bayesian calibration, as it is intrinsically able to capture the uncertainties present in experimental measurements, which is the biggest advantage of the Bayesian approach. Bayesian calibration also enables prior knowledge to be seamlessly integrated. The predictive probability density of the tumour volume resulting from forward uncertainty quantification using the obtained posterior clearly reflects the ability of Bayesian methodology to capture the entire *in vitro* variability. In future studies, the Bayesian approach offers a natural way of integrating

additional data as it becomes available: knowledge of the uncertain input parameters can be further updated using the posterior obtained in the present study as a prior. Further research could entail modelling other sources of uncertainty, such as the effect of spatial- and/or time-variable nutrient distribution. Such effects can be included in the analysis as additional random variables, in a similar way to [399], and might indeed result in a more expressive posterior.

This study aims to better understand how spheroid growth evolves over time and how mechanical stimuli regulate it. In this context, we are able to monitor tumour-spheroid growth under physiological conditions using 3D microfluidic devices and collagen hydrogels to mimic the ECM. Nevertheless, it is impossible to measure certain cell or organoid properties in such experiments, a limitation of the presented workflow. To characterise the mechanical properties of the spheroids, they usually must be separated from the collagen network and subjected to further tests, such as atomic force microscopy. This is rather complicated and no longer physiological because cells must be separated from the organoid. The presented workflow may be more appropriate, as it not only allows the properties of the whole spheroid to be estimated but also focuses on the properties of the cells embedded in the spheroid.

Additionally, replicating the experimental outcomes reduces cost significantly since it allows new experimental scenarios to be tested computationally *a priori*. This is of major importance when we study infant cancer, where early diagnosis is key: in paediatric malignancies, trial sample sizes are kept as low as possible while maintaining the ability and power to address the scientific objectives of interest. Therefore, the availability of childhood cancer cells, specifically neuroblastoma cells, is low; hence, computational modelling plays a crucial role in exploring these cancers.

5.5 Outlook to Bayesian inference with coupled multi-physics observations

The posterior PDF in Fig. 5.7 shows that the Bayesian calibration is not able to infer a clearly peaked posterior PDF for four out of the five parameters based on experimental measurements of the tumour volume. This raises the question of whether including additional data could benefit the Bayesian inference task and to what extent. In particular, the tumour spheroid growing in the ECM is a multi-physics system; hence, we can consider additional observations from other fields. For example, we can consider the displacement of the ECM, which is a direct consequence of the growth of the spheroid. We here briefly sketch an outlook on how such additional observations can benefit the Bayesian inference task, based on [400].

The tumour volume is a function of the saturation of tumour cells, hence, part of the fluid field. Based on the theory of porous media, the fluid field is fully coupled to the displacement field of the solid phase, the ECM. We now assume that we can measure the displacement of the ECM, e.g., by using a fluorescent marker and applying image analysis [401] or by tracking microbeads embedded in the ECM [402]. In our *in silico* setup, we focus on two parameters: the growth coefficient γ^t_{growth} and the interfacial tension $\sigma_{t\ell}$. We generate artificial data by solving the fully coupled problem for a given set of parameters, the ground truth, and then adding Gaussian noise. The tumour volume is

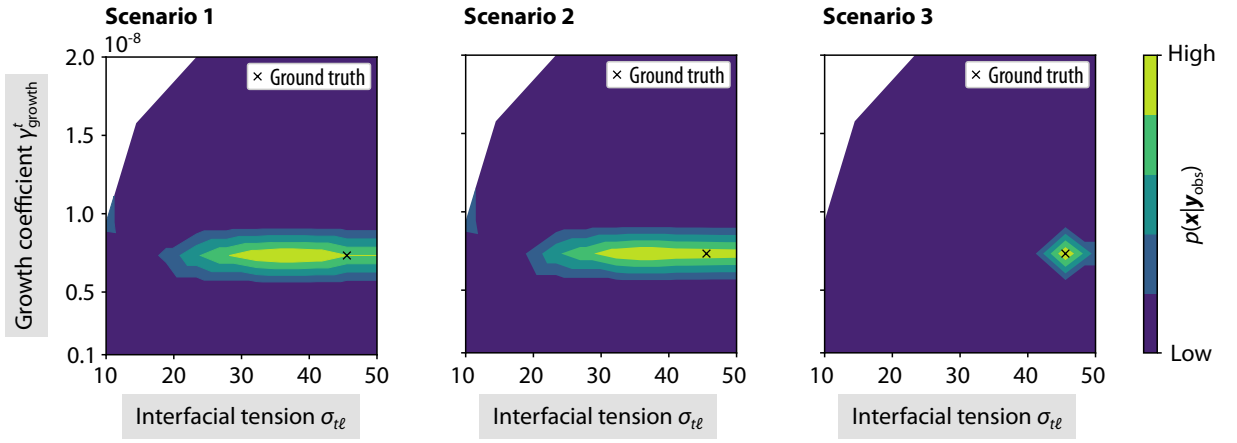

Figure 5.8 Posterior PDFs. Scenario 1: The ECM is assumed to be rigid, and only observations of the tumour volume are considered. Scenario 2: The fully coupled problem is solved, but only observations of the tumour volume are considered. Scenario 3: The fully coupled problem is solved, and observations of the tumour volume and the ECM displacement are considered.

measured at two time points, and the ECM displacement is measured at two positions at the last time point (day seven). We investigate and compare the following three scenarios:

Scenario 1: We assume the ECM to be rigid and only consider observations of the tumour volume.

Scenario 2: We solve the fully coupled problem but only consider observations of the tumour volume, similar to the previous example in Section 5.3.

Scenario 3: We solve the fully coupled problem and consider observations of the tumour volume and the ECM displacement.

Fig. 5.8 shows the posterior PDFs for the three scenarios. While the posterior PDF recovers the ground truth for the growth coefficient γ^t_{growth} in all three scenarios, the posterior PDF for the interfacial tension $\sigma_{t\ell}$ is clearly improved when the ECM displacement is included as an additional observation in Scenario 3.

This example demonstrates how additional observations from other fields can indeed improve the inference of the posterior PDF—a promising direction for future research. Moreover, the computational setup can also guide the experimental design: it can be used to investigate *in silico* which additional observations are most beneficial for the inference task and how many observations are required to obtain a sufficiently peaked posterior PDF.

5.6 Conclusion

Two notable challenges currently hinder the way towards clinical application of tumour-growth simulations as a prognostic tool: the limited integration of *in silico* studies with experiments, and missing characterisation of uncertainties in the models and the data [403]. In addition, the tumour microenvironment is now known to be an active promoter of tumour growth and must hence be taken into account [404]. To tackle all of these challenges, we combine novel *in vitro* experiments

with a computational model in such a way that both include the interactions with the tumour microenvironment. This unique combination is the essential building block that then allows us to infer knowledge about our model parameters by applying state-of-the-art techniques: our global sensitivity analysis based on the Sobol method and our Bayesian calibration based on the sequential Monte Carlo approach (both using Gaussian processes as a metamodel) account for the underlying uncertainties.

Properly identifying the posterior distributions by Bayesian calibration for such a complex model (as our multiphase porous-media tumour growth model) is often limited by insufficient and noisy experimental data. The required experimental design needs to be able to precisely monitor the spatiotemporal evolution of the spheroid while also providing a stable and controlled microenvironment—a challenging task given the currently available technologies [403]. This study reveals that the knowledge gained for the uncertain parameters is obviously still limited. However, our results show that the inferred posterior distribution allows us to match the experimental data, including the high variability. Hence, the demonstrated workflow shall be considered a first step towards a Bayesian calibration of all uncertain parameters, which suggests which next steps shall be taken: from the experimental side, additional data such as cell count, tumour mass or ECM displacement is required—and would indeed benefit the Bayesian inference task. From the mathematical side, future model improvements need to consider the interfaces between the phases [82].

6 Conclusion and outlook

This thesis presented an interdisciplinary approach to integrating a computational model into cancer research, bridging the gaps to probabilistic approaches, physics, and experimental research in biology and medicine.

We presented a continuum-based approach to model nanoparticle transport in the tumour and its microenvironment. When studying passive targeting of drug-loaded nanoparticles, the tumour microenvironment and its physical properties are key factors for the success of the treatment. In this context, our model can reproduce important transport characteristics and barriers, including the endothelial barrier, the non-perfused tumour core, and the outward flow of the interstitial fluid. Hence, our model enables a systematic exploration of the nanoparticle design space and can help to design novel prototypes. We showed that the size of vessel wall pores and the permeability of the blood vessel wall have a significant impact on the successful delivery of nanoparticles to the tumour. Considering only the interendothelial pathway might not be sufficient to overcome the major challenges observed in the literature. Furthermore, only if the transport in the interstitial fluid is diffusion-dominated can the nanoparticles reach the tumour core, i.e., only small nanoparticles with higher diffusivity can reach the tumour core.

Since passive targeting is insufficient to overcome the nanoparticle transport barriers, we further extended our model to include active targeting of magnetic nanoparticles. Based on the Smoluchowski advection-diffusion equation, we investigated the capture of magnetic nanoparticles under the combined effect of magnetic forces and fluid flow—the latter again being an important transport mechanism in the tumour microenvironment. The analytical expression we derived for the magnetic force exerted by a cylindrical magnet provides an efficient way to model the capture of magnetic nanoparticles in a more realistic setup in three dimensions. We studied a simplified test setup with a tumour spheroid in a flow chamber and a cylindrical magnet below the chamber, the configuration commonly used in experiments. Combining such a *in silico* study with *in vitro* experiments in a controlled flow environment forms the basis for further next steps to more complex scenarios, e.g., in a vascular *in vivo* model.

Many novel nanoparticle prototypes fail in clinical trials [24]. The computational model presented in this thesis can help to gain insight into nanoparticle transport and, as a next step, support the design of novel systems. Developing a comprehensive *in silico* model will enable a fast and systematic exploration of the nanoparticle design space, which is impossible in experimental research alone: this reduces the number of experiments required to the most promising candidates, bypassing costly

and time-consuming trial-and-error design methods. A collaboration between experimentalists, computational modellers, and clinicians will allow us to build an integrated framework for drug development and accelerate the translation of the results into clinical practice.

However, our model still entails many uncertain input parameters. While the parameters have a clear physical meaning—one of the attractive features of physics-based models—the determination of these parameters is often very elaborate and costly or even impossible in practice. To distinguish the most influential parameters from non-influential ones, we performed a global variance-based sensitivity analysis based on the Sobol method. Since such a global sensitivity analysis is computationally expensive, modellers often resort to local methods alone, which may result in a deficient analysis [50]. We instead used a Gaussian process as a metamodel to reduce the computational cost of the sensitivity analysis. We showed that this approach indeed enables a global sensitivity analysis to be performed at a reasonable computational cost, even for complex, computationally expensive models. A small number of training samples is enough to identify which parameters are the most influential ones, all while keeping the uncertainty introduced by the Gaussian process metamodel small. The metamodel-based approach also enables the estimation of higher-order Sobol indices: such a study of interaction effects is often neglected, but it can be crucial to understanding the underlying mechanisms of a model.

After identifying the most influential parameters, we performed a Bayesian calibration of the model to experimental data. We combined state-of-the-art experimental techniques based on tumour spheroids in collagen hydrogels in a microfluidic device with our computational tumour-growth model and a sequential Monte Carlo approach to perform the calibration. While the inferred posterior distribution allows us to match the experimental data and its high variability, the limitations also become apparent: even with state-of-the-art techniques for all workflow steps, the knowledge gained for the uncertain parameters is clearly limited, and insufficient, noisy data derived from cell culture experiments restrains us from properly identifying the posterior distribution. Since high variability is an inherent property of cell culture experiments—even among standardised experiments in a world-leading research environment [405]—a probabilistic approach to calibration is essential to support realistic data interpretation and conclusions.

So far, we have studied solid tumours very generically. In particular, we have not distinguished between benign and malignant tumours. The crucial difference between these two types of tumours is the ability of malignant tumours to invade the host tissue and to metastasise, i.e., to spread to other parts of the body. Since metastasis is the main cause of death in cancer patients, focusing on the mechanisms of metastasis is of utmost importance. In addition to genetic factors, the physical interactions of tumour cells with the surrounding microenvironment and their mechanical properties were found to determine metastatic spreading [406, 407]: the stiffness of the extracellular matrix and the interstitial fluid flow both regulate cell mechanics [408, 409]. Gottheil *et al.* [410] correlated the metastatic potential with the state of cell unjamming—a concept of soft condensed matter physics. In addition, the transport of oxygen is also critical: Rankin and Giaccia [411] showed that hypoxia is a potent driver of metastasis and resistance to chemo- and radiotherapy, and Plodinec *et al.* [412] concluded that metastatic spreading correlates with low stiffness of hypoxia-associated cancer cells.

Our model already includes many of these factors, e.g., the stiffness of the extracellular matrix, the interstitial fluid flow, and the oxygen transport, and can thus readily be applied to study metastasis.

In addition to the distinction between benign and malignant tumours, we also have not considered the tumour-specific and patient-specific heterogeneity. Different tumour types have different properties, and the properties of the same tumour type can vary significantly between patients, and even one specific tumour is heterogeneous in itself [10]. While Deisboeck *et al.* [27] see continuum-based approaches as a lesser choice for the exploration of heterogeneity, the combination of a continuum-based with a cell-based approach in the form of a hybrid model may be a promising way to overcome this limitation. Considering heterogeneity is an important next step towards a patient-specific model, which can ultimately predict the evolution of a tumour and design personalised treatment strategies.

On the way towards a comprehensive patient-specific tumour growth model, we believe that we should not limit ourselves to finding the final, perfect model with all parameters precisely determined as such a model would not even represent the real heterogeneous world: we must instead focus on building incomplete, tentative and falsifiable models in the most predictive and expressive fashion currently feasible [413].

A Parameters

A.1 Parameters for the *in vitro* growth example of a tumour spheroid

Table A.1 Parameters based on the literature.

Symbol	Parameter	Value	Units	Ref.
r_o	Initial tumour radius	0.010	mm	Measured
ρ^t, ρ^ℓ, ρ^s	Density of the fluid phases and the ECM	$1 \cdot 10^{-3}$	g/mm³	[414]
S_o^t	Initial tumour saturation	0.875	–	[67]
ε_o	Initial porosity	0.89	–	[344, 354, 415–417]
$\omega_{crit}^{n\ell}$	Critical mass fraction of oxygen	$1 \cdot 10^{-6}$	–	[70]
$\omega_{env}^{n\ell}$	Environmental mass fraction of oxygen	$4.2 \cdot 10^{-6}$	–	[67]
$D_o^{n\ell}$	Interstitial diffusivity of oxygen	$3.2 \cdot 10^{-3}$	mm²/s	[67]
δ	Non-linear diffusion law of oxygen	2	–	[67]
μ^ℓ	Dynamic viscosity of medium	$0.95 \cdot 10^{-3}$	Pa s	[414]
γ_o^{nt}	Oxygen consumption due to metabolism of TC*	$6 \cdot 10^{-10}$	g/(mm³s)	[67]

* TC denotes the tumour cell phase.

Table A.2 Parameters based on the sensitivity analysis and Bayesian calibration in Chapter 5.

Symbol	Parameter	Value	Units
$\sigma_{t\ell}$	Interfacial tension	49.989	µN/m
μ^t	Dynamic viscosity of TC	706.56	Pa s
A_t	Relative permeability exponent for TC	2.5259	–
A_ℓ	Relative permeability exponent for IF	4.0	–
γ_{growth}^t	Tumour-growth coefficient	1.7919×10^{-8}	g/(mm³ s)
$\gamma_{necrosis}^t$	Necrosis coefficient of TC	5.5×10^{-9}	g/(mm³ s)
γ_{growth}^{nt}	Oxygen consumption due to growth	3.0×10^{-10}	g/(mm³ s)
k	Intrinsic permeability of the ECM	0.8291×10^{-9}	mm²
ν	Poisson's ratio of the ECM	0.415	–
G	Shear modulus of the ECM	415	Pa
μ^s	Dynamic viscosity of the ECM	22.5	Pa s

A.2 Parameters for the *in vivo* growth example of a vascularised tumour

Table A.3 Parameters of the extracellular matrix (ECM) as the solid phase.

Symbol	Parameter	Value	Units	Ref.
ρ^s	Density of the ECM	1×10^{-3}	g/mm³	[33]
ν	Poisson's ratio of the ECM	0.4	-	[33]
E	Young's modulus of the ECM	800	Pa	[72]
k	Intrinsic permeability of the ECM	1×10^{-9}	mm²	[72]

Table A.4 Parameters of the host cells, the tumour cells, and the interstitial fluid (IF).

Symbol	Parameter	Value	Units	Ref.
ε_0	Initial volume fraction of HC, TC and IF	0.78	-	[72]
ρ^h, ρ^t, ρ^ℓ	Density of fluid phases	1.0×10^{-3}	g/mm³	[33]
μ^h, μ^t	Dynamic viscosity of host cells and tumour cells	20	Pa s	[68]
μ^ℓ	Dynamic viscosity of IF	1.0×10^{-3}	Pa s	[33]
A_h, A_t	Exponent in Eq (2.30) for host cells and tumour cells	2	-	[33]
A_ℓ	Exponent in Eq (2.30) for IF	4	-	[72]
$\sigma_{h\ell}$	Host cells-IF interfacial tension	72	g/s²	[33]
σ_{th}	Tumour cells—host cells interfacial tension	36	g/s²	[33]
a	Coefficient in Eq (2.31) and (2.32)	590	Pa	[33]
b	Coefficient in Eq (2.31) and (2.32)	1	-	[33]
γ^t_{growth}	Growth coefficient of tumour cells	4.0×10^{-8}	g/(mm³ s)	[68]
$\left(L_p \frac{S}{V}\right)^{\text{ly}}$	Lymphatic filtration coefficient	1.04×10^{-6}	1/(Pa s)	[187]
p^{ly}	Lymphatic pressure	0	mmHg	[72]
$p^{\text{ly}}_{\text{coll}}$	Threshold for lymphatic vessel collapse	1000	Pa	

Table A.5 Parameters of the vasculature and for leakage from the vasculature to the interstitial fluid.

Symbol	Parameter	Value	Units	Ref.
ρ^v	Density of blood	1.0×10^{-3}	g/mm³	[73]
p^v	Blood pressure	20	mmHg	
μ^v	Dynamic viscosity of blood	4.0×10^{-3}	Pa s	[202]
D^v	Endothelial cell random-motility coefficient	5.0×10^{-9}	mm²/s	[72]
$\sigma(\pi^v - \pi^\ell)$	Osmotic pressure difference	1333	Pa	[111]
L^v_p	Hydraulic conductivity for transcapillary flow ⋆	0.7×10^{-6}	mm/(Pa s)	[125]
S/V	Surface-to-volume ratio	20	1/mm	[181]

⋆ We assume a pore radius of $r_0 = 200$ nm [107] and a vessel wall thickness of $t = 1$ nm [178]. The fraction of pores $\gamma_{\text{pore}} = 10 \times 10^{-4}$, defining the fraction of the endothelium surface occupied by pores, is based on [125]. Altogether, this results in a hydraulic conductivity of $L^v_p = 1.25 \times 10^{-6}$ mm/(Pa s).

Table A.6 Parameters for transport of necrotic tumour cells and oxygen.

Symbol	Parameter	Value	Units	Ref.
$D_{\mathrm{o}}^{n\ell}$	Interstitial diffusivity of oxygen	3.2×10^{-3}	mm^2/s	[33]
δ	Nonlinear diffusion law of oxygen	2	-	[33]
D_{eff}^{Nt}	Diffusion coefficient of necrotic tumour cells	0	mm^2/s	[72]
$\gamma_{\mathrm{necrosis}}^{t}$	Necrosis coefficient	1.0×10^{-8}	$\mathrm{g}/(\mathrm{mm}^3\,\mathrm{s})$	[70]
$\gamma_{\mathrm{growth}}^{nt}$	Consumption related to growth	2.4×10^{-10}	$\mathrm{g}/(\mathrm{mm}^3\,\mathrm{s})$	[33]
γ_{o}^{nt}	Consumption due to metabolism of tumour cells	6.0×10^{-10}	$\mathrm{g}/(\mathrm{mm}^3\,\mathrm{s})$	[33]
γ_{o}^{nh}	Consumption due to metabolism of host cells	2.0×10^{-10}	$\mathrm{g}/(\mathrm{mm}^3\,\mathrm{s})$	[73]
$\omega_{\mathrm{crit}}^{n\ell}$	Critical mass fraction of oxygen	1.0×10^{-6}	-	[68]
$\omega_{\mathrm{env}}^{n\ell}$	Environmental mass fraction of oxygen	4.2×10^{-6}	-	[33]

Table A.7 Parameters for oxygen exchange based on [73].

Symbol	Parameter	Value	Units	Ref.
ρ^n	Density of oxygen	1.429×10^{-6}	$\mathrm{g/mm}^3$	[73]
α_ℓ	Solubility of oxygen in the IF	3.0×10^{-5}	mmHg^{-1}	[418]
$\alpha_{v,\mathrm{eff}}$	Effective solubility of oxygen in blood	3.1×10^{-5}	mmHg^{-1}	[419]
H_D	Discharge hematocrit	0.45	-	[419]
C_{o}^{nv}	Concentration of oxygen at maximum saturation	0.5	-	[419]
n	Hill exponent	2.7	-	[420]
$P_{\mathrm{oxy,50}}^{v}$	Partial pressure at 50% oxygen saturation	37	mmHg	[420]
γ_{tv}	Coefficient for transvascular oxygen exchange	1.429×10^{-5}	$\mathrm{mm}/(\mathrm{mmHg\,s})$	[419]

Bibliography

[1] R. Hesketh. *Understanding Cancer*. Understanding Life. Cambridge, UK: Cambridge University Press, 2022. DOI: 10.1017/9781009043243.

[2] D. Hanahan and R. A. Weinberg. 'The Hallmarks of Cancer'. *Cell* 100.1 (2000), 57–70. DOI: 10.1016/S0092-8674(00)81683-9.

[3] D. Hanahan and R. A. Weinberg. 'Hallmarks of Cancer: The Next Generation'. *Cell* 144.5 (2011), 646–674. DOI: 10.1016/j.cell.2011.02.013.

[4] R. Rubin. *Rubin's Pathology: Clinicopathologic Foundations of Medicine*. Ed. by D. S. Ph. D. Strayer, E. Rubin, J. M. M. D. McDonald and G. K. Ph. D. Michalopoulos. 5th edition. Philadelphia: Lippincott Williams & Wilkins, 2008.

[5] Y. Lazebnik. 'What Are the Hallmarks of Cancer?' *Nature Reviews Cancer* 10.4 (2010), 232–233. DOI: 10.1038/nrc2827.

[6] Surveillance, Epidemiology, and End Results (SEER) Program. *SEER Research Data*. 2023. URL: https://seer.cancer.gov/statfacts/.

[7] Cell editorial team. 'Cancer: Untangling Complexity Together'. *Cell* 186.8 (2023), 1513–1514. DOI: 10.1016/j.cell.2023.03.021.

[8] F. M. White, R. A. Gatenby and C. Fischbach. 'The Physics of Cancer'. *Cancer Research* 79.9 (2019), 2107–2110. DOI: 10.1158/0008-5472.CAN-18-3937.

[9] H. T. Nia, L. L. Munn and R. K. Jain. 'Physical Traits of Cancer'. *Science* 370.6516 (2020), eaaz0868. DOI: 10.1126/science.aaz0868.

[10] S. C. P. Williams. 'Capturing Cancer's Complexity'. *Proceedings of the National Academy of Sciences* 112.15 (2015), 4509–4511. DOI: 10.1073/pnas.1500963112.

[11] S. Maman and I. P. Witz. 'A History of Exploring Cancer in Context'. *Nature Reviews Cancer* 18.6 (2018), 359–376. DOI: 10.1038/s41568-018-0006-7.

[12] N. Howlader, A. M. Noone, M. Krapcho, N. Neyman, R. Aminou, W. Waldron, S. F. Altekruse, C. L. Kosary, J. Ruhl and Z. Tatalovich. 'SEER Cancer Statistics Review, 1975–2008'. *Bethesda, MD: National Cancer Institute* (2011), 140–143. URL: https://seer.cancer.gov/archive/csr/1975_2008/.

[13] T. E. Arpawong, S. H. Richeimer, F. Weinstein, A. Elghamrawy and J. E. Milam. 'Posttraumatic Growth, Quality of Life, and Treatment Symptoms among Cancer Chemotherapy Outpatients.' *Health Psychology* 32.4 (2013), 397–408. DOI: 10.1037/a0028223.

[14] F. Mols, A. J. J. M. Vingerhoets, J. W. Coebergh and L. V. van de Poll-Franse. 'Quality of Life among Long-Term Breast Cancer Survivors: A Systematic Review'. *European Journal of Cancer* 41.17 (2005), 2613–2619. DOI: 10.1016/j.ejca.2005.05.017.

[15] C. B. Harrington, J. A. Hansen, M. Moskowitz, B. L. Todd and M. Feuerstein. 'It's Not over When It's Over: Long-Term Symptoms in Cancer Survivors—A Systematic Review'. *The International Journal of Psychiatry in Medicine* 40.2 (2010), 163–181. DOI: 10.2190/PM.40.2.c.

[16] K. Shimizu and N. Oku. 'Cancer Anti-angiogenic Therapy'. *Biological and Pharmaceutical Bulletin* 27.5 (2004), 599–605. DOI: 10.1248/bpb.27.599.

[17] H. H. Wong and S. Halford. 'Dose-Limiting Toxicity and Maximum Tolerated Dose: Still Fit for Purpose?' *The Lancet Oncology* 16.13 (2015), 1287–1288. DOI: 10.1016/S1470-2045(15)00248-X.

[18] P. Ehrlich. 'The Harben Lectures, 1907. Experimental Researches on Specific Therapeutics'. *Journal of the Royal Institute of Public Health* 15.6 (1907), 321–340. URL: https://www.jstor.org/stable/45163479.

[19] P. Ehrlich. 'Aus Theorie und Praxis der Chemotherapie'. *Folia Serologica* 7 (1911), 698–714.

[20] J.-F. Chen, H.-M. Ding, J.-X. Wang and L. Shao. 'Preparation and Characterization of Porous Hollow Silica Nanoparticles for Drug Delivery Application'. *Biomaterials* 25.4 (2004), 723–727. DOI: 10.1016/S0142-9612(03)00566-0.

[21] Q. Dai, S. Wilhelm, D. Ding, A. M. Syed, S. Sindhwani, Y. Zhang, Y. Y. Chen, P. MacMillan and W. C. W. Chan. 'Quantifying the Ligand-Coated Nanoparticle Delivery to Cancer Cells in Solid Tumors'. *ACS Nano* 12.8 (2018), 8423–8435. DOI: 10.1021/acsnano.8b03900.

[22] C. Janko, S. Dürr, L. E. Munoz, S. Lyer, R. Chaurio, R. Tietze, S. V. Löhneysen, C. Schorn, M. Herrmann and C. Alexiou. 'Magnetic Drug Targeting Reduces the Chemotherapeutic Burden on Circulating Leukocytes'. *International Journal of Molecular Sciences* 14.4 (2013), 7341–7355. DOI: 10.3390/ijms14047341.

[23] R. Tietze, S. Lyer, S. Dürr, T. Struffert, T. Engelhorn, M. Schwarz, E. Eckert, T. Göen, S. Vasylyev, W. Peukert, F. Wiekhorst, L. Trahms *et al.* 'Efficient Drug-Delivery Using Magnetic Nanoparticles — Biodistribution and Therapeutic Effects in Tumour Bearing Rabbits'. *Nanomedicine: Nanotechnology, Biology and Medicine* 9.7 (2013), 961–971. DOI: 10.1016/J.NANO.2013.05.001.

[24] N. R. Stillman, M. Kovacevic, I. Balaz and S. Hauert. 'In Silico Modelling of Cancer Nanomedicine, across Scales and Transport Barriers'. *npj Computational Materials* 6.1 (2020), 1–10. DOI: 10.1038/s41524-020-00366-8.

[25] A. Gelman, J. B. Carlin, H. S. Stern, D. B. Dunson, A. Vehtari and D. B. Rubin. *Bayesian Data Analysis*. 3rd ed. New York: Chapman and Hall/CRC, 2013. DOI: 10.1201/b16018.

[26] R. C. Rockne, A. Hawkins-Daarud, K. R. Swanson, J. P. Sluka, J. A. Glazier, P. Macklin, D. A. Hormuth, A. M. Jarrett, E. A. B. F. Lima, J Tinsley Oden, G. Biros, T. E. Yankeelov *et al.* 'The 2019 Mathematical Oncology Roadmap'. *Physical Biology* 16.4 (2019), 41005. DOI: 10.1088/1478-3975/ab1a09.

[27] T. S. Deisboeck, Z. Wang, P. Macklin and V. Cristini. 'Multiscale Cancer Modeling'. *Annual Review of Biomedical Engineering* 13.1 (2011), 127–155. DOI: 10.1146/annurev-bioeng-071910-124729.

[28] B. Di Ventura, C. Lemerle, K. Michalodimitrakis and L. Serrano. 'From in Vivo to in Silico Biology and Back'. *Nature* 443.7111 (2006), 527–533. DOI: 10.1038/nature05127.

[29] B. B. Aldridge, J. M. Burke, D. A. Lauffenburger and P. K. Sorger. 'Physicochemical Modelling of Cell Signalling Pathways'. *Nature Cell Biology* 8.11 (2006), 1195–1203. DOI: 10.1038/ncb1497.

[30] J. Metzcar, Y. Wang, R. Heiland and P. Macklin. 'A Review of Cell-Based Computational Modeling in Cancer Biology'. *JCO Clinical Cancer Informatics* 3 (2019), 1–13. DOI: 10.1200/CCI.18.00069.

[31] C. M. Phillips, E. A. B. F. Lima, R. T. Woodall, A. Brock and T. E. Yankeelov. 'A Hybrid Model of Tumor Growth and Angiogenesis: In Silico Experiments'. *PLOS ONE* 15.4 (2020), e0231137. DOI: 10.1371/journal.pone.0231137.

[32] G. Sciumè, W. G. Gray, M. Ferrari, P. Decuzzi and B. A. Schrefler. 'On Computational Modeling in Tumor Growth'. *Archives of Computational Methods in Engineering* 20.4 (2013), 327–352. DOI: 10.1007/s11831-013-9090-8.

[33] G. Sciumè, R. Santagiuliana, M. Ferrari, P. Decuzzi and B. A. Schrefler. 'A Tumor Growth Model with Deformable ECM'. *Physical Biology* 11.6 (2014), 065004. DOI: 10.1088/1478-3975/11/6/065004.

[34] M. Ferrari. 'Frontiers in Cancer Nanomedicine: Directing Mass Transport through Biological Barriers'. *Trends in Biotechnology* 28.4 (2010), 181–188. DOI: 10.1016/j.tibtech.2009.12.007.

[35] E. J. Koay and M. Ferrari. 'Transport Oncophysics in Silico, in Vitro, and in Vivo'. *Physical Biology* 11.6 (2014), 060201. DOI: 10.1088/1478-3975/11/6/060201.

[36] S. Nizzero, A. Ziemys and M. Ferrari. 'Transport Barriers and Oncophysics in Cancer Treatment'. *Trends in Cancer* 4.4 (2018), 277–280. DOI: 10.1016/j.trecan.2018.02.008.

[37] S. Nizzero, H. Shen, M. Ferrari and B. Corradetti. 'Immunotherapeutic Transport Oncophysics: Space, Time, and Immune Activation in Cancer'. *Trends in Cancer* 6.1 (2020), 40–48. DOI: 10.1016/j.trecan.2019.11.008.

[38] D. K. Chatterjee, P. Diagaradjane and S. Krishnan. 'Nanoparticle-Mediated Hyperthermia in Cancer Therapy'. *Therapeutic Delivery* 2.8 (2011), 1001–1014. DOI: 10.4155/tde.11.72.

[39] Y. Li, Y. Lian, L. T. Zhang, S. M. Aldousari, H. S. Hedia, S. A. Asiri and W. K. Liu. 'Cell and Nanoparticle Transport in Tumour Microvasculature: The Role of Size, Shape and Surface Functionality of Nanoparticles'. *Interface Focus* 6.1 (2016), 20150086. DOI: 10.1098/rsfs.2015.0086.

[40] Y. Matsumura and H. Maeda. 'A New Concept for Macromolecular Therapeutics in Cancer Chemotherapy: Mechanism of Tumoritropic Accumulation of Proteins and the Antitumor Agent Smancs.' *Cancer Research* 46.12 (1986), 6387–6392.

[41] H. Maeda. 'The Enhanced Permeability and Retention (EPR) Effect in Tumor Vasculature: The Key Role of Tumor-Selective Macromolecular Drug Targeting'. *Advances in Enzyme Regulation* 41.1 (2001), 189–207. DOI: 10.1016/S0065-2571(00)00013-3.

[42] A. K. Iyer, G. Khaled, J. Fang and H. Maeda. 'Exploiting the Enhanced Permeability and Retention Effect for Tumor Targeting'. *Drug Discovery Today* 11.17-18 (2006), 812–818. DOI: 10.1016/J.DRUDIS.2006.07.005.

[43] Q. A. Pankhurst, J. Connolly, S. K. Jones and J. Dobson. 'Applications of Magnetic Nanoparticles in Biomedicine'. *Journal of Physics D: Applied Physics* 36.13 (2003), R167. DOI: 10.1088/0022-3727/36/13/201.

[44] A. Saltelli, ed. *Global Sensitivity Analysis: The Primer*. Chichester, England; Hoboken, NJ: John Wiley & Sons, Ltd., 2008. DOI: 10.1002/9780470725184.

[45] A. Saltelli, G. Bammer, I. Bruno, E. Charters, M. Di Fiore, E. Didier, W. Nelson Espeland, J. Kay, S. Lo Piano, D. Mayo, R. Pielke, T. Portaluri *et al.* 'Five Ways to Ensure That Models Serve Society: A Manifesto'. *Nature* 582.7813 (2020), 482–484. DOI: 10.1038/d41586-020-01812-9.

[46] A. Saltelli. 'Sensitivity Analysis for Importance Assessment'. *Risk Analysis* 22.3 (2002), 579–590. DOI: 10.1111/0272-4332.00040.

[47] A. Saltelli, ed. *Sensitivity Analysis in Practice: A Guide to Assessing Scientific Models*. Hoboken, NJ: John Wiley & Sons, Ltd., 2004.

[48] I. M. Sobol. 'Sensitivity Estimates for Nonlinear Mathematical Models'. *Mathematical modelling and computational experiments* 1.4 (1993), 407–414.

[49] I. M. Sobol. 'Global Sensitivity Indices for Nonlinear Mathematical Models and Their Monte Carlo Estimates'. *Mathematics and Computers in Simulation*. The Second IMACS Seminar on Monte Carlo Methods 55.1 (2001), 271–280. DOI: 10.1016/S0378-4754(00)00270-6.

[50] A. Saltelli, K. Aleksankina, W. Becker, P. Fennell, F. Ferretti, N. Holst, S. Li and Q. Wu. 'Why so Many Published Sensitivity Analyses Are False: A Systematic Review of Sensitivity Analysis Practices'. *Environmental Modelling & Software* 114 (2019), 29–39. DOI: 10.1016/j.envsoft.2019.01.012.

[51] C. E. Rasmussen and C. K. I. Williams. *Gaussian Processes for Machine Learning*. Cambridge, Massachusetts: The MIT Press, 2006. URL: http://www.gaussianprocess.org/gpml.

[52] L. Le Gratiet, C. Cannamela and B. Iooss. 'A Bayesian Approach for Global Sensitivity Analysis of (Multifidelity) Computer Codes'. *SIAM/ASA Journal on Uncertainty Quantification* 2.1 (2014), 336–363. DOI: 10.1137/130926869.

[53] K. Levenberg. 'A Method for the Solution of Certain Non-Linear Problems in Least Squares'. *Quarterly of Applied Mathematics* 2.2 (1944), 164–168. DOI: 10.1090/qam/10666.

[54] D. W. Marquardt. 'An Algorithm for Least-Squares Estimation of Nonlinear Parameters'. *Journal of the Society for Industrial and Applied Mathematics* 11.2 (1963), 431–441. DOI: 10.1137/0111030.

[55] P. Del Moral, A. Doucet and A. Jasra. 'Sequential Monte Carlo Samplers'. *Journal of the Royal Statistical Society. Series B (Statistical Methodology)* 68.3 (2006), 411–436. URL: https://www.jstor.org/stable/3879283.

[56] N. Chopin. 'A Sequential Particle Filter Method for Static Models'. *Biometrika* 89.3 (2002), 539–551. URL: https://www.jstor.org/stable/4140600.

[57] H.-D. Dau and N. Chopin. 'Waste-Free Sequential Monte Carlo'. *Journal of the Royal Statistical Society: Series B (Statistical Methodology)* 84.1 (2022), 114–148. DOI: 10.1111/rssb.12475.

[58] B. Wirthl, J. Kremheller, B. A. Schrefler and W. A. Wall. 'Extension of a Multiphase Tumour Growth Model to Study Nanoparticle Delivery to Solid Tumours'. *PLOS ONE* 15.2 (2020), e0228443. DOI: 10.1371/journal.pone.0228443.

[59] B. Wirthl, V. Wirthl and W. A. Wall. 'Efficient Computational Model of the In-Flow Capturing of Magnetic Nanoparticles by a Cylindrical Magnet for Cancer Nanomedicine'. *Physical Review E* 109.6 (2024), 065309. DOI: 10.1103/PhysRevE.109.065309.

[60] B. Wirthl, C. Janko, S. Lyer, B. A. Schrefler, C. Alexiou and W. A. Wall. 'An in silico model of the capturing of magnetic nanoparticles in tumour spheroids in the presence of flow'. *Biomedical Microdevices* 26.1 (2024). DOI: 10.1007/s10544-023-00685-9.

[61] B. Wirthl, S. Brandstaeter, J. Nitzler, B. A. Schrefler and W. A. Wall. 'Global Sensitivity Analysis Based on Gaussian-process Metamodelling for Complex Biomechanical Problems'. *International Journal for Numerical Methods in Biomedical Engineering* 39.3 (2023), e3675. DOI: 10.1002/cnm.3675.

[62] S. Hervas-Raluy, B. Wirthl, P. E. Guerrero, G. Robalo Rei, J. Nitzler, E. Coronado, J. F. de Mora Sainz, B. A. Schrefler, M. J. Gomez-Benito, J. M. Garcia-Aznar and W. A. Wall. 'Tumour Growth: An Approach to Calibrate Parameters of a Multiphase Porous Media Model Based on in Vitro Observations of Neuroblastoma Spheroid Growth in a Hydrogel Microenvironment'. *Computers in Biology and Medicine* 159 (2023), 106895. DOI: 10.1016/j.compbiomed.2023.106895.

[63] B. Wirthl. *Implementation of the Analytical Expressions for the Magnetic Field and Force of Finite-Length Cylindrical Permanent Magnet*. 2023. URL: https://github.com/bwirthl/cylindrical-magnet-functions.

[64] G. Sciumè, S. Shelton, W. Gray, C. Miller, F. Hussain, M. Ferrari, P. Decuzzi and B. Schrefler. 'Tumor Growth Modeling from the Perspective of Multiphase Porous Media Mechanics'. *MCB: Molecular & Cellular Biomechanics* 9.3 (2012), 193–212. DOI: 10.3970/MCB.2012.009.193.

[65] G. Sciumè, S. Shelton, W. G. Gray, C. T. Miller, F. Hussain, M. Ferrari, P. Decuzzi and B. A. Schrefler. 'A Multiphase Model for Three-Dimensional Tumor Growth'. *New Journal of Physics* 15 (2013). DOI: 10.1088/1367-2630/15/1/015005.

[66] G. Sciume. 'Thermo-Hygro-Chemo-Mechanical Model of Concrete At Early Ages and Its Extension To Tumor Growth Numerical Analysis'. PhD thesis. Padua, Paris: Università degli Studi di Padova, École normale supérieure de Cachan, 2013.

[67] G. Sciumè, W. G. Gray, F. Hussain, M. Ferrari, P. Decuzzi and B. A. Schrefler. 'Three Phase Flow Dynamics in Tumor Growth'. *Computational Mechanics* 53.3 (2014), 465–484. DOI: 10.1007/s00466-013-0956-2.

[68] G. Sciumè, M. Ferrari and B. A. Schrefler. 'Saturation–Pressure Relationships for Two- and Three-Phase Flow Analogies for Soft Matter'. *Mechanics Research Communications* 62 (2014), 132–137. DOI: 10.1016/j.mechrescom.2014.10.001.

[69] R. Santagiuliana, C. Stigliano, P. Mascheroni, M. Ferrari, P. Decuzzi and B. A. Schrefler. 'The Role of Cell Lysis and Matrix Deposition in Tumor Growth Modeling'. *Advanced Modeling and Simulation in Engineering Sciences* 2.19 (2015). DOI: 10.1186/s40323-015-0040-x.

[70] R. Santagiuliana, M. Ferrari and B. A. Schrefler. 'Simulation of Angiogenesis in a Multiphase Tumor Growth Model'. *Computer Methods in Applied Mechanics and Engineering* 304 (2016), 197–216. DOI: 10.1016/j.cma.2016.02.022.

[71] G. Sciumè. 'Mechanistic Modeling of Vascular Tumor Growth: An Extension of Biot's Theory to Hierarchical Bi-Compartment Porous Medium Systems'. *Acta Mechanica* 232.4 (2021), 1445–1478. DOI: 10.1007/s00707-020-02908-z.

[72] J. Kremheller, A.-T. Vuong, L. Yoshihara, W. A. Wall and B. A. Schrefler. 'A Monolithic Multiphase Porous Medium Framework for (a-)Vascular Tumor Growth'. *Computer Methods in Applied Mechanics and Engineering* 340 (2018), 657–683. DOI: 10.1016/j.cma.2018.06.009.

[73] J. Kremheller, A.-T. Vuong, B. A. Schrefler and W. A. Wall. 'An Approach for Vascular Tumor Growth Based on a Hybrid Embedded/Homogenized Treatment of the Vasculature within a Multiphase Porous Medium Model'. *International Journal for Numerical Methods in Biomedical Engineering* 35.11 (2019), e3253. DOI: 10.1002/cnm.3253.

[74] J. Kremheller, S. Brandstaeter, B. A. Schrefler and W. A. Wall. 'Validation and Parameter Optimization of a Hybrid Embedded/Homogenized Solid Tumor Perfusion Model'. *International Journal for Numerical Methods in Biomedical Engineering* 37.8 (2021), e3508. DOI: 10.1002/cnm.3508.

[75] J. J. Kremheller. 'Continuum-based Computational Approaches for Modeling Tumor Growth'. PhD thesis. München: Technische Universität München, 2021.

[76] J. Winkler, A. Abisoye-Ogunniyan, K. J. Metcalf and Z. Werb. 'Concepts of Extracellular Matrix Remodelling in Tumour Progression and Metastasis'. *Nature Communications* 11.1 (2020), 5120. DOI: 10.1038/s41467-020-18794-x.

[77] W. G. Gray and C. T. Miller. *Introduction to the Thermodynamically Constrained Averaging Theory for Porous Medium Systems*. Springer, 2014.

[78] C. T. Miller, F. J. Valdés-Parada and B. D. Wood. 'A Pedagogical Approach to the Thermodynamically Constrained Averaging Theory'. *Transport in Porous Media* 119.3 (2017), 585–609. DOI: 10.1007/s11242-017-0900-6.

[79] F. Pesavento, B. A. Schrefler and G. Sciumè. 'Multiphase Flow in Deforming Porous Media: A Review'. *Archives of Computational Methods in Engineering* (2016). DOI: 10.1007/s11831-016-9171-6.

[80] C. T. Miller and W. G. Gray. 'Thermodynamically Constrained Averaging Theory Approach for Modeling Flow and Transport Phenomena in Porous Medium Systems: 2. Foundation'. *Advances in Water Resources* 28.2 (2005), 181–202. DOI: 10.1016/J.ADVWATRES.2004.09.006.

[81] W. G. Gray, C. T. Miller and B. A. Schrefler. 'Averaging Theory for Description of Environmental Problems: What Have We Learned?' *Advances in Water Resources* 51 (2013), 123–138. DOI: 10.1016/j.advwatres.2011.12.005.

[82] C. T. Miller, W. G. Gray and B. A. Schrefler. 'A Continuum Mechanical Framework for Modeling Tumor Growth and Treatment in Two- and Three-Phase Systems'. *Archive of Applied Mechanics* (2021). DOI: 10.1007/s00419-021-01891-8.

[83] S. E. Shelton. 'Mechanistic Modeling of Cancer Tumor Growth Using a Porous Media Approach'. Master's Thesis. University of North Carolina at Chapel Hill, 2011.

[84] B. Yue. 'Biology of the Extracellular Matrix: An Overview'. *Journal of Glaucoma* 23 (2014), S20–S23. DOI: 10.1097/IJG.0000000000000108.

[85] O. Coussy. 'Thermodynamics'. In: *Poromechanics*. Hoboken, NJ, USA: John Wiley & Sons, Ltd, 2003, pp. 37–70. DOI: 10.1002/0470092718.ch3.

[86] J. Bear and Y. Bachmat. *Introduction to Modeling of Transport Phenomena in Porous Media*. Dordrecht, Boston, London: Springer Netherlands, 1990. DOI: 10.1007/978-94-009-1926-6_1.

[87] G. A. Holzapfel. *Nonlinear Solid Mechanics : A Continuum Approach for Engineering*. Hoboken, NJ, USA: John Wiley & Sons, Ltd., 2000.

[88] B. Babaei, A. J. Velasquez-Mao, K. M. Pryse, W. B. McConnaughey, E. L. Elson and G. M. Genin. 'Energy Dissipation in Quasi-Linear Viscoelastic Tissues, Cells, and Extracellular Matrix'. *Journal of the Mechanical Behavior of Biomedical Materials* 84 (2018), 198–207. DOI: 10.1016/j.jmbbm.2018.05.011.

[89] C. Valero, H. Amaveda, M. Mora and J. M. García-Aznar. 'Combined Experimental and Computational Characterization of Crosslinked Collagen-Based Hydrogels'. *PLOS ONE* 13.4 (2018), e0195820. DOI: 10.1371/journal.pone.0195820.

[90] A. Malandrino, M. Mak, R. D. Kamm and E. Moeendarbary. 'Complex Mechanics of the Heterogeneous Extracellular Matrix in Cancer'. *Extreme Mechanics Letters* 21 (2018), 25–34. DOI: 10.1016/j.eml.2018.02.003.

[91] G. A. Holzapfel and T. C. Gasser. 'A Viscoelastic Model for Fiber-Reinforced Composites at Finite Strains: Continuum Basis, Computational Aspects and Applications'. *Computer Methods in Applied Mechanics and Engineering* 190.34 (2001), 4379–4403. DOI: 10.1016/S0045-7825(00)00323-6.

[92] G. Vilanova, M. Burés, I. Colominas and H. Gomez. 'Computational Modelling Suggests Complex Interactions between Interstitial Flow and Tumour Angiogenesis'. *Journal of The Royal Society Interface* 15.146 (2018), 20180415. DOI: 10.1098/rsif.2018.0415.

[93] A. Moure, G. Vilanova and H. Gomez. 'Inverting Angiogenesis with Interstitial Flow and Chemokine Matrix-Binding Affinity'. *Scientific Reports* 12.1 (2022), 4237. DOI: 10.1038/s41598-022-08186-0.

[94] J. Donea, A. Huerta, J.-P. Ponthot and A. Rodriguez-Ferran. 'Arbitrary Lagrangian–Eulerian Methods'. In: *Encyclopedia of Computational Mechanics*. Hoboken, NJ, USA: John Wiley & Sons, Ltd., 2004. Chap. 14. DOI: 10.1002/0470091355.ecm009.

[95] S. Whitaker. 'Flow in Porous Media I: A Theoretical Derivation of Darcy's Law'. *Transport in Porous Media* 1.1 (1986), 3–25. DOI: 10.1007/BF01036523.

[96] I. Tice. *From Stokes Flow to Darcy's Law*. Carnegie Mellon University, 2014. URL: https://www.math.cmu.edu/~iantice/notes/stokes_to_darcy.pdf.

[97] A.-T. Vuong. 'Computational Approach to Coupled Poroelastic Media Problems'. PhD thesis. München: Technische Universität München, 2016.

[98] R. H. Brooks and A. T. Corey. 'Properties of Porous Media Affecting Fluid Flow'. *Journal of the Irrigation and Drainage Division* 92.2 (1966), 61–88. DOI: 10.1061/JRCEA4.0000425.

[99] J. C. Parker and R. J. Lenhard. 'A Model for Hysteretic Constitutive Relations Governing Multiphase Flow: 1. Saturation-pressure Relations'. *Water Resources Research* 23.12 (1987), 2187–2196. DOI: 10.1029/WR023i012p02187.

[100] D. W. Siemann. 'The Unique Characteristics of Tumor Vasculature and Preclinical Evidence for Its Selective Disruption by Tumor-Vascular Disrupting Agents'. *Cancer Treatment Reviews* 37.1 (2011), 63–74. DOI: 10.1016/j.ctrv.2010.05.001.

[101] J.-P. Gratton, M. I. Lin, J. Yu, E. D. Weiss, Z. L. Jiang, T. A. Fairchild, Y. Iwakiri, R. Groszmann, K. P. Claffey, Y.-C. Cheng and W. C. Sessa. 'Selective Inhibition of Tumor Microvascular Permeability by Cavtratin Blocks Tumor Progression in Mice'. *Cancer Cell* 4.1 (2003), 31–39. DOI: 10.1016/S1535-6108(03)00168-5.

[102] H. Hashizume, P. Baluk, S. Morikawa, J. W. McLean, G. Thurston, S. Roberge, R. K. Jain and D. M. McDonald. 'Openings between Defective Endothelial Cells Explain Tumor Vessel Leakiness'. *The American Journal of Pathology* 156.4 (2000), 1363–1380. DOI: 10.1016/S0002-9440(10)65006-7.

[103] C.-H. Heldin, K. Rubin, K. Pietras and A. Östman. 'High Interstitial Fluid Pressure — an Obstacle in Cancer Therapy'. *Nature Reviews Cancer* 4.10 (2004), 806–813. DOI: 10.1038/nrc1456.

[104] J. Folkman. 'Tumor Angiogenesis: Therapeutic Implications'. *New England Journal of Medicine* 285.21 (1971), 1182–1186. DOI: 10.1056/NEJM197111182852108.

[105] N. Weidner, J. P. Semple, W. R. Welch and J. Folkman. 'Tumor Angiogenesis and Metastasis — Correlation in Invasive Breast Carcinoma'. *New England Journal of Medicine* 324.1 (1991), 1–8. DOI: 10.1056/NEJM199101033240101.

[106] S. M. Weis and D. A. Cheresh. 'Tumor Angiogenesis: Molecular Pathways and Therapeutic Targets'. *Nature Medicine* 17.11 (2011), 1359–1370. DOI: 10.1038/nm.2537.

[107] T. Stylianopoulos and R. K. Jain. 'Combining Two Strategies to Improve Perfusion and Drug Delivery in Solid Tumors.' *Proceedings of the National Academy of Sciences of the United States of America* 110.46 (2013), 18632–18637. DOI: 10.1073/pnas.1318415110.

[108] T. P. Padera, A. Kadambi, E. di Tomaso, C. M. Carreira, E. B. Brown, Y. Boucher, N. C. Choi, D. Mathisen, J. Wain, E. J. Mark, L. L. Munn and R. K. Jain. 'Lymphatic Metastasis in the Absence of Functional Intratumor Lymphatics'. *Science* 296.5574 (2002), 1883–1886. DOI: 10.1126/science.1071420.

[109] K. Alitalo and P. Carmeliet. 'Molecular Mechanisms of Lymphangiogenesis in Health and Disease'. *Cancer Cell* 1.3 (2002), 219–227. DOI: 10.1016/S1535-6108(02)00051-X.

[110] T. P. Padera, B. R. Stoll, J. B. Tooredman, D. Capen, E. di Tomaso and R. K. Jain. 'Cancer Cells Compress Intratumour Vessels'. *Nature* 427.6976 (2004), 695–695. DOI: 10.1038/427695a.

[111] M. Wu, H. B. Frieboes, S. R. McDougall, M. A. Chaplain, V. Cristini and J. Lowengrub. 'The Effect of Interstitial Pressure on Tumor Growth: Coupling with the Blood and Lymphatic Vascular Systems'. *Journal of Theoretical Biology* 320 (2013), 131–151. DOI: 10.1016/J.JTBI.2012.11.031.

[112] F. Verdugo and W. A. Wall. 'Unified Computational Framework for the Efficient Solution of N-Field Coupled Problems with Monolithic Schemes'. *Computer Methods in Applied Mechanics and Engineering* 310 (2016), 335–366. DOI: 10.1016/j.cma.2016.07.016.

[113] F. Verdugo, C. J. Roth, L. Yoshihara and W. A. Wall. 'Efficient Solvers for Coupled Models in Respiratory Mechanics'. *International Journal for Numerical Methods in Biomedical Engineering* 33.2 (2017), e02795. DOI: 10.1002/cnm.2795.

[114] R. Fang, M. Kronbichler, M. Wurzer and W. A. Wall. 'Parallel, Physics-Oriented, Monolithic Solvers for Three-Dimensional, Coupled Finite Element Models of Lithium-Ion Cells'. *Computer Methods in Applied Mechanics and Engineering* 350 (2019), 803–835. DOI: 10.1016/j.cma.2019.03.017.

[115] BACI. *A Comprehensive Multi-Physics Simulation Framework*. 2023. URL: https://baci.pages.gitlab.lrz.de/website/.

[116] A. N. Brooks and T. J. R. Hughes. 'Streamline Upwind/Petrov-Galerkin Formulations for Convection Dominated Flows with Particular Emphasis on the Incompressible Navier-Stokes Equations'. *Computer Methods in Applied Mechanics and Engineering* 32.1 (1982), 199–259. DOI: 10.1016/0045-7825(82)90071-8.

[117] R. Codina. 'Stabilized Finite Element Approximation of Transient Incompressible Flows Using Orthogonal Subscales'. *Computer Methods in Applied Mechanics and Engineering* 191.39 (2002), 4295–4321. DOI: 10.1016/S0045-7825(02)00337-7.

[118] R. Chignola, A. Schenetti, G. Andrighetto, E. Chiesa, R. Foroni, S. Sartoris, G. Tridente and D. Liberati. 'Forecasting the Growth of Multicell Tumour Spheroids: Implications for the Dynamic Growth of Solid Tumours'. *Cell Proliferation* 33.4 (2000), 219–229. DOI: 10.1046/j.1365-2184.2000.00174.x.

[119] T. W. Secomb, R. Hsu, R. D. Braun, J. R. Ross, J. F. Gross and M. W. Dewhirst. 'Theoretical Simulation of Oxygen Transport to Tumors by Three-Dimensional Networks of Microvessels'. In: *Oxygen Transport to Tissue XX*. Ed. by A. G. Hudetz and D. F. Bruley. Advances in Experimental Medicine and Biology. Boston, MA: Springer US, 1998, pp. 629–634. DOI: 10.1007/978-1-4615-4863-8_74.

[120] T. W. Secomb. *Three-Dimensional Network Data: Rat Tumor*. 1998. URL: https://physiology.arizona.edu/people/secomb/network/rattum98.

[121] R. K. Jain. 'Determinants of Tumor Blood Flow: A Review'. *Cancer Research* 48.10 (1988), 2641–2658.

[122] T. Stylianopoulos, J. D. Martin, V. P. Chauhan, S. R. Jain, B. Diop-Frimpong, N. Bardeesy, B. L. Smith, C. R. Ferrone, F. J. Hornicek, Y. Boucher, L. L. Munn and R. K. Jain. 'Causes, Consequences, and Remedies for Growth-Induced Solid Stress in Murine and Human Tumors'. *Proceedings of the National Academy of Sciences* 109.38 (2012), 15101–15108. DOI: 10.1073/pnas.1213353109.

[123] P. P. Provenzano, C. Cuevas, A. E. Chang, V. K. Goel, D. D. Von Hoff and S. R. Hingorani. 'Enzymatic Targeting of the Stroma Ablates Physical Barriers to Treatment of Pancreatic Ductal Adenocarcinoma'. *Cancer Cell* 21.3 (2012), 418–429. DOI: 10.1016/J.CCR.2012.01.007.

[124] V. P. Chauhan, Y. Boucher, C. R. Ferrone, S. Roberge, J. D. Martin, T. Stylianopoulos, N. Bardeesy, R. A. DePinho, T. P. Padera, L. L. Munn and R. K. Jain. 'Compression of Pancreatic Tumor Blood Vessels by Hyaluronan Is Caused by Solid Stress and Not Interstitial Fluid Pressure.' *Cancer Cell* 26.1 (2014), 14–5. DOI: 10.1016/j.ccr.2014.06.003.

[125] V. Vavourakis, T. Stylianopoulos and P. A. Wijeratne. 'In-Silico Dynamic Analysis of Cytotoxic Drug Administration to Solid Tumours: Effect of Binding Affinity and Vessel Permeability'. *PLOS Computational Biology* 14.10 (2018), e1006460. DOI: 10.1371/journal.pcbi.1006460.

[126] S. Cui. 'Formation of Necrotic Cores in the Growth of Tumors: Analytic Results'. *Acta Mathematica Scientia* 26.4 (2006), 781–796. DOI: 10.1016/S0252-9602(06)60104-5.

[127] P. Macklin, S. McDougall, A. R. A. Anderson, M. A. J. Chaplain, V. Cristini and J. Lowengrub. 'Multiscale Modelling and Nonlinear Simulation of Vascular Tumour Growth'. *Journal of Mathematical Biology* 58.4 (2009), 765–798. DOI: 10.1007/s00285-008-0216-9.

[128] P. Carmeliet and R. K. Jain. 'Angiogenesis in Cancer and Other Diseases'. *Nature* 407.6801 (2000), 249–257. DOI: 10.1038/35025220.

[129] M. W. Dewhirst and T. W. Secomb. 'Transport of Drugs from Blood Vessels to Tumour Tissue'. *Nature Reviews Cancer* 17 (2017), 738. DOI: 10.1038/nrc.2017.93.

[130] R. K. Jain, R. T. Tong and L. L. Munn. 'Effect of Vascular Normalization by Antiangiogenic Therapy on Interstitial Hypertension, Peritumor Edema, and Lymphatic Metastasis:Insights from a Mathematical Model'. *Cancer Research* 67.6 (2007), 2729–2735. DOI: 10.1158/0008-5472.can-06-4102.

[131] Y. Boucher, L. T. Baxter and R. K. Jain. 'Interstitial Pressure Gradients in Tissue-Isolated and Subcutaneous Tumors: Implications for Therapy.' *Cancer Research* 50.15 (1990), 4478–4484.

[132] B. Lince Valadares Onofre. 'Computational Modelling of Interactions between Interstitial Fluid Flow and Angiogenesis in Solid Tumours'. Term Paper. München: Technische Universität München, 2023.

[133] B. Lince Valadares Onofre. 'Computational Modelling of Angiogenesis Governed by the Tumour Microenvironment'. Master's Thesis. München: Technische Universität München, 2023.

[134] C. P. Ng, C.-L. E. Helm and M. A. Swartz. 'Interstitial Flow Differentially Stimulates Blood and Lymphatic Endothelial Cell Morphogenesis in Vitro'. *Microvascular Research* 68.3 (2004), 258–264. DOI: 10.1016/j.mvr.2004.08.002.

[135] C.-L. E. Helm, M. E. Fleury, A. H. Zisch, F. Boschetti and M. A. Swartz. 'Synergy between Interstitial Flow and VEGF Directs Capillary Morphogenesis in Vitro through a Gradient Amplification Mechanism'. *Proceedings of the National Academy of Sciences* 102.44 (2005), 15779–15784. DOI: 10.1073/pnas.0503681102.

[136] S. Kim, M. Chung, J. Ahn, S. Lee and N. L. Jeon. 'Interstitial Flow Regulates the Angiogenic Response and Phenotype of Endothelial Cells in a 3D Culture Model'. *Lab on a Chip* 16.21 (2016), 4189–4199. DOI: 10.1039/C6LC00910G.

[137] V. S. Shirure, A. Lezia, A. Tao, L. F. Alonzo and S. C. George. 'Low Levels of Physiological Interstitial Flow Eliminate Morphogen Gradients and Guide Angiogenesis'. *Angiogenesis* 20.4 (2017), 493–504. DOI: 10.1007/s10456-017-9559-4.

[138] Y. Abe, M. Watanabe, S. Chung, R. D. Kamm, K. Tanishita and R. Sudo. 'Balance of Interstitial Flow Magnitude and Vascular Endothelial Growth Factor Concentration Modulates Three-Dimensional Microvascular Network Formation'. *APL Bioengineering* 3.3 (2019). DOI: 10.1063/1.5094735.

[139] J. W. Song and L. L. Munn. 'Fluid Forces Control Endothelial Sprouting'. *Proceedings of the National Academy of Sciences* 108.37 (2011), 15342–15347. DOI: 10.1073/pnas.1105316108.

[140] M. Aubert, M. A. J. Chaplain, S. R. McDougall, A. Devlin and C. A. Mitchell. 'A Continuum Mathematical Model of the Developing Murine Retinal Vasculature'. *Bulletin of Mathematical Biology* 73.10 (2011), 2430–2451. DOI: 10.1007/s11538-011-9631-y.

[141] B. Wirthl. 'Modelling of Drug Delivery and Hyperthermia Treatment in a Multiphase Tumour Growth Model'. Master's Thesis. München: Technische Universität München, 2018.

[142] D. Peer, J. M. Karp, S. Hong, O. C. Farokhzad, R. Margalit and R. Langer. 'Nanocarriers as an Emerging Platform for Cancer Therapy'. *Nature Nanotechnology* 2.12 (2007), 751–760. DOI: 10.1038/nnano.2007.387.

[143] J. M. de la Fuente, V Grazu and R. E. Palmer, eds. *Nanobiotechnology: Inorganic Nanoparticles Vs Organic Nanoparticles*. 1st ed. Vol. 4. Frontier of Nanoscience. Oxford, UK: Elsevier Ltd., 2012.

[144] B. Bahrami, M. Hojjat-Farsangi, H. Mohammadi, E. Anvari, G. Ghalamfarsa, M. Yousefi and F. Jadidi-Niaragh. 'Nanoparticles and Targeted Drug Delivery in Cancer Therapy'. *Immunology Letters* 190 (2017), 64–83. DOI: 10.1016/J.IMLET.2017.07.015.

[145] S. Dürr, C. Janko, S. Lyer, P. Tripal, M. Schwarz, J. Zaloga, R. Tietze and C. Alexiou. 'Magnetic Nanoparticles for Cancer Therapy'. *Nanotechnology Reviews* 2.4 (2013), 395–409. DOI: 10.1515/ntrev-2013-0011.

[146] O. L. Gobbo, K. Sjaastad, M. W. Radomski, Y. Volkov and A. Prina-Mello. 'Magnetic Nanoparticles in Cancer Theranostics'. *Theranostics* 5.11 (2015), 1249–1263. DOI: 10.7150/thno.11544.

[147] A. Farzin, S. A. Etesami, J. Quint, A. Memic and A. Tamayol. 'Magnetic Nanoparticles in Cancer Therapy and Diagnosis'. *Advanced Healthcare Materials* 9.9 (2020), 1901058. DOI: 10.1002/adhm.201901058.

[148] Y. H. Bae and K. Park. 'Targeted Drug Delivery to Tumors: Myths, Reality and Possibility'. *Journal of Controlled Release* 153.3 (2011), 198–205. DOI: 10.1016/j.jconrel.2011.06.001.

[149] C. von Roemeling, W. Jiang, C. K. Chan, I. L. Weissman and B. Y. S. Kim. 'Breaking Down the Barriers to Precision Cancer Nanomedicine'. *Trends in Biotechnology* 35.2 (2017), 159–171. DOI: 10.1016/j.tibtech.2016.07.006.

[150] K. Park. 'The Beginning of the End of the Nanomedicine Hype'. *Journal of Controlled Release* 305 (2019), 221–222. DOI: 10.1016/j.jconrel.2019.05.044.

[151] E. Blanco, H. Shen and M. Ferrari. 'Principles of Nanoparticle Design for Overcoming Biological Barriers to Drug Delivery.' *Nature biotechnology* 33.9 (2015), 941–51. DOI: 10.1038/nbt.3330.

[152] X. He, Y. Yang, Y. Han, C. Cao, Z. Zhang, L. Li, C. Xiao, H. Guo, L. Wang, L. Han, Z. Qu, N. Liu *et al.* 'Extracellular Matrix Physical Properties Govern the Diffusion of Nanoparticles in Tumor Microenvironment'. *Proceedings of the National Academy of Sciences* 120.1 (2023), e2209260120. DOI: 10.1073/pnas.2209260120.

[153] J. Friedrich, C. Seidel, R. Ebner and L. A. Kunz-Schughart. 'Spheroid-Based Drug Screen: Considerations and Practical Approach'. *Nature Protocols* 4.3 (2009), 309–324. DOI: 10.1038/nprot.2008.226.

[154] A. S. Nunes, A. S. Barros, E. C. Costa, A. F. Moreira and I. J. Correia. '3D Tumor Spheroids as in Vitro Models to Mimic in Vivo Human Solid Tumors Resistance to Therapeutic Drugs'. *Biotechnology and Bioengineering* 116.1 (2019), 206–226. DOI: 10.1002/bit.26845.

[155] F. Hirschhaeuser, H. Menne, C. Dittfeld, J. West, W. Mueller-Klieser and L. A. Kunz-Schughart. 'Multicellular Tumor Spheroids: An Underestimated Tool Is Catching up Again'. *Journal of Biotechnology*. Organotypic Tissue Culture for Substance Testing 148.1 (2010), 3–15. DOI: 10.1016/j.jbiotec.2010.01.012.

[156] L. T. Curtis, M. Wu, J. Lowengrub, P. Decuzzi and H. B. Frieboes. 'Computational Modeling of Tumor Response to Drug Release from Vasculature-Bound Nanoparticles'. *PLOS ONE* (2015). DOI: 10.1371/journal.pone.0144888.

[157] Y. Feng, D. Fuentes, A. Hawkins, J. Bass, M. N. Rylander, A. Elliott, A. Shetty, R. J. Stafford and J. T. Oden. 'Nanoshell-Mediated Laser Surgery Simulation for Prostate Cancer Treatment'. *Engineering with Computers* 25.1 (2009), 3–13. DOI: 10.1007/s00366-008-0109-y.

[158] M. Nabil, P. Decuzzi and P. Zunino. 'Modelling Mass and Heat Transfer in Nano-Based Cancer Hyperthermia'. *Royal Society Open Science* 2.10 (2015), 150447. DOI: 10.1098/rsos.150447.

[159] E. Tasciotti, X. Liu, R. Bhavane, K. Plant, A. D. Leonard, B. K. Price, M. M. C. Cheng, P. Decuzzi, J. M. Tour, F. Robertson and M. Ferrari. 'Mesoporous Silicon Particles as a Multistage Delivery System for Imaging and Therapeutic Applications'. *Nature Nanotechnology* 3.3 (2008), 151–157. DOI: 10.1038/nnano.2008.34.

[160] A. Venuta, J. Wolfram, H. Shen and M. Ferrari. 'Post-Nano Strategies for Drug Delivery: Multistage Porous Silicon Microvectors'. *Journal of Materials Chemistry B* 5.2 (2017), 207–219. DOI: 10.1039/C6TB01978A.

[161] M. Nabil and P. Zunino. 'A Computational Study of Cancer Hyperthermia Based on Vascular Magnetic Nanoconstructs'. *Royal Society Open Science* 3.9 (2016), 160287. DOI: 10.1098/rsos.160287.

[162] J. R. Levick and C. C. Michel. 'Microvascular Fluid Exchange and the Revised Starling Principle'. *Cardiovascular Research* 87.2 (2010), 198–210. DOI: 10.1093/cvr/cvq062.

[163] S. Wilhelm, A. J. Tavares, Q. Dai, S. Ohta, J. Audet, H. F. Dvorak and W. C. W. Chan. 'Analysis of Nanoparticle Delivery to Tumours'. *Nature Reviews Materials* 1.5 (2016), 16014. DOI: 10.1038/natrevmats.2016.14.

[164] S. M. Moghimi and D. Simberg. 'Nanoparticle Transport Pathways into Tumors'. *Journal of Nanoparticle Research* 20.6 (2018), 169. DOI: 10.1007/s11051-018-4273-8.

[165] O. Kedem and A. Katchalsky. 'A Physical Interpretation of the Phenomenological Coefficients of Membrane Permeability'. *Journal of General Physiology* 45.1 (1961), 143–179. DOI: 10.1085/jgp.45.1.143.

[166] O. Kedem and A. Katchalsky. 'Permeability of Composite Membranes. Part 3.—Series Array of Elements'. *Transactions of the Faraday Society* 59.0 (1963), 1941–1953. DOI: 10.1039/TF9635901941.

[167] A. Katchalsky and P. F. Curran. 'Nonequilibrium Thermodynamics in Biophysics'. In: *Nonequilibrium Thermodynamics in Biophysics*. Harvard University Press, 1965. DOI: 10.4159/harvard.9780674494121.

[168] R. K. Jain. 'Transport of Molecules across Tumor Vasculature'. *Cancer and Metastasis Review* 6.4 (1987), 559–593. DOI: 10.1007/BF00047468.

[169] R. K. Jain and T. Stylianopoulos. 'Delivering Nanomedicine to Solid Tumors'. *Nature Reviews Clinical Oncology* 7.11 (2010), 653–664. DOI: 10.1038/nrclinonc.2010.139.

[170] R. K. Jain. 'Delivery of Molecular and Cellular Medicine to Solid Tumors'. *Advanced Drug Delivery Reviews* 46.1-3 (2002), 149–168. DOI: 10.1016/s0169-409x(00)00131-9.

[171] P. Mascheroni and B. A. Schrefler. 'In Silico Models for Nanomedicine: Recent Developments'. *Current Medicinal Chemistry* 25.34 (2018), 4192–4207. DOI: 10.2174/0929867324666170417120725.

[172] A. Ziemys, K. Yokoi, M. Kai, Y. T. Liu, M. Kojic, V. Simic, M. Milosevic, A. Holder and M. Ferrari. 'Progression-Dependent Transport Heterogeneity of Breast Cancer Liver Metastases as a Factor in Therapeutic Resistance'. *Journal of Controlled Release* 291 (2018), 99–105. DOI: 10.1016/j.jconrel.2018.10.014.

[173] T. A. Ahmed. 'Pharmacokinetics of Drugs Following IV Bolus, IV Infusion, and Oral Administration'. In: *Basic Pharmacokinetic Concepts and Some Clinical Applications*. IntechOpen, 2015.

[174] G. S. Terentyuk, G. N. Maslyakova, L. V. Suleymanova, N. G. Khlebtsov, B. N. Khlebtsov, G. G. Akchurin, I. L. Maksimova and V. V. Tuchin. 'Laser-Induced Tissue Hyperthermia Mediated by Gold Nanoparticles: Toward Cancer Phototherapy'. *Journal of Biomedical Optics* 14.2 (2009), 021016. DOI: 10.1117/1.3122371.

[175] Y. T. Ho, G. Adriani, S. Beyer, P.-T. Nhan, R. D. Kamm and J. C. Y. Kah. 'A Facile Method to Probe the Vascular Permeability of Nanoparticles in Nanomedicine Applications'. *Scientific Reports* 7.1 (2017), 707. DOI: 10.1038/s41598-017-00750-3.

[176] M. R. Dreher, W. Liu, C. R. Michelich, M. W. Dewhirst, F. Yuan and A. Chilkoti. 'Tumor Vascular Permeability, Accumulation, and Penetration of Macromolecular Drug Carriers'. *JNCI: Journal of the National Cancer Institute* 98.5 (2006), 335–344. DOI: 10.1093/jnci/djj070.

[177] C.-Y. Chou, C.-K. Huang, K.-W. Lu, T.-L. Horng and W.-L. Lin. 'Investigation of the Spatiotemporal Responses of Nanoparticles in Tumor Tissues with a Small-Scale Mathematical Model'. *PLOS ONE* 8.4 (2013). Ed. by J. S. Burns, e59135. DOI: 10.1371/journal.pone.0059135.

[178] B. Müller, S. Lang, M. Dominietto, M. Rudin, G. Schulz, H. Deyhle, M. Germann, F. Pfeiffer, C. David and T. Weitkamp. 'High-Resolution Tomographic Imaging of Microvessels'. *Developments in X-Ray Tomography VI* 7078 (2008), 70780B. DOI: 10.1117/12.794157.

[179] J. W. Nichols and Y. H. Bae. 'EPR: Evidence and Fallacy'. *Journal of Controlled Release* 190 (2014), 451–464. DOI: 10.1016/J.JCONREL.2014.03.057.

[180] F. Danhier. 'To Exploit the Tumor Microenvironment: Since the EPR Effect Fails in the Clinic, What Is the Future of Nanomedicine?' *Journal of Controlled Release* 244 (2016), 108–121. DOI: 10.1016/J.JCONREL.2016.11.015.

[181] L. T. Baxter and R. K. Jain. 'Transport of Fluid and Macromolecules in Tumors. I. Role of Interstitial Pressure and Convection'. *Microvascular Research* 37.1 (1989), 77–104. DOI: 10.1016/0026-2862(89)90074-5.

[182] M. Stohrer, Y. Boucher, M. Stangassinger and R. K. Jain. 'Oncotic Pressure in Solid Tumors Is Elevated'. *Cancer Research* 60.15 (2000), 4251–4255.

[183] R. T. Tong, Y. Boucher, S. Kozin, F. Winkler, D. Hicklin and R. K. Jain. 'Vascular Normalization by Vascular Endothelial Growth Factor Receptor 2 Blockade Induces a Pressure Gradient Across the Vasculature and Improves Drug Penetration in Tumors'. *Cancer Research* 64.617 (2004), 3731–3736. DOI: 10.1158/0008-5472.CAN-04-0074.

[184] Y.-R. Zhang, R. Lin, H.-J. Li, W.-l. He, J.-Z. Du and J. Wang. 'Strategies to Improve Tumor Penetration of Nanomedicines through Nanoparticle Design'. *Wiley Interdisciplinary Reviews: Nanomedicine and Nanobiotechnology* 11.1 (2019), e1519. DOI: 10.1002/wnan.1519.

[185] S. Goel, D. G. Duda, L. Xu, L. L. Munn, Y. Boucher, D. Fukumura and R. K. Jain. 'Normalization of the Vasculature for Treatment of Cancer and Other Diseases'. *Physiological Reviews* 91.3 (2011), 1071–1121. DOI: 10.1152/physrev.00038.2010.

[186] V. P. Chauhan, T. Stylianopoulos, J. D. Martin, Z. Popović, O. Chen, W. S. Kamoun, M. G. Bawendi, D. Fukumura and R. K. Jain. 'Normalization of Tumour Blood Vessels Improves the Delivery of Nanomedicines in a Size-Dependent Manner'. *Nature Nanotechnology* 7.6 (2012), 383–388. DOI: 10.1038/nnano.2012.45.

[187] L. T. Baxter and R. K. Jain. 'Transport of Fluid and Macromolecules in Tumors. II. Role of Heterogeneous Perfusion and Lymphatics'. *Microvascular Research* 40.2 (1990), 246–263. DOI: 10.1016/0026-2862(90)90023-K.

[188] F. Danhier and V. Preat. 'Strategies to Improve the EPR Effect for the Delivery of Anti-Cancer Nanomedicines'. *Cancer Cell & Microenvironment* 2.3 (2015), 1–7. DOI: 10.14800/ccm.808.

[189] J. E. Moore and C. D. Bertram. 'Lymphatic System Flows'. *Annual Review of Fluid Mechanics* 50.1 (2018), 459–482. DOI: 10.1146/annurev-fluid-122316-045259.

[190] R. J. Shipley and S. J. Chapman. 'Multiscale Modelling of Fluid and Drug Transport in Vascular Tumours'. *Bulletin of Mathematical Biology* 72 (2010), 1464–1491. DOI: 10.1007/s11538-010-9504-9.

[191] R. J. Gillies, P. A. Schomack, T. W. Secomb and N. Raghunand. 'Causes and Effects of Heterogeneous Perfusion in Tumors'. *Neoplasia* 1.3 (1999), 197–207. DOI: 10.1038/SJ.NEO.7900037.

[192] S. Purushotham and R. V. Ramanujan. 'Modeling the Performance of Magnetic Nanoparticles in Multimodal Cancer Therapy'. *Journal of Applied Physics* 107.114701 (2010). DOI: 10.1063/1.3432757.

[193] L. Rast and J. G. Harrison. 'Computational Modeling of Electromagnetically Induced Heating of Magnetic Nanoparticle Materials for Hyperthermic Cancer Treatment'. *PIERS Online* 6.7 (2010), 690–694. DOI: 10.2529/PIERS091218133748.

[194] R. K. Jain. 'Normalization of Tumor Vasculature: An Emerging Concept in Antiangiogenic Therapy'. *Science* 307.5706 (2005), 58–62. DOI: 10.1126/science.1104819.

[195] G. G. Flores-Rojas, F. López-Saucedo, R. Vera-Graziano, E. Mendizabal and E. Bucio. 'Magnetic Nanoparticles for Medical Applications: Updated Review'. *Macromol* 2.3 (2022), 374–390. DOI: 10.3390/macromol2030024.

[196] J. Dobson. 'Magnetic Nanoparticles for Drug Delivery'. *Drug Development Research* 67.1 (2006), 55–60. DOI: 10.1002/ddr.20067.

[197] V. V. Mody, A. Singh and B. Wesley. 'Basics of Magnetic Nanoparticles for Their Application in the Field of Magnetic Fluid Hyperthermia'. *European Journal of Nanomedicine* 5.1 (2013), 11–21. DOI: 10.1515/ejnm-2012-0008.

[198] L. C. Barnsley, D. Carugo, J. Owen and E. Stride. 'Halbach Arrays Consisting of Cubic Elements Optimised for High Field Gradients in Magnetic Drug Targeting Applications'. *Physics in Medicine & Biology* 60.21 (2015), 8303. DOI: 10.1088/0031-9155/60/21/8303.

[199] A. D. Grief and G. Richardson. 'Mathematical Modelling of Magnetically Targeted Drug Delivery'. *Journal of Magnetism and Magnetic Materials*. Proceedings of the Fifth International Conference on Scientific and Clinical Apllications of Magnetic Carriers 293.1 (2005), 455–463. DOI: 10.1016/j.jmmm.2005.02.040.

[200] J. Behr, L. R. Carnell, R. Stein, F. Pfister, B. Friedrich, C. Huber, S. Lyer, J. Band, E. Schreiber, C. Alexiou and C. Janko. 'In Vitro Setup for Determination of Nanoparticle-Mediated Magnetic Cell and Drug Accumulation in Tumor Spheroids under Flow Conditions'. *Cancers* 14.23 (2022), 5978. DOI: 10.3390/cancers14235978.

[201] M. Welter and H. Rieger. 'Interstitial Fluid Flow and Drug Delivery in Vascularized Tumors: A Computational Model'. *PLOS ONE* 8.8 (2013). DOI: 10.1371/journal.pone.0070395.

[202] L. Cattaneo and P. Zunino. 'A Computational Model of Drug Delivery through Microcirculation to Compare Different Tumor Treatments'. *International Journal for Numerical Methods in Biomedical Engineering* 30.11 (2014), 1347–1371. DOI: 10.1002/cnm.2661.

[203] A. Karolak, D. A. Markov, L. J. McCawley and K. A. Rejniak. 'Towards Personalized Computational Oncology: From Spatial Models of Tumour Spheroids, to Organoids, to Tissues'. *Journal of The Royal Society Interface* 15.138 (2018), 20170703. DOI: 10.1098/rsif.2017.0703.

[204] H. B. Frieboes, M. Wu, J. Lowengrub, P. Decuzzi and V. Cristini. 'A Computational Model for Predicting Nanoparticle Accumulation in Tumor Vasculature'. *PLOS ONE* 8.2 (2013). Ed. by E. Karathanasis, e56876. DOI: 10.1371/journal.pone.0056876.

[205] E. P. Furlani and K. C. Ng. 'Analytical Model of Magnetic Nanoparticle Transport and Capture in the Microvasculature'. *Physical Review E* 73.6 (2006), 061919. DOI: 10.1103/PhysRevE.73.061919.

[206] E. J. Furlani and E. P. Furlani. 'A Model for Predicting Magnetic Targeting of Multifunctional Particles in the Microvasculature'. *Journal of Magnetism and Magnetic Materials* 312.1 (2007), 187–193. DOI: 10.1016/j.jmmm.2006.09.026.

[207] R. L. Hewlin and J. M. Tindall. 'Computational Assessment of Magnetic Nanoparticle Targeting Efficiency in a Simplified Circle of Willis Arterial Model'. *International Journal of Molecular Sciences* 24.3 (2023), 2545. DOI: 10.3390/ijms24032545.

[208] M. Shamsi, A. Sedaghatkish, M. Dejam, M. Saghafian, M. Mohammadi and A. Sanati-Nezhad. 'Magnetically Assisted Intraperitoneal Drug Delivery for Cancer Chemotherapy'. *Drug Delivery* 25.1 (2018), 846–861. DOI: 10.1080/10717544.2018.1455764.

[209] M. Rezaeian, M. Soltani, A. Naseri Karimvand and K. Raahemifar. 'Mathematical Modeling of Targeted Drug Delivery Using Magnetic Nanoparticles during Intraperitoneal Chemotherapy'. *Pharmaceutics* 14.2 (2022), 324. DOI: 10.3390/pharmaceutics14020324.

[210] A. Boussommier-Calleja, R. Li, M. B. Chen, S. C. Wong and R. D. Kamm. 'Microfluidics: A New Tool for Modeling Cancer–Immune Interactions'. *Trends in Cancer* 2.1 (2016), 6–19. DOI: 10.1016/j.trecan.2015.12.003.

[211] E. Y. Adashi, D. P. O'Mahony and I. G. Cohen. 'The FDA Modernization Act 2.0: Drug Testing in Animals Is Rendered Optional'. *The American Journal of Medicine* 136.9 (2023), 853–854. DOI: 10.1016/j.amjmed.2023.03.033.

[212] C. Sun, J. S. H. Lee and M. Zhang. 'Magnetic Nanoparticles in MR Imaging and Drug Delivery'. *Advanced Drug Delivery Reviews*. Inorganic Nanoparticles in Drug Delivery 60.11 (2008), 1252–1265. DOI: 10.1016/j.addr.2008.03.018.

[213] T. Lunnoo and T. Puangmali. 'Capture Efficiency of Biocompatible Magnetic Nanoparticles in Arterial Flow: A Computer Simulation for Magnetic Drug Targeting'. *Nanoscale Research Letters* 10.1 (2015), 426. DOI: 10.1186/s11671-015-1127-5.

[214] M. Momeni Larimi, A. Ramiar and A. A. Ranjbar. 'Magnetic Nanoparticles and Blood Flow Behavior in Non-Newtonian Pulsating Flow within the Carotid Artery in Drug Delivery Application'. *Proceedings of the Institution of Mechanical Engineers, Part H: Journal of Engineering in Medicine* 230.9 (2016), 876–891. DOI: 10.1177/0954411916656663.

[215] P. Pálovics and M. Rencz. 'Investigation of the Motion of Magnetic Nanoparticles in Microfluidics with a Micro Domain Model'. *Microsystem Technologies* 28.6 (2022), 1545–1559. DOI: 10.1007/s00542-020-05077-0.

[216] S. Sharma, A. Gaur, U. Singh and V. K. Katiyar. 'Capture Efficiency of Magnetic Nanoparticles in a Tube under Magnetic Field'. *Procedia Materials Science*. 2nd International Conference on Nanomaterials and Technologies (CNT 2014) 10 (2015), 64–69. DOI: 10.1016/j.mspro.2015.06.026.

[217] J. W. Haverkort, S. Kenjereš and C. R. Kleijn. 'Computational Simulations of Magnetic Particle Capture in Arterial Flows'. *Annals of Biomedical Engineering* 37 (2009), 2436. DOI: 10.1007/s10439-009-9786-y.

[218] J. P. Brody, P. Yager, R. E. Goldstein and R. H. Austin. 'Biotechnology at Low Reynolds Numbers.' *Biophysical Journal* 71.6 (1996), 3430–3441. DOI: 10.1016/S0006-3495(96)79538-3.

[219] H. Stone, A. Stroock and A. Ajdari. 'Engineering Flows in Small Devices: Microfluidics Toward a Lab-on-a-Chip'. *Annual Review of Fluid Mechanics* 36.1 (2004), 381–411. DOI: 10.1146/annurev.fluid.36.050802.122124.

[220] F. J. Valdés-Parada and D. Lasseux. 'A Novel One-Domain Approach for Modeling Flow in a Fluid-Porous System Including Inertia and Slip Effects'. *Physics of Fluids* 33.2 (2021), 022106. DOI: 10.1063/5.0036812.

[221] J. M. Munson and A. C. Shieh. 'Interstitial Fluid Flow in Cancer: Implications for Disease Progression and Treatment'. *Cancer Management and Research* 6 (2014), 317–328. DOI: 10.2147/CMAR.S65444.

[222] E. Henke, R. Nandigama and S. Ergün. 'Extracellular Matrix in the Tumor Microenvironment and Its Impact on Cancer Therapy'. *Frontiers in Molecular Biosciences* 6 (2020). DOI: 10.3389/fmolb.2019.00160.

[223] A. O. Ayansiji, A. V. Dighe, A. A. Linninger and M. R. Singh. 'Constitutive Relationship and Governing Physical Properties for Magnetophoresis'. *Proceedings of the National Academy of Sciences* 117.48 (2020), 30208–30214. DOI: 10.1073/pnas.2018568117.

[224] M. Takayasu, R. Gerber and F. Friedlaender. 'Magnetic Separation of Submicron Particles'. *IEEE Transactions on Magnetics* 19.5 (1983), 2112–2114. DOI: 10.1109/TMAG.1983.1062681.

[225] D. Pimponi, M. Chinappi, P. Gualtieri and C. M. Casciola. 'Mobility Tensor of a Sphere Moving on a Superhydrophobic Wall: Application to Particle Separation'. *Microfluidics and Nanofluidics* 16.3 (2014), 571–585. DOI: 10.1007/s10404-013-1243-4.

[226] K. Chen, J. Han, X. Pan and D. J. Srolovitz. 'The Grain Boundary Mobility Tensor'. *Proceedings of the National Academy of Sciences* 117.9 (2020), 4533–4538. DOI: 10.1073/pnas.1920504117.

[227] L. M. Roa-Barrantes and D. J. Rodriguez Patarroyo. 'Magnetic Field Effect on the Magnetic Nanoparticles Trajectories in Pulsating Blood Flow: A Computational Model'. *BioNanoScience* 12.2 (2022), 571–581. DOI: 10.1007/s12668-022-00949-3.

[228] M. Smoluchowski. 'Über Brownsche Molekularbewegung unter Einwirkung äußerer Kräfte und deren Zusammenhang mit der verallgemeinerten Diffusionsgleichung'. *Annalen der Physik* 4.48 (1915), 1103–1112. DOI: 10.1002/andp.19163532408.

[229] T. B. Jones. 'Fundamentals'. In: *Electromechanics of Particles*. Cambridge: Cambridge University Press, 1995, pp. 5–33. DOI: 10.1017/CBO9780511574498.004.

[230] B. Hallmark, N. J. Darton and D. Pearce. 'Modeling the In-Flow Capture of Magnetic Nanoparticles'. In: *Magnetic Nanoparticles in Biosensing and Medicine*. Ed. by A. Ionescu, J. Llandro and N. J. Darton. Cambridge: Cambridge University Press, 2019, pp. 151–171. DOI: 10.1017/9781139381222.006.

[231] E. Tiesinga, P. J. Mohr, D. B. Newell and B. N. Taylor. 'CODATA Recommended Values of the Fundamental Physical Constants: 2018'. *Reviews of Modern Physics* 93.2 (2021), 025010. DOI: 10.1103/RevModPhys.93.025010.

[232] S. A. Khashan, E. Elnajjar and Y. Haik. 'CFD Simulation of the Magnetophoretic Separation in a Microchannel'. *Journal of Magnetism and Magnetic Materials* 323.23 (2011), 2960–2967. DOI: 10.1016/j.jmmm.2011.06.001.

[233] E. E. Keaveny and M. R. Maxey. 'Modeling the Magnetic Interactions between Paramagnetic Beads in Magnetorheological Fluids'. *Journal of Computational Physics* 227.22 (2008), 9554–9571. DOI: 10.1016/j.jcp.2008.07.008.

[234] K. Han, Y. T. Feng and D. R. J. Owen. 'Three-Dimensional Modelling and Simulation of Magnetorheological Fluids'. *International Journal for Numerical Methods in Engineering* 84.11 (2010), 1273–1302. DOI: 10.1002/nme.2940.

[235] M. Woińska, J. Szczytko, A. Majhofer, J. Gosk, K. Dziatkowski and A. Twardowski. 'Magnetic Interactions in an Ensemble of Cubic Nanoparticles: A Monte Carlo Study'. *Physical Review B* 88.14 (2013), 144421. DOI: 10.1103/PhysRevB.88.144421.

[236] K. McNamara and S. A. M. Tofail. 'Nanoparticles in Biomedical Applications'. *Advances in Physics: X* 2.1 (2017), 54–88. DOI: 10.1080/23746149.2016.1254570.

[237] J. D. Jackson. *Classical Electrodynamics: International Adaptation*. 3rd ed. Hoboken, NY: Wiley, 2021.

[238] N. Derby and S. Olbert. 'Cylindrical Magnets and Ideal Solenoids'. *American Journal of Physics* 78.3 (2010), 229. DOI: 10.1119/1.3256157.

[239] A. Caciagli, R. J. Baars, A. P. Philipse and B. W. M. Kuipers. 'Exact Expression for the Magnetic Field of a Finite Cylinder with Arbitrary Uniform Magnetization'. *Journal of Magnetism and Magnetic Materials* 456 (2018), 423–432. DOI: 10.1016/j.jmmm.2018.02.003.

[240] B. C. Carlson. 'Computing Elliptic Integrals by Duplication'. *Numerische Mathematik* 33.1 (1979), 1–16. DOI: 10.1007/BF01396491.

[241] B. C. Carlson and E. M. Notis. 'Algorithms for Incomplete Elliptic Integrals'. *ACM Transactions on Mathematical Software* 7.3 (1981), 398–403. DOI: 10.1145/355958.355970.

[242] W. H. Press, S. A. Teukolsky, W. T. Vetterling and B. P. Flannery. *Numerical Recipes 3rd Edition: The Art of Scientific Computing*. Cambridge, UK: Cambridge University Press, 2007.

[243] Wolfram Research, Inc. *Mathematica, Version 13.3*. Champaign, IL, 2023. URL: https://www.wolfram.com/mathematica/.

[244] P. Virtanen, R. Gommers, T. E. Oliphant, M. Haberland, T. Reddy, D. Cournapeau, E. Burovski, P. Peterson, W. Weckesser, J. Bright, S. J. van der Walt, M. Brett *et al.* 'SciPy 1.0: Fundamental Algorithms for Scientific Computing in Python'. *Nature Methods* 17.3 (2020), 261–272. DOI: 10.1038/s41592-019-0686-2.

[245] M. Kappes, B. Friedrich, F. Pfister, C. Huber, R. P. Friedrich, R. Stein, C. Braun, J. Band, E. Schreiber, C. Alexiou and C. Janko. 'Superparamagnetic Iron Oxide Nanoparticles for Targeted Cell Seeding: Magnetic Patterning and Magnetic 3D Cell Culture'. *Advanced Functional Materials* (2022), 2203672. DOI: 10.1002/adfm.202203672.

[246] L. Etgar, A. Nakhmani, A. Tannenbaum, E. Lifshitz and R. Tannenbaum. 'Trajectory Control of PbSe–γ-Fe2O3 Nanoplatforms under Viscous Flow and an External Magnetic Field'. *Nanotechnology* 21.17 (2010), 175702. DOI: 10.1088/0957-4484/21/17/175702.

[247] S. Shaw. 'Mathematical Model on Magnetic Drug Targeting in Microvessel'. In: *Magnetism and Magnetic Materials*. IntechOpen, 2018. DOI: 10.5772/intechopen.73678.

[248] E. F. Yeo, H. Markides, A. T. Schade, A. J. Studd, J. M. Oliver, S. L. Waters and A. J. El Haj. 'Experimental and Mathematical Modelling of Magnetically Labelled Mesenchymal Stromal Cell Delivery'. *Journal of The Royal Society Interface* 18.175 (2021), 20200558. DOI: 10.1098/rsif.2020.0558.

[249] M. Marzagalli, G. Pelizzoni, A. Fedi, C. Vitale, F. Fontana, S. Bruno, A. Poggi, A. Dondero, M. Aiello, R. Castriconi, C. Bottino and S. Scaglione. 'A Multi-Organ-on-Chip to Recapitulate the Infiltration and the Cytotoxic Activity of Circulating NK Cells in 3D Matrix-Based Tumor Model'. *Frontiers in Bioengineering and Biotechnology* 10 (2022). DOI: 10.3389/fbioe.2022.945149.

[250] M. Lahonian. 'Diffusion of Magnetic Nanoparticles Within a Biological Tissue During Magnetic Fluid Hyperthermia'. In: *Hyperthermia*. Ed. by N. Huilgol. Rijeka: IntechOpen, 2013. DOI: 10.5772/52305.

[251] M. Coroneo, L. Yoshihara and W. A. Wall. 'Biofilm Growth: A Multi-Scale and Coupled Fluid-Structure Interaction and Mass Transport Approach'. *Biotechnology and Bioengineering* 111.7 (2014), 1385–1395. DOI: 10.1002/bit.25191.

[252] C. Ager, B. Schott, M. Winter and W. A. Wall. 'A Nitsche-based Cut Finite Element Method for the Coupling of Incompressible Fluid Flow with Poroelasticity'. *Computer Methods in Applied Mechanics and Engineering* 351 (2019), 253–280. DOI: 10.1016/j.cma.2019.03.015.

[253] V. Girault, G. Kanschat and B. Rivière. 'On the Coupling of Incompressible Stokes or Navier–Stokes and Darcy Flows Through Porous Media'. In: *Modelling and Simulation in Fluid Dynamics in Porous Media*. Ed. by J. A. Ferreira, S. Barbeiro, G. Pena and M. F. Wheeler. Springer Proceedings in Mathematics & Statistics. New York, NY: Springer, 2013, 1–25. DOI: 10.1007/978-1-4614-5055-9_1.

[254] K. Nguyen, B. Nuß, M. Mühlberger, H. Unterweger, R. Friedrich, C. Alexiou and C. Janko. 'Superparamagnetic Iron Oxide Nanoparticles Carrying Chemotherapeutics Improve Drug Efficacy in Monolayer and Spheroid Cell Culture by Enabling Active Accumulation'. *Nanomaterials* 10.8 (2020), 1–21. DOI: 10.3390/nano10081577.

[255] A. Tchoryk, V. Taresco, R. H. Argent, M. Ashford, P. R. Gellert, S. Stolnik, A. Grabowska and M. C. Garnett. 'Penetration and Uptake of Nanoparticles in 3D Tumor Spheroids'. *Bioconjugate Chemistry* 30.5 (2019), 1371–1384. DOI: 10.1021/acs.bioconjchem.9b00136.

[256] A. Ahmed-Cox, E. Pandzic, S. T. Johnston, C. Heu, J. McGhee, F. M. Mansfeld, E. J. Crampin, T. P. Davis, R. M. Whan and M. Kavallaris. 'Spatio-Temporal Analysis of Nanoparticles in Live Tumor Spheroids Impacted by Cell Origin and Density'. *Journal of Controlled Release* 341 (2022), 661–675. DOI: 10.1016/j.jconrel.2021.12.014.

[257] I. D. Boutopoulos, D. S. Lampropoulos, G. C. Bourantas, K. Miller and V. C. Loukopoulos. 'Two-Phase Biofluid Flow Model for Magnetic Drug Targeting'. *Symmetry* 12.7 (2020), 1083. DOI: 10.3390/sym12071083.

[258] G. Barrera, P. Allia and P. Tiberto. 'Dipolar Interactions among Magnetite Nanoparticles for Magnetic Hyperthermia: A Rate-Equation Approach'. *Nanoscale* 13.7 (2021), 4103–4121. DOI: 10.1039/D0NR07397K.

[259] P. Pálovics, M. Németh and M. Rencz. 'Investigation and Modeling of the Magnetic Nanoparticle Aggregation with a Two-Phase CFD Model'. *Energies* 13.18 (2020), 4871. DOI: 10.3390/en13184871.

[260] P. J. Cregg, K. Murphy and A. Mardinoglu. 'Inclusion of Magnetic Dipole–Dipole and Hydrodynamic Interactions in Implant-Assisted Magnetic Drug Targeting'. *Journal of Magnetism and Magnetic Materials* 321.23 (2009), 3893–3898. DOI: 10.1016/j.jmmm.2009.07.056.

[261] P. J. Cregg, K. Murphy, A. Mardinoglu and A. Prina-Mello. 'Many Particle Magnetic Dipole–Dipole and Hydrodynamic Interactions in Magnetizable Stent Assisted Magnetic Drug Targeting'. *Journal of Magnetism and Magnetic Materials* 322.15 (2010), 2087–2094. DOI: 10.1016/j.jmmm.2010.01.038.

[262] D. J. Griffiths. *Introduction to Electrodynamics*. 3rd ed. Upper Saddle River, N.J.: Prentice Hall, 2017.

[263] R. Durrett. 'Cancer Modelling: A Personal Perspective'. *Notices of the AMS* 60.3 (2013), 304–309. DOI: 10.1090/noti953.

[264] R. Durrett. 'Branching Process Models of Cancer'. In: *Branching Process Models of Cancer*. Ed. by R. Durrett. Mathematical Biosciences Institute Lecture Series. Cham: Springer International Publishing, 2015, pp. 1–63. DOI: 10.1007/978-3-319-16065-8_1.

[265] M. Baar, L. Coquille, H. Mayer, M. Hölzel, M. Rogava, T. Tüting and A. Bovier. 'A Stochastic Model for Immunotherapy of Cancer'. *Scientific Reports* 6.1 (2016), 24169. DOI: 10.1038/srep24169.

[266] G. White and I. Farrance. 'Uncertainty of Measurement in Quantitative Medical Testing'. *The Clinical Biochemist Reviews* 25.4 (2004), S1–S24. URL: https://www.ncbi.nlm.nih.gov/pubmed/18650962.

[267] S. Razavi, A. Jakeman, A. Saltelli, C. Prieur, B. Iooss, E. Borgonovo, E. Plischke, S. Lo Piano, T. Iwanaga, W. Becker, S. Tarantola, J. H. A. Guillaume *et al.* 'The Future of Sensitivity Analysis: An Essential Discipline for Systems Modeling and Policy Support'. *Environmental Modelling & Software* 137 (2021), 104954. DOI: 10.1016/j.envsoft.2020.104954.

[268] M. D. Morris. 'Factorial Sampling Plans for Preliminary Computational Experiments'. *Technometrics* 33.2 (1991), 161–174. DOI: 10.1080/00401706.1991.10484804.

[269] G. Qian and A. Mahdi. 'Sensitivity Analysis Methods in the Biomedical Sciences'. *Mathematical Biosciences* 323 (2020), 108306. DOI: 10.1016/j.mbs.2020.108306.

[270] O. K. Oyebamiji, D. J. Wilkinson, P. G. Jayathilake, T. P. Curtis, S. P. Rushton, B. Li and P. Gupta. 'Gaussian Process Emulation of an Individual-Based Model Simulation of Microbial Communities'. *Journal of Computational Science* 22 (2017), 69–84. DOI: 10.1016/j.jocs.2017.08.006.

[271] G. Karagiannis, W. Hao and G. Lin. 'Calibrations and Validations of Biological Models with an Application on the Renal Fibrosis'. *International Journal for Numerical Methods in Biomedical Engineering* 36.5 (2020), e3329. DOI: 10.1002/cnm.3329.

[272] A. C. Ross, R. G. Najjar and M. Li. 'A Metamodel-Based Analysis of the Sensitivity and Uncertainty of the Response of Chesapeake Bay Salinity and Circulation to Projected Climate Change'. *Estuaries and Coasts* (2020). DOI: 10.1007/s12237-020-00761-w.

[273] A. Hirvoas, C. Prieur, E. Arnaud, F. Caleyron and M. M. Zuniga. 'Quantification and Reduction of Uncertainties in a Wind Turbine Numerical Model Based on a Global Sensitivity Analysis and a Recursive Bayesian Inference Approach'. *International Journal for Numerical Methods in Engineering* 122.10 (2021), 2528–2544. DOI: 10.1002/nme.6630.

[274] F. Sahli Costabal, K. Matsuno, J. Yao, P. Perdikaris and E. Kuhl. 'Machine Learning in Drug Development: Characterizing the Effect of 30 Drugs on the QT Interval Using Gaussian Process Regression, Sensitivity Analysis, and Uncertainty Quantification'. *Computer Methods in Applied Mechanics and Engineering* 348 (2019), 313–333. DOI: 10.1016/j.cma.2019.01.033.

[275] I. M. Sobol'. 'On Sensitivity Estimation for Nonlinear Mathematical Models'. *Matematicheskoe modelirovanie* 2.1 (1990), 112–118.

[276] J. H. A. Guillaume, J. D. Jakeman, S. Marsili-Libelli, M. Asher, P. Brunner, B. Croke, M. C. Hill, A. J. Jakeman, K. J. Keesman, S. Razavi and J. D. Stigter. 'Introductory Overview of Identifiability Analysis: A Guide to Evaluating Whether You Have the Right Type of Data for Your Modeling Purpose'. *Environmental Modelling & Software* 119 (2019), 418–432. DOI: 10.1016/j.envsoft.2019.07.007.

[277] G. E. P. Box and R. D. Meyer. 'An Analysis for Unreplicated Fractional Factorials'. *Technometrics* 28.1 (1986), 11–18. DOI: 10.1080/00401706.1986.10488093.

[278] S. Asmussen and P. W. Glynn. *Stochastic Simulation: Algorithms and Analysis*. New York, NY, USA: Springer, 2007. DOI: 10.1007/978-0-387-69033-9.

[279] T. Ishigami and T. Homma. 'An Importance Quantification Technique in Uncertainty Analysis for Computer Models'. In: *[1990] Proceedings. First International Symposium on Uncertainty Modeling and Analysis*. 1990, 398–403. DOI: 10.1109/ISUMA.1990.151285.

[280] W. Jarosz. 'Efficient Monte Carlo Methods for Light Transport in Scattering Media'. PhD thesis. San Diego, USA: University of California, 2008.

[281] A. Saltelli. 'Making Best Use of Model Evaluations to Compute Sensitivity Indices'. *Computer Physics Communications* 145.2 (2002), 280–297. DOI: 10.1016/S0010-4655(02)00280-1.

[282] A. Saltelli, P. Annoni, I. Azzini, F. Campolongo, M. Ratto and S. Tarantola. 'Variance Based Sensitivity Analysis of Model Output. Design and Estimator for the Total Sensitivity Index'. *Computer Physics Communications* 181.2 (2010), 259–270. DOI: 10.1016/j.cpc.2009.09.018.

[283] M. J. W. Jansen. 'Analysis of Variance Designs for Model Output'. *Computer Physics Communications* 117.1-2 (1999), 35–43. DOI: 10.1016/S0010-4655(98)00154-4.

[284] I. M. Sobol', S. Tarantola, D. Gatelli, S. S. Kucherenko and W. Mauntz. 'Estimating the Approximation Error When Fixing Unessential Factors in Global Sensitivity Analysis'. *Reliability Engineering & System Safety* 92.7 (2007), 957–960. DOI: 10.1016/j.ress.2006.07.001.

[285] A. Janon, T. Klein, A. Lagnoux, M. Nodet and C. Prieur. 'Asymptotic Normality and Efficiency of Two Sobol Index Estimators'. *ESAIM: Probability and Statistics* 18 (2014), 342–364. DOI: 10.1051/ps/2013040.

[286] H. Niederreiter. *Random Number Generation and Quasi-Monte Carlo Methods*. CBMS-NSF Regional Conference Series in Applied Mathematics. Society for Industrial and Applied Mathematics, 1992. DOI: 10.1137/1.9781611970081.

[287] B. Iooss, L. Boussouf, V. Feuillard and A. Marrel. 'Numerical Studies of the Metamodel Fitting and Validation Processes'. *International Journal on Advances in Systems and Measurements* 3.1-2 (2010), 11–21. DOI: 10.48550/arXiv.1001.1049.

[288] K. Cheng, Z. Lu, C. Ling and S. Zhou. 'Surrogate-Assisted Global Sensitivity Analysis: An Overview'. *Structural and Multidisciplinary Optimization* 61.3 (2020), 1187–1213. DOI: 10.1007/s00158-019-02413-5.

[289] I. Sobol'. 'On the Distribution of Points in a Cube and the Approximate Evaluation of Integrals'. *USSR Computational Mathematics and Mathematical Physics* 7.4 (1967), 86–112. DOI: 10.1016/0041-5553(67)90144-9.

[290] M. McKay, R. Beckman and W. Conover. 'A Comparison of Three Methods for Selecting Vales of Input Variables in the Analysis of Output From a Computer Code'. *Technometrics* 21.2 (1979), 239–245. DOI: 10.1080/00401706.1979.10489755.

[291] F. Xiong, Y. Xiong, W. Chen and S. Yang. 'Optimizing Latin Hypercube Design for Sequential Sampling of Computer Experiments'. *Engineering Optimization* 41.8 (2009), 793–810. DOI: 10.1080/03052150902852999.

[292] X. Zhou, D. K. J. Lin, X. Hu and L. Ouyang. 'Sequential Latin Hypercube Design with Both Space-Filling and Projective Properties'. *Quality and Reliability Engineering International* 35.6 (2019), 1941–1951. DOI: 10.1002/qre.2485.

[293] S. Kucherenko, D. Albrecht and A. Saltelli. 'Exploring Multi-Dimensional Spaces: A Comparison of Latin Hypercube and Quasi Monte Carlo Sampling Techniques'. *arXiv:1505.02350 [stat.AP]* (2015). URL: http://arxiv.org/abs/1505.02350.

[294] J. E. Oakley and A. O'Hagan. 'Probabilistic Sensitivity Analysis of Complex Models: A Bayesian Approach'. *Journal of the Royal Statistical Society: Series B (Statistical Methodology)* 66.3 (2004), 751–769. DOI: 10.1111/j.1467-9868.2004.05304.x.

[295] A. Marrel, B. Iooss, B. Laurent and O. Roustant. 'Calculations of Sobol Indices for the Gaussian Process Metamodel'. *Reliability Engineering & System Safety* 94.3 (2009), 742–751. DOI: 10.1016/j.ress.2008.07.008.

[296] D. K. Duvenaud. 'Automatic Model Construction with Gaussian Processes'. PhD thesis. Cambridge, UK: University of Cambridge, 2014. DOI: 10.17863/CAM.14087.

[297] N. D. Goodman, T. D. Ullman and J. B. Tenenbaum. 'Learning a Theory of Causality'. *Psychological Review* 118.1 (2011), 110–119. DOI: 10.1037/a0021336.

[298] A. Pepelyshev. 'The Role of the Nugget Term in the Gaussian Process Method'. In: *mODa 9 – Advances in Model-Oriented Design and Analysis*. Ed. by A. Giovagnoli, A. C. Atkinson, B. Torsney and C. May. Contributions to Statistics. Heidelberg: Physica-Verlag HD, 2010, 149–156. DOI: 10.1007/978-3-7908-2410-0_20.

[299] I. Andrianakis and P. G. Challenor. 'The Effect of the Nugget on Gaussian Process Emulators of Computer Models'. *Computational Statistics & Data Analysis* 56.12 (2012), 4215–4228. DOI: 10.1016/j.csda.2012.04.020.

[300] Y. Bengio, O. Delalleau and N. Roux. 'The Curse of Highly Variable Functions for Local Kernel Machines'. In: *Advances in Neural Information Processing Systems (NIPS 2005)*. Vol. 18. MIT Press, 2005. URL: https://proceedings.neurips.cc/paper/2005.

[301] R. Tripathy, I. Bilionis and M. Gonzalez. 'Gaussian Processes with Built-in Dimensionality Reduction: Applications to High-Dimensional Uncertainty Propagation'. *Journal of Computational Physics* 321 (2016), 191–223. DOI: 10.1016/j.jcp.2016.05.039.

[302] H. Liu, Y.-S. Ong, X. Shen and J. Cai. 'When Gaussian Process Meets Big Data: A Review of Scalable GPs'. *IEEE Transactions on Neural Networks and Learning Systems* 31.11 (2020), 4405–4423. DOI: 10.1109/TNNLS.2019.2957109.

[303] J. Hensman, N. Fusi and N. D. Lawrence. 'Gaussian Processes for Big Data'. In: *Proceedings of the Twenty-Ninth Conference on Uncertainty in Artificial Intelligence*. UAI'13. Arlington, Virginia, USA: AUAI Press, 2013, 282–290.

[304] B. Efron. 'Bootstrap Methods: Another Look at the Jackknife'. *The Annals of Statistics* 7.1 (1979), 1–26. DOI: 10.1214/aos/1176344552.

[305] A. Janon, M. Nodet and C. Prieur. 'Uncertainties Assessment in Global Sensitivity Indices Estimation from Metamodels'. *International Journal for Uncertainty Quantification* 4.1 (2014). DOI: 10.1615/Int.J.UncertaintyQuantification.2012004291.

[306] I. Panin. 'Risk of Estimators for Sobol' Sensitivity Indices Based on Metamodels'. *Electronic Journal of Statistics* 15.1 (2021), 235–281. DOI: 10.1214/20-EJS1793.

[307] G. E. B. Archer, A. Saltelli and I. M. Sobol. 'Sensitivity Measures, Anova-like Techniques and the Use of Bootstrap'. *Journal of Statistical Computation and Simulation* 58.2 (1997), 99–120. DOI: 10.1080/00949659708811825.

[308] B. Efron and R. J. Tibshirani. *An Introduction to the Bootstrap*. 1. Edition. New York: Chapman and Hall/CRC, 1993.

[309] G. James, D. Witten, T. Hastie and R. Tibshirani. *An Introduction to Statistical Learning: With Applications in R*. Springer Texts in Statistics. New York: Springer-Verlag, 2013. DOI: 10.1007/978-1-4614-7138-7.

[310] C. E. Shannon. 'A Mathematical Theory of Communication'. *The Bell system technical journal* 27.3 (1948), 379–423. DOI: 10.1002/j.1538-7305.1948.tb01338.x.

[311] S. Kullback. *Information Theory and Statistics*. Mineola, NY, USA: Dover Publications, Inc., 1997.

[312] B. Matern. *Spatial Variation*. 2nd ed. Lecture Notes in Statistics. New York, NY: Springer, 1986. DOI: 10.1007/978-1-4615-7892-5.

[313] M. L. Stein. *Interpolation of Spatial Data: Some Theory for Kriging*. Springer Series in Statistics. New York: Springer-Verlag, 1999. DOI: 10.1007/978-1-4612-1494-6.

[314] J. E. Nash and J. V. Sutcliffe. 'River Flow Forecasting through Conceptual Models Part I — A Discussion of Principles'. *Journal of Hydrology* 10.3 (1970), 282–290. DOI: 10.1016/0022-1694(70)90255-6.

[315] T. Van Steenkiste, J. van der Herten, I. Couckuyt and T. Dhaene. 'Sequential Sensitivity Analysis of Expensive Black-Box Simulators with Metamodelling'. *Applied Mathematical Modelling* 61 (2018), 668–681. DOI: 10.1016/j.apm.2018.05.023.

[316] C. A. Micchelli, Y. Xu and H. Zhang. 'Universal Kernels'. *The Journal of Machine Learning Research* 7 (2006), 2651–2667. URL: http://jmlr.org/papers/v7/micchelli06a.html.

[317] GPy. *GPy: A Gaussian Process Framework in Python*. 2012. URL: http://github.com/SheffieldML/GPy.

[318] D. P. Kingma and J. Ba. 'Adam: A Method for Stochastic Optimization'. *arXiv:1412.6980v9 [cs.LG]* (2017). URL: http://arxiv.org/abs/1412.6980.

[319] M. Fritz, E. A. B. F. Lima, J. T. Oden and B. Wohlmuth. 'On the Unsteady Darcy–Forchheimer–Brinkman Equation in Local and Nonlocal Tumor Growth Models'. *Mathematical Models and Methods in Applied Sciences* (2019). DOI: 10.1142/S0218202519500325.

[320] F. Sarrazin, F. Pianosi and T. Wagener. 'Global Sensitivity Analysis of Environmental Models: Convergence and Validation'. *Environmental Modelling & Software* 79 (2016), 135–152. DOI: 10.1016/j.envsoft.2016.02.005.

[321] C. J. Cyron, R. C. Aydin and J. D. Humphrey. 'A Homogenized Constrained Mixture (and Mechanical Analog) Model for Growth and Remodeling of Soft Tissue'. *Biomechanics and Modeling in Mechanobiology* 15.6 (2016), 1389–1403. DOI: 10.1007/s10237-016-0770-9.

[322] C. J. Cyron and J. D. Humphrey. 'Growth and Remodeling of Load-Bearing Biological Soft Tissues'. *Meccanica* 52.3 (2017), 645–664. DOI: 10.1007/s11012-016-0472-5.

[323] F. A. Braeu. 'Three-Dimensional Homogenized Constrained Mixture Model of Anisotropic Vascular Growth and Remodeling'. PhD thesis. München: Technische Universität München, 2019.

[324] S. Brandstaeter, S. L. Fuchs, J. Biehler, R. C. Aydin, W. A. Wall and C. J. Cyron. 'Global Sensitivity Analysis of a Homogenized Constrained Mixture Model of Arterial Growth and Remodeling'. *Journal of Elasticity* (2021). DOI: 10.1007/s10659-021-09833-9.

[325] D. Rudlstorfer. 'Metamodel-Based Global Sensitivity Analysis of Reduced-Dimensional Models for Recruitment/Derecruitment Dynamics in Lung Tissue'. Term Paper. München: Technische Universität München, 2023.

[326] C. M. Geitner, L. J. Köglmeier, I. Frerichs, P. Langguth, M. Lindner, D. Schädler, N. Weiler, T. Becher and W. A. Wall. 'Pressure- and time-dependent alveolar recruitment/derecruitment in a spatially resolved patient-specific computational model for injured human lungs'. *International Journal for Numerical Methods in Biomedical Engineering* (2023), e3787. DOI: 10.1002/cnm.3787.

[327] M. Waldmann. 'Global Sensitivity Analysis of Laser Powder Bed Fusion Additive Manufacturing Process Simulation'. Bachelor's Thesis. München: Technische Universität München, 2023.

[328] S. D. Proell, P. Munch, M. Kronbichler, W. A. Wall and C. Meier. 'A Highly Efficient Computational Approach for Fast Scan-Resolved Simulations of Metal Additive Manufacturing Processes on the Scale of Real Parts'. *Additive Manufacturing* 79 (2024), 103921. DOI: 10.1016/j.addma.2023.103921.

[329] A. Wendl. 'Sensitivity Analysis for Coating Layers in All-Solid-State Batteries'. Term Paper. München: Technische Universität München, 2023.

[330] S. Sinzig, C. P. Schmidt and W. A. Wall. 'An Efficient Approach to Include Transport Effects in Thin Coating Layers in Electrochemo-Mechanical Models for All-Solid-State Batteries'. *Journal of The Electrochemical Society* 170.10 (2023), 100532. DOI: 10.1149/1945-7111/ad0264.

[331] A. Hawkins-Daarud, S. Prudhomme, K. G. van der Zee and J. T. Oden. 'Bayesian Calibration, Validation, and Uncertainty Quantification of Diffuse Interface Models of Tumor Growth'. *Journal of Mathematical Biology* 67.6 (2013), 1457–1485. DOI: 10.1007/s00285-012-0595-9.

[332] J. Collis, A. J. Connor, M. Paczkowski, P. Kannan, J. Pitt-Francis, H. M. Byrne and M. E. Hubbard. 'Bayesian Calibration, Validation and Uncertainty Quantification for Predictive Modelling of Tumour Growth: A Tutorial'. *Bulletin of Mathematical Biology* 79.4 (2017), 939–974. DOI: 10.1007/s11538-017-0258-5.

[333] S. Urcun, P.-Y. Rohan, W. Skalli, P. Nassoy, S. P. A. Bordas and G. Sciumè. 'Digital Twinning of Cellular Capsule Technology: Emerging Outcomes from the Perspective of Porous Media Mechanics'. *PLOS ONE* 16.7 (2021), e0254512. DOI: 10.1371/journal.pone.0254512.

[334] E. A. B. F. Lima, D. Faghihi, R. Philley, J. Yang, J. Virostko, C. M. Phillips and T. E. Yankeelov. 'Bayesian Calibration of a Stochastic, Multiscale Agent-Based Model for Predicting in Vitro Tumor Growth'. *PLOS Computational Biology* 17.11 (2021), e1008845. DOI: 10.1371/journal.pcbi.1008845.

[335] J. P. H. Fisher and D. A. Tweddle. 'Neonatal Neuroblastoma'. *Seminars in Fetal and Neonatal Medicine*. Cancer in the Perinatal Period 17.4 (2012), 207–215. DOI: 10.1016/j.siny.2012.05.002.

[336] W. London, R. Castleberry, K. Matthay, A. Look, R. Seeger, H. Shimada, P. Thorner, G. Brodeur, J. Maris, C. Reynolds and S. Cohn. 'Evidence for an Age Cutoff Greater Than 365 Days for Neuroblastoma Risk Group Stratification in the Children's Oncology Group'. *Journal of Clinical Oncology* 23.27 (2005), 6459–6465. DOI: 10.1200/JCO.2005.05.571.

[337] M. S. Irwin and J. R. Park. 'Neuroblastoma: Paradigm for Precision Medicine'. *Pediatric Clinics of North America*. Childhood Leukemia and Cancer 62.1 (2015), 225–256. DOI: 10.1016/j.pcl.2014.09.015.

[338] J. M. Maris. 'Recent Advances in Neuroblastoma'. *New England Journal of Medicine* 362.23 (2010), 2202–2211. DOI: 10.1056/NEJMra0804577.

[339] L. Marti-Bonmati, Á. Alberich-Bayarri, R. Ladenstein, I. Blanquer, J. D. Segrelles, L. Cerdá-Alberich, P. Gkontra, B. Hero, J. M. Garcia-Aznar, D. Keim, W. Jentner, K. Seymour *et al.* 'PRIMAGE Project: Predictive in Silico Multiscale Analytics to Support Childhood Cancer Personalised Evaluation Empowered by Imaging Biomarkers'. *European Radiology Experimental* 4.1 (2020), 22. DOI: 10.1186/s41747-020-00150-9.

[340] G. Papaioannou and K. McHugh. 'Neuroblastoma in Childhood: Review and Radiological Findings'. *Cancer Imaging* 5.1 (2005), 116–127. DOI: 10.1102/1470-7330.2005.0104.

[341] N.-K. V. Cheung and M. A. Dyer. 'Neuroblastoma: Developmental Biology, Cancer Genomics and Immunotherapy'. *Nature Reviews Cancer* 13.6 (2013), 397–411. DOI: 10.1038/nrc3526.

[342] J. M. Maris, M. D. Hogarty, R. Bagatell and S. L. Cohn. 'Neuroblastoma'. *The Lancet* 369.9579 (2007), 2106–2120. DOI: 10.1016/S0140-6736(07)60983-0.

[343] J. Wienke, M. P. Dierselhuis, G. A. M. Tytgat, A. Künkele, S. Nierkens and J. J. Molenaar. 'The Immune Landscape of Neuroblastoma: Challenges and Opportunities for Novel Therapeutic Strategies in Pediatric Oncology'. *European Journal of Cancer* 144 (2021), 123–150. DOI: 10.1016/j.ejca.2020.11.014.

[344] J. Plou, Y. Juste-Lanas, V. Olivares, C. del Amo, C. Borau and J. M. Garcia-Aznar. 'From Individual to Collective 3D Cancer Dissemination: Roles of Collagen Concentration and TGF-β'. *Scientific Reports* 8.1 (2018), 1–14. DOI: 10.1038/s41598-018-30683-4.

[345] Y. Li and E. Kumacheva. 'Hydrogel Microenvironments for Cancer Spheroid Growth and Drug Screening'. *Science Advances* 4.4 (2018), eaas8998. DOI: 10.1126/sciadv.aas8998.

[346] R. J. Murphy, A. P. Browning, G. Gunasingh, N. K. Haass and M. J. Simpson. 'Designing and Interpreting 4D Tumour Spheroid Experiments'. *Communications Biology* 5.1 (2022), 1–11. DOI: 10.1038/s42003-022-03018-3.

[347] S. M. Grist, S. S. Nasseri, L. Laplatine, J. C. Schmok, D. Yao, J. Hua, L. Chrostowski and K. C. Cheung. 'Long-Term Monitoring in a Microfluidic System to Study Tumour Spheroid Response to Chronic and Cycling Hypoxia'. *Scientific Reports* 9.1 (2019), 17782. DOI: 10.1038/s41598-019-54001-8.

[348] S. Pérez-Rodriguez, J. M. Garcia-Aznar and J. Gonzalo-Asensio. 'Microfluidic Devices for Studying Bacterial Taxis, Drug Testing and Biofilm Formation'. *Microbial Biotechnology* 15.2 (2022), 395–414. DOI: 10.1111/1751-7915.13775.

[349] Y. Shin, S. Han, J. S. Jeon, K. Yamamoto, I. K. Zervantonakis, R. Sudo, R. D. Kamm and S. Chung. 'Microfluidic Assay for Simultaneous Culture of Multiple Cell Types on Surfaces or within Hydrogels'. *Nature Protocols* 7.7 (2012), 1247–1259. DOI: 10.1038/nprot.2012.051.

[350] S. Halldorsson, E. Lucumi, R. Gómez-Sjöberg and R. M. T. Fleming. 'Advantages and Challenges of Microfluidic Cell Culture in Polydimethylsiloxane Devices'. *Biosensors and Bioelectronics* 63 (2015), 218–231. DOI: 10.1016/j.bios.2014.07.029.

[351] P. Del Moral, A. Doucet and A. Jasra. 'Sequential Monte Carlo for Bayesian Computation'. In: *Bayesian Statistics 8*. Ed. by J. M. Bernardo, M. J. Bayarri, J. O. Berger, A. P. Dawid, D. Heckerman, A. F. M. Smith and M. West. Oxford, UK: Oxford University Press, 2007, 1–34. URL: https://people.bordeaux.inria.fr/pierre.delmoral/valencia.pdf.

[352] M. Latour. 'Undifferentiated urothelial carcinomas'. In: *Uropathology, Second Edition*. 2022, pp. 253–254. DOI: 10.1016/B978-0-323-65395-4.00120-2.

[353] V. Mlakar, S. Jurkovic Mlakar, G. Lopez, J. M. Maris, M. Ansari and F. Gumy-Pause. '11q deletion in neuroblastoma: a review of biological and clinical implications'. *Molecular Cancer* 16.1 (2017), 114. DOI: 10.1186/s12943-017-0686-8.

[354] O. Moreno-Arotzena, J. G. Meier, C. Del Amo and J. M. Garcia-Aznar. 'Characterization of Fibrin and Collagen Gels for Engineering Wound Healing Models'. *Materials* 8.4 (2015), 1636–1651. DOI: 10.3390/ma8041636.

[355] L. Mohee, G. S. Offeddu, A. Husmann, M. L. Oyen and R. E. Cameron. 'Investigation of the Intrinsic Permeability of Ice-Templated Collagen Scaffolds as a Function of Their Structural and Mechanical Properties'. *Acta Biomaterialia* 83 (2019), 189–198. DOI: 10.1016/j.actbio.2018.10.034.

[356] M. T. Islam, S. Tang, C. Liverani, S. Saha, E. Tasciotti and R. Righetti. 'Non-Invasive Imaging of Young's Modulus and Poisson's Ratio in Cancers in Vivo'. *Scientific Reports* 10.1 (2020), 7266. DOI: 10.1038/s41598-020-64162-6.

[357] A. P. G. Castro, P. Laity, M. Shariatzadeh, C. Wittkowske, C. Holland and D. Lacroix. 'Combined Numerical and Experimental Biomechanical Characterization of Soft Collagen Hydrogel Substrate'. *Journal of Materials Science: Materials in Medicine* 27.4 (2016), 79. DOI: 10.1007/s10856-016-5688-3.

[358] R. C. Pereira, R. Santagiuliana, L. Ceseracciu, D. P. Boso, B. A. Schrefler and P. Decuzzi. 'Elucidating the Role of Matrix Porosity and Rigidity in Glioblastoma Type IV Progression'. *Applied Sciences* 10.24 (2020), 9076. DOI: 10.3390/app10249076.

[359] E. Monferrer, S. Martin-Vañó, A. Carretero, A. Garcia-Lizarribar, R. Burgos-Panadero, S. Navarro, J. Samitier and R. Noguera. 'A Three-Dimensional Bioprinted Model to Evaluate the Effect of Stiffness on Neuroblastoma Cell Cluster Dynamics and Behavior'. *Scientific Reports* 10.1 (2020), 6370. DOI: 10.1038/s41598-020-62986-w.

[360] Y.-L. Yang, L. M. Leone and L. J. Kaufman. 'Elastic Moduli of Collagen Gels Can Be Predicted from Two-Dimensional Confocal Microscopy'. *Biophysical Journal* 97.7 (2009), 2051–2060. DOI: 10.1016/j.bpj.2009.07.035.

[361] W. A. Lam, L. Cao, V. Umesh, A. J. Keung, S. Sen and S. Kumar. 'Extracellular Matrix Rigidity Modulates Neuroblastoma Cell Differentiation and N-myc Expression'. *Molecular Cancer* 9.1 (2010), 35. DOI: 10.1186/1476-4598-9-35.

[362] L. Brazdaru, M. Micutz, T. Staicu, M. Albu, D. Sulea and M. Leca. 'Structural and Rheological Properties of Collagen Hydrogels Containing Tannic Acid and Chlorhexidine Digluconate Intended for Topical Applications'. *Comptes Rendus Chimie* 18.2 (2015), 160–169. DOI: 10.1016/j.crci.2014.07.007.

[363] J. Stepanovska, M. Supova, K. Hanzalek, A. Broz and R. Matejka. 'Collagen Bioinks for Bioprinting: A Systematic Review of Hydrogel Properties, Bioprinting Parameters, Protocols, and Bioprinted Structure Characteristics'. *Biomedicines* 9.9 (2021), 1137. DOI: 10.3390/biomedicines9091137.

[364] C. Rianna and M. Radmacher. 'Comparison of Viscoelastic Properties of Cancer and Normal Thyroid Cells on Different Stiffness Substrates'. *European Biophysics Journal* 46.4 (2017), 309–324. DOI: 10.1007/s00249-016-1168-4.

[365] X. Zhang, X. Chen and H. Tan. 'On the Thin-Film-Dominated Passing Pressure of Cancer Cell Squeezing through a Microfluidic CTC Chip'. *Microfluidics and Nanofluidics* 21.9 (2017), 146. DOI: 10.1007/s10404-017-1986-4.

[366] E. Evans and A. Yeung. 'Apparent Viscosity and Cortical Tension of Blood Granulocytes Determined by Micropipet Aspiration.' *Biophysical Journal* 56.1 (1989), 151–160. DOI: 10.1016/S0006-3495(89)82660-8.

[367] M. A. Tsai, R. S. Frank and R. E. Waugh. 'Passive Mechanical Behavior of Human Neutrophils: Power-Law Fluid.' *Biophysical Journal* 65.5 (1993), 2078–2088. DOI: 10.1016/S0006-3495(93)81238-4.

[368] C. T. Lim, E. H. Zhou and S. T. Quek. 'Mechanical Models for Living Cells—a Review'. *Journal of Biomechanics* 39.2 (2006), 195–216. DOI: 10.1016/j.jbiomech.2004.12.008.

[369] T. Vicar, J. Chmelik, J. Navratil, R. Kolar, L. Chmelikova, V. Cmiel, J. Jagos, I. Provaznik, M. Masarik and J. Gumulec. 'Cancer Cell Viscoelasticity Measurement by Quantitative Phase and Flow Stress Induction'. *Biophysical Journal* 121.9 (2022), 1632–1642. DOI: 10.1016/j.bpj.2022.04.002.

[370] K. Wang, X. H. Sun, Y. Zhang, T. Zhang, Y. Zheng, Y. C. Wei, P. Zhao, D. Y. Chen, H. A. Wu, W. H. Wang, R. Long, J. B. Wang *et al.* 'Characterization of Cytoplasmic Viscosity of Hundreds of Single Tumour Cells Based on Micropipette Aspiration'. *Royal Society Open Science* 6.3 (2019), 181707. DOI: 10.1098/rsos.181707.

[371] A. Preetha, N. Huilgol and R. Banerjee. 'Interfacial Properties as Biophysical Markers of Cervical Cancer'. *Biomedicine & Pharmacotherapy* 59.9 (2005), 491–497. DOI: 10.1016/j.biopha.2005.02.005.

[372] T. Bayes and R. Price. 'LII. An Essay towards Solving a Problem in the Doctrine of Chances. By the Late Rev. Mr. Bayes, F. R. S. Communicated by Mr. Price, in a Letter to John Canton, A. M. F. R. S'. *Philosophical Transactions of the Royal Society of London* 53 (1763), 370–418. DOI: 10.1098/rstl.1763.0053.

[373] A. Tarantola. *Inverse Problem Theory and Methods for Model Parameter Estimation*. Philadelphia: SIAM, 2005. DOI: 10.1137/1.9780898717921.

[374] H. Jalal, T. A. Trikalinos and F. Alarid-Escudero. 'BayCANN: Streamlining Bayesian Calibration With Artificial Neural Network Metamodeling'. *Frontiers in Physiology* 12 (2021). DOI: 10.3389/fphys.2021.662314.

[375] I. Bilionis and N. Zabaras. 'Solution of Inverse Problems with Limited Forward Solver Evaluations: A Bayesian Perspective'. *Inverse Problems* 30.1 (2013), 015004. DOI: 10.1088/0266-5611/30/1/015004.

[376] C. Kahle, K. F. Lam, J. Latz and E. Ullmann. 'Bayesian Parameter Identification in Cahn–Hilliard Models for Biological Growth'. *SIAM/ASA Journal on Uncertainty Quantification* 7.2 (2019), 526–552. DOI: 10.1137/18M1210034.

[377] N. Chopin and O. Papaspiliopoulos. *An Introduction to Sequential Monte Carlo*. Springer Series in Statistics. Cham: Springer International Publishing, 2020. DOI: 10.1007/978-3-030-47845-2.

[378] P. S. Koutsourelakis. 'A Multi-Resolution, Non-Parametric, Bayesian Framework for Identification of Spatially-Varying Model Parameters'. *Journal of Computational Physics* 228.17 (2009), 6184–6211. DOI: 10.1016/j.jcp.2009.05.016.

[379] C. A. Naesseth, F. Lindsten and T. B. Schön. 'Elements of Sequential Monte Carlo'. *Foundations and Trends® in Machine Learning* 12.3 (2019), 307–392. DOI: 10.1561/2200000074.

[380] B. Larson and E. Abueg. *Z-Stacking of Single Plane Digital Widefield Fluorescent Images Incorporation of the Cytation™ 3 Cell Imaging Multi-Mode Reader and CombineZP Software to Create Deconvoluted, Stacked Images of 3D in Vitro Cell Models Application Note*. 2013. URL: https://www.semanticscholar.org/paper/Z-Stacking-of-Single-Plane-Digital-Widefield-Images-Larson-Abueg/occ73956561604994 88be0a748d59a869cf7bcf1.

[381] M. A. G. Barbosa, C. P. R. Xavier, R. F. Pereira, V. Petrikaitė and M. H. Vasconcelos. '3D Cell Culture Models as Recapitulators of the Tumor Microenvironment for the Screening of Anti-Cancer Drugs'. *Cancers* 14.1 (2022), 190. DOI: 10.3390/cancers14010190.

[382] M. K. Hall, A. P. Burch and R. A. Schwalbe. 'Functional Analysis of N-acetylglucosaminyltransferase-I Knockdown in 2D and 3D Neuroblastoma Cell Cultures'. *PLOS ONE* 16.11 (2021), e0259743. DOI: 10.1371/journal.pone.0259743.

[383] C. H. Quinn, A. M. Beierle and E. A. Beierle. 'Artificial Tumor Microenvironments in Neuroblastoma'. *Cancers* 13.7 (2021), 1629. DOI: 10.3390/cancers13071629.

[384] V. Zingales, N. Torriero, L. Zanella, M. Fernández-Franzón, M.-J. Ruiz, M. R. Esposito and E. Cimetta. 'Development of an in Vitro Neuroblastoma 3D Model and Its Application for Sterigmatocystin-Induced Cytotoxicity Testing'. *Food and Chemical Toxicology* 157 (2021), 112605. DOI: 10.1016/j.fct.2021.112605.

[385] C. Gavin, N. Geerts, B. Cavanagh, M. Haynes, C. P. Reynolds, D. Loessner, A. J. Ewald and O. Piskareva. 'Neuroblastoma Invasion Strategies Are Regulated by the Extracellular Matrix'. *Cancers* 13.4 (2021), 736. DOI: 10.3390/cancers13040736.

[386] A. Kock, F. Bergqvist, J. Steinmetz, L. H. M. Elfman, M. Korotkova, J. I. Johnsen, P.-J. Jakobsson, P. Kogner and K. Larsson. 'Establishment of an in Vitro 3D Model for Neuroblastoma Enables Preclinical Investigation of Combined Tumor-Stroma Drug Targeting'. *The FASEB Journal* 34.8 (2020), 11101–11114. DOI: 10.1096/fj.202000684R.

[387] Q. Wang, T. Nakashima, C. Lai, H. Mutsuda, T. Kanehira, Y. Konishi and H. Okuizumi. 'Modified Algorithms for Fast Construction of Optimal Latin-Hypercube Design'. *IEEE Access* 8 (2020), 191644–191658. DOI: 10.1109/ACCESS.2020.3032122.

[388] S. Joshi. 'Targeting the Tumor Microenvironment in Neuroblastoma: Recent Advances and Future Directions'. *Cancers* 12.8 (2020), 2057. DOI: 10.3390/cancers12082057.

[389] I. Tadeo, A. P. Berbegall, V. Castel, P. García-Miguel, R. Callaghan, S. Påhlman, S. Navarro and R. Noguera. 'Extracellular Matrix Composition Defines an Ultra-High-Risk Group of Neuroblastoma within the High-Risk Patient Cohort'. *British Journal of Cancer* 115.4 (2016), 480–489. DOI: 10.1038/bjc.2016.210.

[390] X. Cao, R. Ashfaq, F. Cheng, S. Maharjan, J. Li, G. Ying, S. Hassan, H. Xiao, K. Yue and Y. S. Zhang. 'A Tumor-on-a-Chip System with Bioprinted Blood and Lymphatic Vessel Pair'. *Advanced Functional Materials* 29.31 (2019), 1807173. DOI: 10.1002/adfm.201807173.

[391] V. Kumar and S. Varghese. 'Ex Vivo Tumor-on-a-Chip Platforms to Study Intercellular Interactions within the Tumor Microenvironment'. *Advanced Healthcare Materials* 8.4 (2019), 1801198. DOI: 10.1002/adhm.201801198.

[392] K. Feng, Z. Lu and C. Yang. 'Enhanced Morris Method for Global Sensitivity Analysis: Good Proxy of Sobol' Index'. *Structural and Multidisciplinary Optimization* 59.2 (2019), 373–387. DOI: 10.1007/s00158-018-2071-7.

[393] Y. Kim, G. Powathil, H. Kang, D. Trucu, H. Kim, S. Lawler and M. Chaplain. 'Strategies of Eradicating Glioma Cells: A Multi-Scale Mathematical Model with MiR-451-AMPK-mTOR Control'. *PLOS ONE* 10.1 (2015), e0114370. DOI: 10.1371/journal.pone.0114370.

[394] D. Alemani, F. Pappalardo, M. Pennisi, S. Motta and V. Brusic. 'Combining Cellular Automata and Lattice Boltzmann Method to Model Multiscale Avascular Tumor Growth Coupled with Nutrient Diffusion and Immune Competition'. *Journal of Immunological Methods* 376.1 (2012), 55–68. DOI: 10.1016/j.jim.2011.11.009.

[395] I. G. Gonçalves and J. M. Garcia-Aznar. 'Extracellular Matrix Density Regulates the Formation of Tumour Spheroids through Cell Migration'. *PLOS Computational Biology* 17.2 (2021), e1008764. DOI: 10.1371/journal.pcbi.1008764.

[396] O. Chaudhuri, L. Gu, M. Darnell, D. Klumpers, S. A. Bencherif, J. C. Weaver, N. Huebsch and D. J. Mooney. 'Substrate Stress Relaxation Regulates Cell Spreading'. *Nature Communications* 6.1 (2015), 6365. DOI: 10.1038/ncomms7365.

[397] Y. Li and E. Kumacheva. 'Hydrogel Microenvironments for Cancer Spheroid Growth and Drug Screening'. *Science Advances* 4.4 (2017), eaas8998. DOI: 10.1126/sciadv.aas8998.

[398] M. L. Oyen. 'Mechanical Characterisation of Hydrogel Materials'. *International Materials Reviews* 59.1 (2014), 44–59. DOI: 10.1179/1743280413Y.0000000022.

[399] P. S. Koutsourelakis. 'Variational Bayesian Strategies for High-Dimensional, Stochastic Design Problems'. *Journal of Computational Physics* 308 (2016), 124–152. DOI: 10.1016/j.jcp.2015.12.031.

[400] W. A. Wall, J. Nitzler, G. Robalo Rei and M. Dinkel. *Inverse Analysis Bonus Option via Multiphysics Modeling*. Athens, 2023. URL: https://2023.uncecomp.org/proceedings/pdf/20011.pdf.

[401] A. Acuna, S. H. Sofronici, C. J. Goergen and S. Calve. 'In Situ Measurement of Native Extracellular Matrix Strain'. *Experimental Mechanics* 59.9 (2019), 1307–1321. DOI: 10.1007/s11340-019-00499-y.

[402] J. A. Mulligan, F. Bordeleau, C. A. Reinhart-King and S. G. Adie. 'Measurement of Dynamic Cell-Induced 3D Displacement Fields in Vitro for Traction Force Optical Coherence Microscopy'. *Biomedical Optics Express* 8.2 (2017), 1152–1171. DOI: 10.1364/BOE.8.001152.

[403] E. A. B. F. Lima, N. Ghousifam, A. Ozkan, J. T. Oden, A. Shahmoradi, M. N. Rylander, B. Wohlmuth and T. E. Yankeelov. 'Calibration of Multi-Parameter Models of Avascular Tumor Growth Using Time Resolved Microscopy Data'. *Scientific Reports* 8.1 (2018), 1–17. DOI: 10.1038/s41598-018-32347-9.

[404] M. Truffi, L. Sorrentino and F. Corsi. 'Fibroblasts in the Tumor Microenvironment'. In: *Tumor Microenvironment: Non-Hematopoietic Cells*. Ed. by A. Birbrair. Advances in Experimental Medicine and Biology. Cham: Springer International Publishing, 2020, pp. 15–29. DOI: 10.1007/978-3-030-37184-5_2.

[405] I. G. Reddin, T. R. Fenton, M. N. Wass and M. Michaelis. 'Large Inherent Variability in Data Derived from Highly Standardised Cell Culture Experiments'. *Pharmacological Research* 188 (2023), 106671. DOI: 10.1016/j.phrs.2023.106671.

[406] D. Wirtz, K. Konstantopoulos and P. C. Searson. 'The Physics of Cancer: The Role of Physical Interactions and Mechanical Forces in Metastasis'. *Nature Reviews Cancer* 11.7 (2011), 512–522. DOI: 10.1038/nrc3080.

[407] O. Ganier, D. Schnerch, P. Oertle, R. Y. H. Lim, M. Plodinec and E. A. Nigg. 'Structural Centrosome Aberrations Promote Non-Cell-Autonomous Invasiveness'. *Embo Journal* 37.9 (2018), e98576. DOI: 10.15252/embj.201798576.

[408] T. Yeung, P. C. Georges, L. A. Flanagan, B. Marg, M. Ortiz, M. Funaki, N. Zahir, W. Ming, V. Weaver and P. A. Janmey. 'Effects of Substrate Stiffness on Cell Morphology, Cytoskeletal Structure, and Adhesion'. *Cell Motility* 60.1 (2005), 24–34. DOI: 10.1002/cm.20041.

[409] J. S. H. Lee, P. Panorchan, C. M. Hale, S. B. Khatau, T. P. Kole, Y. Tseng and D. Wirtz. 'Ballistic Intracellular Nanorheology Reveals ROCK-hard Cytoplasmic Stiffening Response to Fluid Flow'. *Journal of Cell Science* 119.9 (2006), 1760–1768. DOI: 10.1242/jcs.02899.

[410] P. Gottheil, J. Lippoldt, S. Grosser, F. Renner, M. Saibah, D. Tschodu, A.-K. Poßögel, A.-S. Wegscheider, B. Ulm, K. Friedrichs, C. Lindner, C. Engel *et al.* 'State of Cell Unjamming Correlates with Distant Metastasis in Cancer Patients'. *Physical Review X* 13.3 (2023), 031003. DOI: 10.1103/PhysRevX.13.031003.

[411] E. B. Rankin and A. J. Giaccia. 'Hypoxic Control of Metastasis'. *Science* 352.6282 (2016), 175–180. DOI: 10.1126/science.aaf4405.

[412] M. Plodinec, M. Loparic, C. A. Monnier, E. C. Obermann, R. Zanetti-Dallenbach, P. Oertle, J. T. Hyotyla, U. Aebi, M. Bentires-Alj, R. Y. H. Lim and C.-A. Schoenenberger. 'The Nanomechanical Signature of Breast Cancer'. *Nature Nanotechnology* 7.11 (2012), 757–765. DOI: 10.1038/nnano.2012.167.

[413] R. N. Gutenkunst, J. J. Waterfall, F. P. Casey, K. S. Brown, C. R. Myers and J. P. Sethna. 'Universally Sloppy Parameter Sensitivities in Systems Biology Models'. *PLOS Computational Biology* 3.10 (2007), e189. DOI: 10.1371/journal.pcbi.0030189.

[414] C. Poon. 'Measuring the Density and Viscosity of Culture Media for Optimized Computational Fluid Dynamics Analysis of in Vitro Devices'. *Journal of the Mechanical Behavior of Biomedical Materials* 126 (2022), 105024. DOI: 10.1016/j.jmbbm.2021.105024.

[415] W. Li, H.-F. Wang, Z.-Y. Li, T. Wang and C.-X. Zhao. 'Numerical Investigation of Drug Transport from Blood Vessels to Tumour Tissue Using a Tumour-Vasculature-on-a-Chip'. *Chemical Engineering Science* 208 (2019), 115155. DOI: 10.1016/j.ces.2019.115155.

[416] A. G. Mikos and J. S. Temenoff. 'Formation of Highly Porous Biodegradable Scaffolds for Tissue Engineering'. *Electronic Journal of Biotechnology* 3.2 (2000). DOI: 10.2225/vol3-issue2-fulltext-5.

[417] S. Totti, M. C. Allenby, S. B. D. Santos, A. Mantalaris and E. G. Velliou. 'A 3D Bioinspired Highly Porous Polymeric Scaffolding System for in Vitro Simulation of Pancreatic Ductal Adenocarcinoma'. *RSC Advances* 8.37 (2018), 20928–20940. DOI: 10.1039/C8RA02633E.

[418] A. Popel. 'Theory of Oxygen-Transport to Tissue'. *Critical Reviews in Biomedical Engineering* 17.3 (1989), 257–321.

[419] M. Welter, T. Fredrich, H. Rinneberg and H. Rieger. 'Computational Model for Tumor Oxygenation Applied to Clinical Data on Breast Tumor Hemoglobin Concentrations Suggests Vascular Dilatation and Compression'. *PLOS ONE* 11.8 (2016). Ed. by T. W. Secomb, e0161267. DOI: 10.1371/journal.pone.0161267.

[420] D. Goldman. 'Theoretical Models of Microvascular Oxygen Transport to Tissue'. *Microcirculation* 15.8 (2008), 795–811. DOI: 10.1080/10739680801938289.